

**Polymerization of highly viscous  
bicontinuous and droplet  
microemulsions**

Inaugural - Dissertation

zur  
Erlangung des Doktorgrades  
der Mathematisch-Naturwissenschaftlichen Fakultät  
der Universität zu Köln

vorgelegt von

Regina Schwering  
geboren in Münster

Köln 2008

Berichtersteller: Prof. Dr. Reinhard Strey, Universität zu Köln

Prof. Dr. Klaus Meerholz, Universität zu Köln

Prof. Dr. Howard T. Davis, University of Minnesota

Tag der mündlichen Prüfung: 28.10.2008

*Serenity Prayer*

*God grant me  
the Serenity  
to accept things  
I cannot change,  
the courage to change  
the things I can,  
and the Wisdom to know  
the difference.*





## Abstract

Complex fluids are extensively used as templates for the synthesis of nanomaterials due to their large variety of nanostructures. However, up to date the challenge is to copy the microemulsion structure to the desired microstructure of the polymer on a one-to-one scale. Recently *Co et al.* used a new class of highly viscous microemulsions that are composed of surfactant, polymerizable oil, and sugar to maintain the microstructure after polymerization [F. Gao, C.-C. Ho, and C.C. Co, *J. Am. Chem. Soc.* **126**, 12746 (2004)]. The addition of sugar enables the reorganization kinetics of the phase behavior to be slowed down so that a changing monomer/polymer ratio during the polymerization does not lead to a phase separation. In this study, we systematically investigate the phase behavior of highly viscous sugar microemulsions. Starting from the sugar-free nonionic system  $\text{H}_2\text{O} - n\text{-octane} - n\text{-alkylpolyglycoether (C}_i\text{E}_j)$  the amount of sucrose/trehalose within the water phase was increased up to 75%. The addition of sugar shifts the phase boundaries to lower temperatures. The shift of the phase boundaries can be compensated by replacing the  $\text{C}_i\text{E}_j$ -surfactants with a more hydrophilic sugar surfactant. To formulate a highly viscous, polymerizable microemulsion, which can be polymerized via UV-irradiation,  $n$ -octane was replaced with a methacrylate oil. The obtained structures were investigated by dynamic light scattering, scanning electron microscopy and small angle neutron scattering. It is shown for the first time that the size of the polymeric nanoparticles strongly correlates with the size of the underlying microemulsion. Systematic variations in composition and temperature provide polymer particles with radii between 10 to 100 nm. Furthermore for the first time, both lamellar and bicontinuous structures could be copied nearly one-to-one to the nanoporous polymer material. The unpolymerized microemulsion and the nanomaterial were studied by small angle neutron scattering, scanning electron microscopy as well as by transmission electron microscopy.

## Kurzzusammenfassung

Komplexe Fluide werden aufgrund ihrer vielfältigen Nanostrukturen häufig als Template für die Synthese von Nanomaterialien eingesetzt. Allerdings besteht bis heute die Herausforderung, die Mikroemulsionsstruktur eins zu eins auf die gewünschte Mikrostruktur von Polymermaterialien zu übertragen. *Co et al.* haben kürzlich eine neue Klasse von hochviskosen Mikroemulsionen bestehend aus Tensid, polymerisierbarem Öl und Zucker entwickelt, um die Mikrostruktur nach der Polymerisation zu erhalten [F. Gao, C.-C. Ho und C.C. Co, *J. Am. Chem. Soc.* **126**, 12746 (2004)]. Die Zugabe von Zucker ermöglicht die Verlangsamung der Reorganisationskinetik des Phasenverhaltens, so dass das sich während der Polymerisation ändernde Monomer/Polymer Verhältnis nicht zu einer Phasentrennung führt. In dieser Arbeit untersuchen wir erstmals systematisch das Phasenverhalten von hochviskosen Zuckermikroemulsionen. Beginnend mit dem zuckerfreien System H<sub>2</sub>O – *n*-Oktan – *n*-Alkylpolyglykoether (C<sub>i</sub>E<sub>j</sub>) wurde der Anteil an Saccharose/Trehalose in der wässrigen Phase bis auf 75% erhöht. Die Hinzugabe von Zucker verschiebt die Phasengrenzen zu niedrigeren Temperaturen. Dies kann kompensiert werden, indem man die C<sub>i</sub>E<sub>j</sub>-Tenside durch ein hydrophileres Zuckertensid ersetzt. Um eine hochviskose, polymerisierbare Mikroemulsion zu formulieren, die mit Hilfe von UV-Licht polymerisiert werden kann, wurde *n*-Oktan durch ein Methacrylatöl ersetzt. Die erhaltenen Strukturen wurden mit Hilfe von dynamischer Lichtstreuung, Rasterelektronenmikroskopie und Kleinwinkelneutronenstreuung untersucht und zeigen erstmalig, dass die Größe der gebildeten Polymerpartikel stark mit der Größe der zugrundeliegenden Mikroemulsion korreliert. Systematische Variationen von Zusammensetzung und Temperatur liefern Polymerpartikel mit Radien zwischen 10 und 100 nm. Zudem konnten erstmalig sowohl lamellare als auch bikontinuierliche Strukturen fast eins zu eins auf nanoporöse Polymermaterialien kopiert werden. Die unpolymerisierten Mikroemulsionen und die erhaltenen Nanomaterialien wurden mit Hilfe von Kleinwinkelneutronenstreuung, Rasterelektronenmikroskopie sowie Transmissionselektronenmikroskopie untersucht.

# Table of Contents

<b>List of Important Symbols</b>	<b>V</b>
<b>1 Introduction</b>	<b>1</b>
1.1 Task Description	4
<b>2 Basics</b>	<b>7</b>
2.1 Phase Behavior	7
2.2 Polymerization	19
<b>3 Experimental Techniques</b>	<b>27</b>
3.1 Phase behavior	27
3.2 Polymerization	28
3.3 Densitometry	29
3.4 Viscometry	29
3.5 Dynamic Light Scattering	30
3.6 Small Angle Neutron Scattering	32
3.7 Scanning Electron Microscopy	33
3.8 Transmission Electron Microscopy	35
3.9 Polarized Light Transmission Microscopy	36
<b>4 Phase Behavior of Highly Viscous Microemulsions</b>	<b>37</b>
4.1 Influence of Sugar on the Phase Behavior	37
4.2 Highly Viscous Polymerizable Microemulsions	46
4.3 Cross-linker Variation	56
4.4 Blockcopolymers	61
4.5 The $T(W_B)$ -section of highly viscous microemulsions	63
<b>5 Polymerization of Microemulsion Droplets</b>	<b>67</b>
5.1 State of the Art	67
5.2 Initiation via a Microscopy Lamp	69
5.3 Wave Length of Initiation	79
5.4 Initiation via a UV-Lamp	80
5.5 SANS and SEM Study of the Droplet Structure	93
<b>6 Polymerization of Bicontinuously Structured Microemulsions</b>	<b>101</b>
6.1 State of the Art	101
6.2 The Unpolymerized System $H_2O/sugar - C_6MA - surfactant$	104
6.3 The Polymerized System $H_2O/sugar - C_6MA - surfactant$	113
6.4 The Polymerized System $H_2O/sugar - C_6MA/EGDMA - surfactant$	122
6.5 The Polymerized System $H_2O/sugar - C_{12}MA - surfactant$	125
<b>7 Summary</b>	<b>129</b>
<b>A Appendix</b>	<b>133</b>



# List of Important Symbols

## Latin characters

$A$	index for hydrophilic component
$a_c$	surface of a surfactant molecule
$a_2, c_1, c_2$	coefficients of the <i>Teubner-Strey</i> equation
$\alpha(n)$	denotes the correlation function $\langle (u_n - u_0)^2 \rangle / 2d^2$
$B$	index for hydrophobic component
BE	backscattered electrons
$C$	index for surfactant component
$cep_\alpha$	critical end-point on the oil-rich side
$cep_\beta$	critical end-point on the water-rich side
$C_iE_j$	alkylpolyglycoether
$C_mG_n$	$n$ -alkyl glucoside
CLF	Candau-Leong-Fitch
$C_xMA$	methacrylate oil
$C_6MA$	hexyl methacrylate
$C_{12}MA$	dodecyl methacrylate
$D$	index for co-surfactant component
$D$	diffusion coefficient
$D_{c,critical}$	critical value of cross-linking density
$d_{TS}$	domain size according to <i>Teubner-Strey</i> equation
DIC	differential interference contrast
DLS	dynamic light scattering
$D_2O$	deuterium oxide
$E_{photon}$	energy of photons
$efb$	emulsification failure boundary
EGDMA	ethylene glycol dimethacrylate
$F$	<i>Stokes</i> -force
$f_a$	amphiphilicity factor
FFDI	freeze fracture direct imaging
FFEM	freeze fracture electron microscopy
$g$	gravity
$G(\Gamma)$	weight function
$g_1(\tau)$	normalized field correlation function
$g_2(\tau)$	standardized autocorrelation function
$H_i$	hexagonal phase
$H_2O$	water
$I$	intensity
$I_0$	light intensity incident on the monomer
$I_a$	intensity of adsorbed light
$I_{incoh}$	incoherent scattering
$k_B$	<i>Boltzmann</i> constant
$k_p$	rate constant for the propagation step
$k_t$	rate constant of the termination step

$L_a$	lamellar phase
$L_1$	distance to the detector
$L_2$	distance to the collimator
$[M]$	monomer concentration
$[M \cdot]$	total concentration of all chain radicals
$m_A$	mass of hydrophilic phase in the sample
$m_B$	mass of hydrophobic phase in the sample
$m_C$	mass of surfactant in the sample
$m_{C \times MA}$	mass of methacrylate oil in the sample
$m_D$	mass of co-surfactant in the sample
$m_{n-octane}$	mass of <i>n</i> -octane in the sample
$m_{sucrose}$	mass of sucrose in the sample
$m_{sugar}$	mass of sugar in the sample
$m_{trehalose}$	mass of trehalose in the sample
$m_{water}$	mass of water in the sample
$M_e$	critical molecular weight for entanglement
$M_w$	weight-average molecular weight
$n$	refraction index
$N_{droplet}$	number of droplets
$N_{photon}$	number of photons
NMR	nuclear magnetic resonance
o/w	oil-in-water droplets
$p$	polydispersity index
$P(q)$	form factor
PMMA	polymethyl methacrylate
$q$	scattering vector
$\Delta q^2$	resolution function
$r$	radius
$R_{calc}$	calculated radius for a microemulsion droplet
$R_{hydr}$	hydrodynamic radius
$R_i$	rate of the initiation step
$R_p$	rate of propagation
$S(q)$	structure factor
SANS	small angle neutron scattering
SE	secondary electrons
SEM	scanning electron microscopy
$T$	thickness of diffuse interface
$T$	temperature
$\tilde{T}$	temperature at the fish-tail point
$T_l$	<i>T lower</i>
$T_m$	temperature at the optimal state in the phase diagram
$T_u$	<i>T upper</i>
Ta/W	tantalum/tungsten
TEM	transmission electron microscopy
UV	ultraviolet
$\nu$	fallig time
$\nu_c$	volume of a surfactant molecule
$V_i$	cubic phase
w/o	water-in-oil droplets
$w_A$	mass fraction of hydrophilic phase

$w_B$	mass fraction of hydrophobic phase
$w_C$	surfactant mass fraction
wt. %	weight percent
$\tilde{X}$	fish-tail point for arbitrary $\alpha$

**Greek characters**

$\alpha$	mass fraction of oil in the mixture of water and oil
$\beta$	mass fraction of $C_xMA$ in the oil phase or mass fraction of EGDMA in the monomer phase
$\beta$	divergence from ideal correlation
$\chi_t$	initiator concentration in the initiator/monomer mixture
$\delta$	mass fraction of the co-surfactant D in the mixture of the surfactants C and D
$\delta$	geometric thickness of the hydrophobic part
$\Phi$	quantum yield for radical production
$\varepsilon$	molar absorptivity of the monomer
$\phi$	volume fraction of oil in the mixture of water and oil
$\phi_b$	volume fraction of monomer/initiator in the system
$\phi_c$	volume fraction of surfactant in the system
$\gamma$	surfactant mass fraction in the system
$\tilde{\gamma}$	surfactant mass fraction at the $\tilde{X}$ -point
$\gamma_a$	mass fraction of the surfactant in the surfactant/water mixture
$\gamma_0$	mass fraction of maximal dissolved surfactant monomers in the water-oil mixture
$\Gamma$	decay rate
$\eta$	viscosity
$\lambda$	wave length
$\theta$	scattering angle
$\rho$	density
$\Delta\rho$	difference in scattering length density
$\rho_A$	density of the hydrophilic phase
$\rho_B$	density of the hydrophobic phase
$\sigma_R$	standard deviation
$\tau$	delay time
$\xi_{TS}$	correlation length
$\Psi$	mass fraction of the sugar in the mixture of water and sugar
$\zeta$	mass fraction of trehalose in the sucrose/trehalose mixture



# 1 Introduction

Plastic materials, the general term for a wide range of synthetic or semisynthetic polymerized products, are in our world omnipresent and in material properties often unrivaled. The advantages of polymers are the very different material characteristics possible due to the individual combination of different molecular components. With only a few chemical elements such as carbon, hydrogen and oxygen it is possible to formulate elastic, highly flexible or even hard and brittle polymers. The increasing industrial requirements lead to investigations for new and more complex materials that can be formulated easily. Here, the self-assembly of molecules is of eminent importance. Self-organizing polymer structures can be formulated either by an organized monomer system which is polymerized or by implementing a self-organizing polymer. As microemulsions are self-organizing materials and due to the ample fluid structures occurring in microemulsions the polymerization of its structure is of great interest.

Microemulsions are thermodynamically stable and macroscopically homogeneous although ample microscopical structures can be found. They consist of at least two immiscible components: A hydrophilic component such as water (A) and a hydrophobic component which can be an oil (B) [1,2]. To solubilize these two immiscible components, an amphiphile composed of a hydrophobic and a hydrophilic part (C) has to be added. These amphiphilic molecules, which are normally surfactants, adsorb at the water/oil-interface and decrease the interfacial tension between the two immiscible components strongly. On a microscopic level an extended interfacial film is formed that separates the water and the oil domains. Depending on different factors such as temperature, pressure, overall composition, amphiphilicity of the surfactant, etc. microstructures with a typical domain size ranging from 1 to 100 nm can appear [3]. The variety of microstructures ranges from droplets and tubes to networks and sponge-like bicontinuous structures. Depending on the system, also liquid crystalline phases as the lamellar ( $L_\alpha$ ), hexagonal ( $H_i$ ) or cubic phase ( $V_i$ ) occur [4].

The type of the structure formed is mainly determined by the spontaneous curvature of

the amphiphilic film [5]. For strongly hydrated headgroups of an e.g. nonionic surfactant, the amphiphilic film curves spontaneously around the oil, i.e. oil-in-water droplets are formed. With increasing temperature the hydrogen bonds are loosened and the curvature around the oil decreases. At a characteristic temperature the spontaneous curvature becomes zero and sponge-like bicontinuous and lamellar structures can be found. A further increase of the temperature leads to a spontaneous curvature of the amphiphilic film around the water and water-in-oil droplets appear [6-9].

The properties of microemulsions have been studied in detail within the last 3 decades [9-14]. A detailed literature survey is given in chapter 2. While the first microemulsions contained five components, including ionic surfactants and co-surfactants [15], the groups of *Shinoda et al.* and *Kahlweit et al.* prepared microemulsions using only the three necessary components water, oil and nonionic surfactant [16,17]. Systematic studies on nonionic alkylpolyglycoether surfactants demonstrated that the phase behavior of such systems is fairly universal, but changes systematically with the hydrophilicity/hydrophobicity and the overall chain length of the surfactant [12,18-20]. Not only the phase behavior but also the microstructure and the interfacial phenomena of microemulsions show remarkable similarities [18,21,22]. Bearing this in mind, a polymerizable microemulsion can be formulated easily by replacing the components, i.e. either water or oil, with a polymerizable monomer maintaining the features of interest for the polymerization of microemulsions. Such interests are large interfacial areas, optical transparency, thermodynamic stability, length scales in the nanometer range, and the great variety of structures [23].

The concept of copying the fascinating microstructure of microemulsions to the microstructure of the polymeric material on a one-to-one scale via polymerization appeared already in the 1980ies. Since then the research developed rapidly in order to find novel polymeric materials with interesting morphologies and specific properties [23]. A detailed overview of the preparation of novel solid materials using microemulsion polymerization is given in chapters 5.1 (discrete particles) and 6.1 (porous materials). In general, one aim is to use the small length scales of microemulsions to produce thermodynamically stable, monodisperse latexes in the nanometer range which cannot be obtained using the classical emulsion polymerization. These latex particles are desired for certain applications such as drug delivery systems or for microencapsulation. Of great interest is – due to its high surface to volume ratio – also the polymerization of the bicontinuous structure. It leads to porous materials which can be used as microfilters, separation membranes or solid poly-

mers with a sponge-like structure capable of encapsulating the disperse phase [23]. *Gan et al.* as well as *Cheung et al.* worked intensively on the polymerization of bicontinuous microemulsions. *Gan et al.* reproduced the pioneering experiment of *Stoffer* and *Bone* who studied the phase behavior of sodium dodecylsulfate / pentanol / methyl methacrylate or methyl acrylate / water systems before and after polymerization [24-26]. Confirming that transparent methyl methacrylate mixtures could not be fully polymerized *in situ* by using pentanol as co-surfactant, *Gan et al.* extended their studies to microemulsions in which all the components except water were polymerizable [27-30]. The main conclusion reached by *Cheung et al.* was that polymerization in bicontinuous structured microemulsions results in a polymer with an open-cell structure, i.e. an interconnected porous structure with water channels through the polymer [31-35].

However, generally the one-to-one copy of the microstructure of microemulsions to the microstructure of the polymer material could not be obtained due to structure changes occurring during the polymerization process. These changes are mainly caused by the continuous increase of the polymer/monomer ratio changing the composition of the microemulsion. Thus, the characteristic size of the given microemulsion structure often increases by around one order of magnitude during the polymerization process as shown by *Lade et al.* [36]. The microstructure also changes, in particular if only one domain of the bicontinuous microstructure is polymerized [37]. Therefore, thorough research on appropriate formulation rules and characterization of the phase diagrams of the systems that contain not only the monomer but also the polymer must precede any study of microemulsion polymerization [23].

In 2004 *Co et al.* reported for the first time a new class of water-free microemulsions that are composed of surfactant, oil and sugar [38-42]. Glass forming sugars, in particular equimolar mixtures of sucrose and trehalose, which are almost uncrystallizable, are a good choice. With the glass transition temperature for pure sucrose being just below 60°C and for pure trehalose being 107°C [43], these sugar-based microemulsions form amorphous solid and clear glasses that are surprisingly brittle considering that they contain equal masses of liquid oil and sugar [41]. No visible phase separation has been observed when samples containing a thermally stable UV-active initiator are polymerized at temperatures below the glass transition temperature of the sugar domains. Thus, the reorganization kinetics of the microemulsion system is slowed down strongly so the system cannot adjust to the changing monomer/polymer ratio. In 2006 *Co et al.* published the phase behavior of

precursor microemulsions which are composed of sugar, divinylbenzene and alkylglucoside surfactants [42]. Unlike structures reported earlier that collapse upon dissolution of the sugar template [41], cross-linked divinylbenzene / sugar microemulsions yield robust membranes with a pore size  $\sim 25$  nm [42].

## 1.1 Task Description

The task of this study is to polymerize the microstructure of a microemulsion on a one-to-one scale.

For this, the dynamics of the microemulsion must first be slowed down. This is to be done by increasing the viscosity of the hydrophilic phase. Starting from the model system  $\text{H}_2\text{O} - n\text{-octane} - \text{surfactant}$ , water is to be replaced by water/sugar mixtures with increasing sugar content. Different pure and technical-grade nonionic surfactants are to be used to reach this goal. So far, systematic investigations of the effect of sugar on the properties of microemulsions are missing in literature.

Having prepared a polymerizable highly viscous microemulsion, the structure of the unpolymerized microemulsion is to be investigated by dynamic light scattering (DLS), transmission electron microscopy (TEM) and small angle neutron scattering (SANS). Followed by this, the polymerization of the microemulsion is to be carried out using the UV-active initiator Irgacure 819. Having obtained a polymeric material, its structure will be studied in close collaboration with the group of Prof. H. T. Davis at the University of Minnesota using their expertise in cryo-scanning electron microscopy (SEM). In addition scattering techniques as DLS and SANS will be applied to support the results obtained via cryo-SEM. To optimize the material properties, various initiating lamps with varying intensity as well as wave length are planned to be used for the polymerization process. Additionally, different monomers will be chosen to observe if the chain length of the monomer effects the polymer structure. Furthermore, the amount of cross-linker in the monomer phase will be varied.

This thesis is structured as follows: In chapter 2 the basics required for the understanding of the phase behavior of microemulsions and its polymerization are explained. In chap-

---

ter 3 a short description of the experimental techniques used in this work is given. The results of the phase behavior studies to formulate highly viscous, polymerizable microemulsions are discussed in chapter 4. In chapter 5 the outcome of the polymerization of the microemulsion droplet structure is investigated followed by the findings for the polymerized bicontinuous structure in chapter 6. A summary of the obtained results in chapter 7 brings this work to an end.



## 2 Basics

For the understanding of this work a series of basic principles is indispensable. Section 2.1 deals with the most important fundamentals of microemulsions. Starting with definitions of the essential parameters for characterizing microemulsions and a description of the ternary system's phase behavior, the main focus points out the fascinating and multifarious microstructure caused by the adsorption of the surfactant at the interface between water and oil. Consequently, different sections through the Gibbs phase prism with the corresponding microstructure are discussed. This section ends with general trends of the phase behavior using nonionic surfactants. Section 2.2 discusses the basics of polymerization. Having introduced the principles, a detailed description of polymerization in microemulsions follows. The chapter closes with information about the initiator Irgacure 819 used in this work.

### 2.1 Phase Behavior

Microemulsions are thermodynamically stable mixtures of hydrophilic, hydrophobic and amphiphilic components. Macroscopically, microemulsions are isotropic, one-phase solutions. Microscopically, the amphiphilic components, miscible with both oil and water, separate the hydrophilic from the lipophilic components by forming an extended interfacial monolayer which leads to the multifarious structures found within microemulsions. As *Shinoda* and coworkers demonstrated, ternary systems containing water (A) – oil (B) – nonionic surfactant (C) show all the typical microemulsion features [17,44,45]. Systematic studies on nonionic alkylpolyglycoether surfactants by *Kahlweit* and coworkers showed that the phase behavior of all systems is fairly universal, however changes systematically with the surfactant's hydrophilicity/hydrophobicity and efficiency [12,18-20].

### 2.1.1 Definition of used parameters

A number of parameters have been proven useful for the characterization of a microemulsion composition. At constant pressure, in this work normal atmospheric pressure, two composition parameters are needed to characterize a ternary system of water (A), oil (B) and surfactant (C).

The mass fraction of the oil in the oil/water mixture is given by

$$\alpha = \frac{m_B}{m_A + m_B} \quad (2.1)$$

and the surfactant mass fraction in the mixture of all components is

$$\gamma = \frac{m_C}{m_A + m_B + m_C} \quad (2.2)$$

Knowing the densities of the components the volume fraction of the oil in the oil/water mixture

$$\phi = \frac{m_B / \rho_B}{m_A / \rho_A + m_B / \rho_B} \quad (2.3)$$

is often used instead of the mass fraction  $\alpha$ .

Adding more components to the ternary system, additional parameters have to be defined. Thus, if two surfactants C and D are used within the mixture, the mass fraction of the co-surfactant D in the mixture of the surfactants C and D is given by

$$\delta = \frac{m_D}{m_C + m_D} \quad (2.4)$$

Using a surfactant mixture of a hydrophobic nonionic alkylpolyglycoether surfactant and a more hydrophilic nonionic sugar surfactant the latter one is referred to co-surfactant D in the following work.

In this work sucrose and trehalose are added to the water phase (A). The mass fraction of the sugar in the mixture of water and sugar is defined as

$$\Psi = \frac{m_{\text{sugar}}}{m_{\text{sugar}} + m_{\text{water}}} = \frac{m_{\text{sugar}}}{m_A} \quad (2.5)$$

For microemulsion systems containing up to 65 wt.% sugar in the water phase only sucrose is added. For more than 65 wt.% sugar/water mixtures sucrose and trehalose are



used. The mass fraction of trehalose in the sucrose/trehalose mixture is kept constant and given by

$$\zeta = \frac{m_{\text{trehalose}}}{m_{\text{sucrose}} + m_{\text{trehalose}}} = 0.38. \quad (2.6)$$

Due to the change in the density of the water phase if more sugar is added the mass fraction of oil in the oil/water mixture  $\alpha$  is only used in this work and not the volume fraction  $\phi$ .

If the *n*-octane oil is partially replaced by a polymerizable methacrylate oil ( $C_xMA$ ), the mass fraction of  $C_xMA$  in the oil phase is defined by

$$\beta = \frac{m_{C_xMA}}{m_{C_xMA} + m_{n\text{-octane}}}. \quad (2.7)$$

For a detailed investigation of the phase behavior and microstructure of microemulsions other parameters have been proven reasonable for the compositional characterization. The mass fraction of the surfactant in the surfactant/water mixture is given by

$$\gamma_a = \frac{m_C}{m_A + m_C} \quad (2.8)$$

and the mass fraction of the hydrophobic component in the mixture of all components by

$$w_B = \frac{m_B}{m_A + m_B + m_C}. \quad (2.9)$$

### 2.1.2 Phase behavior of ternary systems

At constant pressure the complex phase behavior of the system water (A) – oil (B) – nonionic surfactant (C) can be demonstrated in a phase prism consisting of the Gibbs triangle A-B-C as basis and the temperature  $T$  as ordinate [16,19]. The pressure dependence of the phase behavior is not considered since this effect is rather weak [46]. Figure 2.1 shows such a phase prism [47]. Several Gibbs triangles are included to reveal the phase behavior of a ternary system at constant temperature and pressure.

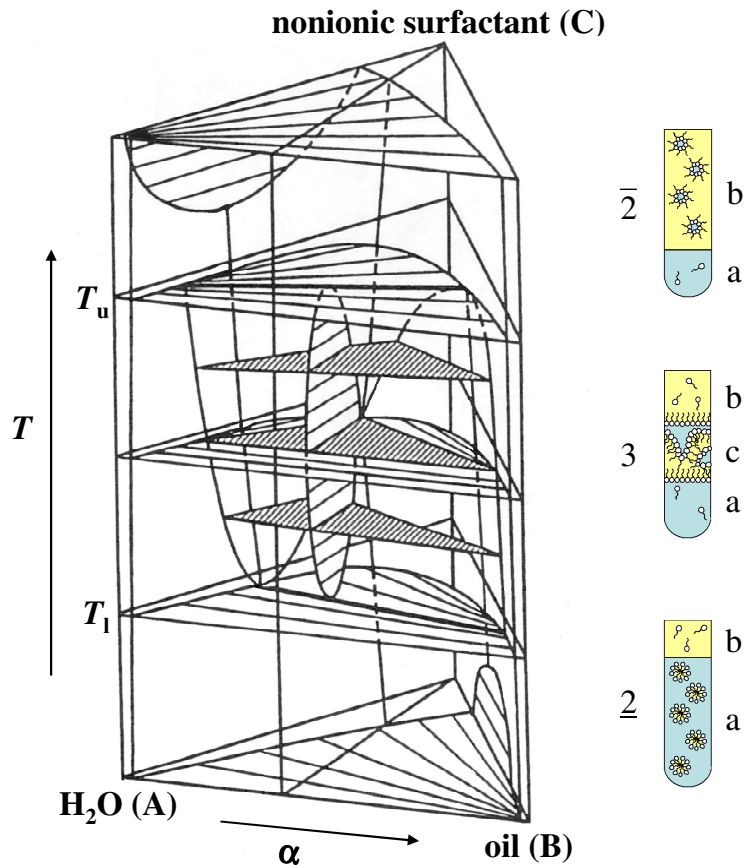


Figure 2.1: Gibbs phase prism of a ternary system containing water (A), oil (B) and nonionic surfactant (C) as a function of the temperature  $T$ . The pressure is kept constant. The Gibbs triangles are plotted at different temperatures within the phase prism (redrawn from [47]).

The phase behavior at low surfactant mass fractions as a function of the temperature is illustrated by the test tubes on the right hand side of the phase prism. At low temperatures two phases are found. The hydrophilic water phase, in this case the lower phase due to the higher density, contains most of the surfactant forming an oil-in-water (o/w) microemulsion (a), the upper phase is the oil excess phase (b). This situation is represented in the bottom test tube and called  $\underline{2}$  as the microemulsion phase is the high density phase. Also the negative slope of the tie-lines in the Gibbs triangle shows that a surfactant-rich water phase coexists with an excess oil phase.

At higher temperatures the headgroups of the surfactant are dehydrated. Thus, water becomes an increasingly poor solvent for the surfactant. At the same time the solubility of the surfactant in oil increases [48]. With the dehydration of the surfactant head group the relative volume of the hydrophilic head group to the hydrophobic chain of the surfactant also decreases. Therefore the curvature of the surfactant film changes characteristically with

temperature. At the temperature  $T_1$  of the lower critical endpoint  $cep_\beta$  the o/w microemulsion splits into two phases (a) and (c). Thus, 3 phases coexist: A surfactant-rich bicontinuously structured microemulsion phase (c) and a water (a) and oil (b) excess phase. Increasing the temperature the major component of the microemulsion phase changes from water-rich (at  $T_1$ ) to oil-rich due to the inversion of surfactant solubility. The maximum dimension of the three phase region is found at  $T_m$ . Here, the microemulsion phase contains the same volumes of water and oil. With further increasing temperature the dimension of the three phase region decreases again.

At the temperature  $T_u$  of the upper critical endpoint  $cep_\alpha$  a water-in-oil (w/o) microemulsion (b) is formed by merging the phases (b) and (c). This upper surfactant-rich phase consists of water-in-oil droplets solubilized by the surfactant and coexists with a water excess phase (a). This situation is called  $\bar{2}$ . In contrast to the  $\underline{2}$ -state the tie-lines of the  $\bar{2}$ -state have a positive slope.

Watching the trajectory of the composition of the microemulsion phase (backmost vertex of the three phase triangle) one can find it moving from the  $H_2O$  – surfactant to the oil – surfactant side. At the medium temperature  $T_m = (T_u + T_1)/2$  the minimal surfactant concentration to solubilize water and oil is maximum.

### 2.1.3 Different sections through the phase prism and their microstructure

For a systematic investigation of the phase behavior and microstructure of ternary microemulsions perpendicular two-dimensional sections through the phase prism have been proven useful [7,49]. Different sections are possible but as the change of composition is irreversible, the isoplethal method (i.e. constant composition) is a common way measuring the phase behavior [50]. Figure 2.2 shows two of these sections: The  $T(\gamma)$ -section drawn in red, also called “*Kahlweit-fish*”, and the  $T(w_B)$ -section drawn in green, also called “*funnel*”.

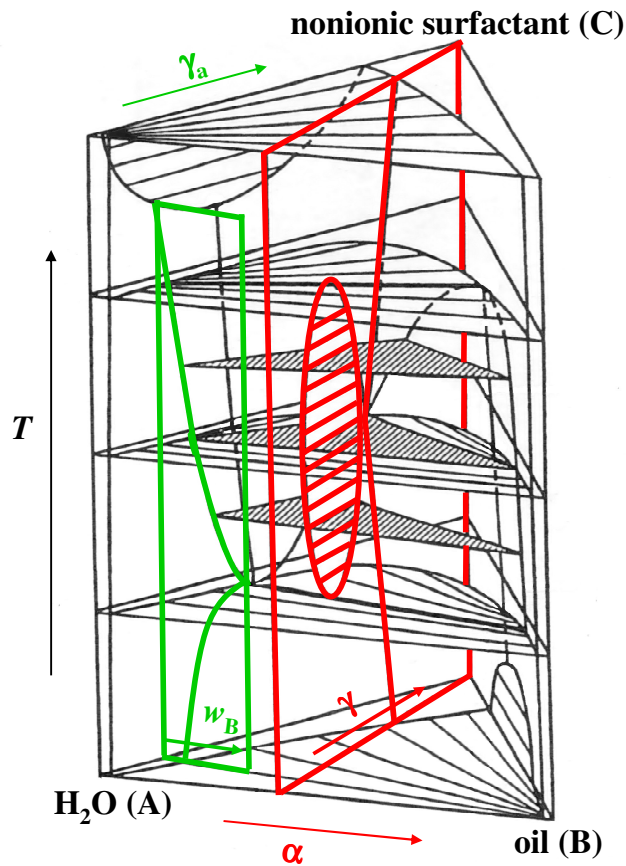


Figure 2.2: Schematic phase prism with different sections through the phase body. The  $T(\gamma)$ -section at constant  $\alpha$  is drawn in red through the phase prism and the  $T(w_B)$ -section at constant  $\gamma_a$  in green.

For the  $T(\gamma)$ -section the temperature dependent phase behavior is determined for different surfactant mass fractions  $\gamma$  at a constant oil-to-water plus oil ratio  $\alpha$  [16,19]. Usually the volumes of oil and water are kept equal ( $\alpha = 0.4125$  with *n*-octane as oil). Figure 2.3 gives an overview of the occurring phases at constant composition with changing temperature [36].

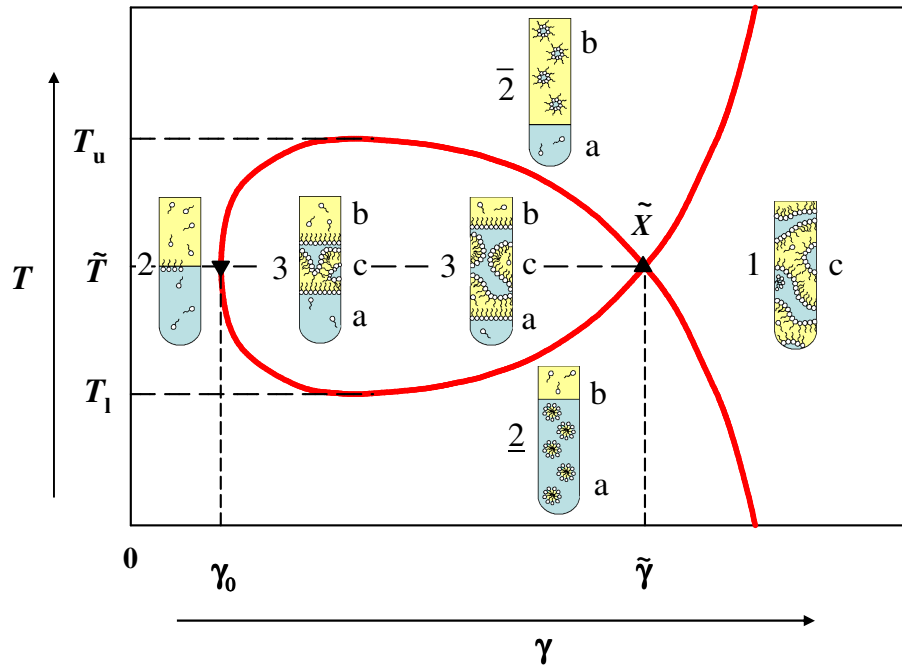


Figure 2.3: Schematic  $T(\gamma)$ -section of the system  $\text{H}_2\text{O}$  – oil – nonionic surfactant at a constant oil-to-water plus oil ratio  $\alpha$ . The phase inversion is illustrated by the test tubes. The  $\tilde{X}$ -point gives the minimum amount of surfactant that is needed to solubilize water and oil at the temperature  $\tilde{T}$  (redrawn from [36]).

A binary system containing  $\text{H}_2\text{O}$  and oil, defined by  $\gamma = 0$ , consists of two phases as water and oil normally do not mix. Adding small amounts of surfactant to the mixture the sample still consists of two phases over the entire temperature range. As the surfactant is amphiphilic, it dissolves monomerically in water and oil and adsorbs at the macroscopic oil/water interface. When the surfactant mass fraction  $\gamma_0$  is reached both excess phases and the macroscopic interface are saturated; i.e.  $\gamma_0$  is a measure for the monomeric solubility of the surfactant in water and oil. Increasing the surfactant mass fraction  $\gamma$  furthermore, at intermediate temperatures (temperatures between  $T_u$  and  $T_l$ ) where the surfactant is equally soluble in water and oil, aggregates are formed in an additional layer of the surfactant-rich middle phase (c). This phase is bicontinuously structured and coexists with an excess oil (b) and excess water (a) phase. With increasing  $\gamma$  the volume of the bicontinuous phase (c) grows until the excess phases (a) and (b) vanish. At this so-called  $\tilde{X}$ -point, the fish-tail point [16], the three-phase region meets the one-phase region. A minimum amount of surfactant  $\tilde{\gamma}$  is needed to solubilize water and oil at the corresponding temperature  $\tilde{T}$ , both  $\tilde{\gamma}$  and  $\tilde{T}$  being unique for each system.  $\tilde{\gamma}$  is a measure of the solubilization efficiency of the particular surfactant. With increasing amount of surfactant in the system the one-phase

region expands. Below the three phase region oil-swollen micelles in a continuous water phase coexist with an oil excess phase ( $\underline{2}$ ) and at high temperatures, above the three phase region, water-swollen micelles in a continuous oil phase coexist with a water excess phase ( $\bar{2}$ ).

The extensive study of the microstructure with a great variety of experimental techniques such as nuclear magnetic resonance (NMR)-diffusometry [51-53], small angle neutron scattering (SANS) [8,54,55], transmission electron microscopy (TEM) [56-63], dynamic light scattering (DLS) [64-66] and electric conductivity delivered detailed knowledge of the structure pattern of microemulsions. Figure 2.4 shows a schematic representation of possible microstructures occurring in the one-phase region behind the  $\tilde{X}$ -point [9].

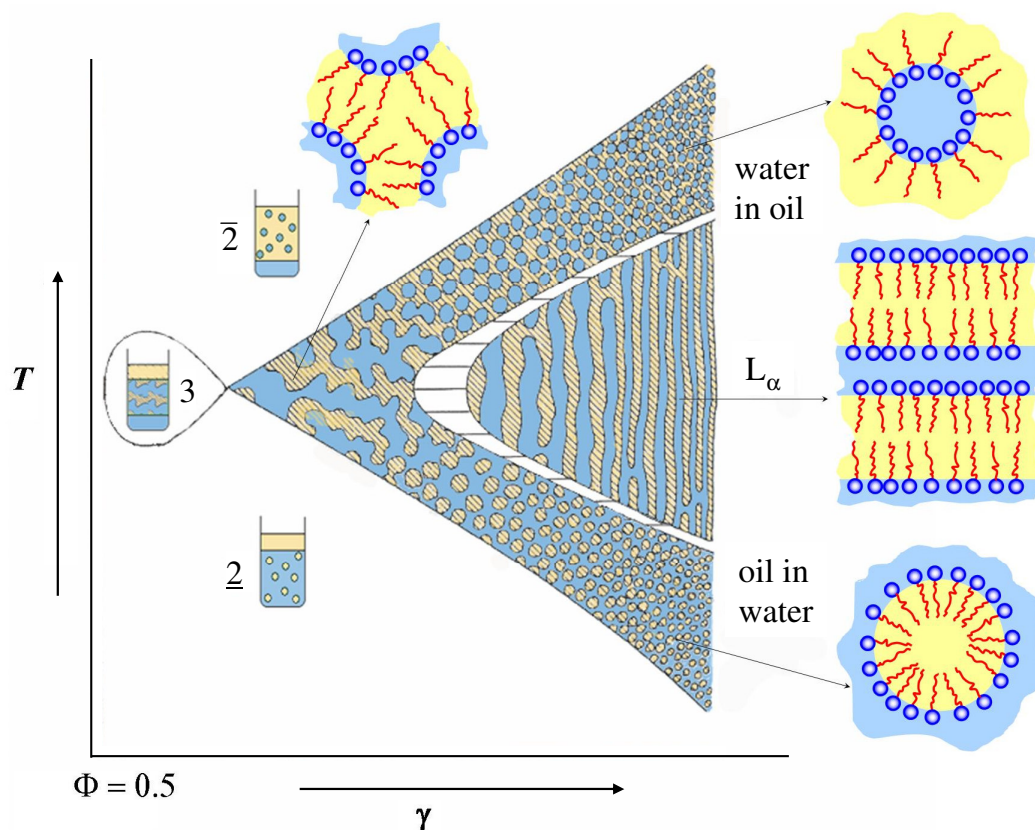


Figure 2.4: Schematic  $T(\gamma)$ -section of the system  $\text{H}_2\text{O}$  – oil – nonionic surfactant containing the microstructures within the one-phase region. At low temperatures oil-in-water structures are found. Increasing the temperature the mean curvature of the amphiphilic film decreases to zero; bicontinuous or lamellar structures are found. With further increase of the temperature the mean curvature turns negative and water-in-oil structures exist (redrawn from [9]).

In the one-phase region close to the  $\tilde{X}$ -point, a bicontinuously structured microemulsion is found over the entire temperature range. With increasing amount of surfactant in the microemulsion, i.e. increasing  $\gamma$ , the bicontinuous structure still exists at intermediate temperatures. As the internal interface between water and oil increases the length scale of the bicontinuous structure becomes smaller. At high surfactant concentrations and intermediate temperatures, a lamellar phase  $L_\alpha$  displaces the bicontinuous structure. Here, not only the mean curvature of the amphiphilic film, but also the Gaussian curvature is zero. For higher surfactant values and temperatures above or below  $\tilde{T}$  the mean curvature decreases/increases which leads to a transition to water-in-oil droplets or the inverse oil-in-water droplets. Again, the droplet size decreases as one moves further away from the  $\tilde{X}$ -point.

To study the phase behavior of diluted microemulsions with e.g. oil droplets dispersed in a continuous hydrophilic phase, vertical sections through the phase prism are considered ( $T(w_B)$ -section) [60]. Starting from the binary system A-C the temperature extension of the one-phase region is measured as a function of the mass fraction of oil in the mixture of all components  $w_B$  at constant mass fraction of the surfactant in the surfactant/water mixture  $\gamma_a$  (Figure 2.5 left) [67].

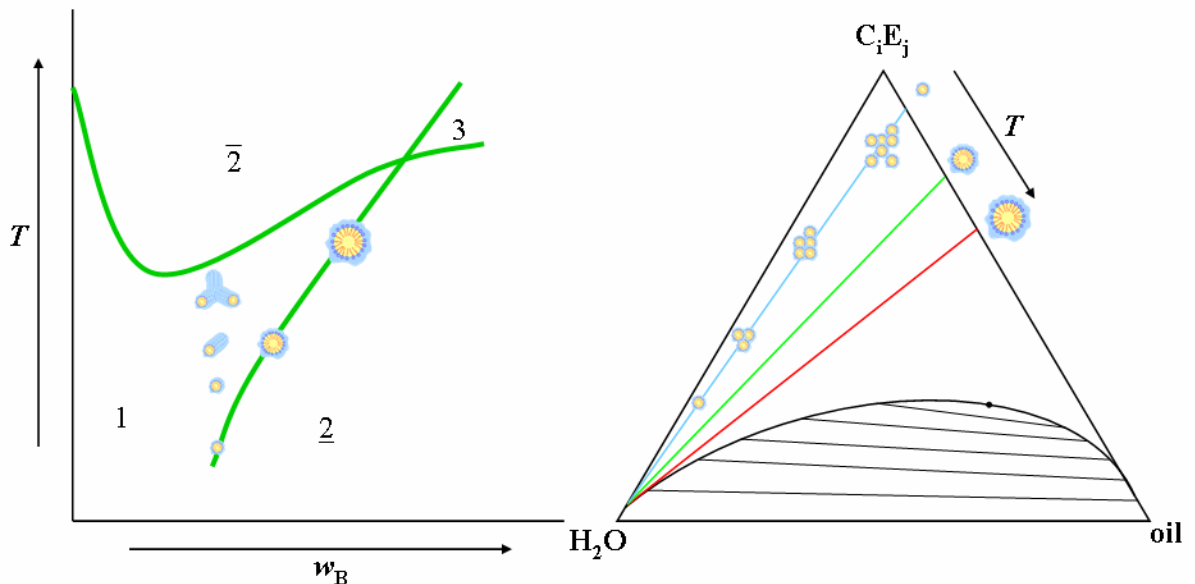


Figure 2.5: Left: Schematic view of a  $T(w_B)$ -section. The two phase regions are found at temperatures above and below the one phase region. The three phase region exists at high amounts of oil in the mixture. Right: Gibbs phase prism containing straight binodals for a system at constant temperature (redrawn from [67]).

The upper phase boundary starts with the cloud point of the binary water-surfactant system and is therefore a near-critical boundary which descends steeply upon the addition of oil. This boundary runs through a minimum as the weight fraction of oil  $w_B$  is further increased. Simultaneously, the lower phase boundary ascends monotonically with increasing  $w_B$ . It marks, for a given temperature, the maximum amount of oil soluble in a one-phase oil-in-water microemulsion and is therefore called the emulsification failure boundary (*efb*). With increasing temperature, the capability of the surfactant to solubilize oil is strongly increased. Near the lower critical endpoint temperature  $T_1$ , the one-phase region closes like a funnel. It terminates at the intersection of the lower oil emulsification failure boundary and the upper near-critical phase boundary [50]. Starting in the two-phase region  $\underline{2}$  and increasing the temperature, the oil swollen micelles continue to swell and the oil excess phase decreases. At temperatures close to the *efb* one determines maximally swollen micelles and thus, spherical oil-in-water droplets are formed. The oil mass fraction  $w_B$  at the *efb* gives the maximum amount of oil which can be solubilized at the respective temperature for the chosen surfactant mass fraction  $\gamma_a$ . With increasing temperature the spontaneous curvature of the amphiphilic film changes and the system forms bigger structures: First elongated micelles are formed which link together to build cylindrical network structures afterwards [68,69]. The size of the droplets along the *efb* increases with higher  $w_B$ .


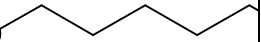
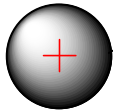
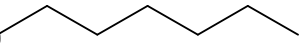
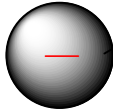
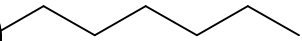
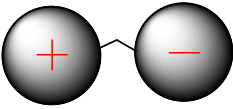
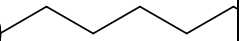
To determine systems with different concentrations of droplets but the same droplet radius the emulsification failure boundary has to be investigated at a constant temperature for different  $\gamma_a$  (Figure 2.5 right). When  $\gamma_a$  is increased at a constant temperature the *efb* is shifted to higher  $w_B$ . With the determined parameter  $w_B$  and known  $\gamma_a$  one can investigate the water and surfactant mass fraction  $w_A$  and  $w_C$ . Plotting this in a Gibbs phase prism one gets a straight binodale. As the proportion of surfactant to oil is kept constant at the straight binodale the radius of the droplets does not differ. Only the concentration of droplets decreases to the water corner as the system is diluted with water saturated with monomerically dissolved surfactant. For higher temperatures the micelles increase in size (see also micelles at the *efb*).



### 2.1.4 Nonionic surfactants

To prepare microemulsions different kinds of surfactants can be used (Table 2.1). In general, one distinguishes between nonionic and ionic surfactants. Thereby almost all surfactants have an alkyl chain that can be linear or branched as hydrophobic part. The hydrophilic part can be nonionic or ionic. In this work only nonionic surfactants are used.

Table 2.1: Classification of surfactants.

surfactant	polar group(s)	hydrophilic	hydrophobic
nonionic	–OH (alcohol), –O– (ether), C <sub>6</sub> H <sub>11</sub> O <sub>6</sub> – (glucose unit)		
anionic	–COO <sup>–</sup> (carboxylate), –SO <sub>3</sub> <sup>–</sup> (sulphonate), –SO <sub>4</sub> <sup>2–</sup> (sulphate)		
cationic	R <sub>4</sub> N <sup>+</sup> (quaternary ammonium group)		
amphoteric	–COO <sup>–</sup> (carboxylate), R <sub>4</sub> N <sup>+</sup> (quaternary ammonium group)		

Nonionic surfactants which are frequently used in technical applications are the alkyl-polyglycoether (C<sub>*i*</sub>E<sub>*j*</sub>). Thereby the index *i* gives the length of the linear alkyl chain (C) and *j* the number of ethylene glycol units (E) in the hydrophilic headgroup. The chemical structure is shown in Figure 2.6.

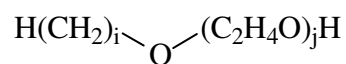


Figure 2.6: Chemical structure of the alkylpolyglycoether C<sub>*i*</sub>E<sub>*j*</sub> surfactants.

These types of surfactants are especially interesting for basic research and application because both, the hydrophilicity and lipophilicity of the surfactant, can be tuned independently and gradually by changing  $i$  and  $j$  (Figure 2.7).

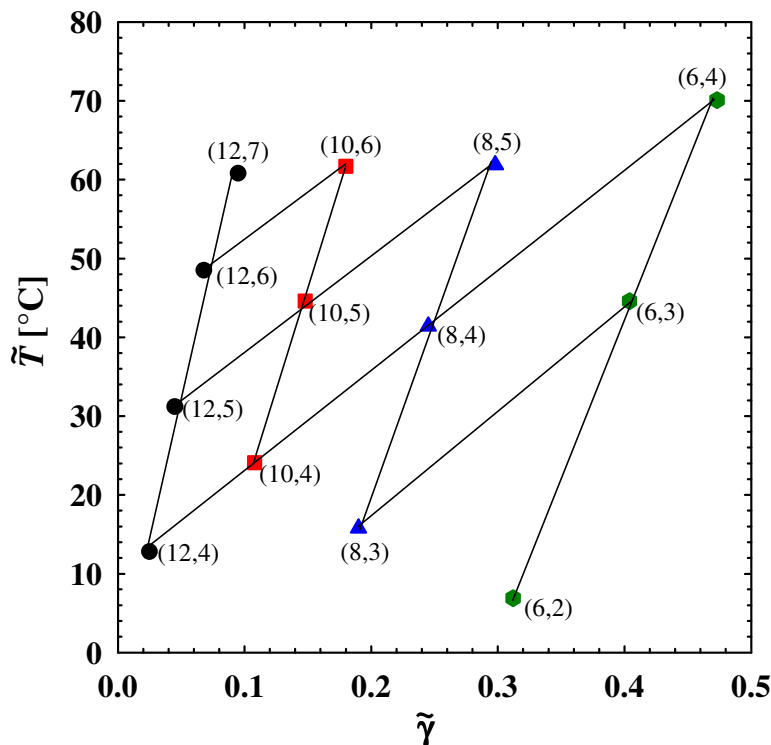


Figure 2.7:  $\tilde{X}$ -points of the system  $\text{H}_2\text{O} - n\text{-octane} - \text{C}_i\text{E}_j$  at constant  $\alpha = 0.4125$ . The systems are characterized by (i,j) pairs (redrawn from [49]).

The influence of  $i$  and  $j$  on the phase behavior of microemulsions is illustrated in Figure 2.7 which shows the  $\tilde{X}$ -points of the system  $\text{H}_2\text{O} - n\text{-octane} - \text{C}_i\text{E}_j$  at constant  $\alpha = 0.4125$  [49]. As shown for  $n$ -alkanes the surfactant becomes more hydrophobic with increasing  $i$  and constant  $j$  and the  $\tilde{X}$ -point shifts to lower temperatures because lower temperatures are sufficient to drive a large amount of surfactant into the oil phase. At the same time the system becomes more efficient;  $\tilde{\gamma}$  decreases strongly. With increasing  $j$  the  $\tilde{X}$ -point shifts to higher temperatures due to the increasing hydrophilicity of the surfactant.  $\tilde{\gamma}$  increases slightly. Thus, the system becomes slightly less efficient.

Also for other oils than the  $n$ -alkanes this trend stays qualitatively the same. The  $\tilde{X}$ -point might shift but the relative position to each other does not change [70].

*n*-Alkylpolyglycoether are also widely used as technical-grade surfactants having therefore a broad distribution of the number of ethoxylate units. Lutensol AO8 and Lutensol XL70 used in this work are such technical-grade alkylpolyglycoether surfactants. Lutensol AO8 is an oxoalcohol ethoxylate on the basis of mainly linear alcohols with 8 ethylene oxide units in the hydrophilic headgroup. Lutensol XL70 is a C10-Guerbet-alcohol with an average of 7 ethylene oxide units.

Other types of nonionic surfactants are *n*-alkyl glucosides. These sugar surfactants  $C_mG_n$  have an alkyl chain with *m* numbers of carbons (C) and a hydrophilic headgroup made up of *n* numbers of glucose units (G). Figure 2.8 shows the chemical structure of the surfactant  $C_8G_1$  as an example. Due to the fact that one glucose group contains 6 hydroxyl groups,  $C_mG_n$ -surfactants are generally rather hydrophilic. In this work, also the equivalent technical-grade sugar surfactants Agnique PG 264-G and Agnique PG 8105-G have been used. The first one has in average 1.4 glucose units and an alkyl chain of 12 – 14 carbons. Agnique PG 8105-G has 1.5 glucose units in average and 8 - 10 carbons as hydrophobic tail group.

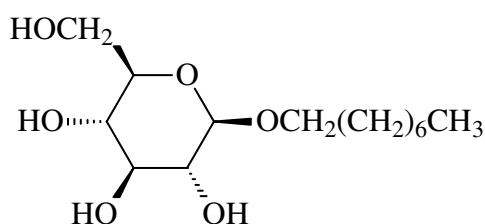


Figure 2.8: Chemical structure of the *n*-alkyl glucoside *n*-Octyl- $\beta$ -D-glucopyranoside  $C_8G_1$ .

## 2.2 Polymerization

Polymerization is a process where reactive monomer molecules, mainly unsaturated organic compounds, undergo a chemical reaction to form polymer chains or three-dimensional networks. With the help of an initiator a double bond is broken and monomer radicals attach to other monomers to build up polymer chains. One distinguishes between two classes of polymerization: The step and the chain polymerization. Whereas any two

molecular species present can react in step polymerization with each other, only monomers and the propagating species react with each other in chain polymerization. At any instant, the reaction mixture contains only monomer, high polymer, and the growing chains. [71] The radical polymerization belongs to the class of chain polymerization.

### 2.2.1 Principles of Photochemical Radical Chain Polymerization

Radical chain polymerization consists of a sequence of three steps: Initiation, propagation, and termination. The initiation step starts with the production of a reactive species. In this case a free-radical is produced by a homolytic dissociation of the initiator which is then added to the first monomer molecule by  $\pi$ -bond opening forming a new radical. This first new radical reacts as a chain initiating species. In the second step, the propagation, the growth of the chain initiation species results from adding a large number of monomer molecules successively. Each addition creates a new radical with the same identity as the previous one, except that it is larger by one monomer unit. Growth propagation of the chain to high polymer proportions takes place very rapidly ( $10^5 - 10^7 \text{ cm}^3 \text{ mol}^{-1} \text{ s}^{-1}$ ). At some point termination takes place: Either two radicals react with each other by recombination or, more rarely, by disproportionation. [71]

But whether a particular monomer can be converted to polymer depends on thermodynamic as well as kinetic considerations. For thermodynamic reasons, polymerization is only possible if the difference in Gibbs energy  $\Delta G$  between monomer and polymer relating to the propagation step is negative. The exothermic nature of chain polymerizations of alkene double bonds arises because the process involves the exothermic conversion of  $\pi$ -bonds in monomer molecules into  $\sigma$ -bonds in the polymer. The negative  $\Delta S$  for polymerizations occurs from the decreased degrees of freedom for the polymer relative to the monomer. Thus, polymerization is favorable from the enthalpy but unfavorable from the entropy point of view and can only occur from thermodynamic considerations if  $\Delta H$  overwhelms  $\Delta S$ . [71]

In order to obtain a kinetic expression for the overall rate of polymerization, the assumption is necessary that the rate constant for the propagation and termination step are independent of the size of the radical. As the monomer concentration depletes by the initiation as well as by the propagation reaction with the number of monomer molecules reacting in the initiation reaction being far less than in the propagation step, the rate of propaga-

tion  $R_p$  is simply given by

$$R_p = -\frac{d[M]}{dt} \quad (2.10)$$

$$R_p = k_p [M][M \cdot] \quad (2.11)$$

with  $k_p$  being the rate constant for the propagation step,  $[M]$  the monomer concentration, and  $[M \cdot]$  the total concentration of all chain radicals. Substituting the concentration of radicals by a steady-state assumption which considers that the concentration of radicals increases initially, but almost instantaneously reaches a constant steady-state value one obtains the rate of polymerization

$$R_p = k_p [M] \left( \frac{R_i}{2k_t} \right)^{1/2} \quad (2.12)$$

where  $R_i$  is the rate of the initiation step and  $k_t$  the rate constant of the termination step. Equation (2.12) shows a dependence of the polymerization rate on the square root of the initiation rate. Considering now that polymerization in this work is initiated by photochemical means the intensity of adsorbed light  $I_a$  must be accounted for in the rate of initiation

$$R_i = 2\Phi I_a = 2\Phi \epsilon I_0 [M]. \quad (2.13)$$

$\Phi$  is called the *quantum yield for radical production*,  $I_0$  is the light intensity incident on the monomer and  $\epsilon$  the molar absorptivity of the monomer for the particular wavelength of radiation. The rate of photo-initiated polymerization is then given by

$$R_p = k_p [M]^{3/2} \left( \frac{\Phi \epsilon I_0}{k_t} \right)^{1/2}. \quad (2.14)$$

In this work the hexyl and dodecyl methacrylate as well as the cross-linker ethylene glycol dimethacrylate have been chosen as polymerizable oil, both containing a carbon-carbon double bond and a carbon-oxygen double bond (Figure 2.9).

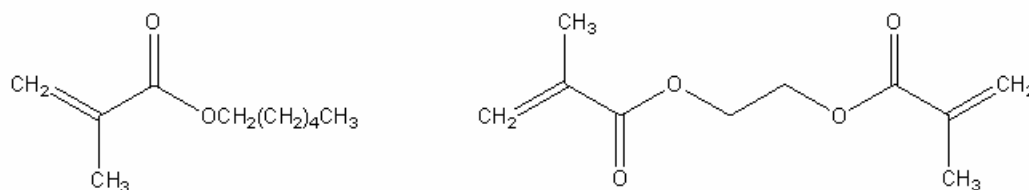


Figure 2.9: Chemical structure of hexyl methacrylate (left) and the cross-linker ethylene glycol dimethacrylate (right).

As known from alkenes and aldehydes/ketones the polymerization of the carbon-carbon double bond is important for photochemical radical chain polymerization as the carbonyl group is not prone to polymerization by radical initiators due to its polarized nature. Unlike the carbonyl linkage, the alkene double bond undergoes polymerization by both radical and ionic initiators because the  $\pi$  -bond of an alkene breaks either homolytically or heterolytically [71]. The structural arrangement of monomer units during propagation depends on both resonance and steric properties. The favored propagating radical must be the more stable one due to resonance effects. For sterical reasons, the approach of a propagating radical at a less or unsubstituted carbon of a monomer molecule is much less hindered compared to the approach at a high substituted carbon [72,73].

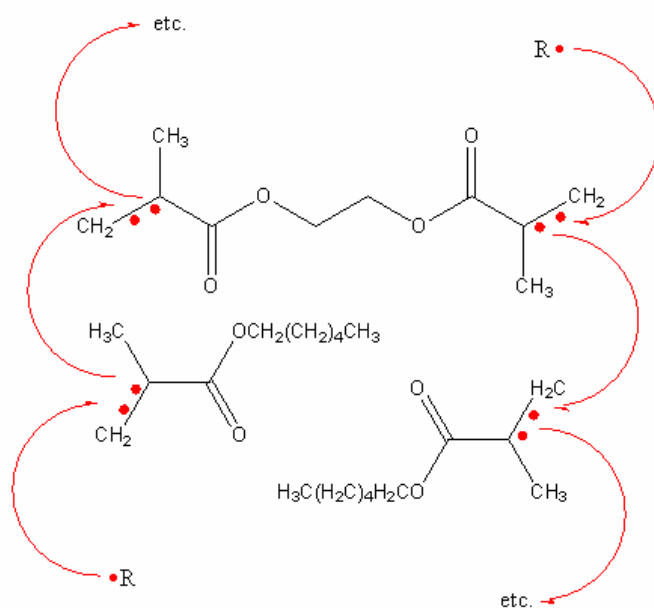


Figure 2.10: Schematic demonstration of the radical polymerization of hexyl methacrylate and the cross-linker ethylene glycol dimethacrylate. By using the cross-linker a polymer network is formed.

Figure 2.10 demonstrates the radical polymerization of a mixture containing hexyl methacrylate and the cross-linker ethylene glycol dimethacrylate schematically. Starting with the reactive species  $R$ , the radical adds to the first hexyl methacrylate monomer molecule to form the more stable propagating radical. Continuing now with only hexyl methacrylate monomers the polymer chain starts growing. As soon as ethylene glycol dimethacrylate as cross-linker is added to the monomer a three-dimensional polymer network is formed.

### 2.2.2 Polymerization in Microemulsions

Due to the well defined nature of the mesophases and the enormous inner surface of microemulsion structures, it is very attractive to perform polymerization reactions inside these systems, either to stabilize the three-dimensional structures or to synthesize new polymer materials [74-80]. But although microemulsions are known since a long time, the first experiments to polymerize its dynamic association structure are reported in 1980 [24,25]. It was noticed soon that the handling of such reactions in microemulsions is not trivial due to the phase separation occurring during the polymerization process. Stable polymer particles with a diameter of about 30 nm were obtained in 1983 [81] but it was still not possible to copy the microstructure of the underlying structure on a one-to-one scale. Reason for this is the fragility of microemulsions towards slight changes of thermodynamic properties. The hydrophobicity of the polymerizable substance changes during the polymerization and the fragile microemulsion ends, in principle, with a different phase structure.

The kinetic of the microemulsion polymerization is in contrast to the emulsion polymerization still not totally understood. A kinetic scenario based on the emulsion polymerization was developed to describe many of the observations found during the polymerization of oil-in-water and water-in-oil microemulsions, the so-called Candau-Leong-Fitch model (CLF-model) [82-85]. Detailed investigations have confirmed this model [86-88]. Figure 2.11 shows a schematic scenario of the CLF-model [74].

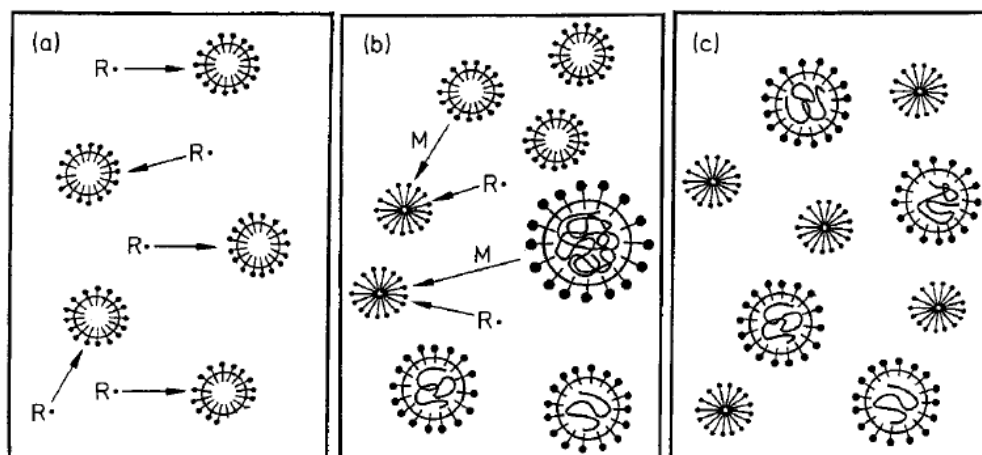


Figure 2.11: Schematic scenario of the CLF-model (taken from [74]). For a detailed description see text.

The polymerization is initiated by the entry of radicals inside the primary microemulsion droplets (a). It is believed that nucleation of the polymer particles occurs for only a small fraction of the final nucleated droplets. The polymer growth leads to a depletion of monomer in these micelles (b). The nucleated particles grow by addition of monomers from non-nucleated droplets serving as monomer reservoirs for the growing particles [89], either by coalescence with neighboring micelles, or by diffusion of monomer through the continuous phase. Monomer diffusion from inactive micelles towards active particles should be the dominant process in aqueous microemulsions. This leads eventually to a reduction in the number of particles and an increase in size [77]. The free initiator radicals are preferentially captured by the empty micelles which might be simply due to their number, but can also be caused by a different permeability through the surfactant layer [74]. The continuous particle nucleation, one of the central principles of the CLF-model, is proved by the independence of the particle size on conversion and the number of chains per particle. At the end of the polymerization, latex particles as well as a large excess of empty micelles coexist (c). The observation of particle growth due to kinetic processes is a contradiction in itself, since microemulsions are defined as thermodynamically stable systems. The kinetic exchange processes are only responsible for fluctuations around the equilibrium size. Therefore the particle growth in such a process must be translated to a change of the thermodynamic properties [74].

An overview about microemulsion polymerization and recent developments of templating within these equilibrium nanostructured fluids is given in e.g. [23,77,78,89-92].



### 2.2.3 Polymerization with Irgacure 819

Polymethyl methacrylate (PMMA) is routinely produced by emulsion polymerization, solution polymerization and bulk polymerization, generally using radical initiation [93-95]. During a photochemical radical polymerization, radiation activates an initiator which forms the intrinsic reactive species for polymerization. Initiators must fulfill a variety of needs [96]. The absorbing region and the absorption maximum should be close to the emission region or maximum of the polymerization radiator. High absorbance coefficients are necessary and the initiator decomposition rate must be reasonably constant during the polymerization reaction. The cage effect, i.e. the recombination of initiator radicals before starting a polymer chain, must be small. Also side reactions of the free radicals should be reduced [97]. Besides, the initiator must dissolve well within the monomer and the radicals must react effectively with the monomer [98].

In this work, the initiator Bis(2,4,6-trimethyl benzoyl)-phenyl phosphine oxide (Irgacure 819) from Ciba has been used. Figure 2.12 illustrates a homolytic  $\alpha$ -cleavage of Irgacure 819, taking place under UV-light (top) and its adsorption spectrum dissolved in different concentrations in acetonitrile (bottom) [99]. At concentrations of 0.1% Irgacure 819 in acetonitrile, the adsorption spectrum runs from wavelengths of  $\lambda = 200$  nm up to  $\lambda = 440$  nm.

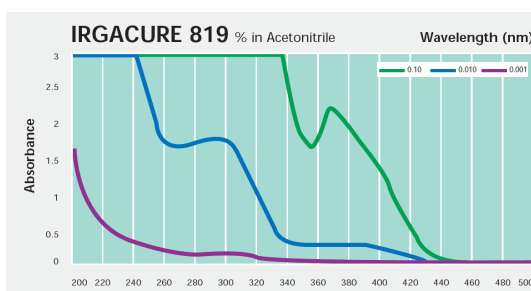
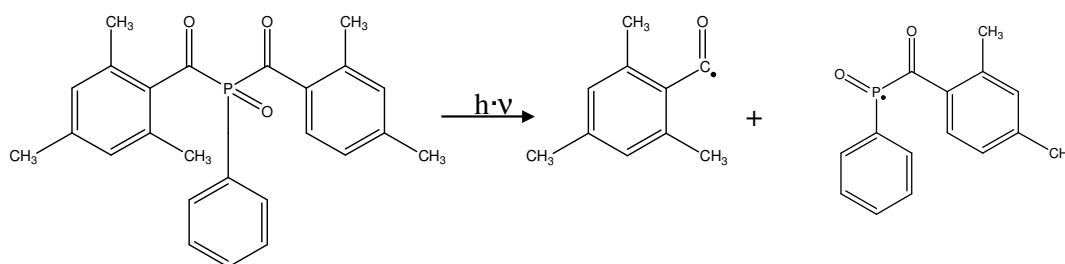


Figure 2.12: Homolytic  $\alpha$ -cleavage of the initiator Irgacure 819 and its adsorption spectrum [99].

The phosphinoyl-radical generated during initiation is more reactive towards unsaturated compounds compared to the benzoyl-radical and therefore particularly effective. The chromophore allowing the long wave adsorption ( $\lambda = 400$  nm) is destroyed during the radical formation by separating the carbon atom of the carbonyl group from the phosphorus atom. In the now following polymerization the radiation of wavelengths around  $\lambda = 400$  nm can enter lower layers due to the missing chromophore adsorption. Therefore, Irgacure 819 is suited well as initiator for samples of higher layer thicknesses. Both monoacyl- and bisacylphosphine oxides contain a methyl group in ortho-position avoiding a nucleophilic attack of the carbonyl group on the carbon atom and increasing the solubility [100].

## 3 Experimental Techniques

This chapter presents the basics needed for the understanding of the experiments carried out in this work. The order is geared to the chronology of the experiments in the lab. At the beginning of this chapter, the basics for the determination of the phase behavior are described followed by the polymerization of microemulsion systems. Various methods for the investigation of the polymerized microstructure are briefly presented. Beginning with the densitometry and the viscometry, needed for dynamic light scattering experiments, a short introduction to small angle neutron scattering experiments follows. This chapter ends with a short mode of operation of the scanning electron microscopy, the transmission electron microscopy and the polarized light transmission microscopy.

### 3.1 Phase behavior

For the preparation of the sample the substances are weighted in a test tube with a flat bottom and a volume of 20 ml. The balance reading is recorded with a precision of  $\Delta m = 0.001$  g. The initial weights can be calculated from the mass fractions (Chapter 2.1.1). After adding a stirring bar the test tube is closed with a polyethylene stopper. For highly viscous microemulsions a neodymium stirring bar ( $\varnothing 7 \times 10$  mm, AstroMedia Vertrieb, Essen) is used.

As the technical-grade surfactant Agnique PG 8105-G contains 35 – 38% and Agnique PG 264-G contains 47 – 50% water these two surfactants were dried up to weight constancy (approximately one week) in a desiccator under blue gel. The other substances are not dried or purified further (see Appendix).

Before the actual investigation of the phase behavior the samples are homogenized by stirring under heat and carefully inspected to ensure that the solid components are completely dissolved. The test tube with sample inside is placed in a transparent, thermostated

water bath (Thermo-Haake DC30; ThermoHaake) with a temperature control up to  $\Delta T = 0.01$  K (digital multimeter M-4650 CR; Voltcraft). While the temperature is regulated the sample has to be stirred. When the desired temperature is reached the stirrer is turned off and the number and kind of coexisting phases are determined by visual inspection of both transmitted and scattered light, using two crossed polarizers to recognize anisotropic phases. At constant composition the temperature is varied. After recording all appearing phases and phase transition temperatures the sample is diluted with water and oil and the process is repeated. Due to the optical rotation of pure sugar it is not possible to determine the presence of liquid crystalline phases at high sugar concentration.

## 3.2 Polymerization

For the polymerization of microemulsion droplets a stock solution containing a 75% sugar/water solution and the surfactant mixture is given into a normal test tube ( $\gamma_a$ ; see Chapter 2.1.1). The following steps are conducted in an almost dark room as the polymerization is already initiated under neon light. Having prepared a 2% mixture of initiator (Irgacure 819) in oil the required amount ( $w_B$ ) is given to the (degassed) stock solution. The stock solution and the oil are mixed with a neodymium stirring bar at temperatures around  $T = 60^\circ\text{C}$  and then thermostated at the desired polymerization temperature. When the phase behavior is adjusted the polymerization lamp is switched on. The duration of polymerization depends on the lamp used: For the microscopy lamp the sample is irradiated for 12 hours. Due to the higher energy of the UV-lamp, here the duration is decreased to 2 hours.

For the polymerization of the bicontinuously structured microemulsion a stock solution could not be provided as the surfactant mixture does not dissolve only in a 75% sugar/water solution. Therefore, the sample was prepared as described in Chapter 3.1, only in a test tube. A spatula tip of the solid initiator (Irgacure 819) has been added shortly before polymerization and stirred into the microemulsion in an almost dark room. Followed by this the polymerization lamp is switched on. The duration of polymerization is  $\sim 30$  min.

The light absorbance of Irgacure 819 is high enough at values between  $\lambda = 300$  nm and  $\lambda = 400$  nm which makes the UV polymerization possible with the sample being in normal glass and not in quartz glass.

### 3.3 Densitometry

Density measurements have been carried out with a commercially available digital density meter (DMA 602 P, PAAR) calibrated with cyclohexane. The sample density  $\rho$  is an important parameter for viscosity measurements which themselves are needed for dynamic light scattering experiments. The mechanical oscillator method is widely used in precision densitometry [101,102], based on the measurement of the natural resonant frequency of a U-shaped glass tube filled with  $\sim 10^{-3}$  l sample and sealed with a teflon stopper. It is possible to measure the ratio between the damping force, introduced by the fluid, and the spring force of the instrument utilizing a phase shifted mode of operation. The absence of bubbles can be controlled through the enlightened inspection window. For temperature dependent measurements an external cryostat (Haake F8; Haake) is connected. The measurement is controlled by a PC. The given density is the average of ten individual measurements.

### 3.4 Viscometry

For the investigation of the viscosity  $\eta$  of low viscous solutions (up to 200 cP) a falling-ball viscometer (Type 001-1926; Haake) is used. Also here, for temperature dependent measurements an external cryostat (Haake F8; Haake) is connected. About 1 ml of the sample is filled into a precision glass syringe in which a gold coated calibrated iron ball is placed. This syringe is brought perpendicular into the thermostated measurement apparatus. A magnetic elevator mechanism lifts the ball up and allows it to fall down again. The falling ball triggers two light barriers with a certain distance. From the fallig time  $\nu$  between these two light barriers (100 – 9999 ms) and with the known ball diameter, -mass, falling distance (2 cm) and temperature, the viscosity can be calculated. With the help of the *Stokes*-force  $F = 6\pi\eta\nu r$ , the dependency between force and acceleration of gravity  $g$  as well as density and volume of the ball, the viscosity is given by

$$\eta = \frac{2 \cdot (\rho_{\text{ball}} - \rho_{\text{sample}}) \cdot g \cdot r_{\text{ball}}^2}{9 \cdot \nu} \quad (3.1)$$

### 3.5 Dynamic Light Scattering

Dynamic light scattering also termed photon correlation spectroscopy has been applied to study a number of system properties, such as particle growth during polymerization and particle size [103-108].

In the experiment, monochromatic and coherent laser light is sent through the sample placed in a toluene bath for index matching. Part of the beam interacts with the sample and the intensity of the scattered light is detected as a function of the time. The number of the scattered photons counted at a certain time by a photomultiplier leads to an interference pattern, arising from the relative positions of the scattering centers. Considering now that the particles are not fixed in space but move randomly due to the *Brownian* motion the distance between the scatter centers in the solution is constantly changing with time. Thus, one observes a time-dependent fluctuation in the scattering intensity  $I(t)$ .

To analyze such fluctuations the concept of autocorrelation function is applied. The correlation of the intensity  $I(t)$  at the time  $t$  with the intensity  $I(t+\tau)$  at the time  $t+\tau$  leads to the intensity-intensity autocorrelation function of the scattering intensity. The standardized autocorrelation function is given by

$$g_2(\tau) = \frac{\langle I(t) \cdot I(t + \tau) \rangle}{\langle I(t) \rangle^2}. \quad (3.2)$$

$\tau$  is in the order of  $\mu\text{s}$  and referred to as the delay time. At short time delays, the correlation is high because the particles do not have a chance to move far from the initial state and therefore, the signals are left almost unchanged. As the time delays become longer, the correlation starts to exponentially decay to zero until no correlation between the scattered intensity of the initial and final states exist. This exponential decay is related to the motion of the particles, specifically to the diffusion coefficient.

The most important components of the dynamic light scattering theory are besides the definition of the intensity autocorrelation function the definition of the electric field autocorrelation function, and the use of the *Siegert* relation [109]

$$g_2(\tau) = 1 + \beta |g_1(\tau)|^2 \quad (3.3)$$

relating the two autocorrelation functions [110,111].  $\beta$  considers the divergence from ideal correlation and is roughly unity and  $g_1(\tau)$  is the normalized field correlation function

related to the properties of the system investigated. If the spectrum under investigation has only one decay process which is given for small, monodisperse droplets, then the electric field autocorrelation function is given by

$$g_1(\tau) = e^{-\Gamma\tau}. \quad (3.4)$$

The decay rate  $\Gamma$  is connected to the diffusion coefficient  $D$  by the *Landau-Platzek* equation

$$\Gamma = q^2 \cdot D. \quad (3.5)$$

$q$  is the scattering vector given by

$$q = \frac{4\pi n}{\lambda} \sin \frac{\theta}{2} \quad (3.6)$$

with  $n$  being the refraction index of the solvent,  $\theta$  the scattering angle and  $\lambda$  the wave length of the laser.

Knowing the diffusion coefficient  $D$  from the *Landau-Platzek* equation the hydrodynamic radius  $R_{\text{hydr}}$  can be determined by using the *Stokes-Einstein* equation

$$D = \frac{k_B T}{6\pi\eta R_{\text{hydr}}}. \quad (3.7)$$

The equation is valid for infinite dilution and spherical, non-interactive particles.  $k_B$  is the *Boltzmann* constant,  $T$  the measuring temperature in Kelvin and  $\eta$  the viscosity of the solvent.

As in reality one considers polydisperse systems with non-spherical or interacting particles the dynamic of the scattering centers cannot be described by a discrete value of  $D$ . For the electric field autocorrelation function a continuous distribution of the decay rate is needed.

$$g_1(\tau) = \int_0^{\infty} G(\Gamma) e^{-\Gamma\tau} d\Gamma \quad (3.8)$$

The weight function  $G(\Gamma)$  is of interest which can be obtained by a Laplace transformation of  $g_1(\tau)$ . For this purpose, the programm CONTIN developed by *S. W. Provencher* is used [112-114] which determines the mean decay rate.

For the light scattering experiments a commercial light scattering spectrometer (ALV, Langen, Germany) with a helium-neon-laser (Laser Technologies, Kleinostheim, Ger-

many) as light source has been used. The scattered light was detected by a photomultiplier (Thorn EMI Electron Tubes, England) installed on a goniometer arm which is free rotatable between scattering angles of  $\theta = 30^\circ$  and  $\theta = 150^\circ$ .

### 3.6 Small Angle Neutron Scattering

Small angle neutron scattering experiments have been applied to characterize the structure of matter since a long time [115-119]. Slow neutrons with a wave length between  $\lambda = 1 \text{ \AA}$  and  $\lambda = 40 \text{ \AA}$  which is in the same range as the internuclear distance in molecules can probe the matter deeply and investigate its volume characteristics as they are not charged. The advantage of neutron to x-ray scattering experiments is that the scattering cross section depends on the characteristics of the atomic nuclei and can be increased specifically by isotope exchange. The large difference in the scattering strength of hydrogen and deuterium allows for contrast matching by selective deuteration (bulk and film contrast). Small angle neutron scattering experiments assume a scattering angle less than  $10^\circ$ . The experiments in this work were carried out using the D22 spectrometer at the Institute Laue Langevin (ILL), Grenoble and at the Forschungsneutronenquelle Heinz Maier-Leibnitz, Garching using the reactor FRM II and the diffractometer KWS 2. The buildup and the procedure of the experiment are described on the basis of the D22 spectrometer at the ILL.

The neutrons produced in a nuclear reaction are slowed down in helium at temperatures around  $T = 25 \text{ K}$  to achieve a smaller velocity range. The subsequent neutron conductor sends thermic neutrons by total reflectance to the selector. The neutron beam with the required velocity ( $4.5 < \lambda / \text{\AA} < 40$ ) is adjusted to the distance of the sample to the detector (between 1.1 m and 36 m) via a collimator before hitting the sample. The sample holder can be thermostatted and quartz cells of various thicknesses can be used. The neutron beam is detected in scattering direction with a 64 x 64 cm  $\text{BF}_3$  detector. A beam stop protects the detector against overloading by the primary beam. Damaged cells and the borders of the detector are masked before the measurement. To produce radially averaged scattering spectra corrections for dark background, pixel efficiency and spatial inhomogeneities are imbedded. The scattering curve is corrected due to the scattering of the empty cell and brought to absolute intensity due to the variable sample to detector distances.



### 3.7 Scanning Electron Microscopy

The scanning electron microscopy (SEM) is a versatile technique for visualizing material structure on scales from hundreds of micrometers down to a few nanometers. The sample surface is imaged by scanning it with a high-energy beam of electrons which interacts with the atoms of the specimen at or near its surface producing signals including backscattered electrons (BEs) and secondary electrons (SEs). BE imaging provides a powerful way to differentiate compositional contrast in the specimen whereas SE imaging only shows the topographic contrast in the specimen surface. One type of SEs (SE1) escapes from the specimen surface and contains high resolution information; SE2 are generated from BEs traveling deeper in the specimen and contain lower resolution information. To achieve high resolution in the images, the SE1 fraction of the total SE yield needs to be increased either by decreasing the accelerating voltage or coating a thin layer of heavy metal on the surface of the specimen. Depositing a layer of metal is also essential when the specimen contains soft polymer because it serves as a conductive layer that helps to prevent a charge on the sample surface to be built up.

High pressure freezing converts a liquid sample to solid state, keeping all atoms and molecules in their natural position, by shifting away from regions containing the phase transition of water to the low density ice I crystals. Figure 3.1 shows a part of the temperature-pressure phase diagram of water.

Increasing pressure shifts both melting and supercooling temperature for homogeneous ice nucleation to lower values leading to a delay in ice crystal nucleation. At the same time, water will not crystallize as low density ice I, imposing the most damage to the cryo-specimen, but as high density ice II or III. Due to the much higher viscosity of water at low temperatures crystallization should, in case it still occurs, proceed slow enough to allow satisfactory freezing. [120]

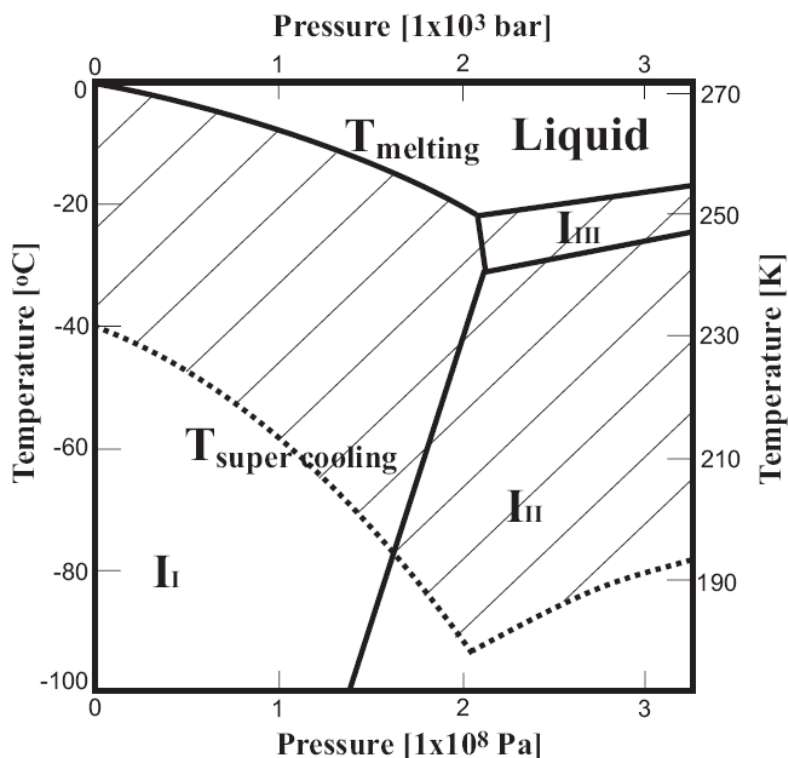


Figure 3.1: Phase diagram from water (taken from [120]).

For the SEM, preparations were done and images were taken at the University of Minnesota – Institute of Technology, Characterization Facility. For the high pressure freezing method, a small piece of the sample is first sandwiched between two freezing hats, shallow dishes made of brass or aluminium, usually 3 mm in diameter and 100  $\mu\text{m}$  to 200  $\mu\text{m}$  in depth. Any air bubble being trapped while putting the dishes together is to be avoided. The assemblage is loaded into a high pressure freezing machine and frozen at 2100 bar within 7 to 8 milliseconds. Having transferred it to a liquid nitrogen container, the sample is fractured by inserting the tip of a cold knife between the rims of the two freezing hats. One half of the fractured sample is mounted on the Gatan 626 cryo-transfer stage (Gatan, Pleasanton, CA, USA) at the atmospheric boiling temperature of liquid nitrogen and transferred to a pre-cooled Balzers MED 010 sputtering device (Balzers Union, Balzers, Liechtenstein) against a counter flow of dry nitrogen gas to avoid the condensation of moisture on the specimen. Inside the sputtering chamber, the sample is allowed to sublime at  $T = -96^{\circ}\text{C}$  and  $p = 2 \times 10^{-9}$  bar. Cryo-sublimation after fracture is needed to remove enough frozen solvent in order to produce topographic contrast for SE imaging. Then, a 5 nm thick layer of platinum is sputtered onto the specimen surface at  $T = -115^{\circ}\text{C}$ , stopping further sublimation of ice during the sputter coating. Finally, the specimen is transferred by the cryo-

transfer to a Hitachi S900 in-the-lens FESEM (Nissei Sangyo America, Ltd., Rolling Meadows, IL, USA) for examination at a low acceleration voltage of 2 to 3 keV. During the SEM imaging, the sample temperature is maintained at  $T = -160^{\circ}\text{C}$ . Only the SE imaging mode was used.

### 3.8 Transmission Electron Microscopy

With the help of the transmission electron microscopy (TEM) direct information about aggregate morphology in microstructured fluids can be obtained, so long as the objects of interest are in the applicable size range. Extremely rapid cooling and freezing with cooling rates of  $> 10000$  K/s are necessary to minimize the occurrence of freezing artifacts [62]. The main goal in the preparation of liquid specimens for TEM is to achieve the formation of thin liquid films so that the electrons are able to run through the sample. With regard to the specimen preparation of liquid samples, there are two well-established techniques, namely the freeze fracture electron microscopy (FFEM) [121,122] and the freeze fracture direct imaging (FFDI) technique [56]. FFEM and FFDI appear to complement each other perfectly; while FFEM visualizes the topography of the structure, the internal structure is imaged by FFDI. For preparation, two electron microscopy grids of  $10\ \mu\text{m}$  thickness (360 mesh, Ted Pella Inc. 8HGC360) are enclosed between two copper plates of  $100\ \mu\text{m}$  thickness (Balzers Union BU 012-056-T). To prevent demixing of the microemulsions, the temperatures of the sandwich and the solution have to equalize before they are brought in contact. Therefore the sandwich and the tweezers by which they are held are placed in a temperature control unit in a manner that they are both passed by an air stream with the same temperature as the solution. After thermal equilibrium the air flow is stopped and the sandwich is brought in contact with the solution. The solution penetrates into the sandwich which is then transferred into liquid ethane with a plunging device for freezing [56,61]. Afterwards, the sandwich is transferred into liquid nitrogen and fractured by separating the copper plates. For the FFDI technique, the grid is mounted into a cryo-holder (CT3500, Oxford Instruments, Oxford, U.K.) and viewed in the TEM (LEO EM 912 Omega). For the FFEM technique, the grid is shadowed with Ta/W and coated with a carbon layer in a Balzers BAF 360 M device (Balzers, Liechtenstein) before investigating in the TEM [61].

### 3.9 Polarized Light Transmission Microscopy

Polarized light transmission microscopy is a technique widely used to study the microstructure of crystals, liquid crystals, polymers and other transparent, optically anisotropic specimens. With a first polarizer located underneath the object slide only light oscillating in one plane is passed through the sample. At the top of the object slide a second polarizer, also called analyzer, is situated, turned by  $90^\circ$ . The sample placed between these two polarizers only allows the light to pass if the sample is able to turn the plane of the light. Such optically active substances are named birefringent or optical anisotropic.

Preparations were viewed using equipment located at the University of Minnesota – College of Biological Sciences, Imaging Center. An Olympus BH-2 upright photomicroscope (Leeds Precision Instruments, Inc., Edina, MN 55439, USA) equipped with bright-field, differential interference contrast (DIC), polarizing and fluorescence optics was used for observation and image acquisition of samples. Digital images were collected using a Diagnostic Instruments Insight 2 MP color camera connected to iMac G5 computer using Spot version 4.5 (Diagnostic Instruments, Sterling Heights, MI).

## 4 Phase Behavior of Highly Viscous Microemulsions

This chapter deals with the investigation of the influence of sucrose or a mixture of sucrose/trehalose, added to the water phase, on the phase behavior of microemulsions containing water, *n*-octane and pure or technical-grade surfactants. The fundamental idea is to increase the viscosity to slow down the reorganization kinetics of the phase behavior so that the oil phase can be polymerized without phase separation. In a second step, the oil has been replaced by a polymerizable methacrylate oil to prepare highly viscous, polymerizable microemulsions.

At the beginning of this chapter the influence of sugar on the phase behavior is shown followed by a journey towards highly viscous, polymerizable microemulsions. Section 4.3 deals with the addition of cross-linker and its influence on the phase behavior. Afterwards the addition of blockcopolymers to the microemulsion system is discussed (section 4.4). Thereby, the influences on the phase behavior by adding sugar to the water phase, using hexyl methacrylate with varying amounts of cross-linker as oil phase as well as adding blockcopolymer to the surfactant mixture are characterized via  $T(\gamma)$ -sections through the phase prism in order to synthesize a polymeric bicontinuous nanostructure. Bearing in mind the synthesis of monodisperse, spherical, polymeric nanoparticles  $T(w_B)$ -sections of highly viscous, polymerizable water/sugar-rich microemulsions are discussed in section 4.5.

### 4.1 Influence of Sugar on the Phase Behavior

The phase behavior of a ternary mixture as function of the temperature is best shown in an upright phase prism with a Gibbs triangle as base and a vertical temperature axis (Figure 2.1). To simplify this 3-dimensional diagram a vertical 2-dimensional section

through this phase prism at a constant oil-to-water/oil ratio  $\alpha$  with varying temperature  $T$  and surfactant mass fraction  $\gamma$  is performed. This so-called  $T(\gamma)$ -section is shown in Figure 4.1.

Starting point of these studies is the temperature dependent phase behavior of the ternary system  $\text{H}_2\text{O} - n\text{-octane} - \text{C}_{10}\text{E}_6$  ( $\Psi = 0.00$ ) (Figure 4.1 top) [49]. At lower temperatures an oil-in-water microemulsion coexists with an excess oil phase ( $\underline{2}$ ), whereas at high temperatures a water-in-oil microemulsion coexisting with an excess water phase ( $\bar{2}$ ) is found. At intermediate temperatures and lower surfactant concentrations the three-phase body occurs (3), meeting the one-phase region (1) at higher surfactant concentrations, the so-called  $\tilde{X}$ -point. Here a minimum amount of surfactant  $\tilde{\gamma}$  is needed to solubilize water and oil at the corresponding temperature  $\tilde{T}$ . The efficiency of a surfactant and the phase inversion temperature are given by  $\tilde{\gamma}$  and  $\tilde{T}$ , respectively. As the bicontinuous nanostructure within the one-phase region shall be finally polymerized, the three-phase region has not been further investigated.

To analyze the influence of sucrose on the phase behavior water is substituted step by step by a water/sucrose mixture with different mass fractions  $\Psi$  of sucrose (equation 2.5). In all cases the  $T(\gamma)$ -sections are recorded at the same mass fraction of oil in the water/oil mixture  $\alpha = 0.4125$ . It is important to remember that the density of the water/sucrose mixture depends on the respective sugar mass fraction. As one can see in Figure 4.1 increasing the sucrose mass fraction in the water phase shifts the phase inversion temperature  $\tilde{T}$  to lower values, i.e. for the pure water system a temperature of  $\tilde{T} = 61.3^\circ\text{C}$  is found, while for the system containing 50% sucrose in the hydrophilic phase ( $\Psi = 0.50$ ) the phase inversion temperature decreases to  $\tilde{T} = 27.7^\circ\text{C}$ . While  $\tilde{T}$  decreases with increasing sucrose mass fractions the mass fraction of surfactant  $\tilde{\gamma}$  stays almost constant.

From literature it is known that microemulsions cannot only be formulated by using monodisperse pure surfactants but also by using technical-grade surfactants [123-125]. The influence of sucrose on the phase behavior of a system containing a technical-grade surfactant is shown in Figure 4.1 bottom. Starting with a mixture of  $\text{H}_2\text{O} - n\text{-octane} - \text{Lutensol XL70}$ , a C10-Guerbet-alcohol and an average of 7 ethylene oxide units, the amount of sugar in the hydrophilic phase is increased stepwise. Again, the  $T(\gamma)$ -sections are recorded at the same mass fraction of oil in the water/oil mixture  $\alpha = 0.4125$ . The phase behavior follows the same trend as found for the system  $\text{H}_2\text{O}/\text{sucrose} - n\text{-octane} - \text{C}_{10}\text{E}_6$ . By in-

creasing the sucrose mass fraction in the water phase the overall phase boundaries shift to lower temperatures. The phase inversion temperature  $\tilde{T}$  shifts from  $\tilde{T} = 72.8^\circ\text{C}$  for the sugarless system to  $\tilde{T} = 37.3^\circ\text{C}$  by replacing 50% water with sucrose. At the same time, the system becomes considerably more efficient, i.e.  $\tilde{\gamma}$  shifts to lower values.

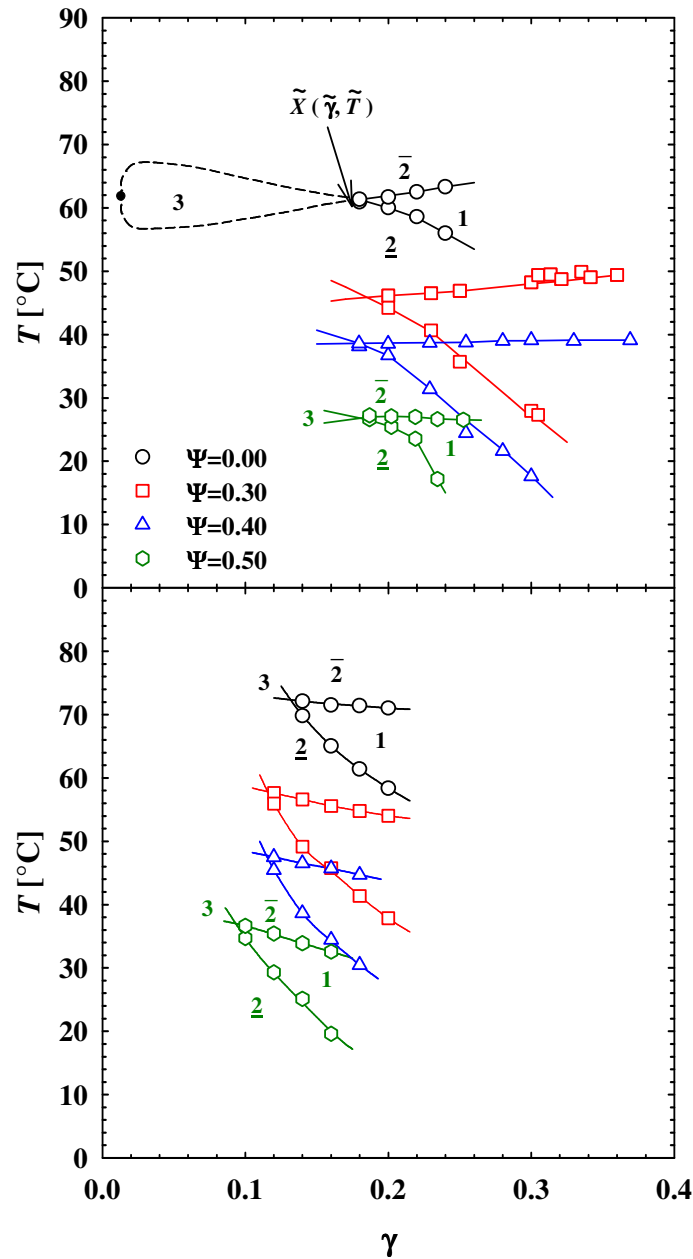


Figure 4.1:  $T(\gamma)$ -sections of the systems  $\text{H}_2\text{O}/\text{sucrose} - n\text{-octane} - \text{C}_{10}\text{E}_6$  (top) and  $\text{H}_2\text{O}/\text{sucrose} - n\text{-octane} - \text{Lutensol XL70}$  (bottom) at a constant mass fraction  $\alpha = 0.4125$ . In both cases, the phase boundaries are shifted to lower temperatures if the sucrose mass fraction in the water phase is increased from  $\Psi = 0.00$  up to  $\Psi = 0.50$ . A considerable increase of the efficiency is found in the technical-grade system due to the decreasing monomeric solubility of the hydrophobic homologues of Lutensol XL70 at lower temperatures.

In Figure 4.2 the temperature  $\tilde{T}$  and the surfactant mass fraction  $\tilde{\gamma}$  of the  $\tilde{X}$ -points are plotted versus the sucrose mass fraction  $\Psi$  in the water phase for the systems  $\text{H}_2\text{O}/\text{sucrose} - n\text{-octane} - \text{C}_{10}\text{E}_6$  and  $\text{H}_2\text{O}/\text{sucrose} - n\text{-octane} - \text{Lutensol XL 70}$  at  $\alpha = 0.4125$ . As one can see in Figure 4.2 top, the decrease of  $\tilde{T}$  with increasing  $\Psi$  follows a parabolic dependence. Reason for the decrease of  $\tilde{T}$  is the dissolving of sucrose in the water phase. Water is needed to hydrate the sucrose molecules and hence, less water is left to hydrate the headgroups of the surfactant. Therefore, the volume of the headgroup decreases resulting in a decrease of the spontaneous curvature of the surfactant film and the phase boundaries shift to lower temperatures. The parabolic decrease suggests a cooperative effect: The amount of  $\text{H}_2\text{O}$  molecules hydrating the surfactant headgroups decreases more strongly as more sucrose is added to the system. One reason for the phase inversion temperatures  $\tilde{T}$  of the technical-grade surfactant Lutensol XL70 system being  $\Delta\tilde{T} \approx 10^\circ\text{C}$  higher compared to the pure surfactant  $\text{C}_{10}\text{E}_6$  system is the higher hydrophilicity of Lutensol XL 70. The hydrophilic headgroup size is larger by one oxyethylene unit. The temperature difference of  $\Delta\tilde{T} \approx 10^\circ\text{C}$  stays almost constant during the parabolic decrease.

Figure 4.2 bottom shows that the surfactant mass fraction  $\tilde{\gamma}$  stays constant for the system  $\text{H}_2\text{O}/\text{sucrose} - n\text{-octane} - \text{C}_{10}\text{E}_6$  whereas the efficiency increases considerably for the system  $\text{H}_2\text{O}/\text{sucrose} - n\text{-octane} - \text{Lutensol XL70}$ . This increase in efficiency can only be due to the surfactant as it is the only component which is varied and might be caused by the decreasing monomeric solubility of the hydrophobic homologues of Lutensol XL 70 at lower temperatures.



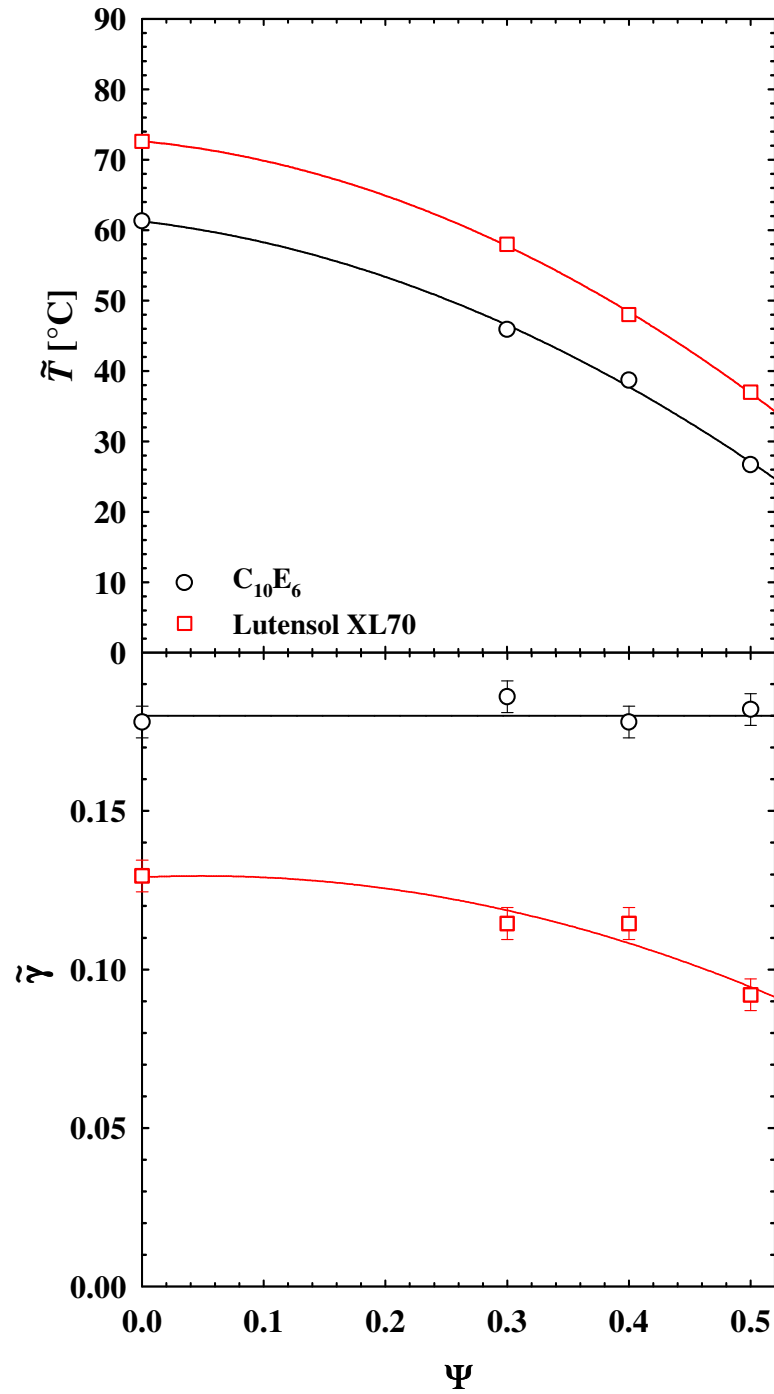


Figure 4.2:  $\tilde{T}$  and  $\tilde{\gamma}$  plotted vs.  $\Psi$  for the systems  $H_2O/sucrose - n\text{-octane} - C_{10}E_6$  and  $H_2O/sucrose - n\text{-octane} - Lutensol XL70$  at  $\alpha = 0.4125$ . The strong decrease of  $\tilde{T}$  with increasing sucrose mass fraction  $\Psi$  in the water phase is due to weaker hydration of the surfactant headgroups by water molecules which are instead needed to hydrate the sucrose. The increase in efficiency is caused by the decreasing monomeric solubility of the hydrophobic homologues of Lutensol XL 70 at lower temperatures.

To investigate in what manner the phase behavior depends on the kind of sugar used, again  $T(\gamma)$ -sections are performed increasing the mass fraction of fructose in the water/fructose mixture. Whereas sucrose is a disaccharide, fructose is a monosaccharide. Starting system is the previously investigated system H<sub>2</sub>O – *n*-octane – Lutensol XL70 at an oil-to-water/oil ratio  $\alpha = 0.4125$ . As expected, with increasing amount of fructose in the water phase, the phase boundaries shift to lower temperatures (Figure 4.3). At the same time the system becomes slightly more efficient.

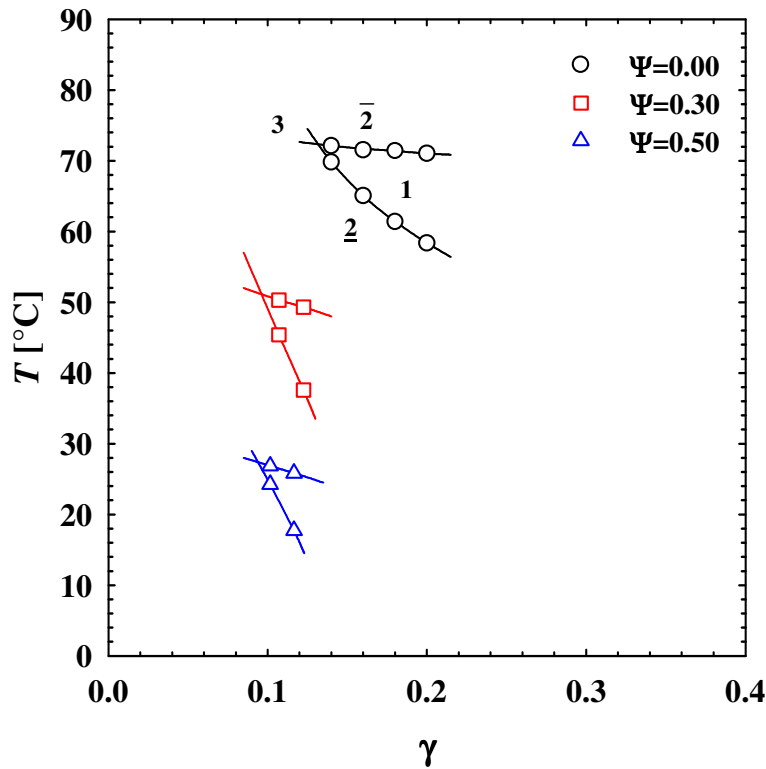


Figure 4.3:  $T(\gamma)$ -sections of the system H<sub>2</sub>O/fructose – *n*-octane – Lutensol XL70 at a constant mass fraction  $\alpha = 0.4125$ . The upper  $T(\gamma)$ -section shows the phase behavior for the system  $\Psi = 0.00$ , then the fructose fraction in the water phase is increased up to  $\Psi = 0.50$ . The phase boundaries shift to lower temperatures with increasing fructose mass fraction and the system becomes slightly more efficient.

In Figure 4.4 the variation of the phase inversion temperature  $\tilde{T}$  with the sugar mass fraction  $\Psi$  in the water phase is compared for the system H<sub>2</sub>O/sucrose – *n*-octane – Lutensol XL70 to the system H<sub>2</sub>O/fructose – *n*-octane – Lutensol XL70 at  $\alpha = 0.4125$ . Increasing the amount of sugar in the hydrophilic phase up to  $\Psi = 0.50$  fructose illustrates a  $\Delta\tilde{T} = 10^\circ\text{C}$  stronger decrease of the phase inversion temperature  $\tilde{T}$  compared to the system containing sucrose as sugar.

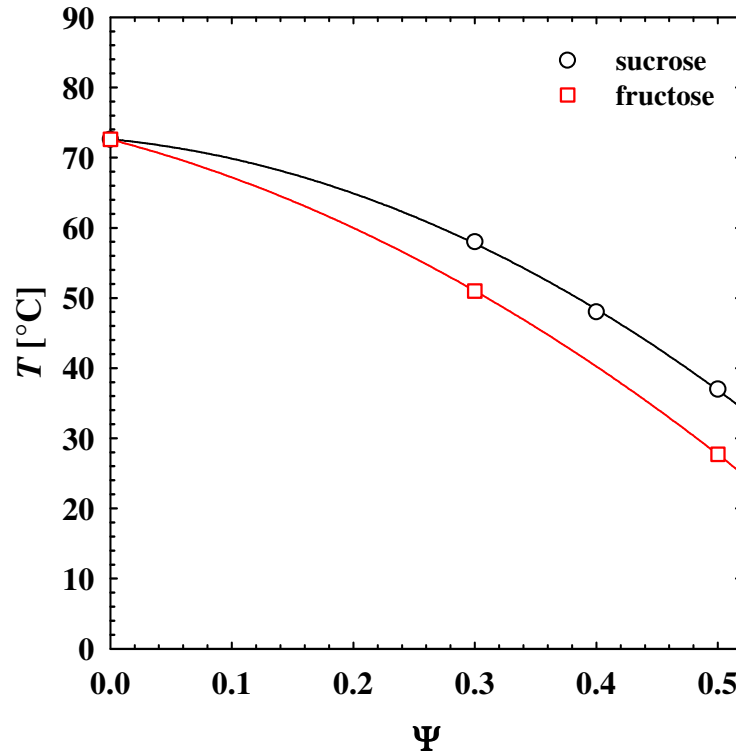


Figure 4.4:  $\tilde{T}$  plotted vs.  $\Psi$  of the systems  $\text{H}_2\text{O}/\text{sucrose} - n\text{-octane} - \text{Lutensol XL 70}$  and  $\text{H}_2\text{O}/\text{fructose} - n\text{-octane} - \text{Lutensol XL70}$  at  $\alpha = 0.4125$ . The phase inversion temperature  $\tilde{T}$  shows a stronger decrease for the systems having added fructose instead of sucrose as sugar to the water phase.

For the following measurements only disaccharides will be used as sugar component.

As  $\tilde{T}$  decreases with increasing mass fraction of sucrose or fructose in the water/sugar mixture, a more hydrophilic surfactant is needed to prepare a highly viscous microemulsion with a sugar mass fraction of up to  $\Psi = 0.75$  within the experimental temperature range. In recent years a class of novel nonionic surfactants, the alkylpolyglycosides, have been of great interest [126-130]. Alkylpolyglycosides are strongly hydrophilic with phase inversion temperatures  $\tilde{T}$  in typical nonionic microemulsion systems being above  $100^\circ\text{C}$  [131]. To induce a temperature-driven phase inversion within the measuring range of aqueous systems usually the use of more “hydrophilic oils” [132,133] or the addition of a hydrophobic co-surfactant [134-137] is necessary. In this work, we utilized the hydrophilicity of the alkylpolyglycosides to compensate for the parabolic decrease of the phase inversion temperature  $\tilde{T}$  with increasing sucrose content in the water phase.

Figure 4.5 top shows the phase behavior of the system  $\text{H}_2\text{O}/\text{sucrose} - n\text{-octane} - \text{C}_{10}\text{E}_6/\text{C}_8\text{G}_1$  for different mass fractions  $\delta$  of  $\text{C}_8\text{G}_1$  in the  $\text{C}_{10}\text{E}_6/\text{C}_8\text{G}_1$  mixture at a mass

fraction of sucrose in the water phase of  $\Psi = 0.50$  and a constant  $\alpha = 0.4125$ . With increasing  $\delta$  and therefore increasing fraction of the hydrophilic  $C_8G_1$  surfactant, the phase boundaries and therewith  $\tilde{T}$  shift to higher temperatures. Starting from the  $T(\gamma)$ -section at  $\delta = 0.00$  the temperature  $\tilde{T}$  increases from  $\tilde{T} = 27.7^\circ\text{C}$  to  $\tilde{T} = 78.8^\circ\text{C}$  at  $\delta = 0.50$ . At the same time the system becomes increasingly inefficient, i.e. the surfactant mass fraction to solubilize *n*-octane in the water/sucrose mixture and vice versa increases from  $\tilde{\gamma} = 0.178$  ( $\delta = 0.00$ ) up to  $\tilde{\gamma} = 0.298$  ( $\delta = 0.50$ ).

The same trend in the phase behavior is found if one uses the technical-grade system and replaces the pure sugar surfactant  $C_8G_1$  by the technical-grade analogon Agnique PG 8105-G, consisting of an average glucose unit of 1.5 as headgroup and 8 to 10 carbons in the tail group (Figure 4.5 bottom). As the charge contains 35 – 38% water Agnique PG 8105-G is dried up to weight constancy (approximately one week) in a desiccator under blue gel before usage. Starting from the system  $\text{H}_2\text{O}/\text{sucrose} - n\text{-octane} - \text{Lutensol XL70}$  containing 50% sucrose in the water phase the phase boundaries shift to higher temperatures by increasing the amount of Agnique PG 8105-G in the surfactant mixture of Lutensol XL 70/Agnique PG 8105-G. Due to the fact that the headgroup size of Agnique PG 8105-G is slightly higher than the one of  $C_8G_1$  (1.5 versus 1) the former is more hydrophilic. Replacing 40% of the *n*-alkylpolyglycoether with a sugar surfactant  $\Delta\tilde{T}$  increases for the pure surfactant system by  $\Delta\tilde{T} = 33^\circ\text{C}$  whereas the technical-grade sugar surfactant leads to an increase of  $\Delta\tilde{T} = 38^\circ\text{C}$ . The decrease in efficiency from  $\tilde{\gamma} = 0.095$  ( $\delta = 0.00$ ) to  $\tilde{\gamma} = 0.235$  ( $\delta = 0.40$ ) is of the same range as the one found for the system  $\text{H}_2\text{O}/\text{sucrose} - n\text{-octane} - C_{10}E_6/C_8G_1$ .

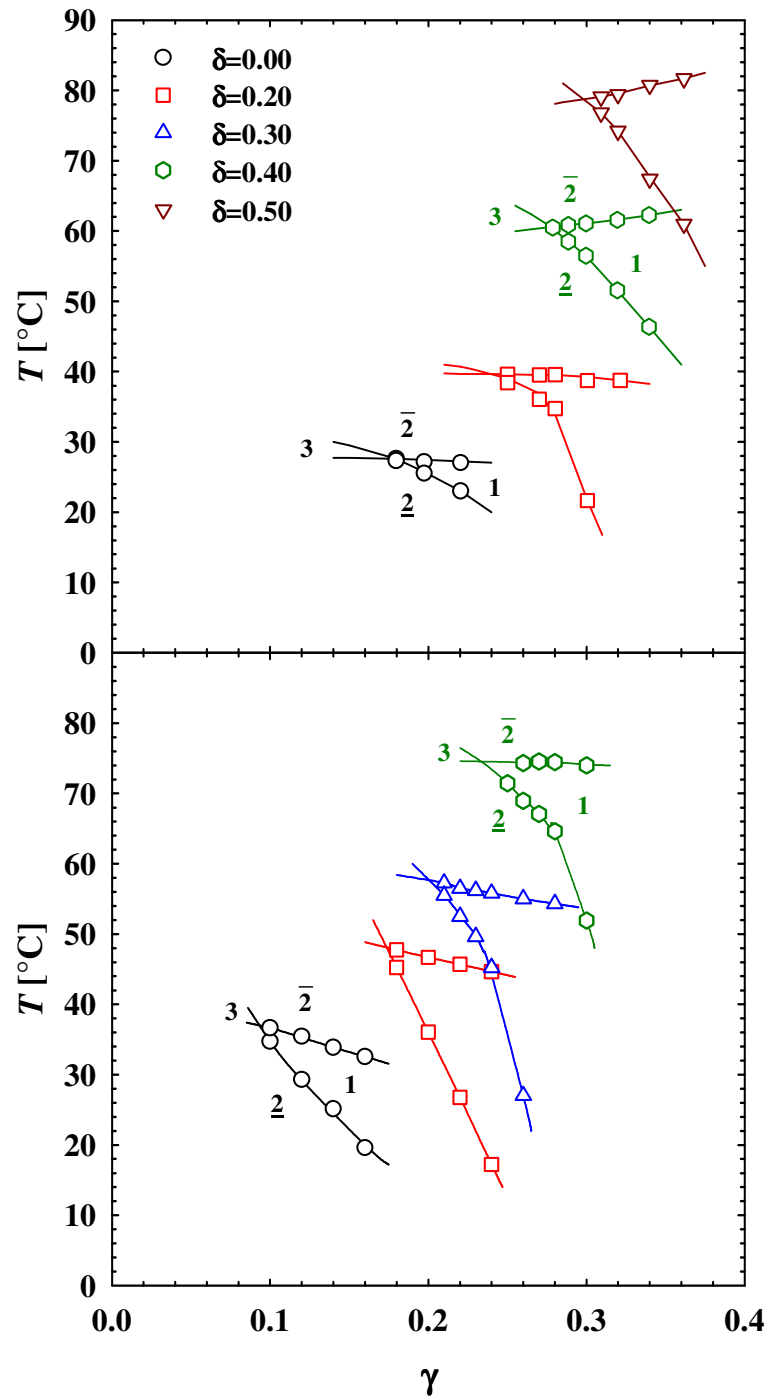


Figure 4.5:  $T(\gamma)$ -sections of the systems  $\text{H}_2\text{O}/\text{sucrose} - n\text{-octane} - \text{C}_{10}\text{E}_6/\text{C}_8\text{G}_1$  (top) and  $\text{H}_2\text{O}/\text{sucrose} - n\text{-octane} - \text{Lutensol XL70}/\text{Agnique PG 8105-G}$  (bottom) at a constant mass fraction  $\alpha = 0.4125$  and a constant sucrose fraction  $\Psi = 0.50$ . In both cases, increasing the fraction of the hydrophilic sugar surfactant shifts the phase boundaries to higher temperatures. At the same time the systems become more inefficient.

## 4.2 Highly Viscous Polymerizable Microemulsions

Due to the inefficiency of the pure surfactant  $C_8G_1$ , the next step to tune the system  $H_2O/sucrose - n\text{-octane} - C_{10}E_6/C_8G_1$  with  $\Psi = 0.50$ ,  $\alpha = 0.4125$  and  $\delta = 0.50$  towards a viscous microemulsion is to find a surfactant mixture that is almost as hydrophilic but more efficient than the  $C_{10}E_6/C_8G_1$  mixture. As known from literature with increasing  $i$  and constant  $j$  the surfactant becomes more hydrophobic and the  $\tilde{X}$ -point shifts to lower temperatures but the surfactant also becomes clearly more efficient [49].

Changing the surfactant mixture in the system  $H_2O/sucrose - n\text{-octane} - C_{10}E_6/C_8G_1$  to a mixture of  $C_{14}E_6/C_8G_1$  the minimal surfactant mass fraction  $\tilde{\gamma}$  to solubilize the water/sugar mixture and  $n\text{-octane}$  decreases as expected strongly to  $\tilde{\gamma} = 0.202$ . Simultaneously the phase inversion temperature  $\tilde{T}$  decreases by  $\Delta\tilde{T} = 9.4^\circ\text{C}$  to  $\tilde{T} = 69.4^\circ\text{C}$ . Comparing this decrease of the phase inversion temperature  $\tilde{T}$  with the one observed for the non-sugar systems  $H_2O - n\text{-octane} - C_{10}E_6$  and  $H_2O - n\text{-octane} - C_{14}E_6$  the temperature decrease is  $\Delta\tilde{T} = 21^\circ\text{C}$  (extrapolated from [49]). Having in mind that the sugar-microemulsion contains only 50%  $C_iE_j$  surfactant in the surfactant mixture the temperature decrease of the non-sugar system is comparable to the temperature decrease of the sugar system.

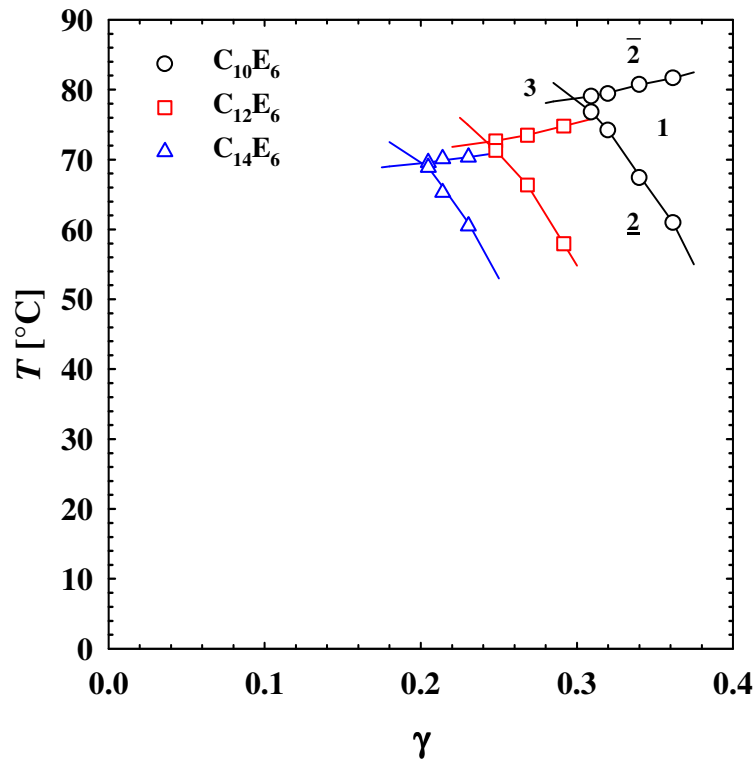


Figure 4.6:  $T(\gamma)$ -sections of the system  $\text{H}_2\text{O}/\text{sucrose} - n\text{-octane} - \text{C}_i\text{E}_j/\text{C}_8\text{G}_1$  at a constant mass fraction  $\alpha = 0.4125$ , sucrose mass fraction  $\Psi = 0.50$  and surfactant mass fraction  $\delta = 0.50$ . Increasing the surfactant chain length from  $\text{C}_{10}\text{E}_6$  over  $\text{C}_{12}\text{E}_6$  to  $\text{C}_{14}\text{E}_6$  the system becomes more efficient. The temperature decrease is comparable with the corresponding temperature decrease found for non-sugar systems (for details see text).

To increase the viscosity of the microemulsion further, the mass fraction of sucrose in water must be increased. In the following, for systems containing more than 65 wt.% of sugar in the aqueous component, a sucrose/trehalose mixture is used due to the better solubility of trehalose in water. The mass fraction of trehalose in the sucrose/trehalose mixture is kept constant with  $\zeta = 0.38$  (equation 2.6).

Figure 4.7 shows on the left part (*a-c*) the journey towards a highly viscous microemulsion containing only pure surfactants. The investigations are carried out for the system  $\text{H}_2\text{O}/(\text{sucrose}/\text{trehalose}) - n\text{-octane} - \text{C}_i\text{E}_j/\text{C}_8\text{G}_1$  at  $\alpha = 0.4125$ . On the right part (*d-f*), the investigations are shown for the system  $\text{H}_2\text{O}/(\text{sucrose}/\text{trehalose}) - n\text{-octane} - \text{Lutensol XL70}/\text{Agnique PG 8105-G}$  at  $\alpha = 0.4125$  where only technical-grade surfactants are applied.

Starting from the system  $\text{H}_2\text{O}/(\text{sucrose}/\text{trehalose}) - n\text{-octane} - \text{C}_{14}\text{E}_6/\text{C}_8\text{G}_1$  with  $\alpha = 0.4125$ ,  $\Psi = 0.50$  and  $\delta = 0.50$  and the system  $\text{H}_2\text{O}/(\text{sucrose}/\text{trehalose}) - n\text{-octane} - \text{Lutensol XL70}/\text{Agnique PG 8105-G}$  with  $\alpha = 0.4125$ ,  $\Psi = 0.50$  and  $\delta = 0.40$  the sucrose

mass fraction is increased for both systems up to  $\Psi = 0.65$  leading in each case to a decrease of the phase inversion temperature  $\tilde{T}$  of around  $\Delta\tilde{T} = 30^\circ\text{C}$  (Figure 4.7, *a*) and *d*). Furthermore, both surfactant mixtures become slightly more efficient.

To compensate for the decrease in temperature the amount of hydrophilic surfactant must be increased. The phase diagram Figure 4.7, *b*) displays the  $T(\gamma)$ -section for the system containing the pure surfactants  $\text{C}_{14}\text{E}_6/\text{C}_8\text{G}_1$  with a sucrose mass fraction of  $\Psi = 0.65$  and a surfactant mass fraction of  $\delta = 0.50$ . The surfactant  $\text{C}_{14}\text{E}_6$  is replaced with the more hydrophilic and efficient surfactant  $\text{C}_{18}\text{E}_8$  to shift the phase boundaries to higher temperatures without losing any efficiency. As one can see, though the phase inversion temperature  $\tilde{T}$  increases up to  $\tilde{T} = 56.2^\circ\text{C}$  the system becomes slightly more efficient. For the technical-grade  $\text{H}_2\text{O}/(\text{sucrose}/\text{trehalose}) - n\text{-octane} - \text{Lutensol XL70}/\text{Agnique PG 8105-G}$  system the amount of Agnique PG 8105-G is increased from  $\delta = 0.40$  to  $\delta = 0.55$  (Figure 4.7, *e*). As one can see the phase boundaries and consequently the phase inversion temperature  $\tilde{T}$  shifts to higher temperatures, i.e.  $\tilde{T} = 78^\circ\text{C}$ . The surfactant mixture system also becomes less efficient ( $\tilde{\gamma} = 0.265$ ).

Finally, in both systems the sugar mass fraction is increased up to  $\Psi = 0.75$ , using a sucrose/trehalose mixture (Figure 4.7, *c*) and *f*). The phase boundaries for the system containing the pure surfactant mixture cannot be measured properly with only 50%  $\text{C}_8\text{G}_1$  in the surfactant mixture because the additional amount of added sucrose/trehalose shifts the phase inversion temperature  $\tilde{T}$  to very low values. Therefore, the  $\text{C}_8\text{G}_1$  mass fraction in the surfactant mixture is increased at the same time to  $\delta = 0.70$ . As  $\delta$  and  $\Psi$  are increased  $\tilde{T}$  is shifted to  $\tilde{T} = 67^\circ\text{C}$  while the surfactant mixture becomes less efficient. For the system containing technical-grade surfactants the expected decrease in the phase inversion temperature  $\tilde{T}$  is found (Figure 4.7, *f*) and the surfactant mixture becomes slightly more efficient.



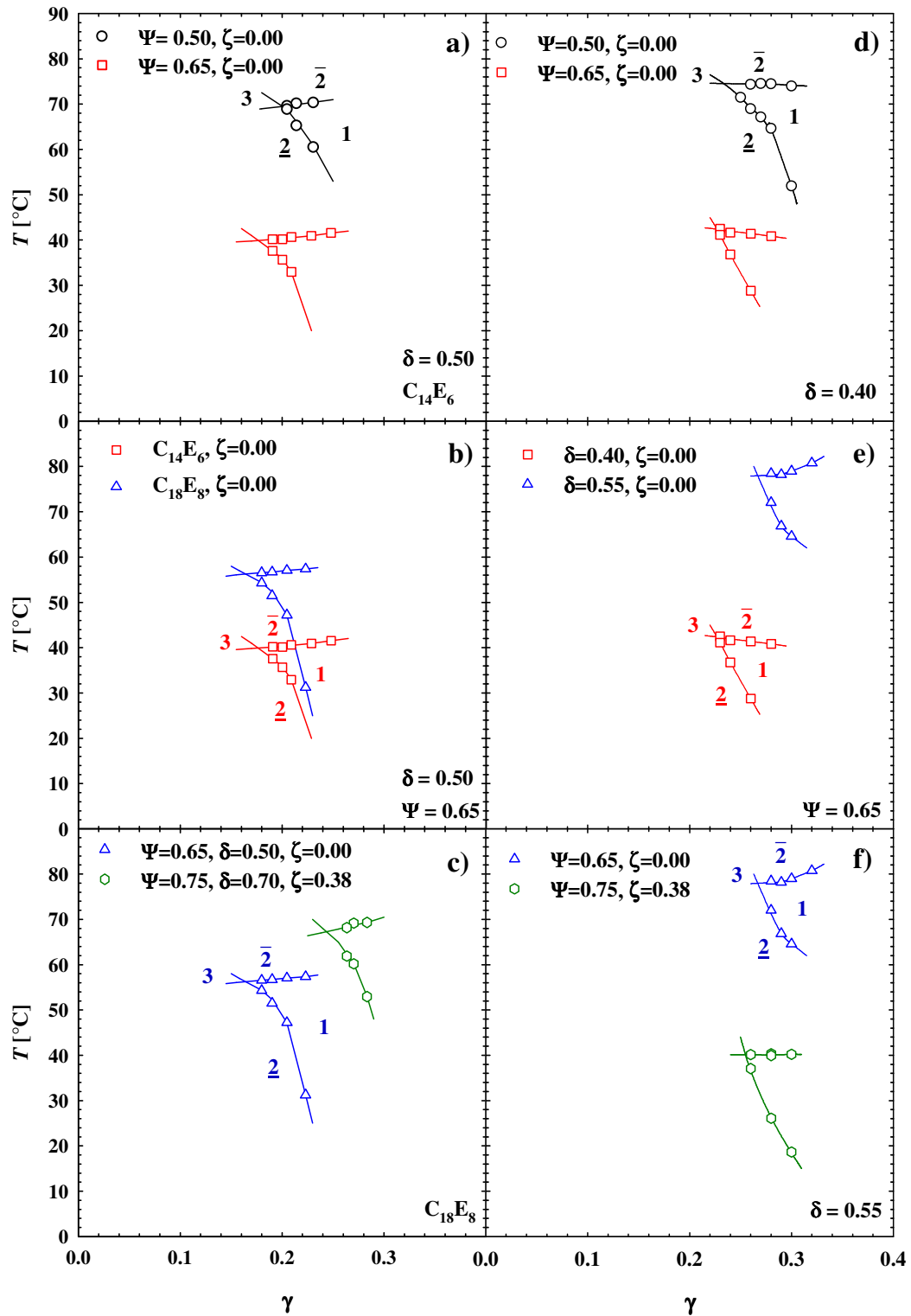


Figure 4.7:  $T(\gamma)$ -sections of the systems  $\text{H}_2\text{O}/(\text{sucrose}/\text{trehalose}) - n\text{-octane} - \text{C}_i\text{E}_j/\text{C}_8\text{G}_1$  and  $\text{H}_2\text{O}/(\text{sucrose}/\text{trehalose}) - n\text{-octane} - \text{Lutensol XL 70}/\text{Agnique PG 8105-G}$  at  $\alpha = 0.4125$ . The amount of sugar in the water phase is increased step by step. To compensate for the temperature decrease of the phase boundaries the surfactant mixture is changed, respectively. Note, that for systems with  $\Psi > 0.65$  a sucrose/trehalose mixture is used. The fraction of trehalose in the sucrose/trehalose mixture is given by  $\zeta = 0.38$ .

Figure 4.8 compares the  $T(\gamma)$ -sections of the pure system  $\text{H}_2\text{O}/(\text{sucrose}/\text{trehalose}) - n\text{-octane} - \text{C}_{18}\text{E}_8/\text{C}_8\text{G}_1$  with  $\alpha = 0.4125$ ,  $\Psi = 0.75$ ,  $\zeta = 0.38$  and  $\delta = 0.70$  and the technical-grade system  $\text{H}_2\text{O}/(\text{sucrose}/\text{trehalose}) - n\text{-octane} - \text{Lutensol XL 70}/\text{Agnique PG 8105-G}$  with  $\alpha = 0.4125$ ,  $\Psi = 0.75$ ,  $\zeta = 0.38$  and  $\delta = 0.55$ . The former has a phase inversion temperature  $\tilde{T}$  of  $\tilde{T} = 67^\circ\text{C}$  and an efficiency of  $\tilde{\gamma}$  of  $\tilde{\gamma} = 0.243$  whereas the phase inversion temperature  $\tilde{T}$  of the latter is found at  $\tilde{T} = 40^\circ\text{C}$  and  $\tilde{\gamma}$  at  $\tilde{\gamma} = 0.256$ . As one can see the general behavior is similar. The advantage of the technical-grade system in terms of application is of course the smaller costs.

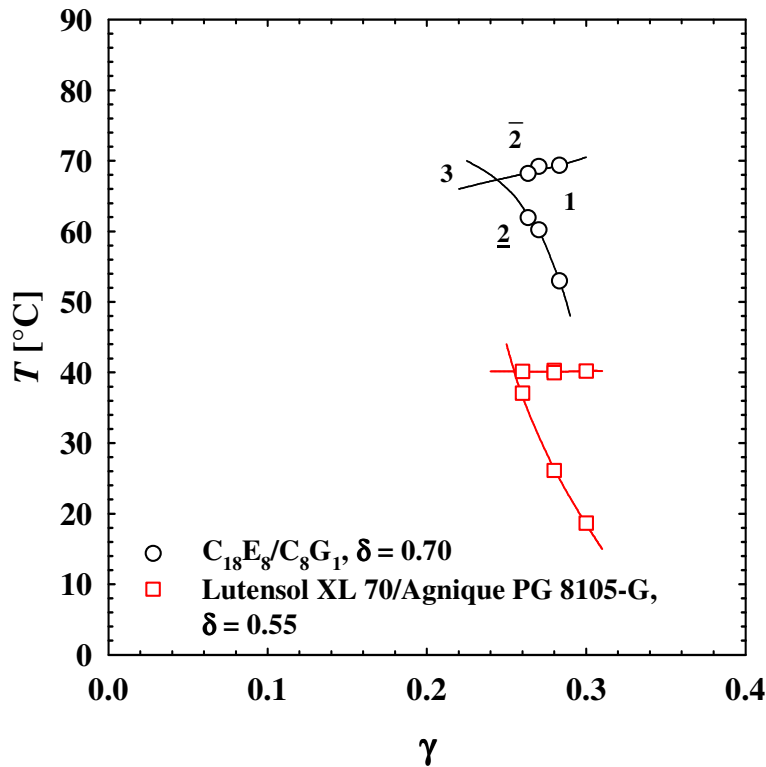


Figure 4.8:  $T(\gamma)$ -sections of the pure system  $\text{H}_2\text{O}/(\text{sucrose}/\text{trehalose}) - n\text{-octane} - \text{C}_{18}\text{E}_8/\text{C}_8\text{G}_1$  with  $\alpha = 0.4125$ ,  $\Psi = 0.75$  and  $\delta = 0.70$  and the technical-grade system  $\text{H}_2\text{O}/(\text{sucrose}/\text{trehalose}) - n\text{-octane} - \text{Lutensol XL 70}/\text{Agnique PG 8105-G}$  with  $\alpha = 0.4125$ ,  $\Psi = 0.75$ ,  $\zeta = 0.38$  and  $\delta = 0.55$ .

One way to fix the microstructure of the highly viscous microemulsion is to replace the oil  $n\text{-octane}$  with a polymerizable oil. Here,  $n\text{-hexyl methacrylate}$  ( $\text{C}_6\text{MA}$ ) has been used since it is the shortest chain methacrylate oil with a very low solubility in water [138]. As it is shown in Figure 4.9 for the system  $\text{H}_2\text{O}/(\text{sucrose}/\text{trehalose}) - n\text{-octane}/\text{C}_6\text{MA} -$

$C_{18}E_8/C_8G_1$  with  $\alpha = 0.4125$ ,  $\Psi = 0.75$ ,  $\zeta = 0.38$  and  $\delta = 0.70$ , the replacement has a strong effect on the phase behavior. Replacing only 15 wt.% of *n*-octane by  $C_6MA$  ( $\beta = 0.15$ ) the phase inversion temperature  $\tilde{T}$  already decreases by  $\Delta\tilde{T} = 22.5^\circ\text{C}$  to  $\tilde{T} = 44.5^\circ\text{C}$ . The effect of the monomer  $C_6MA$  on microemulsions containing sugar in the water phase is surprising. Known from literature the phase inversion temperature  $\tilde{T}$  decreases by only  $\Delta\tilde{T} = 30^\circ\text{C}$  replacing *n*-octane completely by  $C_6MA$  in the system  $H_2O - n\text{-octane} - C_{10}E_6$  [36,70]. The efficiency of the system increases by  $\Delta\tilde{\gamma} = 0.038$  to  $\tilde{\gamma} = 0.205$ . A possible explanation for this decrease could be that  $C_6MA$  does not only act as polymerizable oil in these sugar systems but due to its hydrophobic hexyl group and the more hydrophilic methacrylate group also partially as hydrophobic co-surfactant.

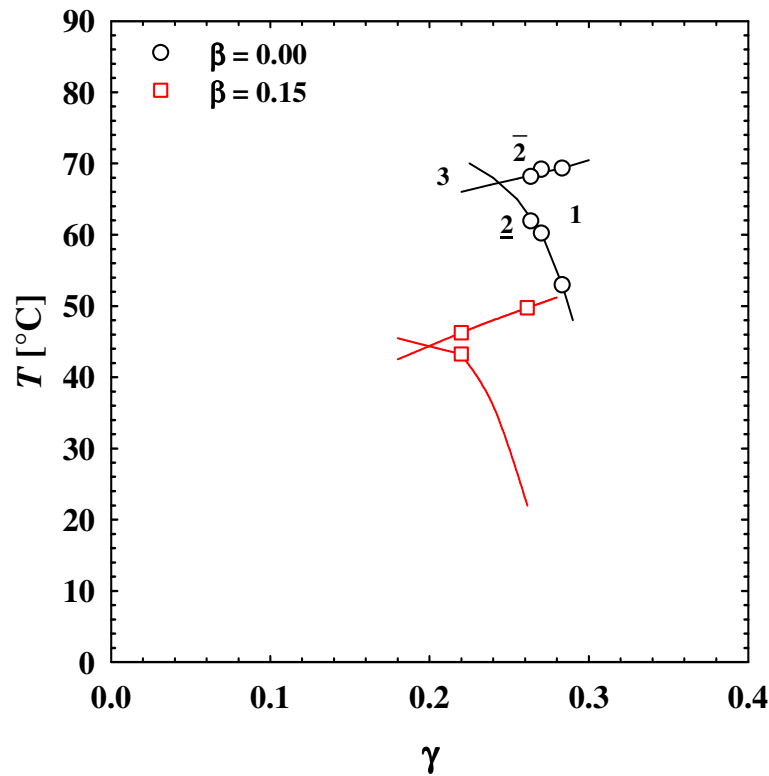


Figure 4.9:  $T(\gamma)$ -sections of the system  $H_2O/(\text{sucrose/trehalose}) - n\text{-octane}/C_6MA - C_{18}E_8/C_8G_1$  at  $\alpha = 0.4125$ ,  $\Psi = 0.75$ ,  $\zeta = 0.38$  and  $\delta = 0.70$ . As one can see  $\tilde{T}$  decreases strongly if *n*-octane is replaced by  $C_6MA$ . Furthermore, the surfactant mixture becomes more efficient. A possible explanation could be that  $C_6MA$  partially acts as a hydrophobic co-surfactant.

The strong decrease of the phase boundaries in temperature does not allow to substitute more *n*-octane by  $C_6MA$  in the system  $H_2O/(\text{sucrose/trehalose}) - n\text{-octane}/C_6MA -$

$C_{18}E_8/C_8G_1$  with  $\Psi = 0.75$ ,  $\zeta = 0.38$ ,  $\alpha = 0.4125$ ,  $\delta = 0.70$  and  $\beta = 0.15$  as the one-phase microemulsion would shift out of the experimental temperature range. Thus, to prepare highly viscous microemulsions with the polymerizable oil  $C_6MA$  an even more hydrophilic surfactant mixture has to be used. As the pure surfactant  $C_8G_2$  is very expensive, in the following the  $C_{18}E_8/C_8G_1$  surfactant mixture is replaced with the technical-grade surfactant Agnique PG 264-G, a sugar surfactant with an alkyl chain of 12-14 carbons and a headgroup which consists of 1.4 sugar groups in average (Figure 4.10). On the other hand, the formulation of a highly viscous microemulsion with a polymerizable oil using the technical-grade surfactant mixture of Lutensol XL 70 and Agnique PG 8105-G is also further investigated (Figure 4.11).

Figure 4.10 shows the stepwise replacement of the surfactant mixture  $C_{18}E_8/C_8G_1$  by the technical-grade surfactant Agnique PG 264-G in the system  $H_2O/(sucrose/trehalose) - n\text{-octane}/C_6MA - C_{18}E_8/C_8G_1$  with  $\alpha = 0.4125$ ,  $\Psi = 0.75$  and  $\zeta = 0.38$ . At the same time the oil  $n\text{-octane}$  is substituted by the polymerizable oil  $C_6MA$ .  $\delta_2$  gives the ratio of Agnique PG 264-G in the overall surfactant mixture whereas  $\delta_1$  is the ratio of  $C_8G_1$  in the  $C_{18}E_8/C_8G_1$  mixture and kept constant at  $\delta_1 = 0.70$ . Starting in Figure 4.10, *a*) with the system  $H_2O/(sucrose/trehalose) - n\text{-octane}/C_6MA - C_{18}E_8/C_8G_1$  with  $\alpha = 0.4125$ ,  $\Psi = 0.75$ ,  $\zeta = 0.38$ ,  $\delta_1 = 0.70$  and  $\beta = 0.15$  the surfactant mixture  $C_{18}E_8/C_8G_1$  is partially replaced with the technical-grade sugar surfactant Agnique PG 264-G ( $\delta_2 = 0.40$ ). The phase boundaries are shifted to higher temperatures as Agnique PG 264-G is compared to the  $C_{18}E_8/C_8G_1$  mixture a more hydrophilic surfactant and the system becomes at the same time more efficient. In a second step, Figure 4.10, *b*), the amount of  $C_6MA$  in the oil is increased from  $\beta = 0.15$  to  $\beta = 0.40$ . As expected, the temperature of the phase boundaries decreases due to the lower hydrophobicity of  $C_6MA$ . At the same time the efficiency of the surfactant mixture increases indicating that  $C_6MA$  acts partially as a co-surfactant. However, if one increases the amount of  $C_6MA$  further (Figure 4.10, *d*)) only a small increase in efficiency is found. Thus, at  $\beta = 0.80$  the interface seems to be saturated so that the further added  $C_6MA$  acts mainly as a monomer. If one now increases the amount of Agnique PG 264-G from  $\delta_2 = 0.70$  up to  $\delta_2 = 1.00$  meaning that the system contains only Agnique PG 264-G as surfactant (Figure 4.10, *e*)) the phase boundaries are shifted again to higher temperatures and the system's efficiency increases at the same time.

Comparing the shape of the phase boundaries of the different systems in Figure 4.10 it is obvious that the phase boundaries for  $\delta_2 < 1$  follow the same trend found for ternary

water – *n*-alkane – C<sub>i</sub>E<sub>j</sub> systems [12,16,19,20,44]. The upper phase boundary decreases in temperature if  $\gamma$  is decreased whereas the lower phase boundary increases in temperature at the same time until they intersect. However, as soon as the system only contains the surfactant Agnique PG 264-G ( $\delta_2 = 1$ ) the lower phase boundary does not increase in temperature with decreasing surfactant concentrations. It even slightly decreases. Reason for this behavior might be a lamellar phase in the lower part of the one-phase region which intrudes even in the  $\bar{2}$ -region of the phase diagram. This situation is already known from literature [139] and schematically shown in the inset of Figure 4.10, *e*) diagram. For this reason, the “real”  $\tilde{X}$ -point cannot be measured.

In Figure 4.10, *f*) *n*-octane is totally replaced by C<sub>6</sub>MA leading to the system H<sub>2</sub>O/(sucrose/trehalose) – C<sub>6</sub>MA – Agnique PG 264-G with  $\alpha = 0.4125$ ,  $\Psi = 0.75$  and  $\zeta = 0.38$ . The mass fraction  $\alpha = 0.4125$  corresponds for this system to a volume fraction of  $\phi = 0.52$  which means that the volume fraction of hydrophilic and hydrophobic phase are nearly the same. The fact that the lower phase boundary still does not increase in temperature with decreasing surfactant concentrations leads to the assumption of a lamellar phase intruding in the  $\bar{2}$ -region of the phase diagram. The decrease in efficiency suggests that not only Agnique PG 264-G but also C<sub>6</sub>MA induces the lamellar phase. A first hint could be the proof of the lamellar phase via the existence of optical anisotropy. However, since not only the lamellar structure but also the sugar molecules itself induce optical anisotropy, the presence of the lamellar phase is ambiguous. In order to proof the existence of a lamellar phase intruding in the  $\bar{2}$ -region of the phase diagram detailed studies of the microstructure of these systems have to be carried out. As it will be shown in chapter 6.2 SANS and TEM studies will proof the existence of the  $L_\alpha$ -phase.

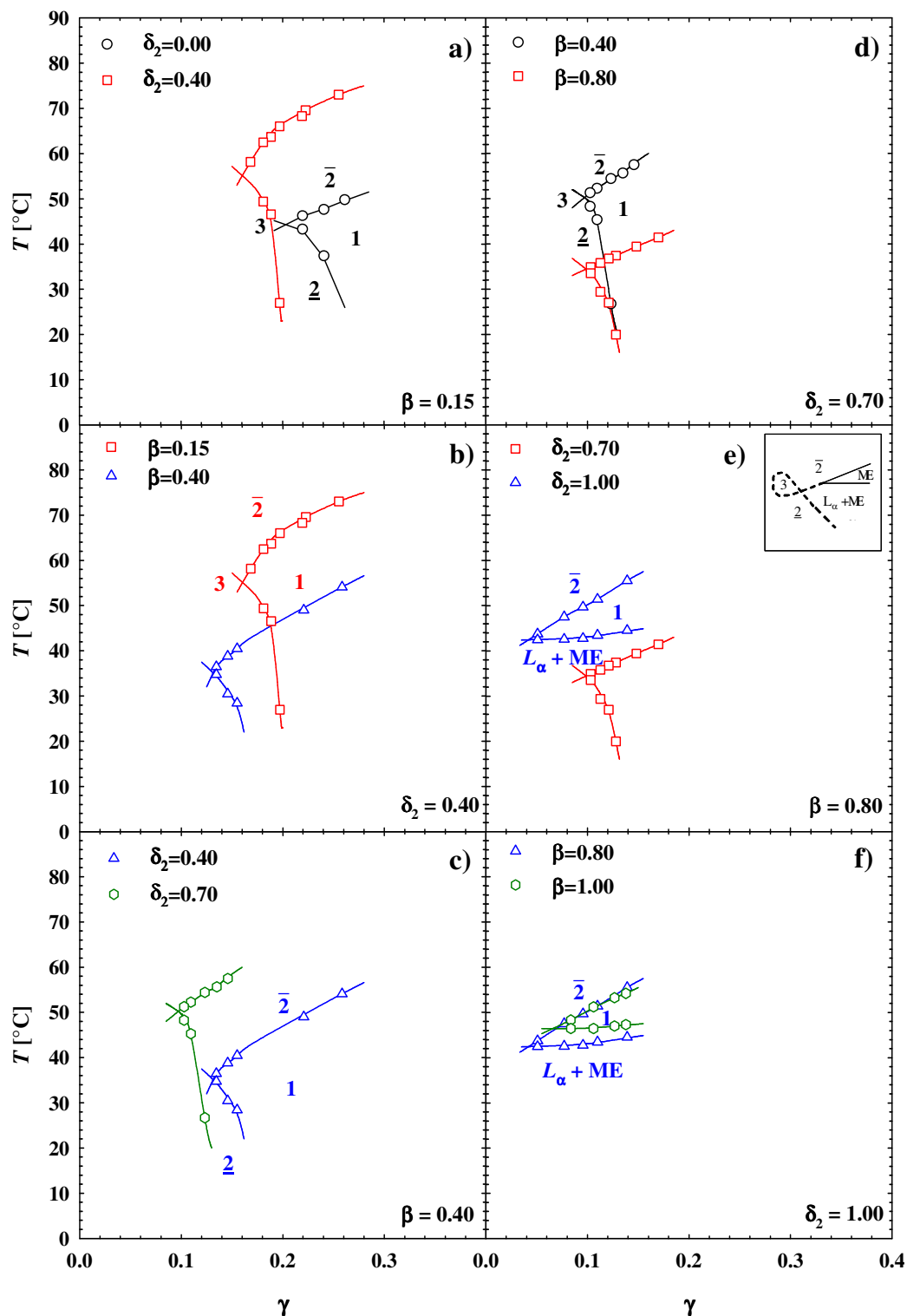


Figure 4.10:  $T(\gamma)$ -sections of the system  $\text{H}_2\text{O}/(\text{sucrose/trehalose}) - n\text{-octane}/\text{C}_6\text{MA} - \text{C}_{18}\text{E}_8/\text{C}_8\text{G}_1/\text{Agnique PG 264-G}$  at  $\alpha = 0.4125$ ,  $\Psi = 0.75$ ,  $\zeta = 0.38$  and  $\delta_1 = 0.70$ . The amount of hexyl methacrylate in the oil phase is increased step by step. To compensate for the shift of the phase boundaries to lower temperatures the surfactant mixture is changed, i.e. the  $\text{C}_{18}\text{E}_8/\text{C}_8\text{G}_1$  surfactant mixture is stepwise replaced with Agnique PG 264-G ( $\delta_2$ ). Note, that at  $\delta_2 = 1$  an extended lamellar phase can be observed in the lower part of the one-phase region which intrudes even in the  $\bar{2}$ -part of the phase diagram (shown schematically in the inset of Figure 4.10, e)).

Figure 4.11 shows the formulation of a highly viscous and polymerizable microemulsion starting from the system  $\text{H}_2\text{O}/(\text{sucrose}/\text{trehalose}) - n\text{-octane} - \text{Lutensol XL70}/\text{Agnique PG 8105-G}$  with  $\Psi = 0.75$ ,  $\zeta = 0.38$ ,  $\delta = 0.60$  and  $\alpha = 0.4125$ . As one can see the amount of sugar surfactant in the surfactant mixture has only been increased slightly to  $\delta = 0.64$  to compensate for the replacement of  $n\text{-octane}$  with  $\text{C}_6\text{MA}$ . Thus, the effect of  $\text{C}_6\text{MA}$  on the phase behavior is reasonably smaller than in the system containing the pure surfactant  $\text{C}_{18}\text{E}_8/\text{C}_8\text{G}_1$  and Agnique PG 264-G. A possible explanation for this behavior can be the large fraction of the technical-grade Lutensol XL 70 in the surfactant mixture. In particular the hydrophobic, low homologous alkylpolyglycoether molecules will dissolve more favourably in the less hydrophobic  $\text{C}_6\text{MA}$  compared to  $n\text{-octane}$ . This leads to a more hydrophilic surfactant mixture in the interface shifting the phase boundaries to higher temperatures. The lower phase boundary of the system  $\text{H}_2\text{O}/(\text{sucrose}/\text{trehalose}) - \text{C}_6\text{MA} - \text{Lutensol XL 70}/\text{Agnique PG 8105-G}$  is dashed as due to its steepness the phase boundary could only be detected for one surfactant mass fraction  $\gamma$  at  $\gamma = 0.241$ . Note, that using the shorter chained sugar-surfactant no lamellar phase has been observed. However, the Lutensol XL 70/Agnique PG 8105-G solubilizes  $\text{H}_2\text{O}/(\text{sucrose}/\text{trehalose})$  and  $\text{C}_6\text{MA}$  less efficient than Agnique PG 264-G.

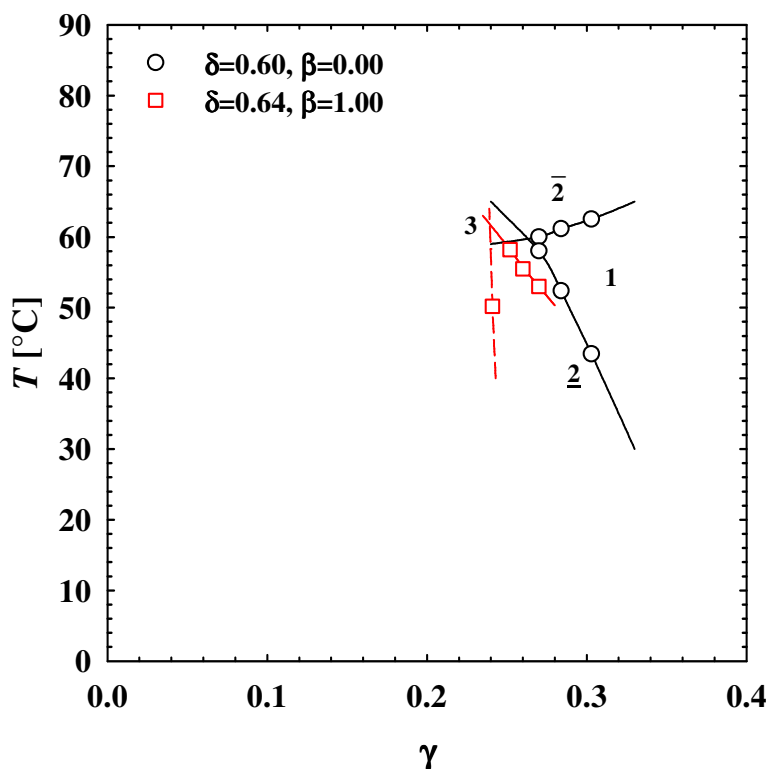


Figure 4.11:  $T(\gamma)$ -sections of the systems  $\text{H}_2\text{O}/(\text{sucrose/trehalose}) - n\text{-octane} - \text{Lutensol XL 70/Agnique PG 8105-G}$  with  $\Psi = 0.75$ ,  $\zeta = 0.38$ ,  $\delta = 0.60$  and  $\alpha = 0.4125$  and  $\text{H}_2\text{O}/(\text{sucrose/trehalose}) - \text{C}_6\text{MA} - \text{Lutensol XL 70/Agnique PG 8105-G}$  with  $\Psi = 0.75$ ,  $\zeta = 0.38$ ,  $\delta = 0.64$  and  $\alpha = 0.4125$ . Note that the phase boundaries surprisingly shift only to somewhat smaller temperatures and  $\gamma$  values if  $n$ -octane is replaced by  $\text{C}_6\text{MA}$ . A reason might be that  $\text{C}_6\text{MA}$  dissolves the hydrophobic, low homologous alkylpolyglycoether better than  $n$ -octane leading to a more hydrophilic surfactant mixture in the interface.

### 4.3 Cross-linker Variation

The addition of cross-linker EGDMA (ethylene glycol dimethacrylate) to the microemulsion is suspected to have advantages for the fixation of the tunable microstructures via polymerization. Aim is to polymerize the microemulsion containing various amounts of cross-linker at the same conditions (e.g. temperature) to investigate the cross-linker's effect on the micro-/nanostructure obtained. Advantages of using a cross-linker within the microemulsion are accelerated gelation and the formation of polymer films around water channels in the microemulsion. Thus, it minimizes the alternation/collapse of water chan-



nels during the early stage of polymerization [140,141].

Figure 4.12 shows the effect of the cross-linker on the phase behavior.  $T(\gamma)$ -sections of the systems  $\text{H}_2\text{O}/(\text{sucrose}/\text{trehalose}) - \text{C}_6\text{MA}/\text{EGDMA} - \text{Agnique PG 264-G}$  with  $\alpha = 0.4125$ ,  $\Psi = 0.75$  and  $\zeta = 0.38$  containing an increasing amount  $\beta$  of cross-linker in the oil phase are recorded. As one can see, the efficiency of the system decreases strongly. At the same time, the phase inversion temperature  $\tilde{T}$  increases. The interpretation of the observed trend is difficult as the lamellar phase is intruding in the  $\bar{2}$ -region of the phase space which makes the determination of the  $\tilde{X}$ -point impossible. The two following trends are suspected because  $\text{C}_6\text{MA}$  acts in contrast to the cross-linker ethylene glycol dimethacrylate as co-surfactant. Thus, an increasing amount of cross-linker in the oil mixture results in a decreasing amount of hydrophobic “co-surfactant”  $\text{C}_6\text{MA}$ , which leads to a decreasing efficiency and a shift of the phase boundaries to higher temperatures. The added EGDMA however contains two methacrylate groups and should behave as a “hydrophilic” oil having an opposite effect. It should increase the efficiency of the surfactant slightly and shift the phase boundaries to lower temperatures.

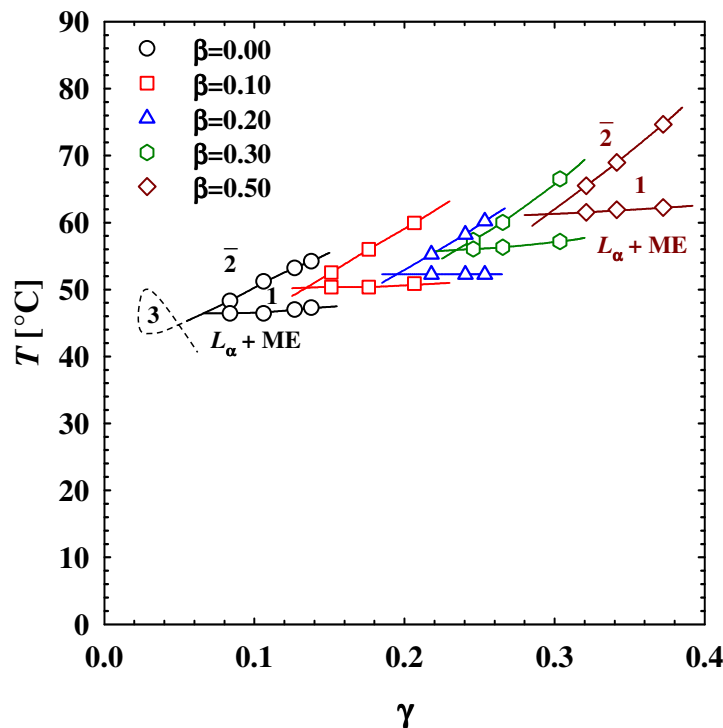


Figure 4.12:  $T(\gamma)$ -sections of the system  $\text{H}_2\text{O}/(\text{sucrose}/\text{trehalose}) - \text{C}_6\text{MA}/\text{EGDMA} - \text{Agnique PG 264-G}$  with  $\alpha = 0.4125$ ,  $\Psi = 0.75$  and  $\zeta = 0.38$ . Increasing amount of cross-linker  $\beta$  in the oil phase shifts the phase boundaries to larger surfactant mass fractions and higher temperatures. For the interpretation of the observed trend see text.

In order to minimize the alternation of the microemulsion structure during the polymerization a high viscosity of the microemulsion is strived for in this work. Due to the inverse temperature dependent increase of viscosity, in a next step the phase boundaries of the systems` shall be dropped to lower values as well as adjusted to each other to investigate the cross-linker`s effect on the polymerized structure under similar conditions. One effective possibility is the addition of a more hydrophobic surfactant. Figure 4.13 shows the phase behavior of the system  $\text{H}_2\text{O}/(\text{sucrose}/\text{trehalose}) - \text{C}_6\text{MA}/\text{EGDMA} - \text{Agnique PG 264-G}/\text{C}_{10}\text{E}_6$  with  $\alpha = 0.4125$ ,  $\Psi = 0.75$ ,  $\zeta = 0.38$ ,  $\beta = 0.50$  and increasing amount of  $\text{C}_{10}\text{E}_6$  in the surfactant mixture ( $\delta$ ). Increasing the amount of  $\text{C}_{10}\text{E}_6$  up to  $\delta = 0.20$  shifts the phase boundaries to lower temperatures and the efficiency of the surfactant mixture decreases significantly. While this shift to lower temperatures is due to the addition of the hydrophobic co-surfactant  $\text{C}_{10}\text{E}_6$  the decrease in efficiency could be a consequence of the high monomeric solubility of  $\text{C}_{10}\text{E}_6$  in the  $\text{C}_6\text{MA}/\text{EGDMA}$  mixture.

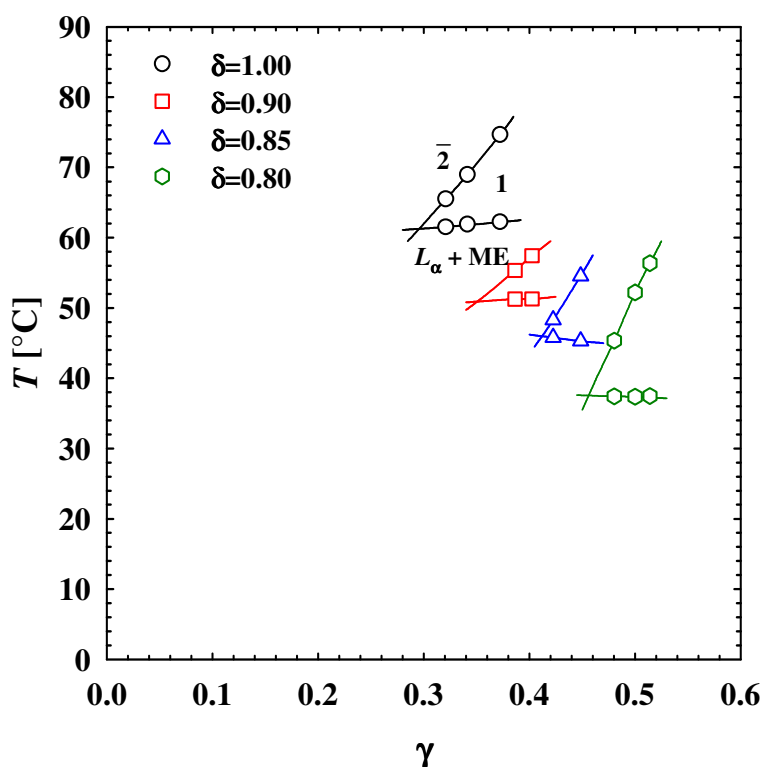


Figure 4.13:  $T(\gamma)$ -sections of the system  $\text{H}_2\text{O}/(\text{sucrose}/\text{trehalose}) - \text{C}_6\text{MA}/\text{EGDMA} - \text{Agnique PG 264-G}/\text{C}_{10}\text{E}_6$  with  $\alpha = 0.4125$ ,  $\Psi = 0.75$ ,  $\zeta = 0.38$ ,  $\beta = 0.50$  with increasing amount of  $\text{C}_{10}\text{E}_6$  in the surfactant mixture ( $\delta$ ). Adding the hydrophobic  $\text{C}_{10}\text{E}_6$  shifts the phase boundaries to lower temperatures and the solubilization of water/sugar and the polymerizable  $\text{C}_6\text{MA}/\text{EGDMA}$  mixture is less efficient.

Combining the opposite temperature effects of the cross-linker and the surfactant, the phase behavior of microemulsion systems containing different amounts of cross-linker can be tuned to reach the same temperature. Figure 4.14 shows the  $T(\gamma)$ -sections of the system  $\text{H}_2\text{O}/(\text{sucrose}/\text{trehalose}) - \text{C}_6\text{MA}/\text{EGDMA} - \text{Agnique PG 264-G}/\text{Lutensol AO 8}$  with  $\alpha = 0.4125$ ,  $\Psi = 0.75$ ,  $\zeta = 0.38$  and varying both  $\beta$  from  $\beta = 0.00$  to  $\beta = 0.20$  and  $\delta$  from  $\delta = 0.93$  to  $\delta = 0.88$ . By adding the technical-grade Lutensol AO8 the shift of the phase boundaries to higher temperatures due to the addition of cross-linker can be compensated for. As the one-phase regions of all systems are located around  $T = 35^\circ\text{C}$  the polymerization of microemulsions containing different amounts of cross-linker can be performed at the same temperature.

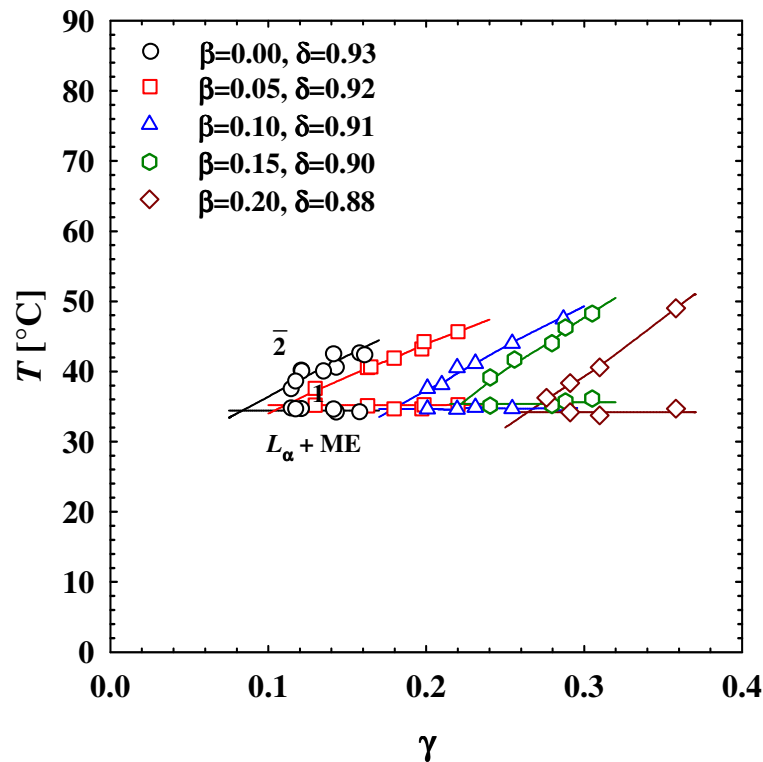


Figure 4.14:  $T(\gamma)$ -sections of the system  $\text{H}_2\text{O}/(\text{sucrose}/\text{trehalose}) - \text{C}_6\text{MA}/\text{EGDMA} - \text{Agnique PG 264-G}/\text{Lutensol AO 8}$  with  $\alpha = 0.4125$ ,  $\Psi = 0.75$ ,  $\zeta = 0.38$  and varying  $\beta$  and  $\delta$ . By adding the hydrophobic technical-grade surfactant Lutensol AO 8 the shift of the phase boundaries to higher temperatures due to the increasing amount of cross-linker can be compensated for.

As mentioned before a typical “fish”-shaped phase behavior is found for the system  $\text{H}_2\text{O}/(\text{sucrose}/\text{trehalose}) - \text{C}_6\text{MA} - \text{Lutensol XL 70}/\text{Agnique PG 8105-G}$  with  $\alpha = 0.4125$ ,  $\Psi = 0.75$ ,  $\zeta = 0.38$  and  $\delta = 0.64$  while the related system containing only the sugar surfac-

tant Agnique PG 264-G shows an extended lamellar phase at low temperatures. The question rises if a combination of both technical-grade sugar surfactants is able to suppress the lamellar phase.

Figure 4.15 shows the  $T(\gamma)$ -sections of the system  $\text{H}_2\text{O}/(\text{sucrose}/\text{trehalose}) - \text{C}_6\text{MA}/\text{EGDMA} - \text{Agnique PG 264-G}$  with  $\alpha = 0.4125$ ,  $\beta = 0.15$ ,  $\Psi = 0.75$ ,  $\zeta = 0.38$  and increasing amount of Agnique PG 8105-G in the surfactant mixture. Replacing only 20% of Agnique PG 264-G the phase boundaries do not shift in temperature but to lower surfactant mass fractions. Furthermore, the extended lamellar phase is still present at low temperatures. For the system  $\text{H}_2\text{O}/(\text{sucrose}/\text{trehalose}) - \text{C}_6\text{MA}/\text{EGDMA} - \text{Agnique PG 264-G}/\text{Agnique PG 8105-G}$  containing 49% Agnique PG 8105-G in the surfactant mixture, the typical phase behavior of nonionic microemulsion systems is found, i.e. the lamellar phase is suppressed. Thus, the addition of the shorter chained and more hydrophilic Agnique PG 8105-G surfactant leads to a shift of the phase boundaries to higher temperatures and makes the solubility of the aqueous sugar-solution and  $\text{C}_6\text{MA}/\text{EGDMA}$  less efficient.

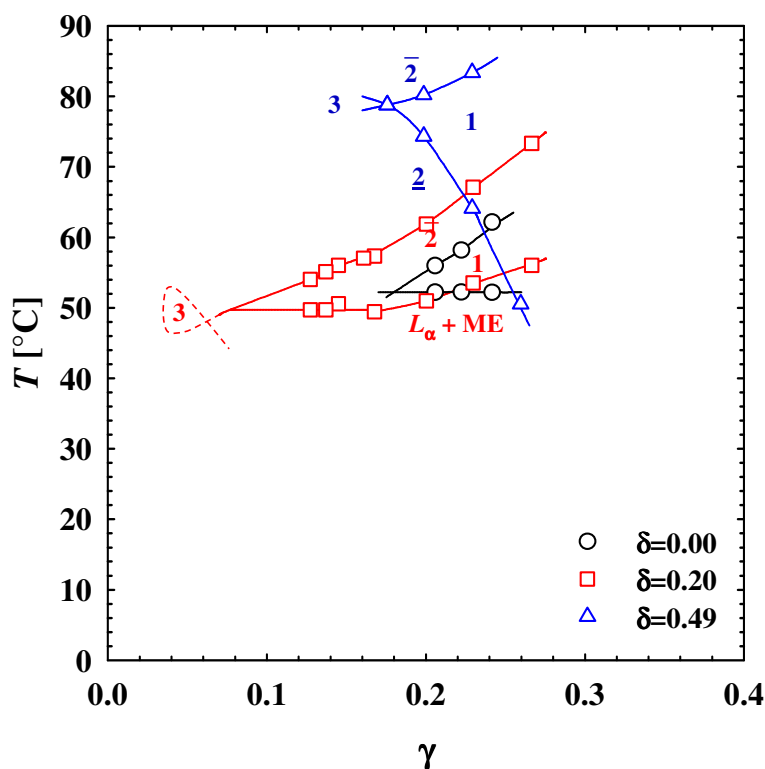


Figure 4.15:  $T(\gamma)$ -sections of the system  $\text{H}_2\text{O}/(\text{sucrose}/\text{trehalose}) - \text{C}_6\text{MA}/\text{EGDMA} - \text{Agnique PG 264-G}/\text{Agnique PG 8105-G}$  with  $\alpha = 0.4125$ ,  $\beta = 0.15$ ,  $\Psi = 0.75$ ,  $\zeta = 0.38$  and increasing amount of Agnique PG 8105-G in the surfactant mixture ( $\delta$ ).

## 4.4 Blockcopolymers

An amphiphilic blockcopolymer acting as sterical barrier could be added to the microemulsion system as one possible option to stabilize the microstructure against coagulation during the polymerization. The effects of several amphiphilic blockcopolymers on the phase behavior and microstructure of conventional microemulsions are to some extent studied in literature [142-148]. The most important effect found is an enormous increase in surfactant efficiency by adding polyethylenepropylene – polyethyleneoxide as blockcopolymer to a  $\text{H}_2\text{O} - n\text{-alkane} - \text{C}_i\text{E}_j$  microemulsion. However, in this study we are mainly interested to add the blockcopolymers to increase the sterical barrier against coagulation.

Figure 4.16 shows the  $T(\gamma)$ -section of the system  $\text{H}_2\text{O}/(\text{sucrose/trehalose}) - \text{C}_6\text{MA/EGDMA} - \text{Agnique PG 264-G/Agnique PG 8105-G}$  with  $\alpha = 0.4125$ ,  $\Psi = 0.75$ ,  $\zeta = 0.38$ ,  $\beta = 0.15$  and  $\delta_1 = 0.49$ . Replacing 16 wt.% ( $\delta_2 = 0.16$ ) of the surfactant mixture by Tween 20, a polyethylene glycol sorbitan monolaurate, the phase boundaries are shifted to lower temperatures and simultaneously the system's efficiency decreases.  $\delta_2$  is the mass fraction of Tween 20 in the total surfactant mixture.

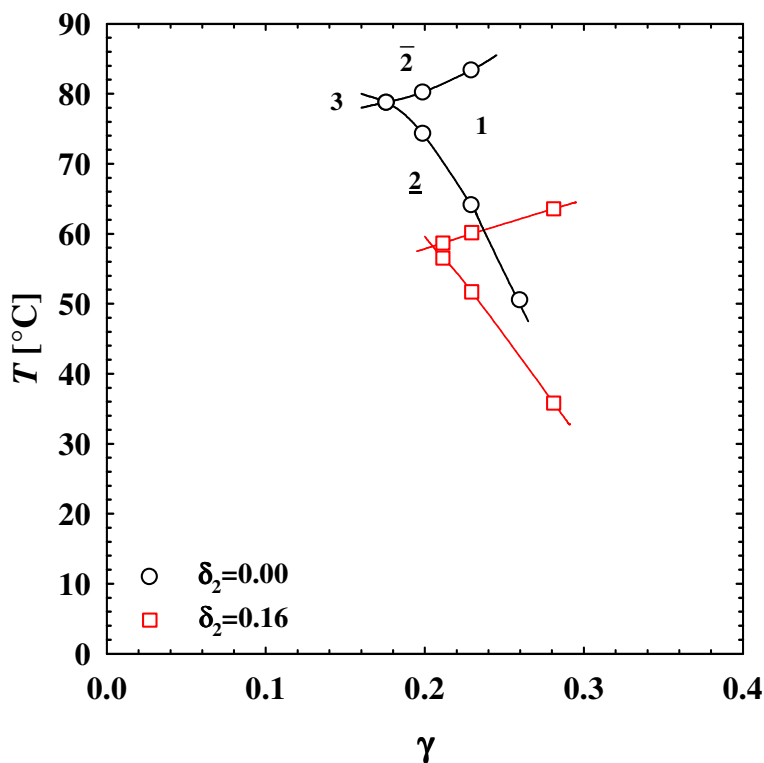


Figure 4.16:  $T(\gamma)$ -sections of the systems  $\text{H}_2\text{O}/(\text{sucrose}/\text{trehalose}) - \text{C}_6\text{MA}/\text{EGDMA} - \text{Agnique PG 264-G}/\text{Agnique PG 8105-G}$  with  $\alpha = 0.4125$ ,  $\Psi = 0.75$ ,  $\zeta = 0.38$ ,  $\beta = 0.15$  and  $\delta_1 = 0.49$  and  $\text{H}_2\text{O}/(\text{sucrose}/\text{trehalose}) - \text{C}_6\text{MA}/\text{EGDMA} - \text{Agnique PG 264-G}/\text{Agnique PG 8105-G}/\text{Tween 20}$  with  $\alpha = 0.4125$ ,  $\Psi = 0.75$ ,  $\zeta = 0.38$ ,  $\beta = 0.15$ ,  $\delta_1 = 0.49$  and  $\delta_2 = 0.16$ .

Instead of Tween 20 which is rather a long chained surfactant than a polymer the amphiphilic blockcopolymer PBMA-*b*-PEO has been added to stabilize the microemulsion. Starting point of this study is the system  $\text{H}_2\text{O}/(\text{sucrose}/\text{trehalose}) - \text{C}_6\text{MA}/\text{EGDMA} - \text{Agnique PG 264-G}/\text{Agnique PG 8105-G}/\text{Lutensol XL 70}$  with  $\alpha = 0.4125$ ,  $\Psi = 0.75$ ,  $\zeta = 0.38$ ,  $\beta = 0.15$ ,  $\delta_1 = 0.49$  and  $\delta_2 = 0.15$ , Lutensol XL 70 has been added to the system to shift the phase boundaries to lower temperatures (Figure 4.17). Here,  $\delta_2$  is the mass fraction of Lutensol XL 70 in the surfactant mixture which consists of Agnique PG 264-G/Agnique PG 8105-G/Lutensol XL 70. Replacing 12% ( $\delta_3 = 0.12$ ) of the overall surfactant mixture with PBMA-*b*-PEO the phase inversion temperature  $\tilde{T}$  nearly stays constant but the efficiency decreases strongly. Assuming that the blockcopolymer PBMA-*b*-PEO does not act as a surfactant, however, is solubilized in the oil or aqueous sugar solution the system is slightly less efficient compared to the starting system; this anti-efficiency boosting effect proves that most of the blockcopolymer does not adsorb at the interface. Thereby, it is more likely that the polymer dissolves in the  $\text{C}_6\text{MA}/\text{EGDMA}$  phase/subphase because the

driving force for the solubility of PEO-block in water is the complexation with water molecules. As there is already 75% of sugar in the water phase there is not enough water left to hydrate the hydrophilic PEO-block of the PBMA-*b*-PEO polymer. The same is seen in case of the amphiphilic polymers on the basis of polysaccharides [149-151]. Even small amounts of the low molecular weight methyl 2-hydroxyethyl cellulose do not dissolve in a 75% sugar solution.

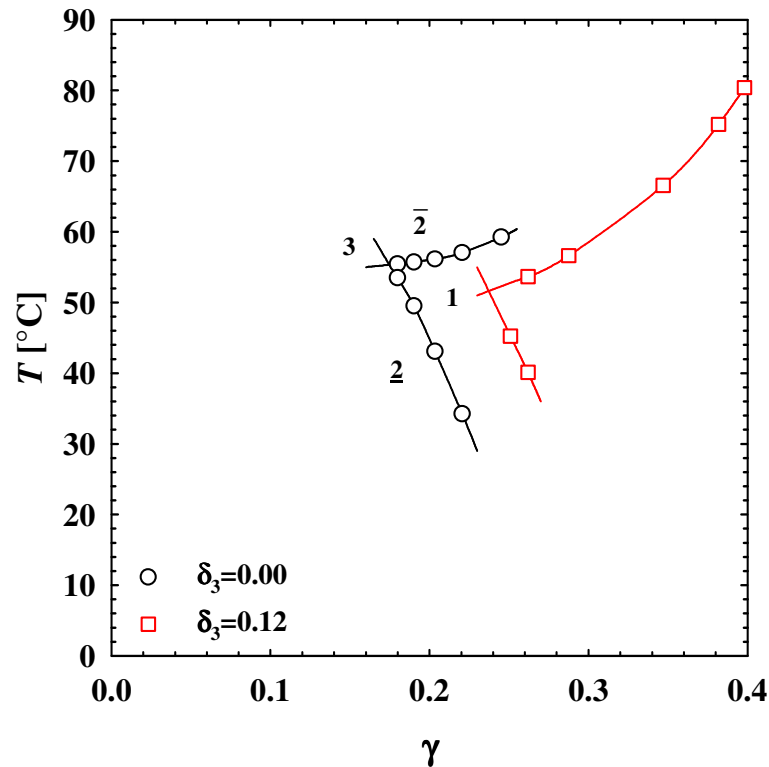


Figure 4.17:  $T(\gamma)$ -sections of the systems  $\text{H}_2\text{O}/(\text{sucrose}/\text{trehalose}) - \text{C}_6\text{MA}/\text{EGDMA} - \text{Agnique PG 264-G}/\text{Agnique PG 8105-G}/\text{Lutensol XL 70}$  with  $\alpha = 0.4125$ ,  $\Psi = 0.75$ ,  $\zeta = 0.38$ ,  $\beta = 0.15$ ,  $\delta_1 = 0.49$  and  $\delta_2 = 0.15$  and  $\text{H}_2\text{O}/(\text{sucrose}/\text{trehalose}) - \text{C}_6\text{MA}/\text{EGDMA} - \text{Agnique PG 264-G}/\text{Agnique PG 8105-G}/\text{Lutensol XL 70}/\text{PBMA-}b\text{-PEO}$  with  $\alpha = 0.4125$ ,  $\Psi = 0.75$ ,  $\zeta = 0.38$ ,  $\beta = 0.15$ ,  $\delta_1 = 0.49$ ,  $\delta_2 = 0.15$  and  $\delta_3 = 0.12$ .

#### 4.5 The $T(w_B)$ -section of highly viscous microemulsions

For the polymerization of diluted monomer droplets dispersed in a highly viscous continuous hydrophilic phase it is indispensable to study this part of the phase region. To in-

investigate the phase behavior of this “region” sections through the phase prism have to be performed as a function of the oil mass fraction  $w_B$  and the temperature  $T$  at a constant mass fraction  $\gamma_a$  of the surfactant mixture in the aqueous sugar phase [152,153]. In Figure 4.18 such a  $T(w_B)$ -section is shown for the system  $H_2O/(sucrose/trehalose) - C_6MA/EGDMA - Lutensol XL 70/Agnique PG 8105-G$  containing 75% sugar in the water phase with a trehalose to sucrose/trehalose mass fraction of  $\zeta = 0.38$  and a Agnique PG 8105-G mass fraction in the surfactant mixture of  $\delta = 0.80$ . The mass fraction of the surfactant in the surfactant/water/(sucrose/trehalose) mixture is kept constant at  $\gamma_a = 0.074$ . The amount of cross-linker in the oil phase varies from  $\beta = 0.00$  (black circles) via  $\beta = 0.15$  (red squares) to  $\beta = 0.30$  (blue triangles).

For all three  $T(w_B)$ -sections one obtains the sequence of phases usually found for water-rich microemulsions formulated with nonionic surfactants. At low temperatures, oil droplets dispersed in the water/sugar phase are found coexisting with the monomer excess phase ( $\underline{2}$ ). At intermediate temperatures the one phase microemulsion (1) occurs. The so-called emulsification failure boundary separates the  $\underline{2}$ -region from the one-phase region and at temperatures just above the *efb*, spherical, monomer-in-water sugar microemulsions are found. With increasing temperature, these droplets form ellipsoidal and cylindrical aggregates which further branch to a connected network structure. A variety of different phases and two-phase regions are found at temperatures above the upper phase boundary ( $1 \rightarrow \bar{2}$ ). Here at first a concentrated network phase coexists with a dilute network phase. Increasing the temperature further reveals a lamellar phase and a water-rich  $L_3$ -phase. As the  $T(w_B)$ -sections are measured in terms of the polymerization of the monomer in aqueous sugar microemulsions, the location of these phases in the phase diagram are not important for this work and thus, not investigated in the following. Therefore, the entire high-temperature region of the phase diagram is simply denoted by “2”.

Increasing the amount of EGDMA in the system from  $\beta = 0.00$  to  $\beta = 0.30$ , the upper phase boundary is continuously shifted to lower temperatures by about  $\Delta T = 5.5^\circ C$ . Reason for this shift might be the slightly higher hydrophilicity of EGDMA compared to  $C_6MA$  (see also Figure 4.12 and text). However, the amount of EGDMA in the oil mixture does not have any influence on the *efb*.

Comparing the  $T(\gamma)$ -section of the system  $H_2O/(sucrose/trehalose) - C_6MA - Lutensol XL 70/Agnique PG 8105-G$  with  $\Psi = 0.75$ ,  $\alpha = 0.4125$  and  $\delta = 0.64$  (Figure 4.11, red squares) with the  $T(w_B)$ -section of the system containing no cross-linker (Figure 4.18,



black circles) the question rises, why for the latter the intersection of the two-phase regions is found at a temperature of  $\tilde{T} = 51.7^\circ\text{C}$  whereas the  $\tilde{X}$ -point of the former is found at a temperature of  $\tilde{T} = 62^\circ\text{C}$  although this system contains less hydrophilic sugar surfactant ( $\delta = 0.64$  versus  $\delta = 0.80$ ). It is known from literature, that the monomeric solubility of alkylpolyglycoether is much higher in the oil phase compared to the hydrophilic phase [49]. Due to the reason that the system investigated by the  $T(\gamma)$ -section contains much more oil, a large fraction of the alkylpolyglycoether surfactant is solubilized in the oil phase leading to a remaining surfactant mixture which is more hydrophilic. Therefore,  $\tilde{T}$  of the  $T(\gamma)$ -sections ( $\delta = 0.64$ ) is lower than  $T_1$  ( $\delta = 0.80$ ).

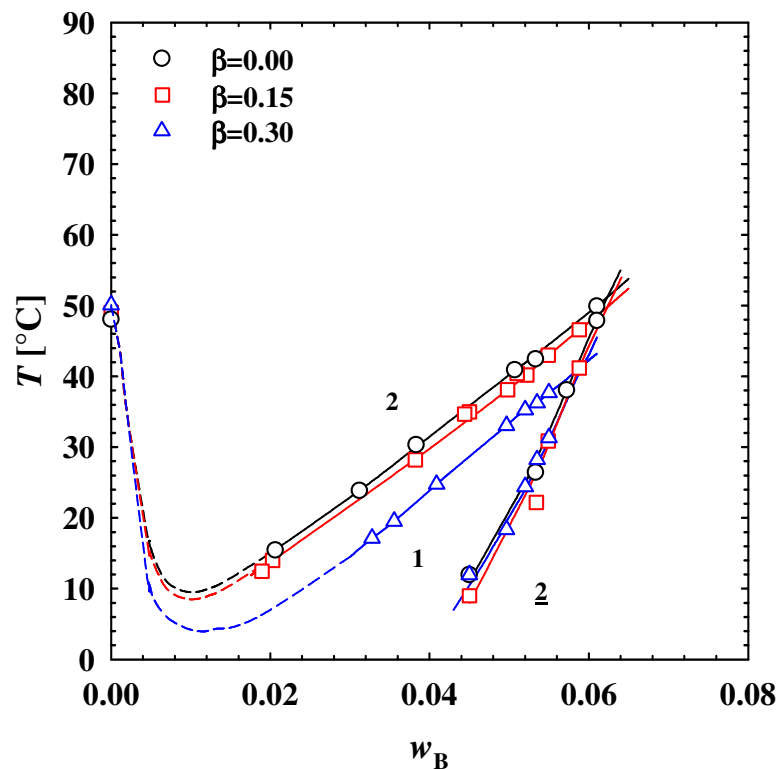


Figure 4.18:  $T(w_B)$ -section of the system  $\text{H}_2\text{O}/\text{sucrose}/\text{trehalose} - \text{C}_6\text{MA}/\text{EGDMA} - \text{Lutensol XL70}/\text{Agnique PG 8105-G}$  with  $\Psi = 0.75$ ,  $\zeta = 0.38$ ,  $\delta = 0.80$  and  $\gamma_a = 0.074$ . The amount of cross-linker in the system varies from  $\beta = 0.00$  (black circles) via  $\beta = 0.15$  (red squares) to  $\beta = 0.30$  (blue triangles).

In the following chapter different samples within the one-phase region with various amounts of cross-linker in the oil phase and various oil mass fractions  $w_B$  will be polymerized at different temperatures  $T$ .



## 5 Polymerization of Microemulsion Droplets

This chapter deals with the polymerization of microemulsion droplets. In the beginning of this chapter a literature overview about its history is given (section 5.1). The polymerization is first carried out using a microscopy lamp to initiate the reaction (section 5.2). Subsequently, the lamp is varied to investigate if the particle size of the polymerized microemulsion droplets is influenced by its wave length (section 5.3). Due to the results obtained, the polymerization is repeated using a UV-lamp in section 5.4. Finally, the polymerized droplet structure is investigated by SANS and SEM in section 5.5.

### 5.1 State of the Art

The polymerization of hydrophobic monomers in oil-in-water microemulsions provides an attractive pathway to produce latex particles. As nanometer sized polymerization in microemulsions occurs only in the monomer reservoir encapsulated in the droplet, the size of latex particles is often smaller than obtained with classical emulsion polymerization [23].

The pioneering attempts by *Stoffer* and *Bone* and by *Atik* and *Thomas* describe a polymerization process in globular oil-in-water microemulsions [24,25,81,154,155]. Most of the earlier studies used an alcohol as co-surfactant for the microemulsion formulation [156]. The latter authors polymerized styrene in an oil-in-water microemulsion based on hexadecyl trimethylammonium bromide and hexanol as co-surfactant and obtained monodisperse latex particles with diameters in the order of 10-30 nm but with a limited stability. In 1979 *Schauber* and *Riess* worked on the polymerization of diverse methacrylates, microemulsified by sodium dodecyl sulfate / alcohol mixtures. They prepared crosslinked and non-crosslinked stable microlatex particles with 5-10% solid content of polymer in the solution [157].

The difficulty in the polymerization of hydrophobic monomers as styrene or methyl methacrylate in oil-in-water microemulsions lies in retaining optical transparency and stability during the polymerization process. Mainly, the polymer products are bluish as well as less transparent compared to the original microemulsion and show a Tyndall effect due to an increase in the particle size during the polymerization process and the higher refractive index of the polymer compared to that of the monomer [77]. The instability and turbidity of the resulting polymer can be related to the change in the phase behavior due to a changing hydrophobicity of the hydrophobic component but also to the fact that the alcohol used as co-surfactant dissolves in the monomer but not in the polymer. Furthermore, alcohols are subject to chain transfer reactions during the polymerization limiting the molecular weight of the polymers and should therefore be avoided [77].

In 1984 the polymerization of a hydrophobic monomer in a three-component oil-in-water microemulsion containing water, styrene and cetyl trimethylammonium bromide, but no co-surfactant was reported by *Jayarkrishnan* and *Shah* [158]. Polymerization delivered very small and spherical particles. In 1989 *Ferrick*, *Murtagh* and *Thomas* used the same system and showed that the polymerized dispersion is stable towards dilution [159]. *Kaler et al.* formulated a similar system replacing cetyl trimethylammonium bromide by the shorter analogon dodecyl trimethylammonium bromide and studied the influence of the initiator used on the polymerization kinetic [160]. Similar investigations were conducted by *Gan et al.* for a system stabilized by tetradecyl trimethylammonium bromide [161-163] as well as for another system stabilized by cetyl trimethylammonium bromide [86]. In 1997 *Kaler et al.* analyzed the kinetics of the polymerization reactions of hexyl methacrylate in mixed dodecyl trimethylammonium bromide / didodecyl dimethylammonium bromide microemulsions. In the absence of bimolecular termination and fast radical capture, analytical expressions are derived for the conversion and reaction rate as a function of time and for the dependence upon the initiator concentration of the maximum reaction rate and the time at which it occurs [164]. Exact analytical expressions are also derived for the particle size and molecular weight distributions [165] verified by the results of an online SANS experiment [166]. Furthermore, they showed that the polymerization mechanism does not depend on the nature of the initiator used. Both water and oil initiated systems produced microlatexes with similar hydrodynamic radii, number of polymer particles, molecular weights of polymer and number of macromolecules per particle [23]. However, the polymerization rates were generally faster with oil soluble initiators compared to water soluble initiators. In 2007 the effects of initiator concentration on the kinetics of methyl

methacrylate and *n*-butyl acrylate dispersion polymerizations were studied and it was found that increasing the initiator concentration increased the reaction rate as well as the particle size [167]. In another attempt to achieve a better understanding of the kinetics of microemulsion polymerization, *Kaler et al.* examined monomer partitioning between micelles and polymer particles during polymerization of aqueous microemulsions of dodecyl trimethylammonium bromide surfactant and styrene, *n*-butyl methacrylate, *tert*-butyl methacrylate, and *n*-hexyl methacrylate monomers [168-170].

Another challenge is the formulation of non-spherical latex particles showing interesting rheological features [23]. *Gerber and Walker* investigated in 2006 the polymerization of elongated micellar structures offering a novel approach to the production of water-soluble amphiphilic nanoparticles [171].

## 5.2 Initiation via a Microscopy Lamp

As already mentioned the phase behavior of monomer droplets dispersed in a continuous hydrophilic phase is studied as a function of the oil mass fraction  $w_B$  and the temperature  $T$  at a constant surfactant to water plus surfactant ratio  $\gamma_a$  [152,153]. Figure 4.18 shows this so-called  $T(w_B)$ -section for the system  $H_2O$ /(sucrose/trehalose) –  $C_6MA$ /EGDMA – Lutensol XL 70/Agnique PG 8105-G at  $\Psi = 0.75$ ,  $\zeta = 0.38$ ,  $\delta = 0.80$ ,  $\beta = 0.15$  and  $\gamma_a = 0.074$ .

In order to start the polymerization reaction the UV-active initiator Irgacure 819 has to be added to the microemulsion. Furthermore, to prevent inhibition by dissolved oxygen, both, the stock solution composed of a 75% aqueous sugar solution plus surfactant and the monomer containing the initiator are carefully degassed before mixing the required amount of the initiator/monomer solution ( $w_B$ ) to the stock solution and polymerizing the microemulsion (for details see chapter 3.2). The polymerization process is initiated using a microscopy lamp Belani (Fa. Gerhard Optik und Feinmechanik GmbH; bulb: LO-100, 6V, 30W, Fa. Richard Schahl GmbH & Co.KG), emitting white light. The microemulsion has been polymerized over night in the transmitted light of the microscopy lamp placed behind the water bath. The polymerized samples have been diluted with water until its viscosity as well as the refractive index reached the same value as for water and are afterwards charac-

terized with the help of dynamic light scattering experiments using the software package BATCON [172].

To obtain the diffusion coefficient  $D$  the decay rate  $\Gamma$  is plotted versus  $q^2$  applying the *Landau-Platzek* equation (equation 3.5). Figure 5.1 top shows the  $\Gamma(q^2)$ -plot exemplarily for the system  $\text{H}_2\text{O}/(\text{sucrose/trehalose}) - \text{C}_6\text{MA}/\text{EGDMA} - \text{Lutensol XL 70}/\text{Agnique PG 8105-G}$  with  $\Psi = 0.75$ ,  $\zeta = 0.38$ ,  $\delta = 0.80$ ,  $\beta = 0.15$ ,  $w_B = 0.043$ ,  $\gamma_a = 0.074$  and an initiator concentration in the initiator/monomer mixture of  $\chi_I = 0.02$  polymerized at a temperature  $T = 15^\circ\text{C}$ . A linear function which passes through the origin (black line) is to be fitted to the data points. From the slope of the curve the diffusion coefficient  $D = 5.44 \cdot 10^{-12} \text{ m}^2\text{s}^{-1}$  can be extracted. The red line just fits the data points not passing through the origin. The slope of both, the black and the red line are in good agreement. Knowing the diffusion coefficient  $D$  and assuming spherical particles the hydrodynamic radius  $R_{\text{hydr}} = 43 \text{ nm}$  can be determined with the *Stokes-Einstein* equation (equation 3.7). Using the decay rate of each scattering angle  $\theta$  to determine the diffusion coefficient the hydrodynamic radius  $R_{\text{hydr}}$  can be calculated and plotted versus the scattering angle  $\theta$  (Figure 5.1 bottom). The mean hydrodynamic radius  $\langle R_{\text{hydr}} \rangle = 45 \pm 4 \text{ nm}$  is in good agreement with the radius obtained from the analysis shown in Figure 5.1 top. However, for an isotropic scattering medium the hydrodynamic radius  $R_{\text{hydr}}$  is expected to be independent from the angle  $\theta$ . In Figure 5.1 bottom one can see a slight trend towards larger values of  $R_{\text{hydr}}$  at small scattering angles which is an indication for larger or non-spherical particles scattering at small angles. However, the polydispersity index  $p = (\sigma_R/R_{\text{hydr}})$  with  $\sigma_R$  being the standard deviation is given by  $p = 0.087$  which indicates that the sample is monodisperse.

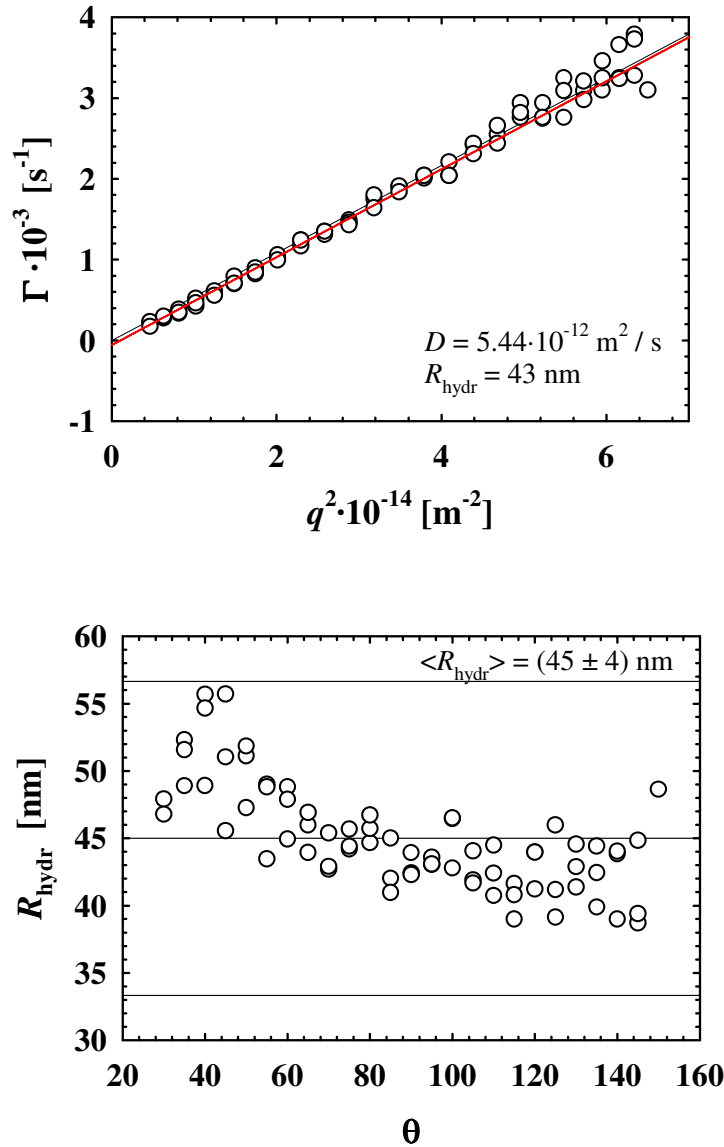


Figure 5.1: top: Decay rate  $\Gamma$  plotted versus  $q^2$  for the system  $\text{H}_2\text{O}/(\text{sucrose}/\text{trehalose}) - \text{C}_6\text{MA}/\text{EGDMA} - \text{Lutensol XL 70}/\text{Agnique PG 8105-G}$  with  $\Psi = 0.75$ ,  $\zeta = 0.38$ ,  $\delta = 0.80$ ,  $\beta = 0.15$ ,  $w_B = 0.043$ ,  $\gamma_a = 0.074$  and  $\chi_I = 0.02$  polymerized with the microscopy lamp at a temperature of  $T = 15^\circ\text{C}$ . bottom: Calculated hydrodynamic radius  $R_{\text{hydr}}$  plotted versus the scattering angle  $\theta$ . The hydrodynamic radius shows a slight trend to higher values at small scattering angles.

To optimize the initiator concentration  $\chi_I$  the influence of  $\chi_I$  on the hydrodynamic radius of the obtained polymer particles has been studied, using the system  $\text{H}_2\text{O}/(\text{sucrose}/\text{trehalose}) - \text{C}_6\text{MA}/\text{EGDMA} - \text{Lutensol XL 70}/\text{Agnique PG 8105-G}$  with  $\Psi = 0.75$ ,  $\zeta = 0.38$ ,  $\delta = 0.80$ ,  $\beta = 0.15$ ,  $\gamma_a = 0.074$  and  $w_B = 0.043$ . As shown in Table 5.1, an initiator concentration of at least  $\chi_I = 0.01$  within the monomer phase is necessary for reproducible results concerning the hydrodynamic polymer radius. Therefore, the initiator

concentration is fixed in the following to  $\chi_I = 0.02$  which is for this composition equivalent to two initiator molecules per microemulsion droplet.

Table 5.1: Radii for the polymer droplets of the system  $H_2O/(sucrose/trehalose) - C_6MA/EGDMA - Lutensol\ XL\ 70/Agnique\ PG\ 8105-G$  with  $\Psi = 0.75$ ,  $\zeta = 0.38$ ,  $\delta = 0.80$ ,  $\beta = 0.15$ ,  $\gamma_a = 0.074$ ,  $w_B = 0.043$  and varying initiator concentrations  $\chi_I$ .

	$\chi_I = 0.002$	$\chi_I = 0.01$	$\chi_I = 0.02$	$\chi_I = 0.05$
$R_{(1)hydr} [nm]$	88	38	31	36
$R_{(2)hydr} [nm]$	113	41	40	36
$R_{(3)hydr} [nm]$	185	35	39	38
$R_{(4)hydr} [nm]$	39	[56]		
$R_{(5)hydr} [nm]$	119			
$\emptyset R_{hydr} [nm]$	----	$38 \pm 3$	$37 \pm 5$	$37 \pm 1$

Figure 5.2 shows the  $T(w_B)$ -section of the system  $H_2O/(sucrose/trehalose) - C_6MA/EGDMA - Lutensol\ XL\ 70/Agnique\ PG\ 8105-G$  with  $\Psi = 0.75$ ,  $\zeta = 0.38$ ,  $\delta = 0.80$  and  $\gamma_a = 0.074$  (see also Figure 4.18). The amount of cross-linker in the monomer phase varies from  $\beta = 0.00$  (black circles) via  $\beta = 0.15$  (red squares) to  $\beta = 0.30$  (blue triangles). The red star indicates the sample's composition and temperature for the polymerization process. The numbers below each star indicate the mean value of the hydrodynamic radius  $R_{hydr}$  of the polymer particles obtained by DLS measurements after polymerization. The mean radius is taken from 4 – 5 measurements for each composition. The color of the numbers specifies the amount of cross-linker in monomer phase.

Comparing the mean radius of polymer particles where the underlying microemulsion contains a constant amount of cross-linker in the monomer phase but the polymerization temperature is increased one finds that the radius stays nearly constant within the experimental error for  $\beta = 0.00$  and  $\beta = 0.15$ . At  $T = 10^\circ C$  the mean radius for the system without cross-linker is  $R_{hydr} = 36 \pm 1$  nm, at  $T = 20^\circ C$   $R_{hydr} = 43 \pm 3$  nm. For the systems containing 15% cross-linker in the monomer phase the radius is  $R_{hydr} = 39 \pm 1$  nm ( $T = 10^\circ C$ ) and  $R_{hydr} = 41 \pm 4$  nm ( $T = 20^\circ C$ ). The size of microemulsion droplets along the *emulsification failure boundary* can be calculated using simple geometric considerations. With the help of



the surface to volume ratio of a spherical droplet and taking into account the polydispersity  $p$  the radius is given by

$$R_{calc} = 3 \frac{v_c}{a_c} \cdot \frac{\phi_b + \phi_c}{\phi_c} \cdot \frac{1 + p^2}{1 + 3p^2} \quad (5.1)$$

Here  $v_c$  is the volume and  $a_c$  the surface of a surfactant molecule,  $\phi_b$  is the volume fraction of monomer/initiator and  $\phi_c$  the volume fraction of surfactant in the sample. Estimating the polydispersity to  $p = 0.15$  and the value of  $v_c/a_c$  to  $v_c/a_c = 11 \text{ \AA}$  [47] a radius of  $R_{calc} = 5.4 \text{ nm}$  is obtained for the corresponding microemulsion system. As known from literature, the curvature of the amphiphilic film decreases with increasing temperature. Thus, for a constant composition of a given oil-in-water microemulsion, the spherical droplets are deformed and ellipsoidal and cylindrical oil-droplets are found [68,173]. A further increase of temperature leads to the formation of a network of branched cylinders found at the upper phase boundary. Considering the size of the obtained polymer particles which are by 7 to 8 times larger than the starting microemulsion droplets the deformation of the spherical droplets due to increasing temperature has no influence on the size of the particles.

Looking at the mean particle radius for the polymerized system containing 30% cross-linker in the monomer phase the value stays constant for  $T = 10^\circ\text{C}$  and  $T = 15^\circ\text{C}$  with  $R_{hydr} = 53 \pm 4 \text{ nm}$  but increases to  $R_{hydr} = 75 \pm 6 \text{ nm}$  for  $T = 20^\circ\text{C}$ . As the upper phase boundary for this system is located nearby the polymerization temperature, the larger particle radius can be attributed to the existence of a cylinder or even a network structure in the starting microemulsion.

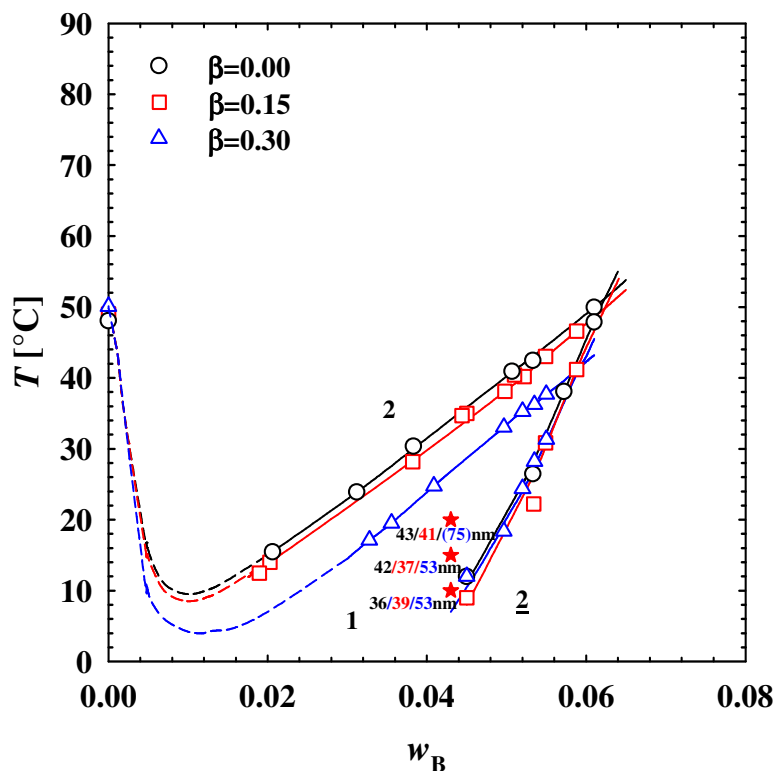


Figure 5.2:  $T(w_B)$ -section of the system  $H_2O/(sucrose/trehalose) - C_6MA/EGDMA - Lutensol XL70/Agnique PG 8105-G$  with  $\Psi = 0.75$ ,  $\zeta = 0.38$ ,  $\delta = 0.80$ ,  $\gamma_a = 0.074$ . The amount of cross-linker in the monomer phase varies from  $\beta = 0.00$  (black circles) via  $\beta = 0.15$  (red squares) to  $\beta = 0.30$  (blue triangles). The red stars indicate the sample's composition and temperature for the polymerization process and the numbers below it the mean radius of the polymer particles. The colors correlate to the amount of cross-linker in the monomer phase.

It is known from literature that spherical microemulsion droplets increase in size along the *efb* due to a larger oil to oil plus surfactant ratio. To be able to solubilize the increasing amount of monomer the droplets must increase in size. Figure 5.3 shows that the particle size slightly increases from  $R_{hydr} = 34 \pm 4$  nm ( $w_B = 0.03$ ,  $T = 7^\circ C$ ) to  $R_{hydr} = 39 \pm 4$  nm ( $w_B = 0.043$ ,  $T = 10^\circ C$ ) for the system  $H_2O/(sucrose/trehalose) - C_6MA/EGDMA - Lutensol XL 70/Agnique PG 8105-G$  with  $\Psi = 0.75$ ,  $\zeta = 0.38$ ,  $\delta = 0.80$ ,  $\beta = 0.15$  and  $\gamma_a = 0.074$ . However, the polymer particles increase compared to the unpolymerized microemulsion droplets by a factor of 7.5 times. Similar results have been obtained by *Lade et al.* polymerizing hexyl methacrylate in water microemulsion stabilized by nonionic surfactants [36].

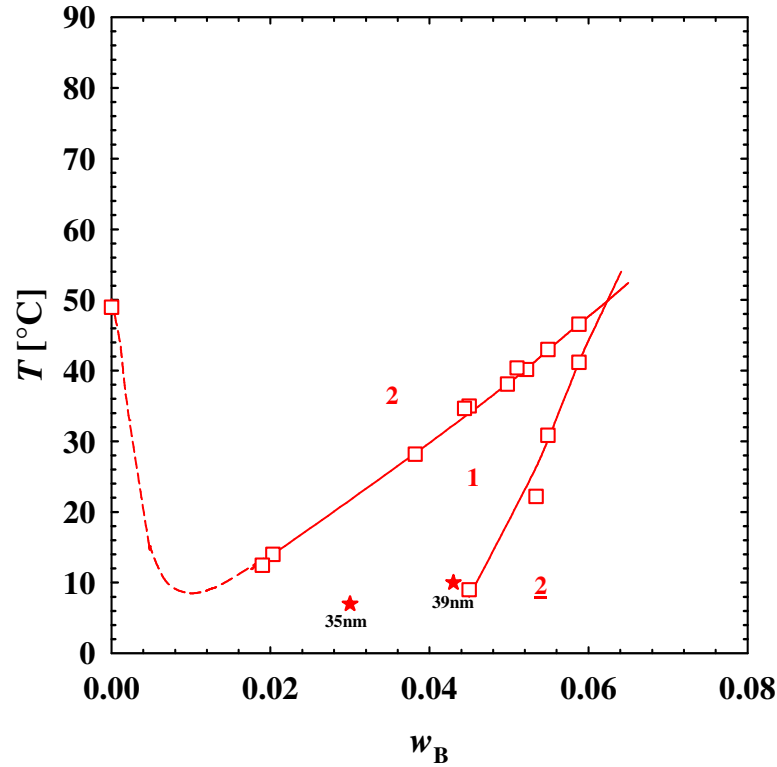


Figure 5.3:  $T(w_B)$ -section of the system  $H_2O/(sucrose/trehalose) - C_6MA/EGDMA - Lutensol XL70/Agnique PG 8105-G$  with  $\Psi = 0.75$ ,  $\zeta = 0.38$ ,  $\delta = 0.80$ ,  $\gamma_a = 0.074$  and  $\beta = 0.15$ . Polymerization was carried out at two compositions:  $w_B = 0.03$  and  $T = 7^\circ C$  leading to a mean droplet radius of  $R_{hydr} = 34 \pm 4$  nm as well as  $w_B = 0.043$  and  $T = 10^\circ C$  with a mean radius of  $R_{hydr} = 39 \pm 4$  nm.

To determine if coagulation is the reason for the increasing particle size microemulsions with different concentrations of droplets but the same droplet radius are polymerized. In order to perform this experiment, the phase behavior ( $T(w_B)$ -section) has to be determined for a different  $\gamma_a$ . The  $T(w_B)$ -sections of the system  $H_2O/(sucrose/trehalose) - C_6MA/EGDMA - Lutensol XL 70/Agnique PG 8105-G$  with  $\Psi = 0.75$ ,  $\zeta = 0.38$ ,  $\delta = 0.80$ ,  $\beta = 0.00$  and  $\gamma_a = 0.074$  (black circles) as well as  $\gamma_a = 0.0247$  (purple hexagonals) are shown in Figure 5.4. As expected, when  $\gamma_a$  is decreased the  $efb$  is shifted to lower  $w_B$ . Polymerizing microemulsions with the same monomer to surfactant ratio but different values of  $\gamma_a$  at the same temperature nearby the  $efb$  presuming a spherical shape of the droplets the radii of the droplet microemulsions should not differ. This is also found for the sizes of the polymer particles obtained ( $R_{hydr} = 36 \pm 1$  nm for  $\gamma_a = 0.074$ ,  $w_B = 0.043$  and  $R_{hydr} = 43 \pm 7$  nm for  $\gamma_a = 0.0247$ ,  $w_B = 0.014$ ). Within the experimental error, the values are the same. This leads to the conclusion that either coagulation is not exclusively the reason for the growing particle sizes during the polymerization process or the amount of

coagulation does not increase within this range of droplet concentration.

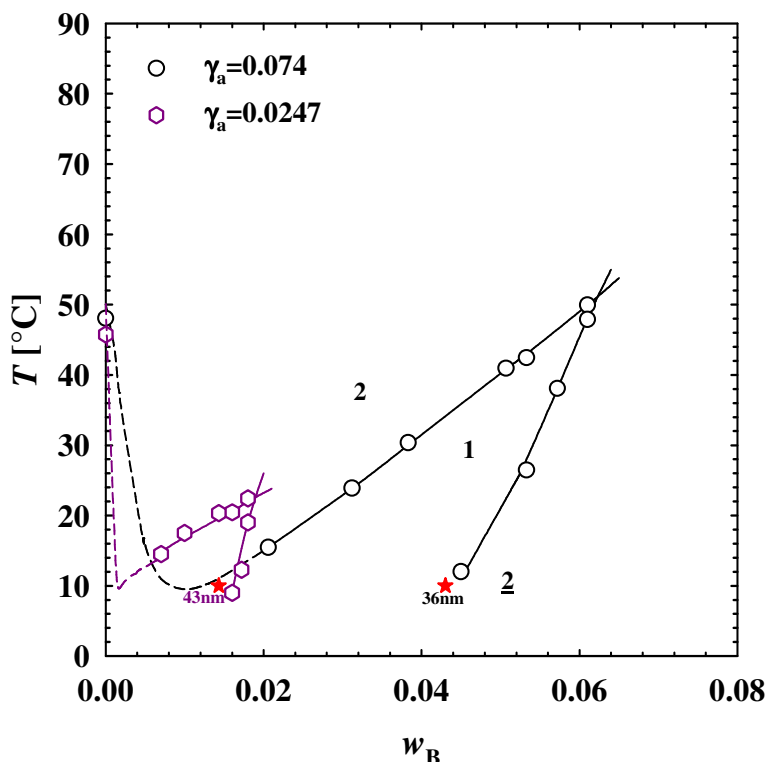


Figure 5.4:  $T(w_B)$ -section of the systems  $H_2O/(sucrose/trehalose) - C_6MA/EGDMA - Lutensol XL70/Agnique PG 8105-G$  with  $\Psi = 0.75$ ,  $\zeta = 0.38$ ,  $\delta = 0.80$ ,  $\beta = 0.00$  and  $\gamma_a = 0.074$  (black circles) as well as  $\gamma_a = 0.0247$  (purple hexagonals). Since the polymer size stays constant within the experimental error and thus, does not depend on the concentrations of microemulsion droplets, coagulation is at least not exclusively the reason for the growing particle sizes during polymerization.

In order to study if monomer diffusion is a dominant process during the polymerization, the  $C_6MA$  monomer is replaced with the more hydrophobic oil  $C_{12}MA$  in the following. Figure 5.5 shows the  $T(w_B)$ -section of the system  $H_2O/(sucrose/trehalose) - C_6MA/EGDMA - Lutensol XL 70/Agnique PG 8105-G$  with  $\Psi = 0.75$ ,  $\zeta = 0.38$ ,  $\delta = 0.80$ ,  $\beta = 0.15$  and  $\gamma_a = 0.074$  (black circles) as well as of the system  $H_2O/(sucrose/trehalose) - C_{12}MA/EGDMA - Lutensol XL 70/Agnique PG 8105-G$  with  $\Psi = 0.75$ ,  $\zeta = 0.38$ ,  $\delta = 0.80$ ,  $\beta = 0.15$  and  $\gamma_a = 0.074$  (red squares). As expected the replacement of  $C_6MA$  by the more hydrophobic monomer  $C_{12}MA$  shifts the phase boundaries to higher temperatures. Furthermore, the *efb* is shifted to lower values of  $w_B$  indicating that the solubilization of  $C_{12}MA$  is less efficient. Polymerizing both systems at a monomer concentration of  $w_B = 0.03$  and a temperature  $T = 10^\circ C$  the mean radius increases from  $R_{hydr} = 35 \pm 4$  nm for

the C<sub>6</sub>MA to  $R_{\text{hydr}} = 51 \pm 5$  nm for the C<sub>12</sub>MA-system. A possible explanation for the larger sizes of the polymer particles might be the longer chain length of the C<sub>12</sub>MA monomer leading to a larger volume of the polymer and thus to a larger radius. The monomer diffusion does not seem to be the dominant process for the growing particle size. Otherwise polymer particles with a smaller radius should have been obtained due to the smaller solubility of the C<sub>12</sub>MA monomers in the continuous aqueous sugar solution.

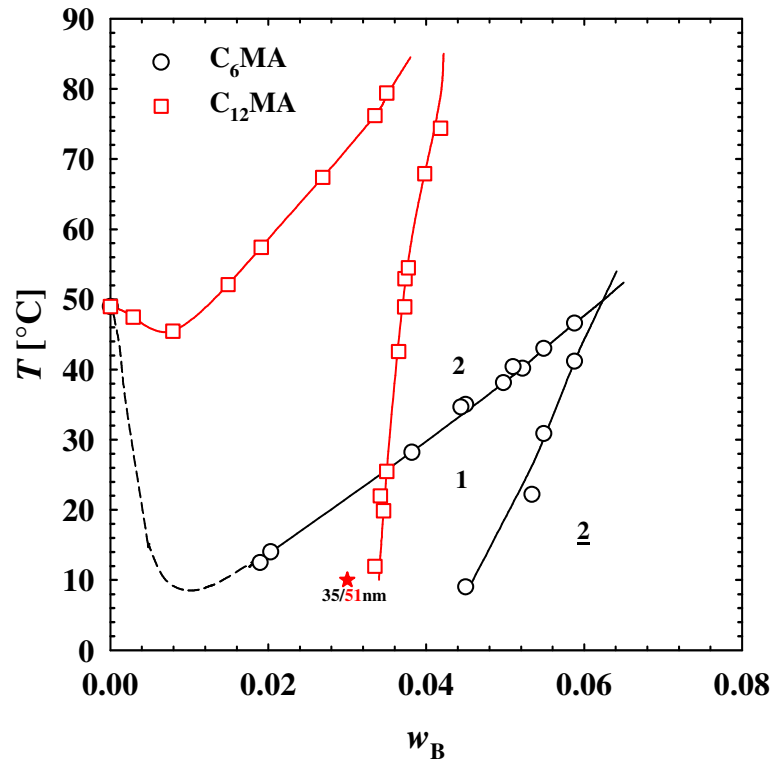


Figure 5.5:  $T(w_B)$ -section of the system H<sub>2</sub>O/(sucrose/trehalose) – C<sub>6</sub>MA/EGDMA – Lutensol XL70/Agnique PG 8105-G with  $\Psi = 0.75$ ,  $\zeta = 0.38$ ,  $\delta = 0.80$ ,  $\beta = 0.15$  and  $\gamma_a = 0.074$  (black circles) as well as of the system H<sub>2</sub>O/(sucrose/trehalose) – C<sub>12</sub>MA/EGDMA – Lutensol XL 70/Agnique PG 8105-G with  $\Psi = 0.75$ ,  $\zeta = 0.38$ ,  $\delta = 0.80$ ,  $\beta = 0.15$  and  $\gamma_a = 0.074$  (red squares). The mean radius increases from  $R_{\text{hydr}} = 35 \pm 4$  nm (C<sub>6</sub>MA-system) to  $R_{\text{hydr}} = 51 \pm 5$  nm (C<sub>12</sub>MA-system). Reason might be the longer chain length of the C<sub>12</sub>MA leading to a larger volume of the polymer.

In the following the duration of the polymerization reaction will be studied. *Uhrmeister* determined the conversion of microemulsion droplets to polymers of the system H<sub>2</sub>O – *n*-octane/hexyl methacrylate – C<sub>10</sub>E<sub>6</sub> online with the help of dynamic light scattering [174]. The polymerization was started thermally and DLS measurements were taken every 30 s during polymerization finding that the reaction is terminated after 100 minutes. To study

the polymerization kinetics of the highly viscous microemulsion polymerized in this work the polymerization reaction is terminated after a defined time by adding a concentrated hydroquinone solution. Afterwards, the sample has been diluted and DLS is used to determine the hydrodynamic radius of the obtained polymers. The experiments have been carried out for the system  $\text{H}_2\text{O}/(\text{sucrose}/\text{trehalose}) - \text{C}_6\text{MA}/\text{EGDMA} - \text{Lutensol XL70}/\text{Agnique PG 8105-G}$  with  $\Psi = 0.75$ ,  $\zeta = 0.38$ ,  $\delta = 0.80$ ,  $\beta = 0.15$ ,  $w_B = 0.043$  and  $\gamma_a = 0.074$  at  $T = 15^\circ\text{C}$ . No difference in particle size could be obtained if the polymerization process is carried out for only 10 minutes or over night. The black circles in Figure 5.6 show the polymer radius determined for 10 minutes, 20 minutes and 30 minutes of polymerization. The red circle shows the mean hydrodynamic radius and its error ( $R_{\text{hydr}} = 37 \pm 4$  nm) obtained after over night polymerization. The mean droplet radius for up to 30 minutes polymerization also shows a value of  $R_{\text{hydr}} = 37 \pm 4$  nm. Thus, no difference in particle size can be obtained if the polymerization process is carried out for only 10 minutes or over night. Shorter polymerization times than 10 minutes were not chosen as the inaccuracy of the experiment increases too much.

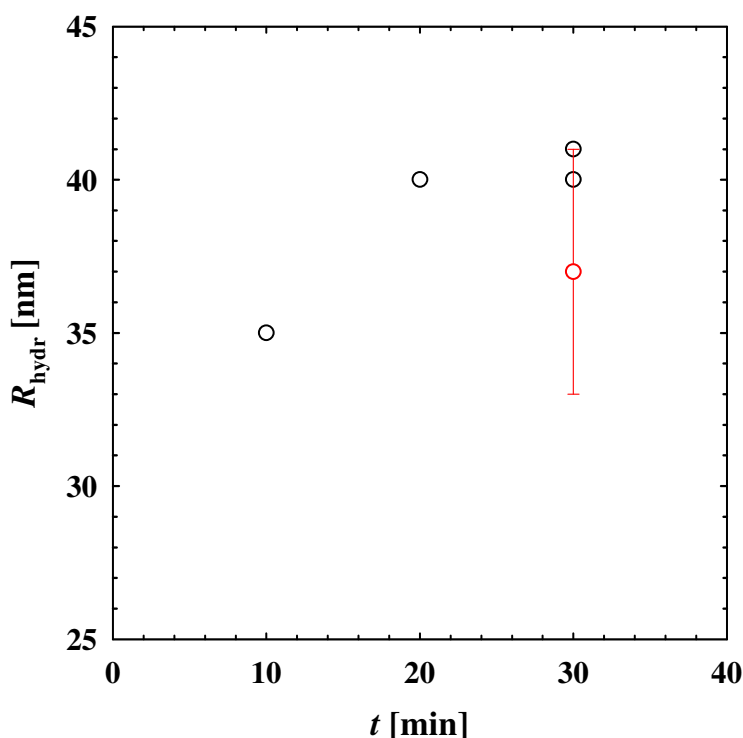


Figure 5.6: The hydrodynamic radius  $R_{\text{hydr}}$  plotted versus the polymerization time for the system  $\text{H}_2\text{O}/(\text{sucrose}/\text{trehalose}) - \text{C}_6\text{MA}/\text{EGDMA} - \text{Lutensol XL 70}/\text{Agnique PG 8105-G}$  with  $\Psi = 0.75$ ,  $\zeta = 0.38$ ,  $\delta = 0.80$ ,  $\beta = 0.15$ ,  $w_B = 0.043$  and  $\gamma_a = 0.074$  at  $T = 15^\circ\text{C}$ . No difference in particle size could be obtained if the polymerization process is carried out for only 10 minutes or over night.

### 5.3 Wave Length of Initiation

The polymerization reactions performed in chapter 5.2 are initiated using a microscopy lamp emitting white light. It was observed that the polymerization process could only be initiated if the sample is stirred. However, exposing the unstirred sample for 48 hours to the transmitted light of the microscopy lamp was unsuccessful. Adding initiator in excess does not influence this observation. It is suspected that the microscopy lamp is not able to activate enough initiator molecules leading to the fact that not every droplet contains one radical. Only by stirring the microemulsion the few radicals are allowed to meet and react with each other making a complete polymerization possible.

Bearing in mind the absorption spectrum of the initiator Irgacure 819 (Figure 2.12) an optimization of the initiation process should be possible using lamps emitting light of shorter wavelengths. In Table 5.2 the mean polymer radius obtained using the microscopy lamp is compared with the radius obtained initiating the polymerization of the system  $\text{H}_2\text{O}/(\text{sucrose}/\text{trehalose}) - \text{C}_{12}\text{MA}/\text{EGDMA} - \text{Lutensol XL 70}/\text{Agnique PG 8105-G}$  with  $\Psi = 0.75$ ,  $\zeta = 0.38$ ,  $\delta = 0.80$ ,  $\beta = 0.15$ ,  $w_B = 0.03$  and  $\gamma_a = 0.074$  and  $T = 30^\circ\text{C}$  with a LED Spot Luxeon Royal Blue lamp (Conrad Electronics, 3W, 220V 25mA) and the SpecBright UV-LED (Laser 2000, COK-AF1-370-VHF100, 24V, 360mA). The LED Spot Luxeon Royal blue lamp emits blue light of  $\lambda = 455$  nm, the SpecBright UV-LED UV-light of  $\lambda = 370$  nm. The mean radius of the polymer particles decreases replacing the microscopy lamp with a lamp emitting light of shorter wave lengths. This leads to the conclusion that coagulation must have taken place for the polymerization started with the microscopy lamp. Replacing the microscopy lamp with a UV-lamp the coagulation is partly eliminated.

Table 5.2: The influence of different initiating lamps motivated by the absorption maximum of Irgacure 819 on the mean radius of the polymer particles for the system  $\text{H}_2\text{O}/(\text{sucrose}/\text{trehalose}) - \text{C}_{12}\text{MA}/\text{EGDMA} - \text{Lutensol XL 70}/\text{Agnique PG 8105-G}$  with  $\Psi = 0.75$ ,  $\zeta = 0.38$ ,  $\delta = 0.80$ ,  $\beta = 0.15$ ,  $w_B = 0.03$  and  $\gamma_a = 0.074$  and a polymerization temperature of  $T = 30^\circ\text{C}$  have been studied.

initiating lamp [wavelength in nm]	mean radius [nm]
microscopy lamp [white light]	$R_{\text{hydr}} = 44 \pm 5$
LED Spot Luxeon Royal Blue lamp [455]	$R_{\text{hydr}} = 35 \pm 2$
SpecBright UV-LED [370]	$R_{\text{hydr}} = 21 \pm 1$

Indicated by the error given in Table 5.2 not only the mean droplet radius decreases but also the reproducibility of the polymer particles obtained increases using UV-light. Reason is the small fraction of light emitted in the UV-area using a microscopy lamp. In contrast to this, the SpecBright UV-LED with a  $30^\circ$  nominal beam cone angle contains a typical irradiance of  $20\text{W}/\text{m}^2$  at a working distance of 100 mm. Calculating the area of the used test tube with  $2.25\text{ cm}^2$  and accounting for the energy of the photons  $E_{\text{photon}} = h\nu = 5.36 \cdot 10^{-19}\text{J}$  the number of photons  $N_{\text{photon}} = 8.39 \cdot 10^{15}$  strike the sample per second. Estimating the number of droplets to  $N_{\text{droplet}} = 2.8\text{--}6.5 \cdot 10^{17}$  per sample each Irgacure 819 molecule should be initiated within 10 – 100 seconds. This short initiating time and the constant intensity lead to a good reproducibility of the polymerization results. Also very monodisperse polymer particles are obtained as shown in the following chapter. In the following, for each microemulsion 3 – 4 samples have been polymerized to obtain a mean value for the polymer radius. Since no difference in the polymer radius can be determined if the sample is stirred or not all samples are stirred during the polymerization process in the following. The obtained results for each measurement are listed in the appendix A.2, Table 7.18.

## 5.4 Initiation via a UV-Lamp

In the following all polymerization experiments are initiated using the SpecBright UV-LED. Thereby, the polymerization process is carried out in the same manner as for the microscopy lamp. Since experiments proved that degassing does not influence the polymer



particle radius in the following the polymerization is conducted without degassing. The samples polymerized with UV-light are diluted 1:12 before investigating the droplet radius using the DLS technique. The dilution leads to a viscosity of the sample of  $\eta = 1.121 \cdot 10^{-3} \text{ kg m}^{-1} \text{ s}^{-1}$  and a refractive index of  $n = 1.339$ . In contrast to the samples polymerized with the microscopy lamp which still stayed turbid after a 1:12 dilution, here the samples become clear.

Figure 5.7 shows the mean hydrodynamic radius of the samples  $\text{H}_2\text{O}/(\text{sucrose/trehalose}) - \text{C}_6\text{MA/EGDMA} - \text{Lutensol XL 70/Agnique PG 8105-G}$  with  $\Psi = 0.75$ ,  $\zeta = 0.38$ ,  $\delta = 0.80$  and  $\gamma_a = 0.074$  and varying  $\beta$  from  $\beta = 0.00$  (black circles) via  $\beta = 0.15$  (red squares) to  $\beta = 0.30$  (blue triangles) polymerized with the UV-lamp. As found before, the polymer size stays constant with  $R_{\text{hydr}} = 20 \pm 1 \text{ nm}$  for the samples with up to 15% of cross-linker in the monomer phase. Compared to the calculated radius of the unpolymerized microemulsion droplet (equation 5.1) the increase in size during the polymerization is reduced by 4 times. Again, the polymer radius of the system  $\text{H}_2\text{O}/(\text{sucrose/trehalose}) - \text{C}_6\text{MA/EGDMA} - \text{Lutensol XL 70/Agnique PG 8105-G}$  with  $\Psi = 0.75$ ,  $\zeta = 0.38$ ,  $\delta = 0.80$  and  $\gamma_a = 0.074$  and  $\beta = 0.30$  is with  $R_{\text{hydr}} = 29 \pm 1 \text{ nm}$  larger in size. The polydispersity index  $p = (\sigma_R/R_H)$  with  $\sigma_R$  being the standard deviation of the polymer radius varies in these samples between  $p = 0.045$  and  $p = 0.071$ . This value indicates that the polymer droplets are comparatively monodisperse.

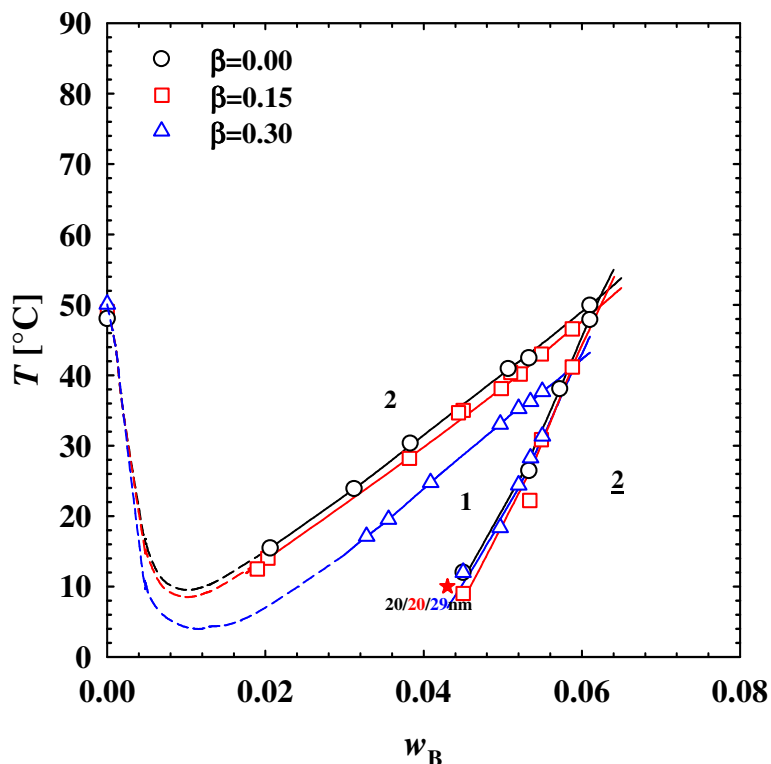


Figure 5.7:  $T(w_B)$ -section of the system  $\text{H}_2\text{O}/(\text{sucrose/trehalose}) - \text{C}_6\text{MA/EGDMA} - \text{Lutensol XL70/Agnique PG 8105-G}$  with  $\Psi = 0.75$ ,  $\zeta = 0.38$ ,  $\delta = 0.80$ ,  $\gamma_a = 0.074$ . The amount of cross-linker in the monomer phase varies from  $\beta = 0.00$  (black circles) via  $\beta = 0.15$  (red squares) to  $\beta = 0.30$  (blue triangles). The red star indicates the sample's composition and temperature for the polymerization process and the numbers below it the mean radius of the polymer particles. The colors correlate to the color of the corresponding phase boundaries.

Figure 5.8 left shows exemplarily a typical shape of the auto correlation function  $g^{(2)}(t) - 1.04$  obtained for the system  $\text{H}_2\text{O}/(\text{sucrose/trehalose}) - \text{C}_6\text{MA/EGDMA} - \text{Lutensol XL 70/Agnique PG 8105-G}$  with  $\Psi = 0.75$ ,  $\zeta = 0.38$ ,  $\delta = 0.80$ ,  $\beta = 0.15$ ,  $w_B = 0.043$  and  $\gamma_a = 0.074$  polymerized with the UV-lamp plotted logarithmically as a function of  $\tau$ . The polymerization temperature is  $T = 10^\circ\text{C}$  and the temperature of the DLS experiment  $T = 23^\circ\text{C}$ . For statistical reasons, each single measurement is repeated three times. The duration of each measurement is 120 s. Figure 5.8 left shows the data of the second run at a scattering angle of  $90^\circ$ . The linear decrease of the logarithm of the correlation function indicates that only one diffusive process exists. Correspondingly, analyzing this autocorrelation function using the automatic CONTIN-evaluation a narrow distribution of decay times around the decay time  $\Gamma_{\max} = 2930 \text{ s}^{-1}$  is found (Figure 5.8 right).

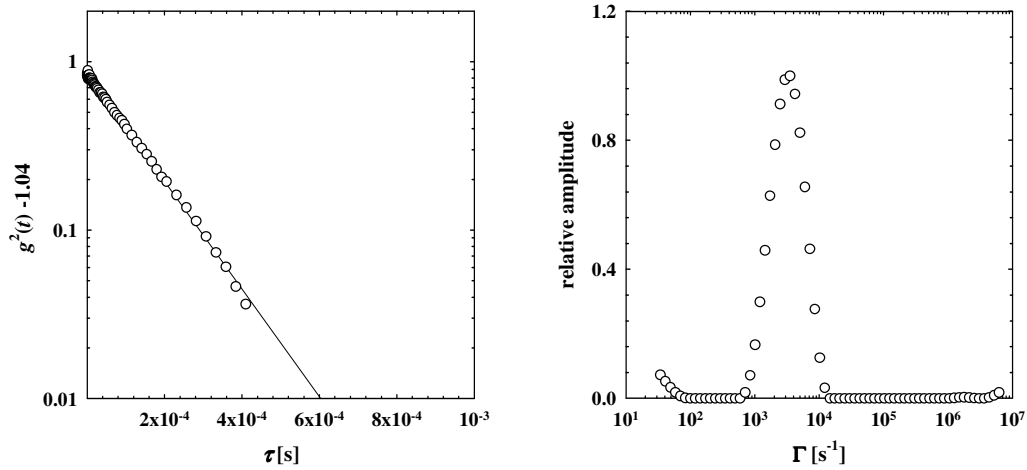


Figure 5.8: Left:  $g^{(2)}(t) - 1.04$  plotted logarithmically as a function of  $\tau$  for a DLS measurement using the sample  $\text{H}_2\text{O}/(\text{sucrose}/\text{trehalose}) - \text{C}_6\text{MA}/\text{EGDMA} - \text{Lutensol XL 70}/\text{Agnique PG 8105-G}$  with  $\Psi = 0.75$ ,  $\zeta = 0.38$ ,  $\delta = 0.80$ ,  $\beta = 0.15$ ,  $w_B = 0.043$  and  $\gamma_a = 0.074$ . The polymerization temperature is  $T = 10^\circ\text{C}$  and the temperature of the DLS experiment  $T = 23^\circ\text{C}$ . The almost linear decrease of the logarithm of the correlation function indicates that only one diffusive process exists. Right: The automated CONTIN-evaluation provides a narrow distribution around the decay time  $\Gamma_{\max} = 2930 \text{ s}^{-1}$  (right).

In Figure 5.9 top the decay rate  $\Gamma$  obtained at the respective scattering wave vectors  $q$  is plotted versus  $q^2$ . From the slope of the straight line the diffusion coefficient  $D = 9.69 \cdot 10^{-12} \text{ m}^2\text{s}^{-1}$  and therewith a hydrodynamic radius  $R_{\text{hydr}} = 20 \text{ nm}$  can be extracted. The slope of both, the black line fitting the data points and passing through the origin as well as the slope of the red line, only fitting the data points is identical – both lines lie on top of each other. Figure 5.9 bottom shows the calculated hydrodynamic radius  $R_{\text{hydr}}$  plotted versus the scattering angle  $\theta$ . The values of the hydrodynamic radius  $R_{\text{hydr}}$  are found in the range of 18 to 23 nm as well as to be totally independent of the scattering angle  $\theta$  as expected for an isotropic scattering medium. The mean hydrodynamic radius obtained is  $\langle R_{\text{hydr}} \rangle = 20 \pm 1 \text{ nm}$ . The polydispersity index of this sample amounts to  $p = 0.051$ .

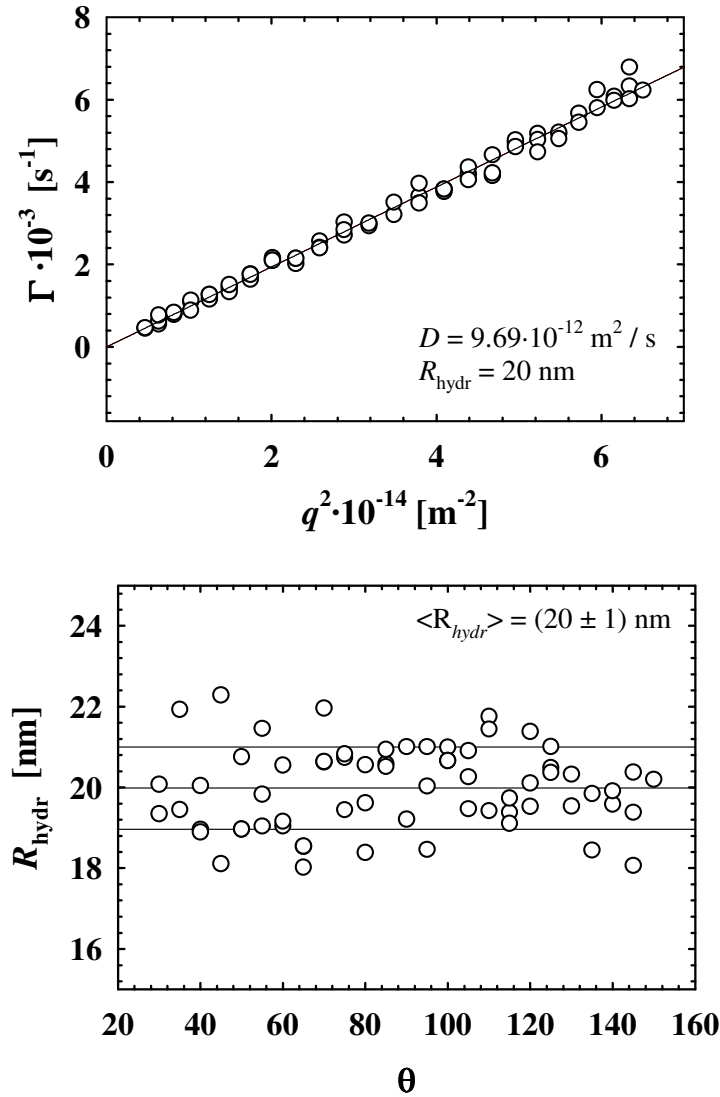


Figure 5.9: top: Decay rate  $\Gamma$  is plotted versus  $q^2$  for the system  $\text{H}_2\text{O}/(\text{sucrose}/\text{trehalose}) - \text{C}_6\text{MA}/\text{EGDMA} - \text{Lutensol XL 70}/\text{Agnique PG 8105-G}$  with  $\Psi = 0.75$ ,  $\zeta = 0.38$ ,  $\delta = 0.80$ ,  $\beta = 0.15$ .  $w_B = 0.043$  and  $\gamma_a = 0.074$  polymerized with the UV-lamp at a polymerization temperature of  $T = 10^\circ\text{C}$  (temperature of the DLS experiment of  $T = 23$ ). bottom: Calculated hydrodynamic radius  $R_{\text{hydr}}$  plotted versus the scattering angle  $\theta$ . The values of the hydrodynamic radius  $R_{\text{hydr}}$  are found in the range of 18 to 23 nm as well as to be totally independent from the angle  $\theta$  as expected for an isotropic scattering medium.

Having found the optimal polymerization conditions samples of the system  $\text{H}_2\text{O}/(\text{sucrose}/\text{trehalose}) - \text{C}_6\text{MA}/\text{EGDMA} - \text{Lutensol XL 70}/\text{Agnique PG 8105-G}$  with  $\Psi = 0.75$ ,  $\zeta = 0.38$ ,  $\delta = 0.80$ ,  $\beta = 0.15$  and  $\gamma_a = 0.074$  (Figure 5.10) are polymerized in the following using UV-light. Thereby, the monomer mass fraction  $w_B$  as well as the polymerization temperature has been varied.

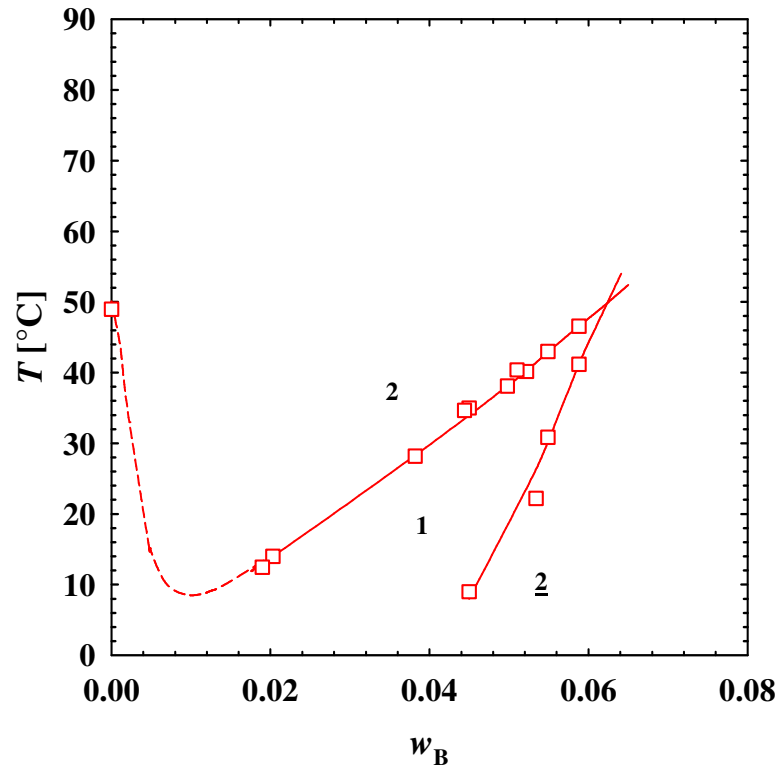


Figure 5.10:  $T(w_B)$ -section of the system  $\text{H}_2\text{O}/(\text{sucrose/trehalose}) - \text{C}_6\text{MA/EGDMA} - \text{Lutensol XL70/Agnique PG 8105-G}$  with  $\Psi = 0.75$ ,  $\zeta = 0.38$ ,  $\delta = 0.80$ ,  $\beta = 0.15$  and  $\gamma_a = 0.074$ .

The variation of the hydrodynamic radius  $R_{\text{hydr}}$  as a function of the monomer concentration within the microemulsion  $w_B$  is plotted in Figure 5.11 for the system  $\text{H}_2\text{O}/(\text{sucrose/trehalose}) - \text{C}_6\text{MA/EGDMA} - \text{Lutensol XL 70/Agnique PG 8105-G}$  with  $\Psi = 0.75$ ,  $\zeta = 0.38$ ,  $\delta = 0.80$ ,  $\beta = 0.15$ ,  $\gamma_a = 0.074$  for a polymerization temperature of  $T = 10^\circ\text{C}$  once polymerized using the microscopy lamp as initiating lamp (red squares) and once polymerized using the UV-lamp (black circles). Comparing the obtained polymer radii to the radii of the unpolymerized microemulsion droplets calculated using equation (5.1) (filled black circles), one can see that the wave length and intensity of the initiating lamp has a significant influence on the size of the obtained polymer particle. Considering the sample with  $w_B = 0.03$  a radius of the microemulsion droplet  $R_{\text{calc}} = 4.4 \text{ nm}$  is calculated. Bear in mind that this is the radius and not the hydrodynamic radius of the droplet. Using the microscopy lamp, the polymer radius size increases by 7.5 times to a hydrodynamic radius of  $R_{\text{hydr}} = 35 \pm 4 \text{ nm}$ , the polymer particles polymerized with the UV-lamp only increase by about 3.5 times to a hydrodynamic radius of  $R_{\text{hydr}} = 15 \pm 1 \text{ nm}$  during the polymerization process. Reason for this is the higher energy of the UV-lamp as well as the emitted shorter wavelength. Bearing in mind the absorption spectrum of the initiator Ir-

gacure 819 more molecules can be activated using the UV-lamp leading to a faster polymerization. Remarkably is the significantly systematic increase of the radius with increasing monomer mass fraction for the particles polymerized using the UV-lamp reflecting the calculated size increase of the underlying microemulsion droplets with increasing monomer mass fraction.

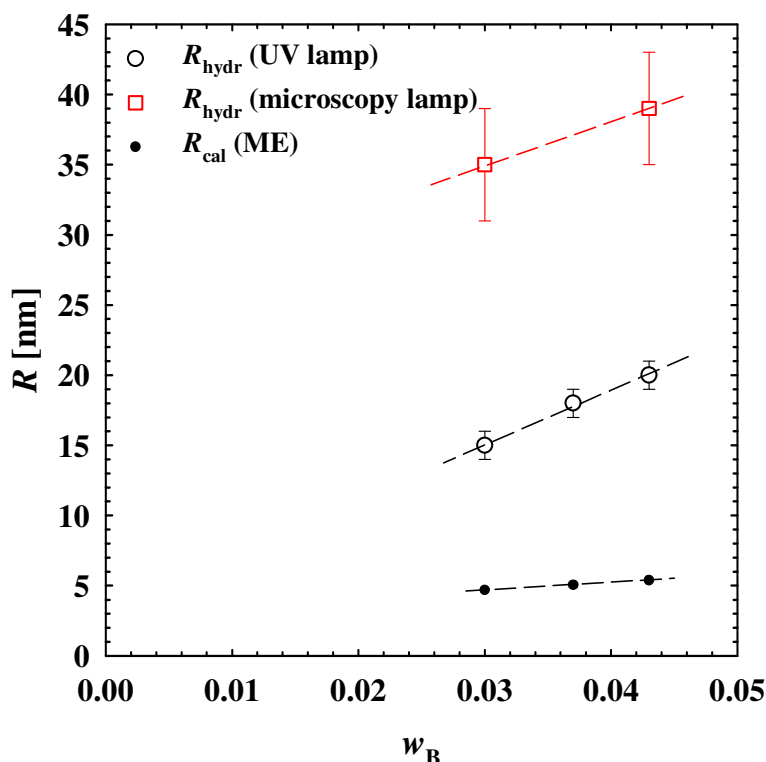


Figure 5.11: The hydrodynamic radius  $R_{\text{hydr}}$  plotted versus the monomer mass fraction  $w_B$  within the microemulsion for the system  $\text{H}_2\text{O}/(\text{sucrose}/\text{trehalose}) - \text{C}_6\text{MA}/\text{EGDMA} - \text{Lutensol XL 70}/\text{Agnique PG 8105-G}$  with  $\Psi = 0.75$ ,  $\zeta = 0.38$ ,  $\delta = 0.80$ ,  $\beta = 0.15$ ,  $\gamma_a = 0.074$  and a polymerization temperature of  $T = 10^\circ\text{C}$  once polymerized using the microscopy lamp as initiating lamp (red squares) and once the UV-lamp (black circles). The increase of the polymer radius compared to the unpolymerized droplet radius decreases replacing the microscopy lamp with a UV-lamp.

Figure 5.12 shows the variation of the hydrodynamic radius with the polymerization temperature at a constant composition for the system  $\text{H}_2\text{O}/(\text{sucrose}/\text{trehalose}) - \text{C}_6\text{MA}/\text{EGDMA} - \text{Lutensol XL 70}/\text{Agnique PG 8105-G}$  with  $\Psi = 0.75$ ,  $\zeta = 0.38$ ,  $\delta = 0.80$ ,  $\beta = 0.15$ ,  $\gamma_a = 0.074$  and  $w_B = 0.03$  (black circle) or  $w_B = 0.043$  (red squares). As one can see, the hydrodynamic radius increases with increasing polymerization temperature. This increase in size is clearly stronger pronounced for the system containing a higher amount

of monomer. Whereas for the system with  $w_B = 0.03$  the radius  $R_{\text{hydr}} = 15 \pm 1$  nm stays constant up to a temperature  $T = 10^\circ\text{C}$  and then only slightly increases up to  $R_{\text{hydr}} = 20 \pm 1$  nm ( $T = 17^\circ\text{C}$ ) the radius of the system with  $w_B = 0.043$  increases from  $R_{\text{hydr}} = 20 \pm 1$  nm ( $T = 10^\circ\text{C}$ ) via  $R_{\text{hydr}} = 25 \pm 1$  nm ( $T = 15^\circ\text{C}$ ) to  $R_{\text{hydr}} = 42 \pm 2$  nm ( $T = 20^\circ\text{C}$ ). An explanation for this trend could be the microstructure of the underlying microemulsion. It is expected that with higher amount of monomer in the microemulsion the transition from spherical droplets to cylindrical and network structures begins at temperatures closer to the *efb*. Thus, it is also found that the underlying microstructure is reflected.

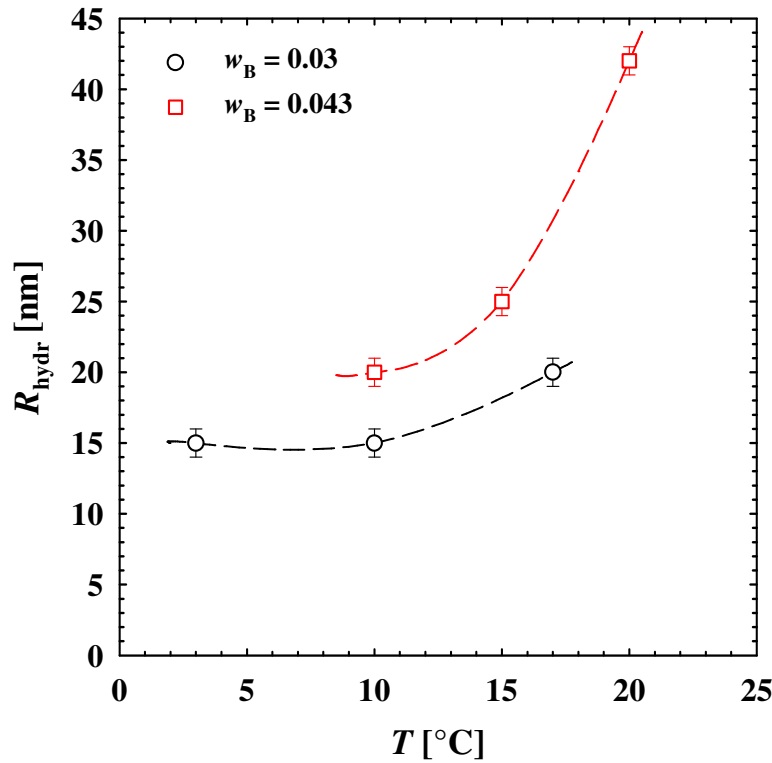


Figure 5.12: The hydrodynamic radius  $R_{\text{hydr}}$  plotted versus the polymerization temperature for the system  $\text{H}_2\text{O}/(\text{sucrose}/\text{trehalose}) - \text{C}_6\text{MA}/\text{EGDMA} - \text{Lutensol XL 70}/\text{Agnique PG 8105-G}$  with  $\Psi = 0.75$ ,  $\zeta = 0.38$ ,  $\delta = 0.80$ ,  $\beta = 0.15$ ,  $\gamma_a = 0.074$  and  $w_B = 0.03$  (black circle) respectively  $w_B = 0.043$  (red squares). The increase in size is clearly stronger pronounced for the system containing a higher amount of monomer since the transition of the spherical droplets to network structures is shifted to temperatures closer to the *efb*.

The variation of the polymer radius along the *efb* is displayed in Figure 5.13. The hydrodynamic radius  $R_{\text{hydr}}$  is plotted versus the monomer mass fraction  $w_B$  for the system  $\text{H}_2\text{O}/(\text{sucrose}/\text{trehalose}) - \text{C}_6\text{MA}/\text{EGDMA} - \text{Lutensol XL 70}/\text{Agnique PG 8105-G}$  with

$\Psi = 0.75$ ,  $\zeta = 0.38$ ,  $\delta = 0.80$ ,  $\beta = 0.15$ ,  $\gamma_a = 0.074$ . The monomer concentration is increased from  $w_B = 0.043$  to  $w_B = 0.055$ . The corresponding polymerization temperature is chosen to be just above the *efb*. As one can see indicated by the red circles the polymer radius increases linearly with increasing monomer concentration and temperature. An increase in size is expected from the increase of the radius of the unpolymerized microemulsion droplet calculated using equation (5.1) as shown by the black filled circles but the increase of the size of the microemulsion droplets is clearly less pronounced. Reason for this might be once again the transition from spherical monomer-droplets to network structures. As mentioned earlier with increasing amount of monomer within the microemulsion mixture this transition starts at temperatures closer to the *efb*. This phenomenon might be strengthened during the polymerization process.

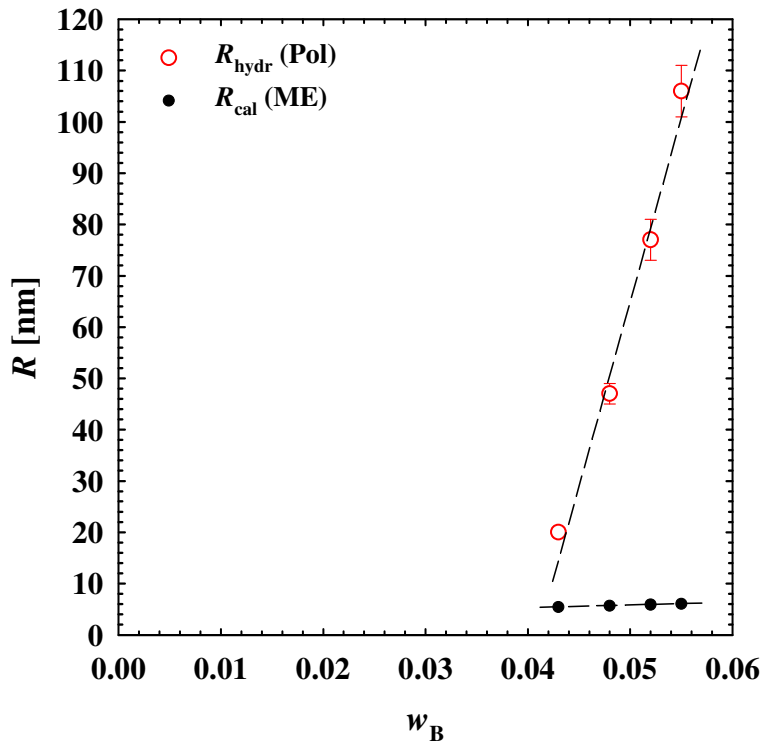


Figure 5.13: The hydrodynamic radius  $R_{\text{hydr}}$  versus the monomer mass fraction within the microemulsion  $w_B$  is plotted for the system  $\text{H}_2\text{O}/(\text{sucrose}/\text{trehalose}) - \text{C}_6\text{MA}/\text{EGDMA} - \text{Lutensol XL 70}/\text{Agnique PG 8105-G}$  with  $\Psi = 0.75$ ,  $\zeta = 0.38$ ,  $\delta = 0.80$ ,  $\beta = 0.15$ ,  $\gamma_a = 0.074$ . The polymerization temperature is chosen to be just above the *efb*. The increase in size is stronger pronounced for the hydrodynamic polymer radius than for the radius of the unpolymerized microemulsion droplets.

In Figure 5.14 the hydrodynamic radii of the UV-polymerized samples of the system  $\text{H}_2\text{O}/(\text{sucrose}/\text{trehalose}) - \text{C}_6\text{MA}/\text{EGDMA} - \text{Lutensol XL 70}/\text{Agnique PG 8105-G}$  with



$\Psi = 0.75$ ,  $\zeta = 0.38$ ,  $\delta = 0.80$ ,  $\beta = 0.15$  and  $\gamma_a = 0.074$  are summarized. The amount of monomer as well as the polymerization temperature is varied whereas the amount of cross-linker in the monomer phase is kept constant at 15% ( $\beta = 0.15$ ). One can clearly see that the hydrodynamic polymer radius increases significantly with increasing amount of monomer in the unpolymerized microemulsion at a constant polymerization temperature ( $T = 10^\circ\text{C}$ ) reflecting the underlying microstructure. With increasing temperature but at a constant monomer composition the underlying microemulsion structure changes from spherical droplets to cylindrical oil-droplets which is also reflected in the increase of the polymer radius. The fact that the polymer radius increases much more strongly along the *efb* compared to the radius of the unpolymerized microemulsion droplet might be caused due to the transition from spherical droplets to elongated objects and networks shifting to temperatures closer to the *efb* with increasing  $w_B$ . The black dashed line displays schematically the starting transition of the spherical droplets to cylindrical monomer-droplets and network structures.

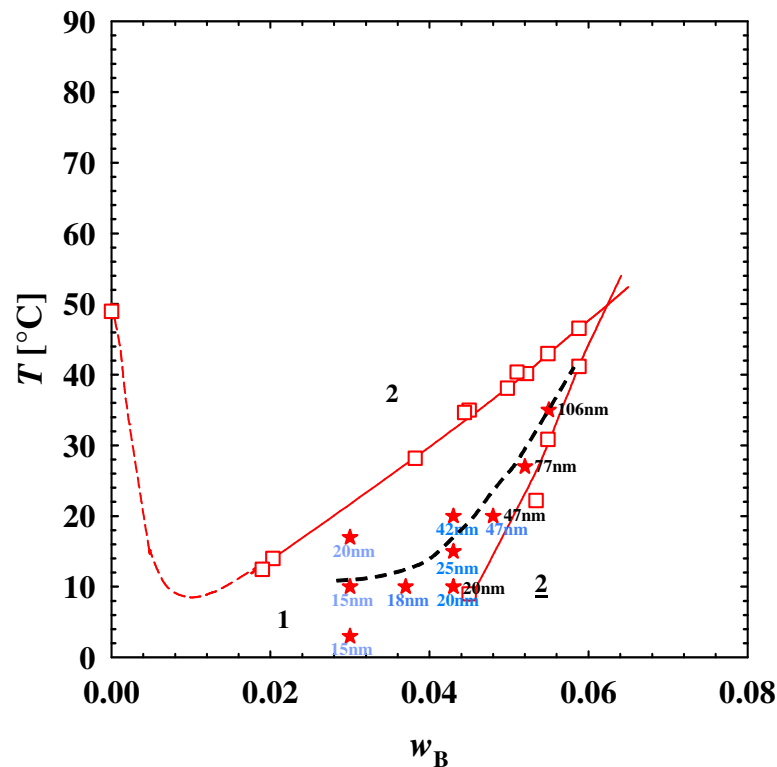


Figure 5.14:  $T(w_B)$ -section of the system  $\text{H}_2\text{O}/(\text{sucrose}/\text{trehalose}) - \text{C}_6\text{MA}/\text{EGDMA} - \text{Lutensol XL70}/\text{Agnique PG 8105-G}$  with  $\Psi = 0.75$ ,  $\zeta = 0.38$ ,  $\delta = 0.80$ ,  $\gamma_a = 0.074$  and  $\beta = 0.15$ . The polymerization is carried out using the UV-lamp at different compositions and polymerization temperatures.

As already investigated for the polymerization process initiated by the microscopy lamp the influence of the number density of droplets on the particle size is of interest to understand to what extent coagulation occurs during the polymerization process. Therefore, microemulsions with different number densities of droplets but the same droplet radius are polymerized in the system  $\text{H}_2\text{O}/(\text{sucrose}/\text{trehalose}) - \text{C}_6\text{MA}/\text{EGDMA} - \text{Lutensol XL70}/\text{Agnique PG 8105-G}$  with  $\Psi = 0.75$ ,  $\zeta = 0.38$ ,  $\delta = 0.80$ ,  $\beta = 0.15$  at a temperature  $T = 10^\circ\text{C}$ . The composition, i.e.  $\gamma_a$  and  $w_B$ , is chosen in such a way that the ratio of  $w_B/\gamma_a$  stays constant around  $w_B/\gamma_a = 0.405$ . As summarized in Table 5.3 no increase in size with increasing droplet concentration can be determined; rather the measured polymer radius fluctuates around an average value of  $R_{\text{hydr}} = 19 \pm 3$  nm.

Table 5.3: The hydrodynamic radius  $R_{\text{hydr}}$  for the system  $\text{H}_2\text{O}/(\text{sucrose}/\text{trehalose}) - \text{C}_6\text{MA}/\text{EGDMA} - \text{Lutensol XL 70}/\text{Agnique PG 8105-G}$  with  $\Psi = 0.75$ ,  $\zeta = 0.38$ ,  $\delta = 0.80$ ,  $\beta = 0.15$  and a polymerization temperature  $T = 10^\circ\text{C}$  with different surfactant mass fractions  $\gamma_a$  and the corresponding monomer mass fraction  $w_B$  keeping the  $w_B/\gamma_a$  constant.

	$\gamma_a = 0.050,$ $w_B = 0.0203$	$\gamma_a = 0.074,$ $w_B = 0.0300$	$\gamma_a = 0.100,$ $w_B = 0.0405$	$\gamma_a = 0.148,$ $w_B = 0.0600$
$R_{(1)\text{hydr}}$ [nm]	22	15	19	20
$R_{(2)\text{hydr}}$ [nm]	23	15	18	23
$R_{(3)\text{hydr}}$ [nm]		15	18	21
$\emptyset R_{\text{hydr}}$ [nm]	$22 \pm 1$	$15 \pm 0$	$18 \pm 1$	$21 \pm 2$

Since coagulation of the microemulsion droplets does not seem to play a significant role during the polymerization process the influence of the monomer diffusion is studied in the next step. To determine if monomer diffusion is a dominant process during the polymerization, again the  $\text{C}_6\text{MA}$  monomer is replaced with the more hydrophobic oil  $\text{C}_{12}\text{MA}$ . Figure 5.15 shows  $T(w_B)$ -sections of the system  $\text{H}_2\text{O}/(\text{sucrose}/\text{trehalose}) - \text{C}_{12}\text{MA}/\text{EGDMA} - \text{Lutensol XL 70}/\text{Agnique PG 8105-G}$  with  $\Psi = 0.75$ ,  $\zeta = 0.38$ ,  $\delta = 0.80$  and  $\gamma_a = 0.074$ . The amount of cross-linker in the monomer phase is varied from  $\beta = 0.15$  (red squares) via  $\beta = 0.30$  (blue triangles) to  $\beta = 0.60$  (green hexagonals). As one can see, the phase boundaries are shifted to lower temperatures with increasing amount of cross-linker in the system

due to its higher hydrophilicity compared to  $C_{12}MA$ . A similar but less pronounced shift of the phase boundaries to lower temperatures is found replacing the  $C_6MA$  monomer with the cross-linker. Polymerizing the system containing  $C_{12}MA$  and varying the amount of cross-linker in the monomer phase at a monomer mass fraction of  $w_B = 0.03$  and a temperature  $T = 10^\circ C$  one finds a mean hydrodynamic radius of  $R_{hydr} = 18 \pm 1$  nm ( $\beta = 0.15$ ),  $R_{hydr} = 21 \pm 1$  nm ( $\beta = 0.30$ ) and  $R_{hydr} = 43 \pm 1$  nm for the system with  $\beta = 0.60$ . A possible explanation for this trend is the shift of the phase boundaries to lower temperatures with increasing  $\beta$ . Thus, the decreasing distance between the polymerization temperatures and the upper  $1-2$  phase boundary very likely induces the existence of elongated or network-like structures in the unpolymerized microemulsion at  $\beta = 0.60$ .

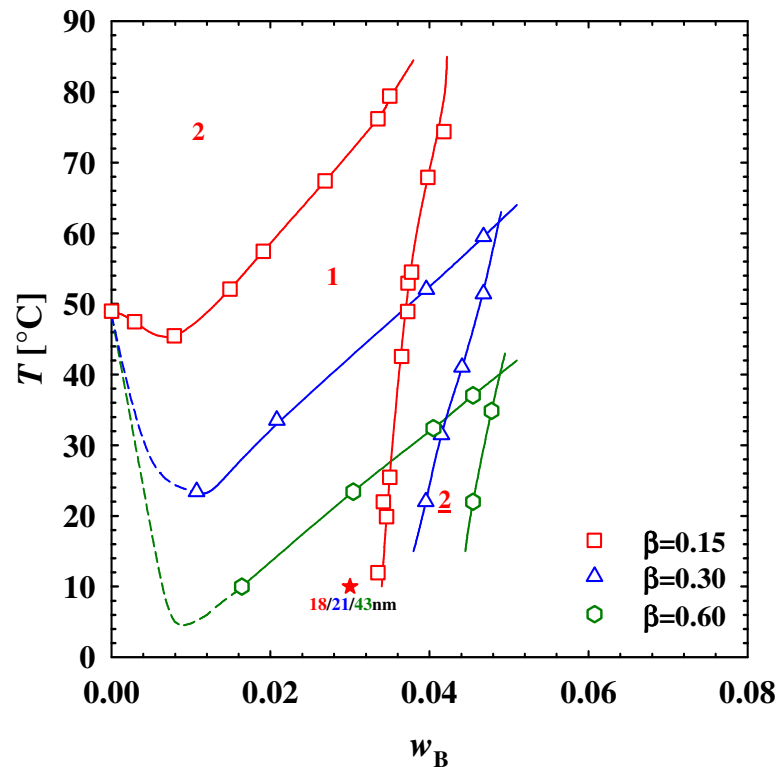


Figure 5.15:  $T(w_B)$ -section of the system  $H_2O/(sucrose/trehalose) - C_{12}MA/EGDMA - Lutensol XL70/Agnique PG 8105-G$  with  $\Psi = 0.75$ ,  $\zeta = 0.38$ ,  $\delta = 0.80$ ,  $\gamma_a = 0.074$  and varying amounts of cross-linker in the monomer phase. The polymerization is carried out at a temperature of  $T = 10^\circ C$  and a monomer mass fraction  $w_B = 0.03$ .

The influence of the monomer mass fraction on the polymer radius is also studied for the system  $H_2O/(sucrose/trehalose) - C_{12}MA/EGDMA - Lutensol XL 70/Agnique PG 8105-G$  with  $\Psi = 0.75$ ,  $\zeta = 0.38$ ,  $\delta = 0.80$ ,  $\gamma_a = 0.074$  and  $\beta = 0.15$  (Figure 5.16). As al-

ready found for the polymerized  $C_6MA$ -microemulsion, the polymer radius depends on the amount of monomer in the system and increases from  $R_{hydr} = 13 \pm 1$  nm for  $w_B = 0.01$  to  $R_{hydr} = 18 \pm 1$  nm for  $w_B = 0.03$  at a constant polymerization temperature  $T = 10^\circ\text{C}$ .

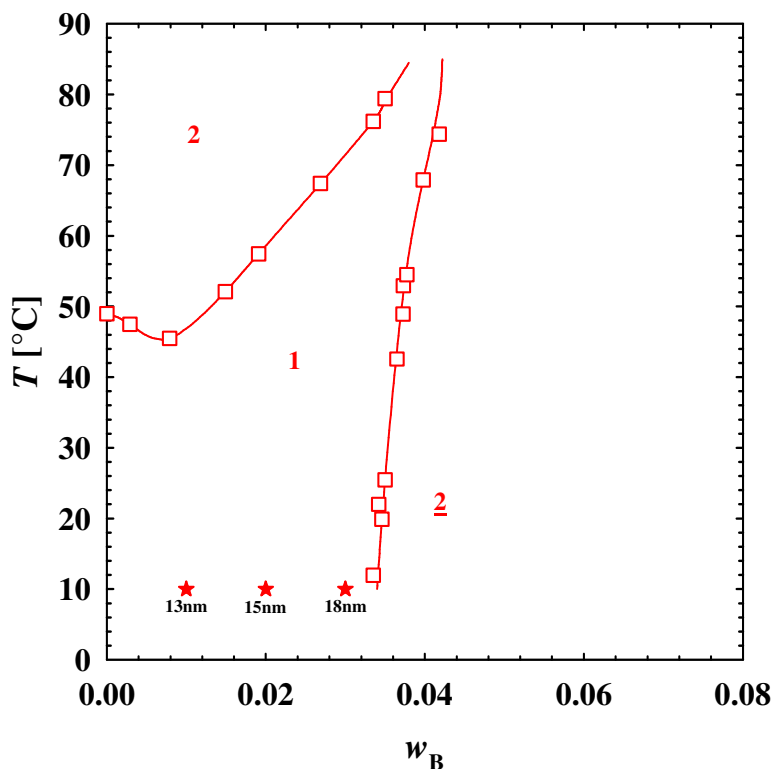


Figure 5.16:  $T(w_B)$ -section of the system  $H_2O/(sucrose/trehalose) - C_{12}MA/EGDMA - Lutensol XL70/Agnique PG 8105-G$  with  $\Psi = 0.75$ ,  $\zeta = 0.38$ ,  $\delta = 0.80$ ,  $\gamma_a = 0.074$  and  $\beta = 0.15$ . The polymerization temperature is kept constant at  $T=10^\circ\text{C}$  and the amount of monomer is increased from  $w_B = 0.01$  to  $w_B = 0.03$ . Therewith, the polymer radius also increases.

In Figure 5.17 the mean hydrodynamic polymer radius obtained polymerizing the system  $H_2O/(sucrose/trehalose) - C_{12}MA/EGDMA - Lutensol XL 70/Agnique PG 8105-G$  with  $\Psi = 0.75$ ,  $\zeta = 0.38$ ,  $\delta = 0.80$ ,  $\gamma_a = 0.074$  and  $\beta = 0.15$  is compared with that obtained for the system  $H_2O/(sucrose/trehalose) - C_6MA/EGDMA - Lutensol XL 70/Agnique PG 8105-G$  with  $\Psi = 0.75$ ,  $\zeta = 0.38$ ,  $\delta = 0.80$ ,  $\gamma_a = 0.074$  and  $\beta = 0.15$  at a polymerization temperature  $T = 10^\circ\text{C}$ . In addition the calculated radius of the unpolymerized droplets is shown. As one can see an overall increase of the size of the obtained polymer particles with increasing  $w_B$  is found. Comparing the hydrodynamic radius obtained polymerizing the  $C_6MA$  as well as the  $C_{12}MA$  microemulsion at  $w_B = 0.03$  a slightly larger  $C_{12}MA$ -particle is observed. Reason for this could be the longer alkyl chain of the  $C_{12}MA$  mono-

mer which could make the polymer stiffer and less flexible leading to the larger particle size.

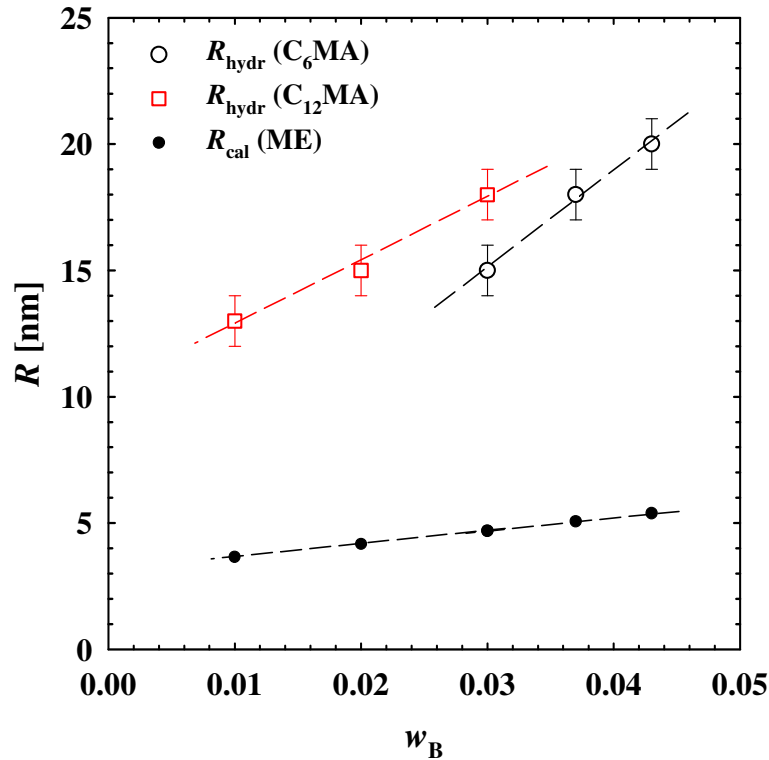


Figure 5.17: The hydrodynamic radius  $R_{\text{hydr}}$  versus the monomer mass fraction within the microemulsion  $w_B$  is compared for the systems  $\text{H}_2\text{O}/(\text{sucrose}/\text{trehalose}) - \text{C}_{12}\text{MA}/\text{EGDMA} - \text{Lutensol XL 70}/\text{Agnique PG 8105-G}$  with  $\Psi = 0.75$ ,  $\zeta = 0.38$ ,  $\delta = 0.80$ ,  $\gamma_a = 0.074$ ,  $\beta = 0.15$  and  $\text{H}_2\text{O}/(\text{sucrose}/\text{trehalose}) - \text{C}_6\text{MA}/\text{EGDMA} - \text{Lutensol XL 70}/\text{Agnique PG 8105-G}$  with  $\Psi = 0.75$ ,  $\zeta = 0.38$ ,  $\delta = 0.80$ ,  $\beta = 0.15$ ,  $\gamma_a = 0.074$ . In addition the calculated radius of the unpolymerized microemulsion droplets are shown. The polymer radius for the system containing  $\text{C}_{12}\text{MA}$  is slightly larger than that containing  $\text{C}_6\text{MA}$ .

## 5.5 SANS and SEM Study of the Droplet Structure

The study of the microstructure by Small Angle Neutron Scattering (SANS) and Scanning Electron Microscopy (SEM) have been exemplarily carried out for the system  $\text{H}_2\text{O}/(\text{sucrose}/\text{trehalose}) - \text{C}_6\text{MA}/\text{EGDMA} - \text{Lutensol XL 70}/\text{Agnique PG 8105-G}$  with  $\Psi = 0.75$ ,  $\zeta = 0.38$ ,  $\delta = 0.80$ ,  $\beta = 0.15$ ,  $\gamma_a = 0.074$  and  $w_B = 0.03$  to prove the results obtained from DLS experiments. The DLS measurements for this sample polymerized at a temperature of  $T = 10^\circ\text{C}$  gave a hydrodynamic radius  $R_{\text{hydr}} = 15 \pm 1$  nm.

To compare the polymer radius with the droplet radius of the unpolymerized microemulsion at  $T = 10^\circ\text{C}$ , first SANS measurements are carried out. Figure 5.19 shows the SANS spectrum by plotting the absolute scattering intensity as a function of the absolute value of the wave vector  $\lambda$ . Both axes are scaled logarithmically. Due to the fact that the isotopes  $^1\text{H}$  (hydrogen) and  $^2\text{H}$  (deuterium) have very different scattering length densities ( $-0.5611 \cdot 10^{10} \text{ cm}^{-2}$  for hydrogen and  $6.3892 \cdot 10^{10} \text{ cm}^{-2}$  for deuterium), contrasts between the single structure elements can be obtained by selective deuteration of one or more components (Figure 5.18). Therefore, measuring in bulk contrast  $\text{H}_2\text{O}$  is replaced by  $\text{D}_2\text{O}$  whereas the oil phase is kept hydrogenised. In this particular case a 75% sugar (also hydrogenised) solution in  $\text{D}_2\text{O}$  is prepared with a total scattering length density of  $3.3596 \cdot 10^{10} \text{ cm}^{-2}$ . Comparing this to the scattering length densities of  $\text{C}_6\text{MA}$  ( $0.34 \cdot 10^{10} \text{ cm}^{-2}$ ) and the surfactant mixture Agnique PG 8105-G/Lutensol XL 70 ( $0.531 \cdot 10^{10} \text{ cm}^{-2}$ ) the contrast adjusted corresponds to bulk contrast conditions.

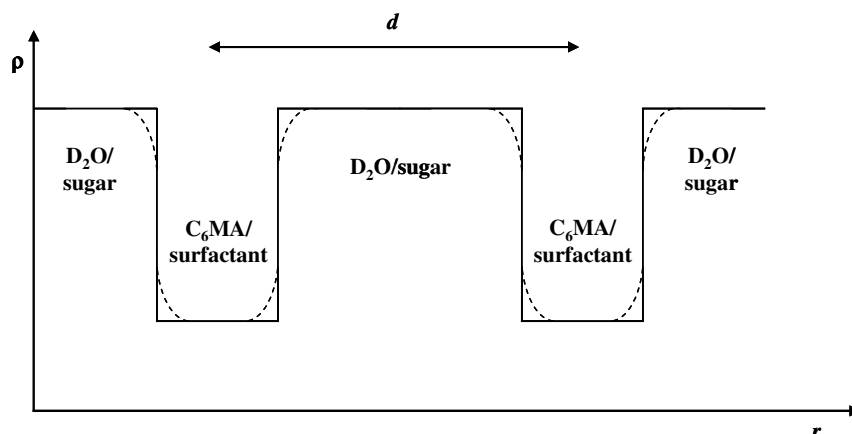


Figure 5.18: Scattering length density profile for the bulk contrast.  $\text{H}_2\text{O}$  is replaced by  $\text{D}_2\text{O}$  whereas the oil and surfactant are kept hydrogenised which gives the contrast. The solid lines indicate the ideal progression of the profile and the dashed line the real one as a diffuse interface between the phases is found altering the rectangular scattering profile to a *Gaussian* profile.

In reality one does not find a clear transition but a diffuse interface between the phases with a high scattering length density and a low scattering length density so that the rectangular scattering profile (solid line in Figure 5.18) alters to a *Gaussian* profile (dashed line in Figure 5.18). One reason for the diffuse profile is that both sub-domains penetrate the interface film.

The scattering curve is fitted assuming a droplet structure which consists of a polydis-

perse *Gaussian* distribution of spheres with a radius  $r$  and a diffuse interface of the thickness  $t$  [175]. In this case the scattering intensity is given by

$$I(q) = \frac{36\pi}{3} \phi r^3 \frac{(\Delta\rho)^2}{(qr)^6} [f(1) + f(2) + f(3) + f(4)] \exp(-q^2 t^2) + I_{\text{incoh}}, \quad (5.2)$$

$$f(1) = \frac{1}{2} [1 - \cos(2qr) \exp(-2\sigma^2 q^2)], \quad (5.3)$$

$$f(2) = -q [r \sin(2qr) + 2q\sigma^2 \cos(2qr)] \exp(-2\sigma^2 q^2), \quad (5.4)$$

$$f(3) = \frac{1}{2} q^2 [-4qr\sigma^2 \sin(2qr) \exp(-2\sigma^2 q^2) + r^2 + \sigma^2], \quad (5.5)$$

$$f(4) = \frac{1}{2} q^2 [r^2 \cos(2qr) \exp(-2\sigma^2 q^2) + \sigma^2 \cos(2qr) \cdot (1 - 4\sigma^2 q^2) \exp(-2\sigma^2 q^2)]. \quad (5.6)$$

$\phi$  is the volume fraction of the scattering microemulsion droplets and  $\Delta\rho$  is the difference in scattering length density between the microemulsion droplets and the hydrophilic D<sub>2</sub>O/sugar phase.  $I_{\text{incoh}}$  is the incoherent scattering of the sample. The red line in Figure 5.19 shows that the fit according to equation (5.2) describes large parts of the scattering curve quantitatively yielding a radius of  $r = 3.3$  nm and a standard deviation of  $\sigma = 0.9$  nm. As one can see at low  $q$ -values a systematic deviation between the scattering curve and model is found. The strong increase of the scattering intensity at low  $q$ -values indicates the existence of structures with larger length scales. Thus, this large scattering intensity could be due to a starting phase separation or H<sub>2</sub>O droplets which are condensed onto the quartz windows of the sample holder due to the lower temperature of the SANS experiment ( $T = 10^\circ\text{C}$ ) or most presumably the existence of cylindrical network structures. Comparing the radius of the microemulsion droplet obtained by SANS measurements ( $r = 3.3$  nm) with the radius obtained from geometrical consideration according to equation (5.1) ( $r_{\text{calc}} = 4.4$  nm) the existence of network structures is most likely.

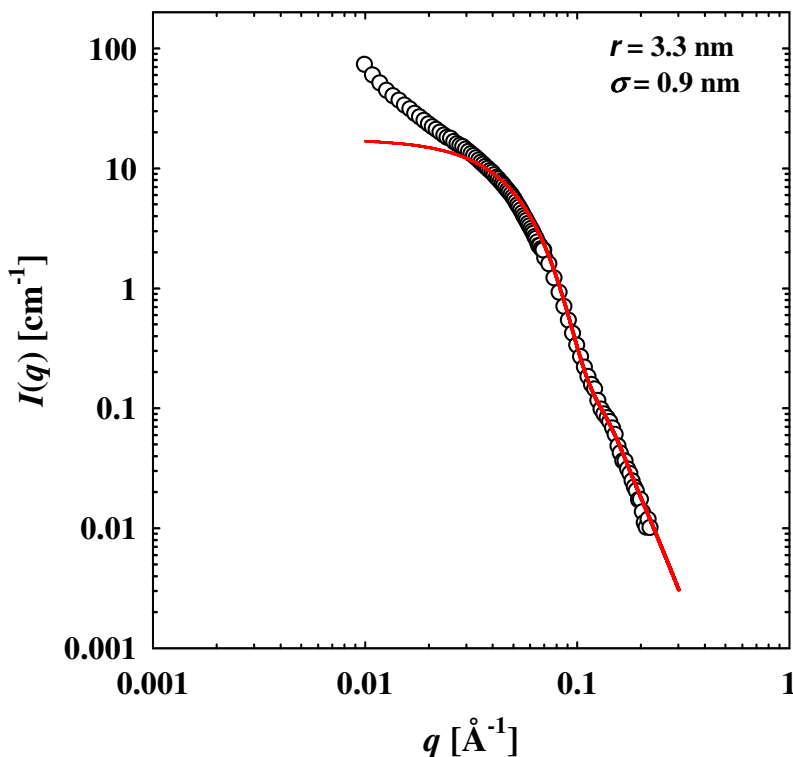


Figure 5.19: SANS-intensity  $I$  plotted versus the scattering vector  $q$  for the unpolymerized sample  $\text{H}_2\text{O}/(\text{sucrose}/\text{trehalose}) - \text{C}_6\text{MA}/\text{EGDMA} - \text{Lutensol XL 70}/\text{Agnique PG 8105-G}$  with  $\Psi = 0.75$ ,  $\zeta = 0.38$ ,  $\delta = 0.80$ ,  $\beta = 0.15$ ,  $\gamma_a = 0.074$  and  $w_B = 0.03$  recorded at  $T = 10^\circ\text{C}$ . The microemulsion droplet radius of  $r = 3.3$  nm with a standard deviation of  $\sigma = 0.9$  nm can be extracted using equation (5.2) to fit the experimental data. The increase of the scattering intensity at low  $q$  is discussed in the text.

The SANS curve of the corresponding polymerized microemulsion droplets is shown in Figure 5.20. As one can see, the fit (dashed red line) according to equation (5.2) describes the data points at low  $q$ -values yielding a polymer radius of  $r = 9.1$  nm with a distribution width of  $\sigma = 2.8$  nm. Bearing in mind that the SANS measurement gives the radius for the polymer without any hydration shell the radius is in good agreement with the hydrodynamic radius of  $R_{\text{hydr}} = 15 \pm 1$  nm obtained by DLS. The data points at higher  $q$ -values can be described taking also the scattering of empty micelles into account which are left after the polymerization process due to the increase of the monomer/polymer droplet radius. Thus, the other dashed red line describes the scattering of empty micelles assuming a radius of  $r = 1.0$  nm. Adding up the scattering contributions of both the empty micelles and the polymer droplets the experimental scattering curve is described quantitatively (blue curve).



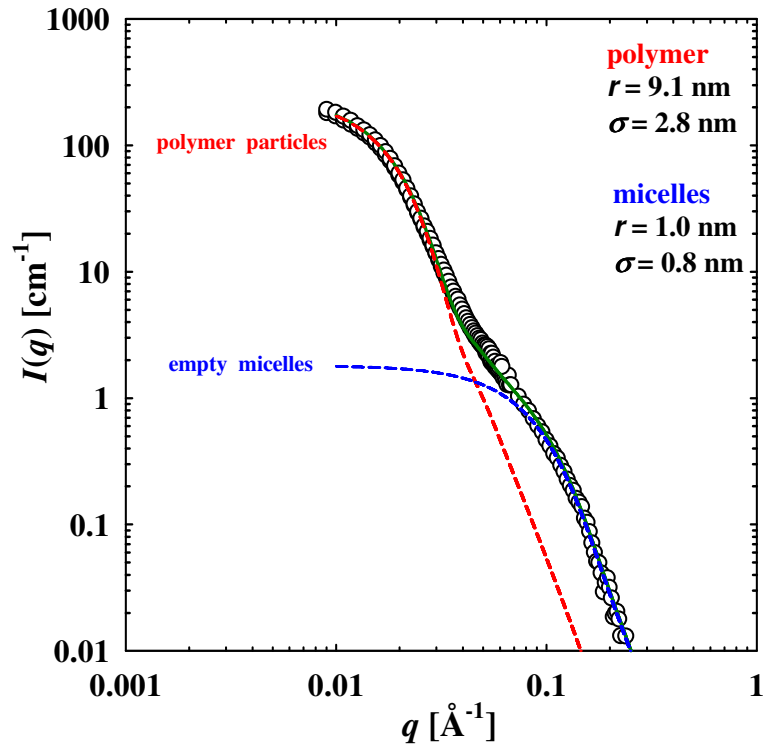


Figure 5.20: The intensity  $I$  plotted versus the scattering vector  $q$  for the polymerized sample  $\text{H}_2\text{O}/(\text{sucrose}/\text{trehalose}) - \text{C}_6\text{MA}/\text{EGDMA} - \text{Lutensol XL 70}/\text{Agnique PG 8105-G}$  with  $\Psi = 0.75$ ,  $\zeta = 0.38$ ,  $\delta = 0.80$ ,  $\beta = 0.15$ ,  $\gamma_a = 0.074$  and  $w_B = 0.03$  polymerized at  $T = 10^\circ\text{C}$ . The fit of the low  $q$ -part of the scattering curve using equation (5.2) gives a radius of the polymer droplets of  $r = 9.1$  nm with a distribution width of  $\sigma = 2.8$ . Fitting the large  $q$ -part of the scattering curve provides the radius of the empty micelles of  $r = 1.0$  nm. Adding these two fits (blue curve) a quantitative description of the experimental data points is obtained.

Figure 5.21 shows a SEM image of the corresponding system  $\text{H}_2\text{O}/(\text{sucrose}/\text{trehalose}) - \text{C}_6\text{MA}/\text{EGDMA} - \text{Lutensol XL 70}/\text{Agnique PG 8105-G}$  with  $\Psi = 0.75$ ,  $\zeta = 0.38$ ,  $\delta = 0.80$ ,  $\beta = 0.15$ ,  $\gamma_a = 0.074$  and  $w_B = 0.03$  polymerized at  $T = 10^\circ\text{C}$ . For the SEM measurement exactly the same sample as for the DLS experiment is used, even with the same dilution (1:12). The big underlying structure seen in Figure 5.21 is formed by a frozen sugar solution which concentration is increased during the cryo-sublimation process [176]. The sublimation time is chosen to be 3 minutes by which the holes in the underlying structure are caused. Having a closer look at the underlying structure one can find a lot of small, bright droplets being the polymer particles.

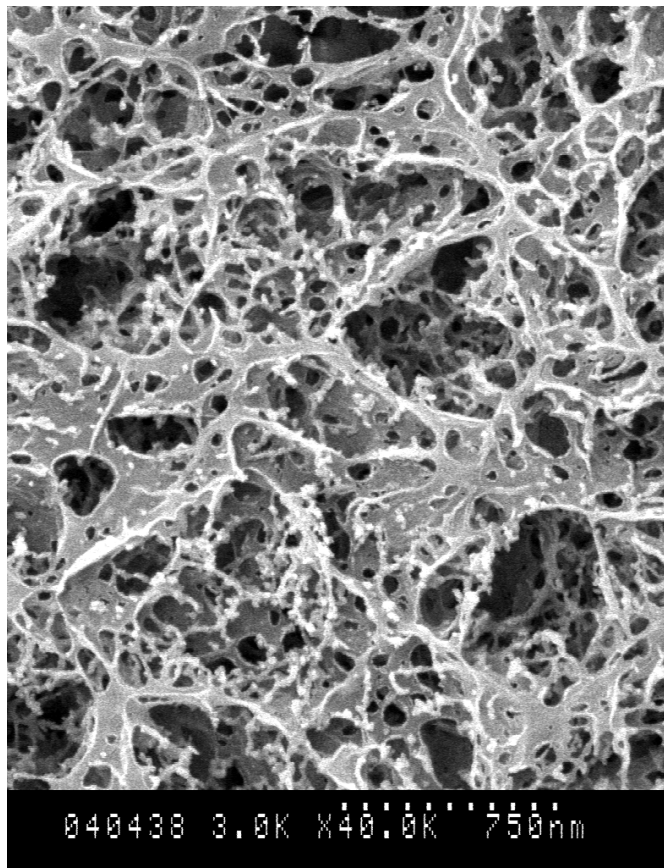


Figure 5.21: SEM image of the sample  $\text{H}_2\text{O}/(\text{sucrose}/\text{trehalose}) - \text{C}_6\text{MA}/\text{EGDMA} - \text{Lutensol XL70}/\text{Agnique PG 8105-G}$  with  $\Psi = 0.75$ ,  $\zeta = 0.38$ ,  $\delta = 0.80$ ,  $\beta = 0.15$ ,  $\gamma_a = 0.074$  and  $w_B = 0.03$  polymerized at  $T = 10^\circ\text{C}$ . The underlying structure is formed by a frozen sugar solution which concentration is increased during the cryo-sublimation process. On the underlying structure one finds small, bright droplets being the polymer particles.

For closer inspection of the polymer droplets a SEM image with higher magnification is taken. Figure 5.22 shows that the polymer particles are all of the same size and have a spherical shape. Therewith, the application of the *Stokes-Einstein* equation requiring spherical objects is justified for the analysis of the DLS experiments. This result is also consistent with the fact that the linear fit for the decay rate  $\Gamma$  plotted versus  $q^2$  (Figure 5.9 top) passes through the origin. The radius of the polymer droplets extracted from the SEM image is around  $r \approx 10$  nm and compares very well with the radius obtained by SANS. However, in Figure 5.22 one does not only find single droplets but also aggregated droplets. As there is no sign of larger elongated structures in the SANS scattering curve of the polymerized sample aggregation might take place during the freezing process or during the sublimation.

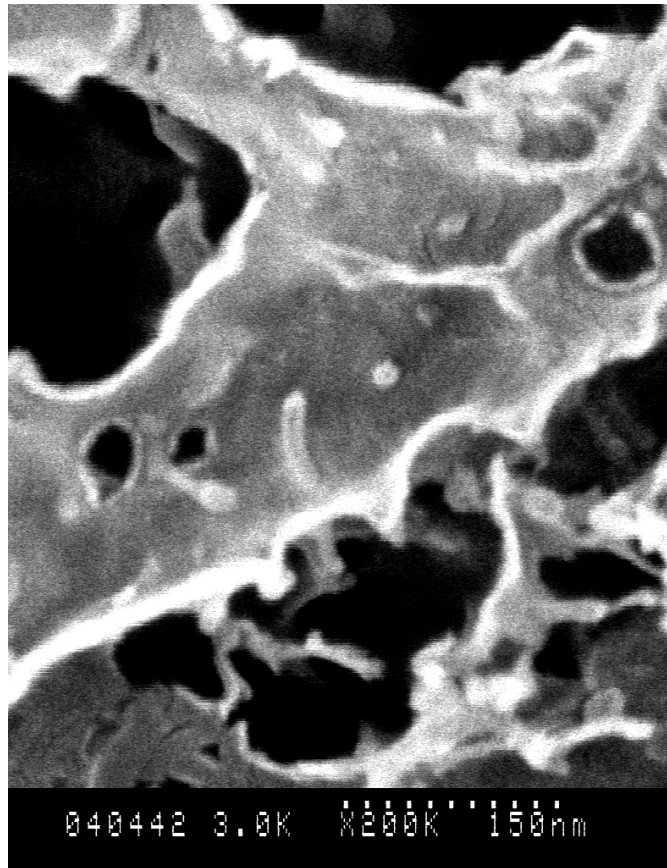


Figure 5.22: SEM image of the system  $\text{H}_2\text{O}/(\text{sucrose}/\text{trehalose}) - \text{C}_6\text{MA}/\text{EGDMA} - \text{Lutensol XL 70}/\text{Agnique PG 8105-G}$  with  $\Psi = 0.75$ ,  $\zeta = 0.38$ ,  $\delta = 0.80$ ,  $\beta = 0.15$ ,  $\gamma_a = 0.074$  and  $w_B = 0.03$  polymerized at  $T = 10^\circ\text{C}$  in magnification. One can see polymer particles with a radius  $r \approx 10$  nm which agrees well with the radius obtained from SANS.



## 6 Polymerization of Bicontinuously Structured Microemulsions

This chapter deals with the polymerization of bicontinuous microemulsions. Starting with a literature overview (section 6.1), the structure of the unpolymerized bicontinuous microemulsion system containing a 75% sugar solution, hexyl methacrylate as monomer and the surfactant is investigated in section 6.2. Subsequently, in section 6.3 the structure of the corresponding polymerized system is examined. In the following, the influence of cross-linker in the monomer phase (section 6.4) as well as the influence of the monomer's hydrophobicity on the polymer structure is studied in section 6.5.

### 6.1 State of the Art

The preparation of novel solid nanomaterials with a large interface is a huge field for applications such as microfiltration, separation membranes or their supports, microstructured polymer blends and porous microcarriers for the culture of living cells and enzymes [23]. Because of its large variety of microstructures microemulsions are extensively used as templates for the synthesis of such nanomaterials.

In their pioneering work, *Stoffer* and *Bone* studied the phase behavior of microemulsion systems containing sodium dodecylsulfate / pentanol / methyl methacrylate or methyl acrylate / water before and after polymerization [24-26] and investigated the phase separation during the polymerization of the continuous microemulsion phase. *Gan* and *Chew* reproduced the previous experiments of *Stoffer* and *Bone*, and confirmed that transparent PMMA mixtures could not be fully polymerized in situ by using pentanol as co-surfactant. *Gan* and *Chew* subsequently replaced pentanol with the hydrophilic and polymerizable co-surfactant acrylic acid and observed the formation of transparent, solid copolymers but without any distinguishable microstructure [29]. Similar investigations have been carried

out by *Raj et al.* using either acrylic acid or methacrylic acid as polymerizable co-surfactants in a methyl methacrylate / ethylene glycol dimethacrylate / sodium dodecylsulfate / water system [33,177]. A close correlation was found between the microstructures of the polymeric material and the nature of the initial microemulsion. Polymerizing a water-in-oil droplet microemulsion structure yields solids with a closed cell porous structure, whereas open-cell porous polymeric solids are obtained by the polymerization of microemulsions with a bicontinuous structure [177]. These results indicate that the morphology of the polymer keeps some memory of the initial structure since their structure is retained to a certain extent. However, the length scale of the porous structure obtained (1-4  $\mu\text{m}$ ) was considerably larger than the length scale characteristic of microemulsions (less than 0.1  $\mu\text{m}$ ), due to phase separation effects or structural changes during polymerization. *Gan* and *Chew* extended their studies to microemulsions in which all the components except water were polymerizable. Polymerization in microemulsions containing a polymerizable surfactant, co-surfactant and methylmethacrylate as the continuous phase, led, under certain conditions, to transparent solid terpolymers with up to 10 – 20% water dispersed in the polymer matrices but as in the case of copolymers, these terpolymers did not represent any particular structure [27,30]. *Cheung et al.* slightly modified *Gan* and *Chew*'s starting system containing sodium dodecylsulfate / pentanol / methyl methacrylate by adding a bifunctional cross-linker agent [31,35,178] with the results indicating that the permeability of the produced membranes is dependent on the composition of the precursor microemulsion. *Antonietti* and *Hentze* showed that a bicontinuous microemulsion containing styrene, acrylic acid and water polymerizes as porous gel after several phase transitions where the composition of the monomer system only indirectly affects the topology. Structures in the range of 50 nm to 2  $\mu\text{m}$  are found [179]. In 1998 *Gan et al.* synthesized transparent bicontinuous nanostructured polymeric materials where the use of polymerizable zwitterionic surfactants has been the key factor to the success of a stable polymerization [140].

The incorporation of cross-linking agents increases the system's viscosity and makes it easier to capture diameters close to those of the precursor microemulsion. Polymerizable surfactants can preserve the interfacial network of the microstructure during polymerization and have been demonstrated to be the most effective method to save the nanostructures of the underlying microemulsions [180].

At high surfactant mass fractions often lamellar phases can be found within the one-phase region of a microemulsion. Acrylamide for example has not only been solubilized

and polymerized in amounts up to 25% inside isotropic bicontinuous microemulsions [181-183] but also in birefringent microemulsions [37]. In both cases, the initial structure of the microemulsion is not preserved during polymerization and the final system consists of a dispersion of spherical latex particles. *Antonietti et al.* showed that the product of the polymerization of a lyotropic phase does not have to be a dispersion of polymer droplets. The gel structure is not cast of the original mesophase architecture, but exhibits structure elements 2 or 3 orders of magnitude larger than those addressed by the lyotropic assembly structure [184,185]. *Meier* showed that the droplet and the lamellar liquid crystalline phase of a pentaethylene glycol monododecyl ether / decane / water system can be used as a matrix to create new amphiphilic polymer network structures from  $\alpha,\omega$ -hydrophobically modified poly(oxyethylene) bearing polymerizable end groups and hydrophobic comonomers. During free radical polymerization of the end group functionalized polymers the microemulsion structure is preserved [186]. In 2004 *Tieke et al.* polymerized lyotropic phases upon gamma-irradiation. Small angle X-ray scattering and polarizing microscopy indicated that the hexagonal and cubic phases were preserved upon polymerization whereas the lamellar phase disappeared [187]. The use of surfactant mesophases such as vesicular and lyotropic mesophases as templates for the preparation of nanostructured polymers by polymerization is reviewed by *Yan and Texter* in 2006 [188].

*Co et al.* proposed in 2004 for the first time an alternative approach to overcome template rearrangement by using solid microemulsion glasses [41]. The central point of this approach is the replacement of water in traditional microemulsions with sugar to form solid microemulsions with bicontinuous domains of hydrophobic monomers and glassy sugar whose robust nanostructures can hold up against forces that arise during polymerization [42]. In 2006 *Co et al.* published for the first time the polymerization in bicontinuous microemulsion glasses without any phase separation [42].

Contrary to *Co et al.* [38] we found a strong dependence of the phase behavior on the sugar concentration within the hydrophilic phase (chapter 4). Therefore, we did not desiccate our microemulsion systems to the anhydrous glassy state but investigated if the increase in viscosity by replacing water with a 75% sugar solution slows down the microemulsion reorganization kinetics sufficiently that the system can be polymerized without phase separation. As the aim is to polymerize the bicontinuous microemulsion structure simple and inexpensive, Irgacure 819 is used as initiator.

## 6.2 The Unpolymerized System H<sub>2</sub>O/sugar – C<sub>6</sub>MA - surfactant

As already mentioned, the  $T(\gamma)$ -sections of the system H<sub>2</sub>O/(sucrose/trehalose) – C<sub>6</sub>MA/ethylene glycol dimethacrylate – Agnique PG 264-G at  $\alpha = 0.4125$ ,  $\Psi = 0.75$ ,  $\zeta = 0.38$  and varying amounts of cross-linker in the monomer phase do not have the familiar “fish”-shape (chapter 4). Therefore, structure investigations must be carried out to make sure that the present system is a microemulsion and to determine its microstructure more precisely.

One indication for the existence of a microemulsion is the three-phase region at low  $\gamma$  values. To investigate its occurrence, phase separation has to be awaited. The system H<sub>2</sub>O/(sucrose/trehalose) – C<sub>6</sub>MA/EGDMA – Agnique PG 264-G at  $\alpha = 0.4125$ ,  $\Psi = 0.75$ ,  $\zeta = 0.38$  and  $\beta = 0.50$  is chosen as phase separation proceeds faster at high temperatures and its temperature  $\tilde{T}$  is found at values being  $\Delta\tilde{T} = 14^\circ\text{C}$  higher than the temperature  $\tilde{T}$  for the system without any cross-linker in the monomer phase.

The red stars in Figure 6.1 indicate the compositions of the microemulsion samples where the phase state has been investigated. Due to the high viscosity of the sample no phase separation can be observed. As can be seen in the photo (Figure 6.1) the monomer starts polymerizing before any phase separation has occurred so that the white solid polymer sticks out of the top of the sample surface.



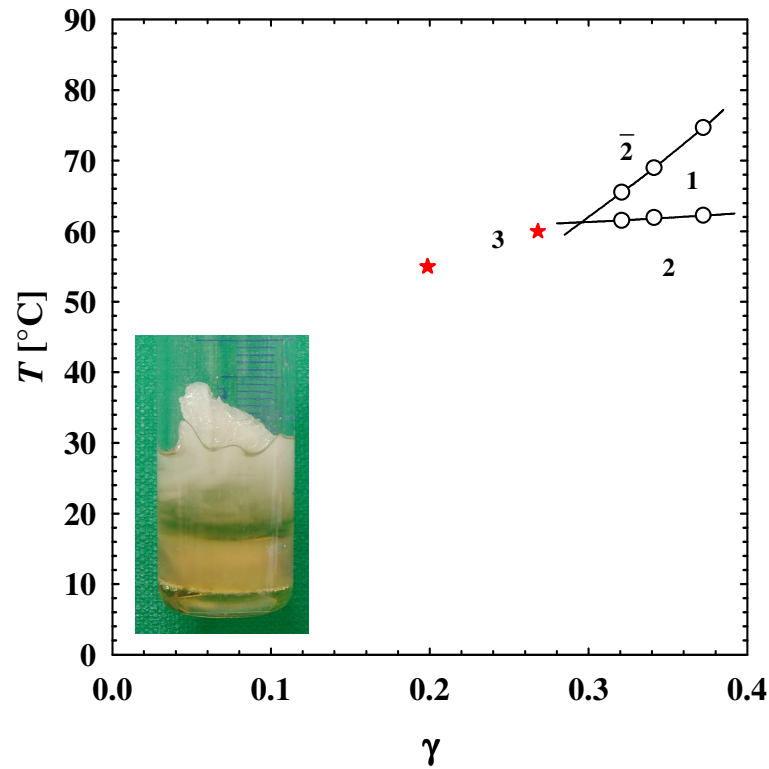


Figure 6.1:  $T(\gamma)$ -section of the system  $\text{H}_2\text{O}/(\text{sucrose}/\text{trehalose}) - \text{C}_6\text{MA}/\text{EGDMA} - \text{Agnique PG 264-G}$  with  $\alpha = 0.4125$ ,  $\beta = 0.50$ ,  $\Psi = 0.75$  and  $\zeta = 0.38$ . The red stars indicate the sample compositions for the investigation of the phase state. The photo shows the sample after 1 month of waiting for phase separation.

Since phase separation experiments cannot prove the existence of a microemulsion, other techniques such as SANS and TEM measurements are used to study the system's structure. For this purpose the system  $\text{H}_2\text{O}/(\text{sucrose}/\text{trehalose}) - \text{C}_6\text{MA} - \text{Agnique PG 264-G}/\text{Lutensol AO 8}$  at  $\alpha = 0.4125$ ,  $\delta = 0.93$ ,  $\Psi = 0.75$  and  $\zeta = 0.38$  is selected since this system is later polymerized. The red star in Figure 6.2 indicates the composition of the system ( $\gamma = 0.12$ ) characterized by SANS and TEM as well as polymerized later on.

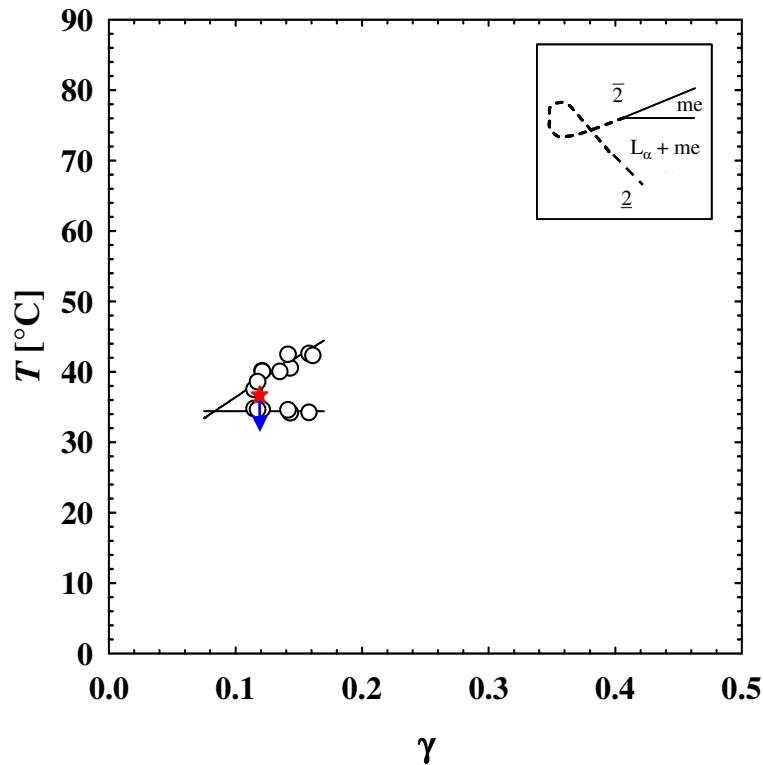


Figure 6.2:  $T(\gamma)$ -section of the system  $\text{H}_2\text{O}/(\text{sucrose/trehalose}) - \text{C}_6\text{MA} - \text{Agnique PG 264-G/Lutensol AO 8}$  at  $\alpha = 0.4125$ ,  $\delta = 0.93$ ,  $\Psi = 0.75$  and  $\zeta = 0.38$ . The red star indicates the sample's composition for the following SANS and TEM measurements as well as the polymerization.

Figure 6.3 shows the SANS spectrum of the microemulsion consisting of  $\text{D}_2\text{O}/(\text{sucrose/trehalose}) - \text{C}_6\text{MA} - \text{Agnique PG 264-G/Lutensol AO 8}$  by plotting the absolute scattering intensity as a function of the absolute value of the wave vector  $q$  in a double logarithmic plot. Discussing the scattering curve in Figure 6.3 qualitatively, this spectrum looks identical to other spectra known for bicontinuous microemulsions from literature. One finds a maximum at low values of the scattering vector  $q$ , the so-called correlation peak, followed by a strong decrease of the intensity to the incoherent background  $I_{\text{incoh}}$  at high  $q$ -values. A distinct peak is equivalent to an increase in structure correlation and a shift to lower  $q$ -values with a larger microstructure. The decrease of the intensity for high  $q$ -values is proportional to  $q^{-4} \cdot e^{-q^2 t^2}$  with  $t$  characterizing the diffusivity of the internal amphiphilic film [189].

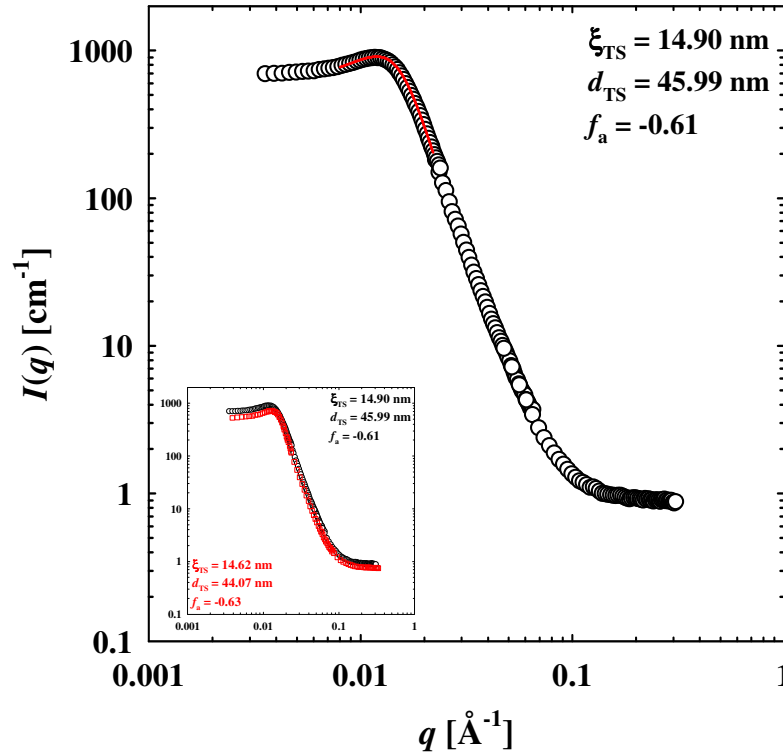


Figure 6.3: The intensity  $I$  is plotted versus the scattering vector  $q$  for the system  $D_2O$ /(sucrose/trehalose) –  $C_6MA$  – Agnique PG 264-G/Lutensol AO 8 at  $\alpha = 0.4125$ ,  $\delta = 0.93$ ,  $\Psi = 0.75$ ,  $\zeta = 0.38$  and  $T = 36.5^\circ\text{C}$ . The measurements shown by the black symbols are carried out at the Forschungsneutronenquelle Heinz Maier-Leibnitz in Garching whereas the measurements indicated by the the red symbols are done at the ILL in Grenoble. In both cases, the composition of the sample is the same.

The quantitative analysis of the SANS spectrum is shown by the red curve in Figure 6.3. The characteristic structure size of a bicontinuous microemulsion in bulk contrast can be determined by analyzing the region of the scattering maximum using the *Teubner-Strey* formula

$$I(q) = \frac{8\pi c_2 \phi_a \phi_b (\Delta\rho)^2}{\xi_{TS} \cdot (a_2 + c_1 q^2 + c_2 q^4)} + I_{\text{incoh}} \quad (6.1)$$

where  $\Delta\rho$  is the scattering length density difference between the two sub-phases  $a$  and  $b$ ,  $\phi_a$  and  $\phi_b$  are the respective volume fractions and the parameters  $a_2$ ,  $c_1$  and  $c_2$  stem from a *Landau-Ginzburg* order parameter expansion of the local free energy density [190]. Equation (6.2) is obtained by the Fourier transformation of a correlation function of the scattering length density, which combines the periodic alternation of the water-containing and oil-containing domains as well as the absence of long-range order. The parameters in equation (6.1) define the periodicity

$$d_{\text{TS}} = \left( \frac{1}{2} \left( \frac{a_2}{c_2} \right)^{1/2} - \left( \frac{c_1}{4c_2} \right) \right)^{-1/2} \quad (6.2)$$

as well as the correlation length

$$\xi_{\text{TS}} = \left( \frac{1}{2} \left( \frac{a_2}{c_2} \right)^{1/2} + \left( \frac{c_1}{4c_2} \right) \right)^{-1/2}. \quad (6.3)$$

The periodicity measures the average length of a single water-water and oil-oil periodicity respectively, whereas the correlation length is a measure for the length scale on which the quasi-periodical order and the film-film correlation is lost [191-193].

Another way to formulate the *Teubner-Strey* equation is

$$I(q) = \frac{I_0}{\left( 1 + \frac{I_0}{I_{\text{max}}} \right) \left( \frac{q^2}{q_{\text{max}}^2} - 1 \right)^2 + \frac{I_0}{I_{\text{max}}}} + I_{\text{incoh}} \quad (6.4)$$

including the intensities obtained from the measurements as well as the incoherent background  $I_{\text{incoh}}$ . With the help of equation (6.5) the typical peak known for bicontinuous microemulsions is described very well.

In order to quantify the amphiphilic strength it has been proven useful to formulate the amphiphilicity factor  $f_a$

$$f_a = \frac{c_1}{\sqrt{4a_2c_2}} \quad (6.5)$$

indicating if a strongly structured microemulsion is on hand. This value correlates with the ratio of the periodicity  $d_{\text{TS}}$  and the correlation length  $\xi_{\text{TS}}$  [194]. For a lamellar or a hexagonal liquid crystalline phase a value of  $f_a = -1$  is expected. In general, the more positive the value of  $f_a$  the less the mixture is structured. If  $f_a$  reaches a value of  $f_a = 1$  a homogeneous mixture without a microstructure is on hand. For a bicontinuous microemulsion with well ordered structures of typically long-chained surfactant films the amphiphilicity factor usually ranges from  $f_a = -0.85$  to  $f_a = -0.70$ .

As already mentioned, the SANS spectrum shown in Figure 6.3 looks similar to spectra known for bicontinuous microemulsions. Therefore, the region of the maximum is fitted using the *Teubner-Strey* formula (red curve). One obtains a value for the periodicity of  $d_{\text{TS}} = 45.99$  nm. Since  $d_{\text{TS}}$  gives the periodicity of the water or oil domains the size of each domain is about  $d_{\text{TS}}/2 \approx 23$  nm. As one can see from the amphiphilicity factor  $f_a = -0.61$

the microemulsion is not very well structured. In the inlet the scattering curve (black symbols) taken at the Forschungsneutronenquelle Heinz Maier-Leibnitz in Garching is compared to the scattering curve (red symbols) taken at the ILL in Grenoble. The measurements are carried out for samples of the same composition. It is truly astonishing that the data measured with different neutron sources and setups are agreeing that well.  $I_{\max}$  is only slightly shifted to lower values for the scattering curve taken at the ILL as well as  $q_{\max}$  is slightly shifted to higher  $q$ -values.

For direct investigations of the microstructure and to prove the results obtained by the SANS measurements electron microscopy images have been taken for the system  $\text{H}_2\text{O}/(\text{sucrose}/\text{trehalose}) - \text{C}_6\text{MA} - \text{Agnique PG 264-G}/\text{Lutensol AO 8}$  at  $\alpha = 0.4125$ ,  $\delta = 0.93$ ,  $\Psi = 0.75$ ,  $\zeta = 0.38$  and  $\gamma = 0.12$  (Figure 6.4). In this work, the freeze fracture electron microscopy technique developed by *Jahn* and *Strey* is used [62]. The preparation technique allows freezing the microemulsion with its underlying structure at a certain temperature extremely quick. The microstructure of the sample is then imaged indirectly by shadowing the fractured sample film with tantalum/tungsten and carbon. Water and oil can be discriminated by a decoration effect of the shadow material on the oil fracture face. Whereas the oil phase is coarse-grained, the water phase is fine-grained. The decoration effect is caused by differing nucleation probabilities and surface mobilities on the various substrates and should not be mistaken for a real microstructure [61]. In most cases the fraction through the water domains is planar, whereas for the oil domains it is along the amphiphilic layer. This difference leads to a three-dimensional impression of the oil phase. Also the roughness of the replica caused by the underlying microemulsion structure leads to a three-dimensional impression of the sample.

Looking at Figure 6.4 one finds instead of a bicontinuously structured microemulsion a rather lamellar structured phase: The multilayer structures are typical for the lamellar phase and easily recognized (yellow squares). The distance of each lamellar layer is in average about 10 nm.



Figure 6.4: FFEM image of the system  $\text{H}_2\text{O}/(\text{sucrose}/\text{trehalose}) - \text{C}_6\text{MA} - \text{Agnique PG 264-G}/\text{Lutensol AO8}$  with  $\alpha = 0.4125$ ,  $\delta = 0.93$ ,  $\Psi = 0.75$ ,  $\zeta = 0.38$  and  $\gamma = 0.12$ . Not the expected bicontinuous structure but a lamellar phase is found.

Reason for the unexpected lamellar phase might be the temperature decrease during the sample preparation which leads to a change in the microstructure. As indicated in Figure 6.2 by the red star the sample preparation should have been occurred at a temperature  $T = 37^\circ\text{C}$ . During the sample preparation probably a shift in the temperature to lower values occurred (marked by the blue arrow) so that the two-phase region is reached where a lamellar phase coexisting with a microemulsion phase is found as shown in the inset. Further details concerning the phase behavior are given in chapter 4.

To prove the results of coexisting lamellar and bicontinuous phases as obtained by TEM, SANS experiments are carried out for the same microemulsion sample as used to investigate the bicontinuous structure (Figure 6.3), but only at a temperature just below the one-phase region. The scattering curve for the sample consisting of  $\text{D}_2\text{O}/(\text{sucrose}/\text{trehalose}) - \text{C}_6\text{MA} - \text{Agnique PG 264-G}/\text{Lutensol AO 8}$  is shown in Figure 6.5 by plotting the scattering intensity as a function of the absolute value of the wave vec-

tor. Comparing the scattering curves in Figure 6.3 for a bicontinuously structured microemulsion and the one in Figure 6.5, one finds in both cases the for a bicontinuous microemulsion typical correlation peak at low  $q$ -values. In the case of Figure 6.5 the following  $q^{-4}$  decrease is interrupted by a second peak at intermediate  $q$ -values.

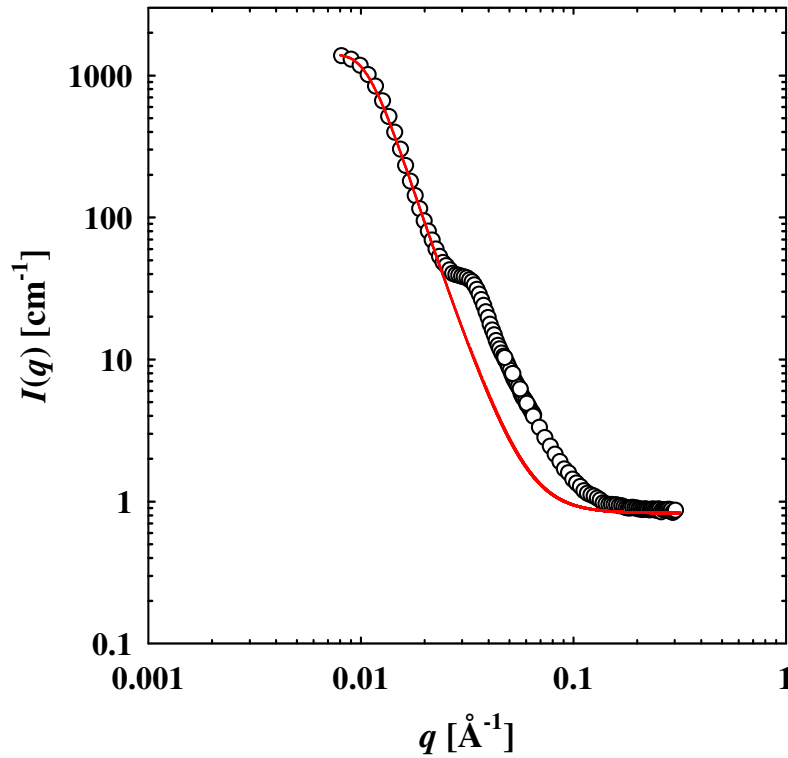


Figure 6.5: The intensity  $I$  is plotted versus the scattering vector  $q$  for the system  $D_2O$ /(sucrose/trehalose) –  $C_6MA$  – Agnique PG 264-G/Lutensol AO 8 at  $\alpha = 0.4125$ ,  $\delta = 0.93$ ,  $\Psi = 0.75$ ,  $\zeta = 0.38$  and at a temperature  $T = 33^\circ C$  just below the one-phase region. At low  $q$ -values the typical peak of bicontinuously structured microemulsions is found which is fitted using the *Teubner-Strey* formula (red curve). The peak at intermediate  $q$ -values indicates the coexistence of a lamellar phase.

The scattering curve is fitted by the *Teubner-Strey* formula yielding  $d_{TS} = 68.74$  nm,  $\xi_{TS} = 20.29$  nm and  $I_{incoh} = 0.83$  (red curve). Subtracting the red curve from the scattering curve should yield the scattering fraction of the coexisting lamellar phase. Figure 6.6 shows a detail of Figure 6.5 displaying the overall scattering curve (black circles) and the *Teubner-Strey* fit (red line). The black squares show the remaining scattering data after subtracting the values of the *Teubner-Strey* fit from the original SANS data. For a clearer view of the peak a linear scale of the intensity  $I$  and the wave vector  $q$  is chosen.

The lamellar peak is fitted (blue curve) using the *Nallet et al.* fit [195]. With the help of a model combining geometry of the bilayers and layer displacement fluctuations, the scat-

tering spectrum of a lyotropic lamellar phase is described quantitatively. As geometrical model a finite-size crystal of a lyotropic lamellar phase is described as the regular stacking – period  $d$  – of  $N$  identical layers of the thickness  $\delta$ . However, the purely geometric model fails for describing the features of the scattering spectrum that are related to thermal fluctuations. These features are the broad shape of the Bragg peak and the occurrence of an anisotropic small angle scattering. The *Caillé* model takes into account properly the thermodynamics of a lyotropic lamellar phase and describes rigorously these two features [196]. *Nallet et al.* combined the relevant features of the previous two models, i.e. taking into account consistently both the geometry – the finite thickness of the membrane – and the thermodynamics – the layer displacement fluctuations. Using this new model, the form factor  $P(q)$  is given by

$$P(q) = \frac{2\Delta\rho^2}{q^2} \left[ 1 - \cos(q\delta) e^{-q^2\sigma^2/2} \right] \quad (6.6)$$

with  $\Delta\rho$  being the contrast between the hydrophobic and hydrophilic part.  $\delta$  is the geometric thickness of the layer. As the sugar surfactant Agnique PG 264-G has a surfactant chain length of 12 – 14 carbons, a geometric thickness of  $\delta = 12 \text{ \AA}$  is chosen [50,115].  $\sigma$  is fixed at  $\delta/4$  [195]. Approximating the effect of a finite resolution, this yields the following expression for the resolution-limited structure factor  $S(q)$

$$S(q) = 1 + 2 \sum_1^{N-1} \left( 1 - \frac{n}{N} \right) \cos \left( \frac{qdn}{1 + 2\Delta q^2 d^2 \alpha(n)} \right) \cdot e^{-\frac{2q^2 d^2 \alpha(n) + \Delta q^2 d^2 n^2}{2(1 + \Delta q^2 d^2 \alpha(n))}} \cdot \frac{1}{\sqrt{1 + 2\Delta q^2 d^2 \alpha(n)}} \quad (6.7)$$

$\alpha(n)$  denotes the correlation function  $\langle (u_n - u_0)^2 \rangle / 2d^2$  and  $\Delta q^2$  is the resolution function. The resolution function is taken from [197] and transformed into the shape as shown in [198].  $L_1$  is the distance to the detector (8 m),  $L_2$  the distance to the collimator (8 m),  $\lambda$  the wave length ( $\lambda = 4.5 \text{ \AA}$ ) and  $\Delta\lambda/\lambda$  is given by  $\Delta\lambda/\lambda = 0.2$  [199]. Whereas the form factor  $P(q)$  is a slowly varying function the structure factor  $S(q)$  is sharply peaked and has much stronger variations.

Fitting now the lamellar peak with the help of the *Nallet et al.* fit, one obtains a spacing of the water domains of  $d = 18.08 \text{ nm}$ . Nearly the same value is obtained by calculating the spacing via  $d = 2\pi/q_{\max}$ ;  $q_{\max} = 0.0334$  is indicated by the blue star. This leads to a spacing of the amphiphilic surfactant layers of  $d/2 = 9.04 \text{ nm}$  of each layer which is in good agree-



ment with the data obtained by TEM.

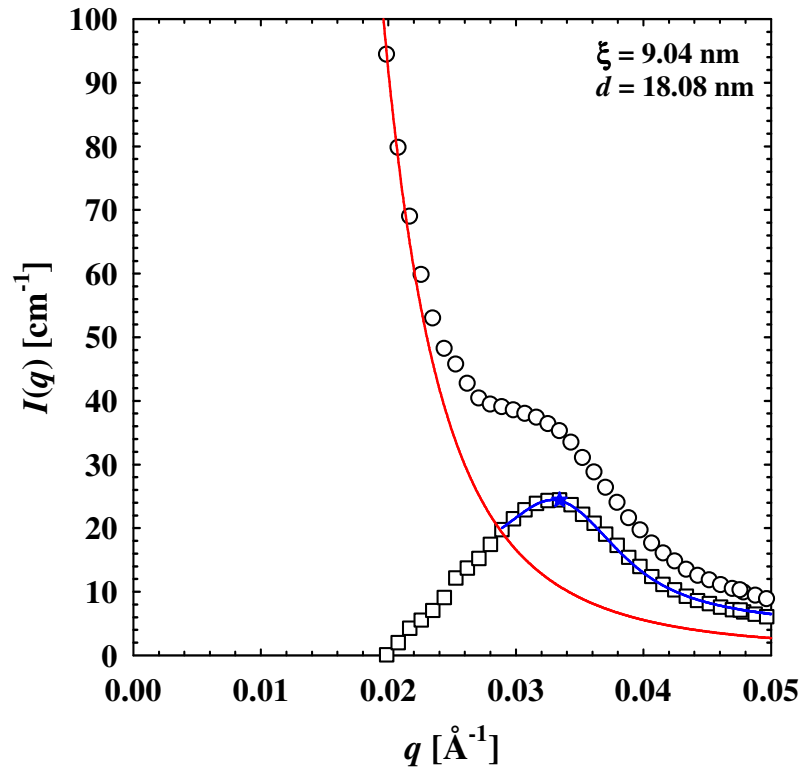


Figure 6.6: Original SANS scattering curve (black circles) for the system  $\text{D}_2\text{O}/(\text{sucrose}/\text{trehalose}) - \text{C}_6\text{MA} - \text{Agnique PG 264-G}/\text{Lutensol AO 8}$  at a temperature just below the one-phase region plotted in a linear scale to point out the peak caused by the lamellar phase clearer. The black squares show the scattering curve after subtracting the values for the *Teubner-Strey* fit (red curve) from the original SANS data. To obtain the lamellar spacing the *Nallet et al.* fit (blue curve) is used. The blue star gives the value for  $q_{\text{max}}$  to calculate the lamellar spacing also from  $d = 2\pi/q_{\text{max}}$ .

### 6.3 The Polymerized System $\text{H}_2\text{O}/\text{sugar} - \text{C}_6\text{MA} - \text{surfactant}$

As known from the structure investigations of the unpolymerized system  $\text{H}_2\text{O}/(\text{sucrose}/\text{trehalose}) - \text{C}_6\text{MA} - \text{Agnique PG 264-G}/\text{Lutensol AO 8}$  at  $\alpha = 0.4125$ ,  $\delta = 0.93$ ,  $\Psi = 0.75$ ,  $\zeta = 0.38$  and  $\gamma = 0.12$ , after polymerization a bicontinuous polymer structure with a domain size of  $d_{\text{TS}}/2 \approx 23 \text{ nm}$  is expected. Since the sample becomes milky during the polymerization process phase separation must occur. However, after the

polymerization is completed the sample appears clear since poly-hexyl methacrylate and the 75% sugar solution have the same refractive index. Due to an increase of the monomer's hydrophobicity during polymerization the phase behavior is shifted to higher temperatures. Therefore, in case the original underlying structure can be copied to the polymer structure, not only a bicontinuous structure but also an anisotropic lamellar structure with a thickness of  $d/2 \approx 9.4$  nm for each lamellar layer can be expected as the lamellar phase region is passed during the polymerization process.

The investigation of any birefringent phase is done with the help of a polarizing microscope. Two polarizers, one located underneath the object slide and one at the top and turned by  $90^\circ$ , let only light pass if the sample is able to turn the plane of the light. As one can see in Figure 6.7 the sample obtains numerous birefringent phases indicated by the maltese crosses which are disrupted by isotropic phases. This leads to the assumption that lamellar phases coexist with bicontinuous ones. The sizes of the birefringent phases vary as can be detected from the different sizes of the maltese crosses. At the left top corner no coexistence of a birefringent and isotropic phase can be found since there are no maltese crosses. This leads to the assumption that phase separation might have occurred here.

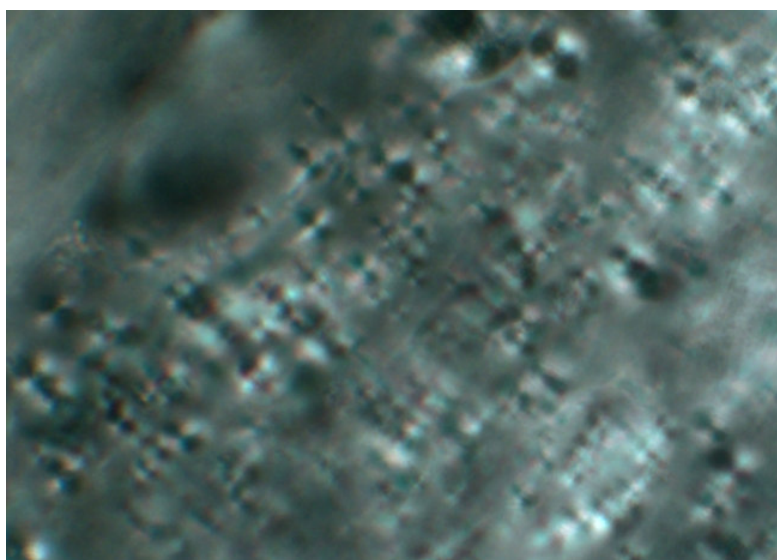


Figure 6.7: Picture taken with the polarizing microscope of the polymerized system  $\text{H}_2\text{O}/(\text{sucrose}/\text{trehalose}) - \text{C}_6\text{MA} - \text{Agnique PG 264-G}/\text{Lutensol AO 8}$  with  $\alpha = 0.4125$ ,  $\delta = 0.93$ ,  $\Psi = 0.75$ ,  $\zeta = 0.38$  and  $\gamma = 0.12$ . The maltese crosses indicate the existence of a birefringent phase.

For further structure investigations of the polymerized sample the scanning electron microscope has been used. Figure 6.8 shows that phase separation still occurs during the polymerization process. Bright polymer droplets varying in size are found all over the picture as well as holes in which polymers were bedded before fracturing the sample. No copy of the original underlying structure can be found.

The magnification of this as well of the following pictures taken varies between 2.0 K and 3.0 K depending on the sample's cracking and charging. An increase to values higher than 3.0 K was not possible.

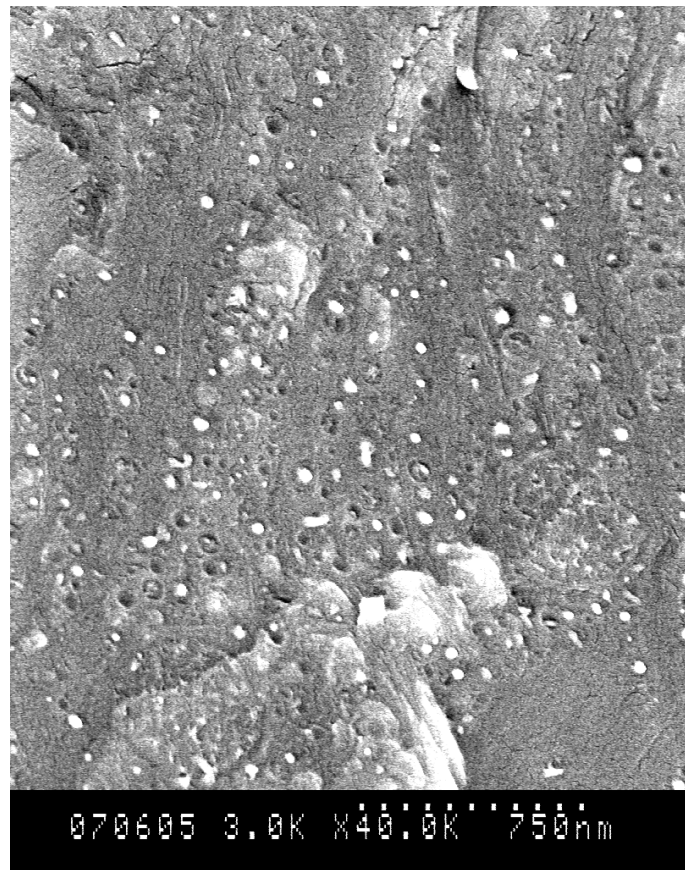


Figure 6.8: SEM picture of the polymerized system  $\text{H}_2\text{O}/(\text{sucrose}/\text{trehalose}) - \text{C}_6\text{MA} - \text{Agnique PG 264-G}/\text{Lutensol AO 8}$  with  $\alpha = 0.4125$ ,  $\delta = 0.93$ ,  $\Psi = 0.75$ ,  $\zeta = 0.38$  and  $\gamma = 0.12$ . One can see that phase separation still occurs.

As already mentioned, during the phase separation also the region of the bicontinuous phase coexisting with a lamellar phase is passed. Figure 6.9 shows the polymerized lamel-

lar phase found within the same sample also the phase separation occurred and proves the results of coexisting birefringent phases as obtained by the polarizing microscope. On both pictures in Figure 6.9 one can clearly see the polymer layers which are separated by water/sugar layers. Comparing both pictures, one finds a different spacing between these layers though the magnification is the same. Explanation might be that the view on the lamellar layers shown in the right picture is not perpendicular.

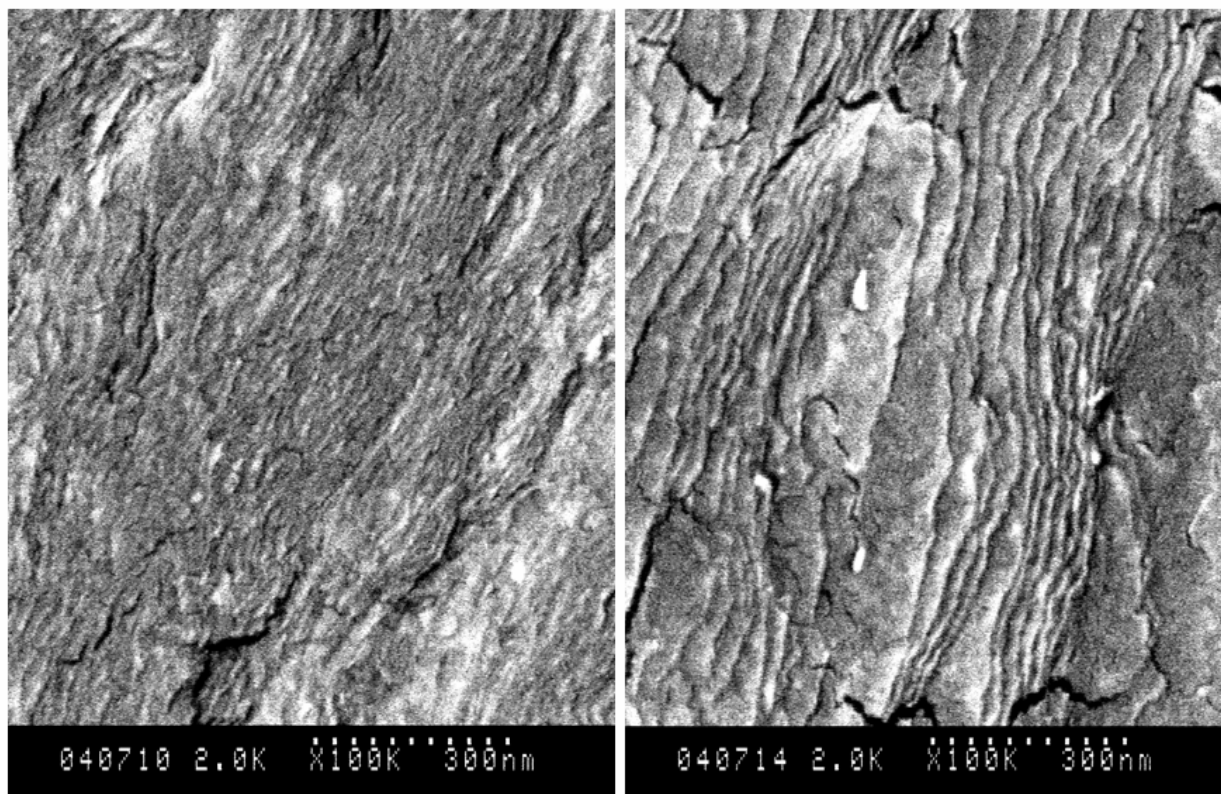


Figure 6.9: SEM pictures of the polymerized system  $\text{H}_2\text{O}/(\text{sucrose}/\text{trehalose}) - \text{C}_6\text{MA} - \text{Agnique PG 264-G}/\text{Lutensol AO 8}$  with  $\alpha = 0.4125$ ,  $\delta = 0.93$ ,  $\Psi = 0.75$ ,  $\zeta = 0.38$  and  $\gamma = 0.12$ . Though phase separation still occurs, the underlying lamellar structure could be polymerized on a one to one scale.

Investigating a magnification of the lamellar structure (Figure 6.10) one can determine the layer distance. One obtains a lamellar spacing of  $d/2 \approx 10$  nm. This value is consistent with the results obtained from the SANS measurements for the unpolymerized sample from which a lamellar spacing of  $d = 18.8$  nm is obtained. This gives a thickness of  $d/2 = 9.4$  nm for each layer and is in good agreement with the data obtained by TEM. The pictures in Figure 6.9 and Figure 6.10 prove that a one to one copy of the underlying lamellar microstructure to the polymer structure has been carried out successful.

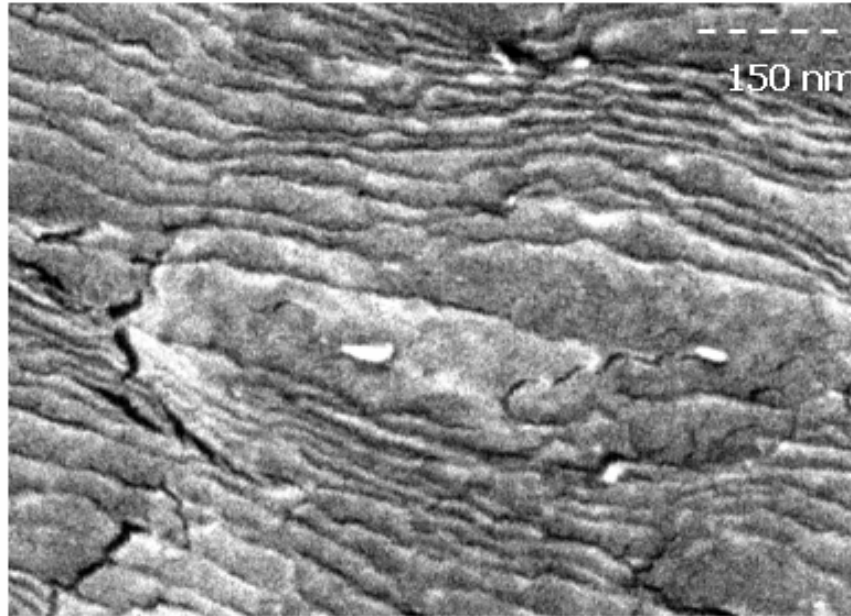


Figure 6.10: Magnification of the polymerized lamellar structure as seen in Figure 6.11. The lamellar spacing is in good agreement with the results obtained for the unpolymerized sample by SANS and TEM measurements.

Besides the phase separation and the lamellar structure, a second structure is found during the structure investigations. Figure 6.11 shows two pictures of this second structure. The polymer forms a uniform network over the entire picture whereas the underlying material is a mixture of frozen water and sugar. Comparing the two pictures in Figure 6.11 the bright spots found over the entire right picture directly catch one's eye whereas the left picture does not have many of these bright spots. As the sample does not contain any cross-linker in the monomer phase the polymer chains remain quite soft and flexible. They can be disentangled upon fracture, and the rest of the polymer chains can still be realigned and finally broken. Therefore, the bright spots, the so-called pullouts, form. The partial occurrence of pullouts clarifies that the fracturing behavior of the sample is not completely uniform over the entire sample. A detailed description how pullouts form is given in Figure 6.12.

The samples have been polymerized in different ways. The UV-lamp has been used as initiating lamp as well as the microscopy lamp (for details considering the initiating lamps see chapter 5). Furthermore, it was the aim to find out if stirring plays any role while polymerizing the sample or if less phase separation occurs if one polymerizes a very thin sample using the "Einfrierküvette" (for details see Appendix A.3). All these things did not influence the observed structure at all; no differences in the polymer structure of the sam-

ples could be found. Therefore, the different polymerization conditions with the corresponding SEM pictures are not discussed here in detail.

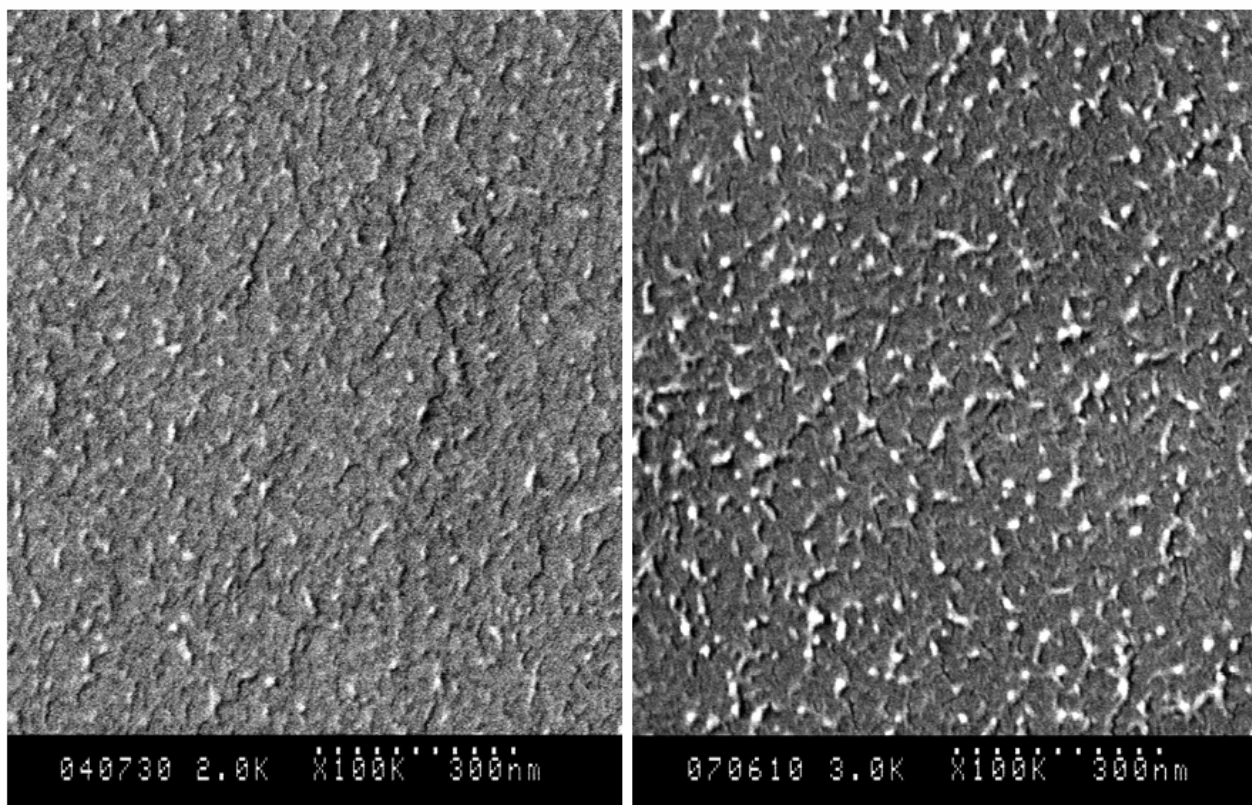


Figure 6.11: SEM pictures of the polymerized system  $\text{H}_2\text{O}/(\text{sucrose}/\text{trehalose}) - \text{C}_6\text{MA} - \text{Agnique PG 264-G}/\text{Lutensol AO 8}$  with  $\alpha = 0.4125$ ,  $\delta = 0.93$ ,  $\Psi = 0.75$ ,  $\zeta = 0.38$  and  $\gamma = 0.12$ . Though phase separation still occurs, the underlying bicontinuous structure could be polymerized on a one to one scale. The bright spots seen in the right picture are pullouts which indicate that the fracturing behavior of the sample is not uniform.

The procedure of prying apart the planchette sandwich and thereby generating a crack that runs through the frozen sample takes less than a second, and the rapidly advancing crack is not accessible to view. What actually happens and why pullouts appear can only be deduced from the end result. It is known that during the freeze-fracture step, interesting features like the so-called pullouts can be produced by the plastic deformation of the polymer into partially elongated shapes that often remain in the fracture surface.

Figure 6.12 illustrates how pullouts form. Before fracture, the polymer in the cryo-immobilized suspension is surrounded by and adhere to vitreous ice from the high-pressure freezing. During fracture, the fracture front, i.e., the crack tip, gets started in ice and passes through the polymer. The separation of the fracture halves plastically draws out a part of



the polymer until it breaks. The resulting protrusions are the pullouts. The last diagram in Figure 6.12 shows the end view of a pullout, which is usually the view that appears in a cryo-SEM image of a fracture surface of a coating that consists of polymer that has not begun coalescing.

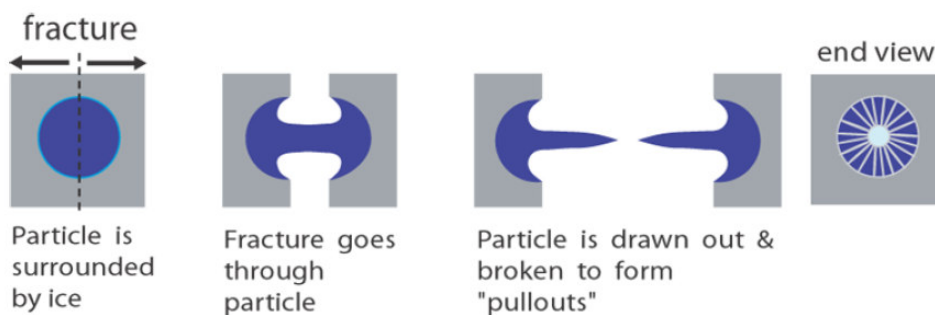


Figure 6.12: The process of forming pullouts.

A magnification of the polymer structure of the sample  $\text{H}_2\text{O}/(\text{sucrose}/\text{trehalose}) - \text{C}_6\text{MA} - \text{Agnique PG 264-G}/\text{Lutensol AO 8}$  at  $\alpha = 0.4125$ ,  $\delta = 0.93$ ,  $\Psi = 0.75$ ,  $\zeta = 0.38$  and  $\gamma = 0.12$  is given in Figure 6.13. One can see that the polymer chains are linked to each other and form a uniform network. This makes the structure look similar to a bicontinuous structure. Investigating the polymer structure more closely one notices that only the top side of the polymer chains can be seen and nothing underneath. Therefore, the sublimation time was increased from 30 minutes up to 3 hours. Aim was to make the structure clearer and as more water should be sublimed to also see underneath the structure. But up to 3 hours sublimation made no difference in the pictures. Sugar is a cryo protector and makes it more difficult for the ice to crystallize but it seems that it also prevents reasonable water sublimation. The same result is observed with other concentrated blockcopolymer samples where there is no three-dimensional view of the structure for the concentrated sample but for less concentrated samples it is also possible to see underneath the bicontinuous structure. In both cases, SANS measurements have prognosed a bicontinuous structure [176]. This leads to the conclusion that also in the existing case the structure is a bicontinuous one though no three-dimensional network can be observed.

The size of the polymer chains is about  $d/2 = 18$  nm. This is consistent with the size the SANS measurements delivered for the bicontinuous structure of the unpolymerized sample ( $d_{\text{TS}}/2 = 23$  nm). Noticeably is that the spacing of the water/sugar region and the polymer chains does not seem to be exactly the same size. The structure of the water/sugar phase is

bigger. This is not to be supposed in a bicontinuous microemulsion containing almost the same volume of hydrophilic and hydrophobic phase ( $\alpha = 0.4125$  is consistent with  $\phi = 0.53$  for the densities of the corresponding compounds). Explanation might be a strong volume contraction which occurs during the polymerization reaction. Compared with other monomers, the volume contraction is relatively high for acrylates [97].

The bright spots are again the pullouts as already mentioned.

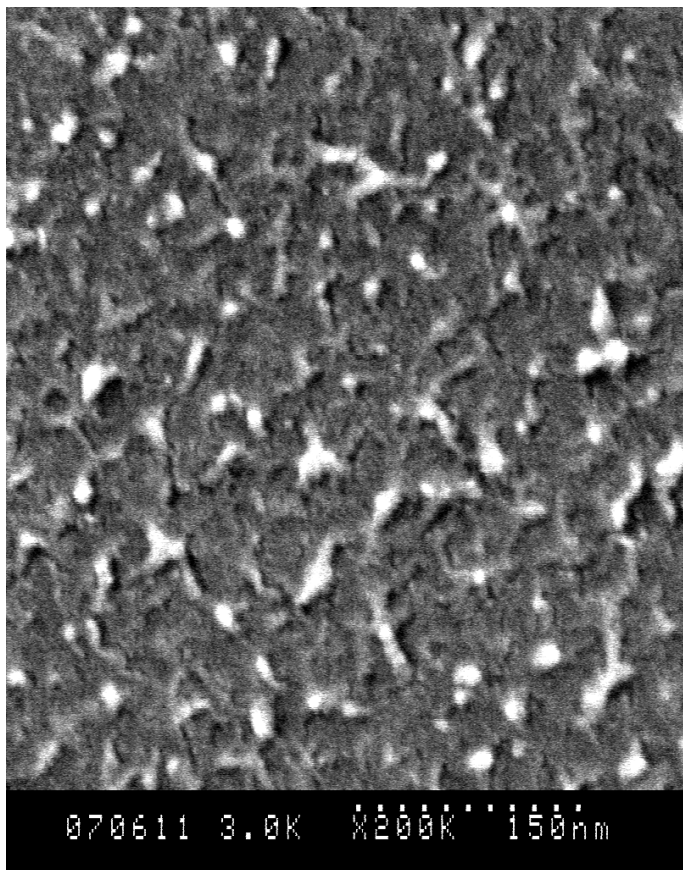


Figure 6.13: The polymerized bicontinuous structure in magnification. The measured domain size is in good agreement with the results obtained for the unpolymerized sample by SANS measurements.

Figure 6.14 shows the polymerized bicontinuous structure under a certain angle, the reason why only the structure in the middle area of the picture is not blurry. The inset shows a detail of this picture in magnification. One can see again the polymer forming a bicontinuous network over the entire picture. This view allows slightly seeing a three-dimensional structure. The hollow spaces between the polymer network are formed by the partly sublimed water/sugar solution.



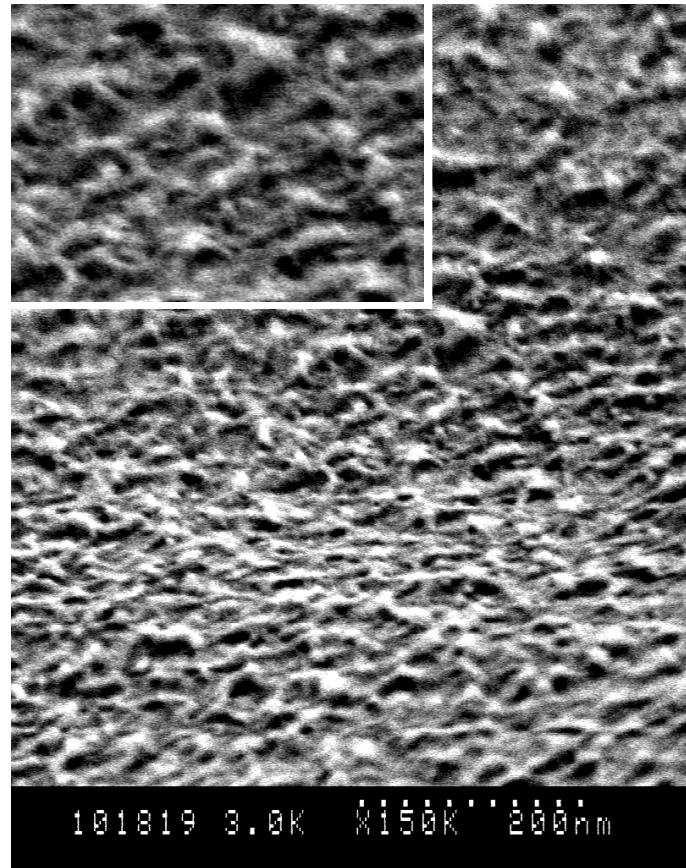


Figure 6.14: SEM pictures of the polymerized system  $\text{H}_2\text{O}/(\text{sucrose}/\text{trehalose}) - \text{C}_6\text{MA} - \text{Agnique PG 264-G}/\text{Lutensol AO 8}$  with  $\alpha = 0.4125$ ,  $\delta = 0.93$ ,  $\Psi = 0.75$ ,  $\zeta = 0.38$  and  $\gamma = 0.12$  under a certain angle. The polymer network structure with the hollow spaces formed by the sublimed water/sugar solution can be seen.

To prove that the polymerized structure is not an artifact a  $\gamma$ -variation is investigated. Figure 6.15 compares SEM images for the sample  $\text{H}_2\text{O}/(\text{sucrose}/\text{trehalose}) - \text{C}_6\text{MA} - \text{Agnique PG 264-G}/\text{Lutensol AO 8}$  at  $\alpha = 0.4125$ ,  $\delta = 0.93$ ,  $\Psi = 0.75$  and  $\zeta = 0.38$  once with a surfactant mass fraction  $\gamma = 0.12$  (left) and once with a surfactant mass fraction  $\gamma = 0.34$  (right). As known from SANS measurements the domain size should decrease from  $d_{\text{TS}}/2 \approx 23$  nm for  $\gamma = 0.12$  to  $d_{\text{TS}}/2 \approx 8$  nm for  $\gamma = 0.34$ . The two pictures in Figure 6.15 show that the polymer structure decreases with increasing surfactant mass fraction. The inset shows a magnification for a clearer view. On the right picture one can see a much finer polymer structure with an average domain size of  $d_{\text{TS}}/2 = 5\text{-}10$  nm. As this result agrees with the information obtained by SANS one can assume that the investigated structure is not an artifact. The polymer structure is dispersed equally over the entire pic-

ture. A clearer and sharper picture of the polymer structure cannot be taken as the magnification cannot be increased. Explanation might be cracking of the sample or charging with increasing magnification. The bright spots which can be found in both pictures are again pullouts as mentioned before.

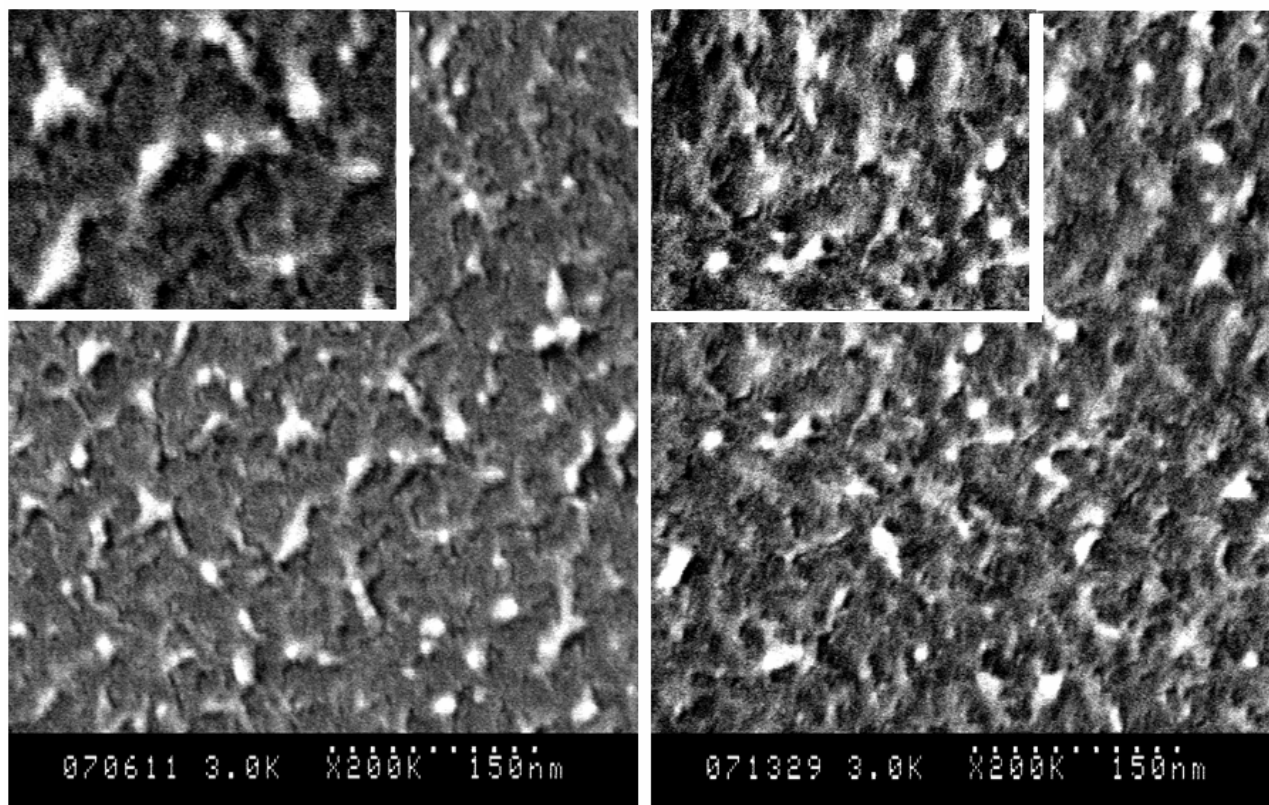


Figure 6.15: SEM pictures of the polymerized system  $\text{H}_2\text{O}/(\text{sucrose}/\text{trehalose}) - \text{C}_6\text{MA} - \text{Agnique PG 264-G}/\text{Lutensol AO 8}$  with  $\alpha = 0.4125$ ,  $\delta = 0.93$ ,  $\Psi = 0.75$  and  $\zeta = 0.38$  once with a lower surfactant mass fraction  $\gamma = 0.12$  (left) and once with a higher surfactant mass fraction  $\gamma = 0.34$  (right). On the right picture one can see a much finer polymer structure dispersed equally over the entire picture.

#### 6.4 The Polymerized System $\text{H}_2\text{O}/\text{sugar} - \text{C}_6\text{MA}/\text{EGDMA} - \text{surfactant}$

To observe if the addition of cross-linker has any effect on the polymerized sample structure in this section the polymer structure of the system  $\text{H}_2\text{O}/(\text{sucrose}/\text{trehalose}) - \text{C}_6\text{MA}/\text{ethylene glycol dimethacrylate} - \text{Agnique PG 264-G}/\text{Lutensol AO 8}$  is investigated.

The corresponding phase behavior of the system is shown in Figure 4.14. The sample composition is given by  $\alpha = 0.4125$ ,  $\delta = 0.91$ ,  $\Psi = 0.75$  and  $\zeta = 0.38$  with a cross-linker mass fraction of  $\beta = 0.10$  in the monomer phase and a surfactant mass fraction of  $\gamma = 0.34$ . This is the corresponding mass fraction as for the sample without cross-linker (Figure 6.15 right).

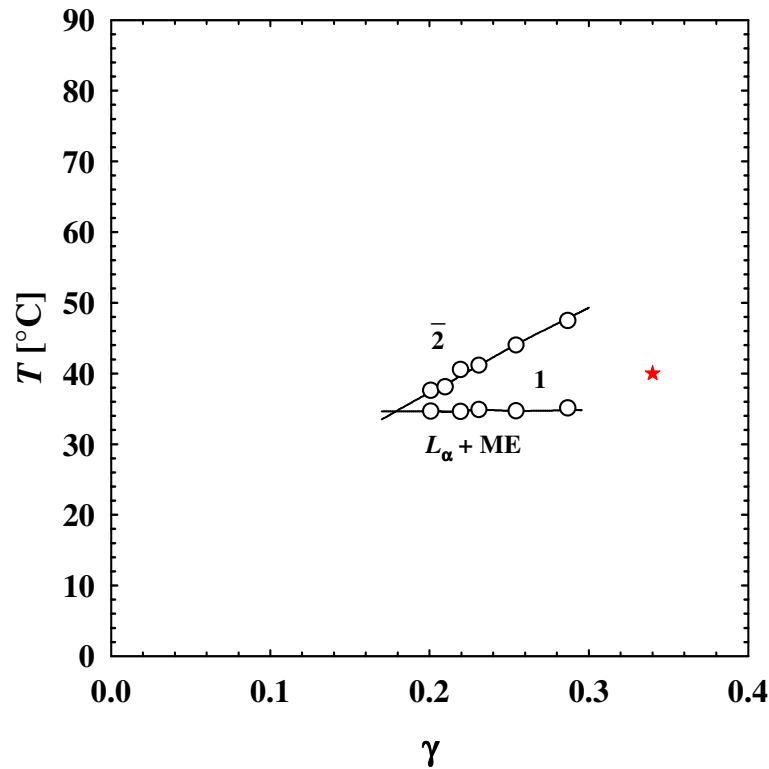


Figure 6.16:  $T(\gamma)$ -section of the system  $H_2O/(sucrose/trehalose) - C_6MA/EGDMA - Agnique PG 264-G$  with  $\alpha = 0.4125$ ,  $\delta = 0.91$ ,  $\beta = 0.10$ ,  $\Psi = 0.75$  and  $\zeta = 0.38$ . The red star indicates the sample compositions for the polymerization.

Comparing now Figure 6.17 where the sample contains 10% of cross-linker within the monomer phase and Figure 6.15 right where the sample does not contain any cross-linker within the monomer phase the main difference is that the pullouts almost completely disappear in the case of cross-linker added to the monomer phase. This result is found over the entire sample. Explanation is that cross-linking of the polymer surely raises tensile yield stress and depresses impact strength [200]. The cross-linked chains that span the incipient fracture must break rather than disentangle and disengage as the crack widens. It is known from literature that there is a critical value of cross-linking density ( $D_{c,critical}$ ), below which a fracture can induce pullouts in frozen suspensions. Apparently, below the  $D_{c,critical}$ ,

enough of the polymer chains are not cross-linked and so remain sufficiently flexible and free to reptate that they can disentangle and align into a stem as the crack opens and thereby form pullouts. But if the cross-linking density exceeds  $D_{c,critical}$ , the three-dimensional network of covalent bonding makes the latex particles so tough that the fracture goes around the particles and propagates through adjacent ice [201].

As known from SANS measurements the domain size of the unpolymerized sample  $H_2O/(sucrose/trehalose) - C_6MA/ethylene\ glycol\ dimethacrylate - Agnique\ PG\ 264-G/Lutensol\ AO\ 8$  at  $\alpha = 0.4125$ ,  $\delta = 0.91$ ,  $\Psi = 0.75$ ,  $\zeta = 0.38$ ,  $\beta = 0.10$  and  $\gamma = 0.34$  corresponds with a value of  $d_{TS}/2 \approx 8\text{ nm}$  to the domain size of the unpolymerized system at the same surfactant mass fraction of but without cross-linker. Investigating the structure size from the Figure 6.17 one obtains a value for the domain size which is in good agreement with the SANS results. If one compares the polymer structure as shown in Figure 6.17 with the polymer structure without cross-linker (Figure 6.15 right) one finds a much clearer and sharper view of the structure.

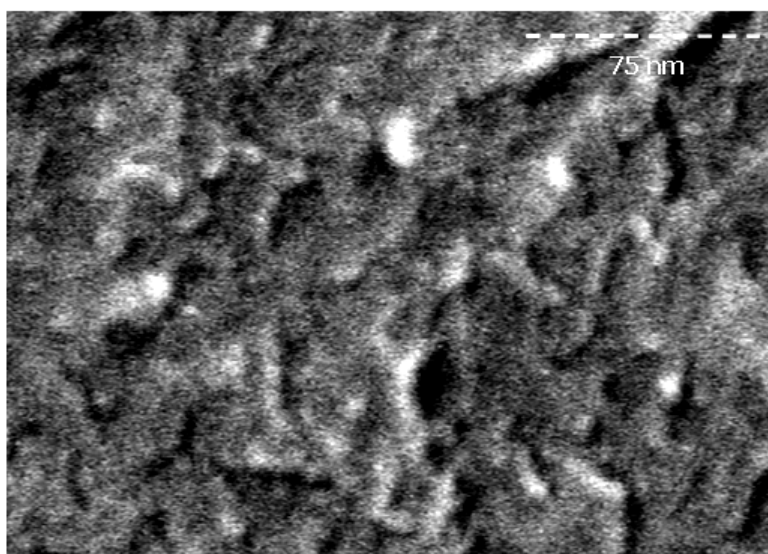


Figure 6.17: SEM pictures of the polymerized system  $H_2O/(sucrose/trehalose) - C_6MA/ethylene\ glycol\ dimethacrylate - Agnique\ PG\ 264-G/Lutensol\ AO\ 8$  with  $\alpha = 0.4125$ ,  $\delta = 0.91$ ,  $\Psi = 0.75$ ,  $\zeta = 0.38$ ,  $\beta = 0.10$  and a surfactant mass fraction of  $\gamma = 0.34$ . The domain size is in good agreement with the results obtained by SANS measurements.

## 6.5 The Polymerized System H<sub>2</sub>O/sugar – C<sub>12</sub>MA - surfactant

As known from the microemulsion droplet polymerization the monomer's hydrophobicity does not have a positive influence on the particle size (for further details see chapter 5). The phase separation occurring during the polymerization process remains about the same. To investigate the influence of the oil's hydrophobicity on the polymeric bicontinuous microemulsion the preceding system is modified by replacing C<sub>6</sub>MA by C<sub>12</sub>MA. The phase behavior for the system H<sub>2</sub>O/(sucrose/trehalose) – C<sub>12</sub>MA – Agnique PG 264-G/Lutensol AO 8 at  $\alpha = 0.4125$ ,  $\delta = 0.70$ ,  $\Psi = 0.75$  and  $\zeta = 0.38$  is shown in Figure 6.18. The red star indicates the sample composition and temperature for the polymerization ( $\gamma = 0.14$ ). As one can see, for this system no lamellar phase cuts off the lower phase boundary. Here, the typical fish-shape as known from literature is found. Therefore, after polymerization a bicontinuous polymer structure is expected. A lamellar phase might not be found.

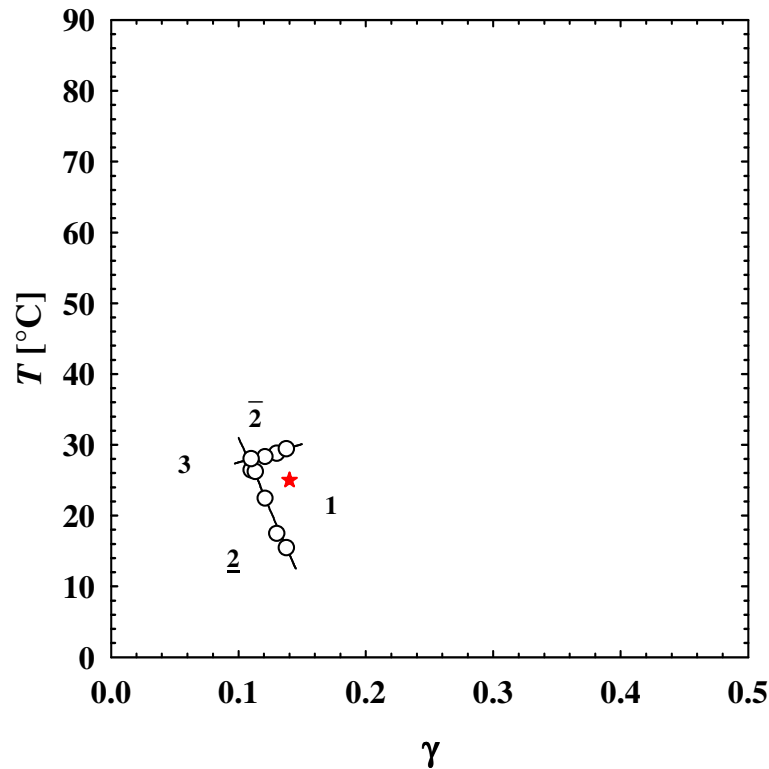


Figure 6.18:  $T(\gamma)$ -section of the system H<sub>2</sub>O/(sucrose/trehalose) – C<sub>12</sub>MA – Agnique PG 264-G/Lutensol AO8 at  $\alpha = 0.4125$ ,  $\delta = 0.70$ ,  $\Psi = 0.75$  and  $\zeta = 0.38$ . The red star indicates the sample's composition for the following polymerization. The phase boundaries for this system are not cut off by a lamellar phase.

The polymer structure of the polymerized system is shown in Figure 6.19. As one can see, there is no big difference to the polymer structure formed during the polymerization process of the system  $\text{H}_2\text{O}/(\text{sucrose}/\text{trehalose}) - \text{C}_6\text{MA} - \text{Agnique PG 264-G}/\text{Lutensol AO8}$  at  $\alpha = 0.4125$ ,  $\delta = 0.93$ ,  $\Psi = 0.75$  and  $\zeta = 0.38$ . Also in this case, phase separation still has occurred. As expected, except for the regions with phase separation, this sample only contains one kind of structure, the bicontinuous one. No spots showing a lamellar phase could be found over the entire sample. Again the polymer chains form a uniform network over the entire picture with a domain size of  $d/2 = 12\text{-}15$  nm. Therewith, the structure size is slightly smaller than the polymer structure formed using  $\text{C}_6\text{MA}$ . As there is less surfactant in the latter system, this result is expected.

Comparing the bicontinuous structure formed by polymerized  $\text{C}_{12}\text{MA}$  with the corresponding structure formed by  $\text{C}_6\text{MA}$  the main difference is that no pullouts are found for the first one over the entire sample. This phenomenon can be explained by the following: If the weight-average molecular weight  $M_w$  is greater or close to the critical molecular weight for entanglement  $M_e$ , polymer chains are highly entangled, and chain scission and disentanglement must compete during fracture. Presumably the entangled chains realign and the ligaments can elongate until they finally break. But if  $M_w$  is much lower than  $M_e$ , polymer chains are weakly or less entangled, and consequently the friction force within chains is smaller so that chains can be easily pulled out upon fracture; thus ligaments cannot form and neither do pullouts [201]. For the case of poly- $\text{C}_{12}\text{MA}$   $M_w$  seems to be much lower than  $M_e$ .

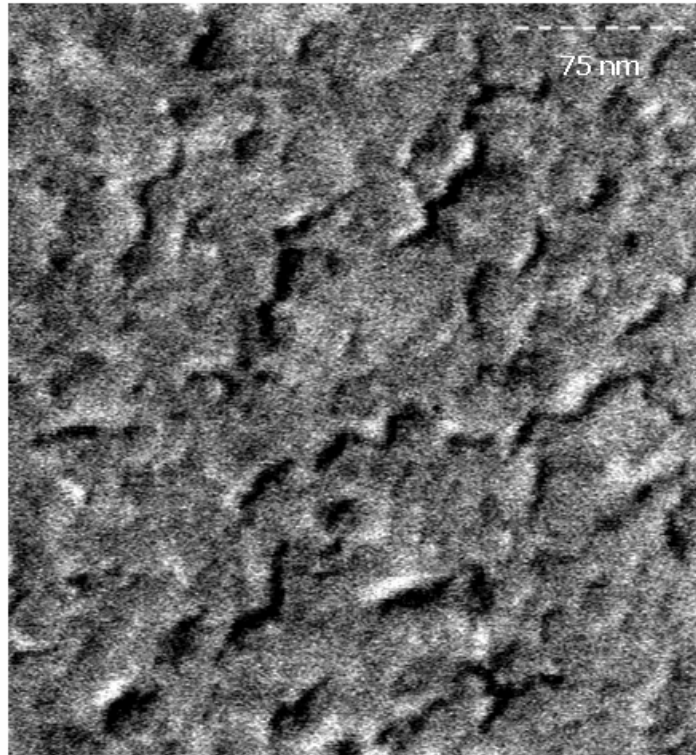


Figure 6.19: SEM pictures of the polymerized system  $\text{H}_2\text{O}/(\text{sucrose}/\text{trehalose}) - \text{C}_{12}\text{MA} - \text{Agnique PG 264-G}/\text{Lutensol AO 8}$  with  $\alpha = 0.4125$ ,  $\delta = 0.70$ ,  $\Psi = 0.75$ ,  $\zeta = 0.38$ , and a surfactant mass fraction of  $\gamma = 0.14$ . Compared to the corresponding system containing poly- $\text{C}_6\text{MA}$  the same bicontinuous structure is found but no pullouts.





## 7 Summary

Thermodynamic in material, the micellar, rod-like, bicontinuous, and liquid-crystalline structures formed by amphiphiles are in a constant flux. In many applications however, it is desired to lock-in these structures and eliminate sensitivity to temperature or compositional changes. From early cryo-TEM studies to visualize micelles, bicontinuous microemulsions, and liquid-crystalline phases to current transcriptive templating efforts for preparing nanostructured materials, the fixation of self-assembled complex fluids has proven to be an elusive target. While resisting arrest, self-assembled structures may crystallize when frozen, form gradients when dehydrated, or phase separate when polymerized. One promising idea is to lock the nanostructures formed in microemulsion systems by adding sugar and therewith increasing the viscosity of the water phase. Thus, the reorganization kinetics of the phase behavior is slowed down so that the oil/monomer phase can be polymerized without phase separation. Following this idea the main focus of this work is the polymerization of the droplet and bicontinuous microstructures locked-in via the formulation of a highly viscous microemulsion.

Though highly viscous polymerizable microemulsions containing a concentrated water/sugar solution as hydrophilic phase are known from literature [38-42] there is no systematic study which investigates the influence of sugar onto the phase behavior of microemulsions. Starting point of this work is the phase behavior of the well-known ternary nonionic microemulsions of the type  $H_2O - n\text{-octane} - \text{polyethyleneglycolalkylether } (C_iE_j)$  characterized as a function of temperature and surfactant mass fraction ( $T(\gamma)$ -section). Increasing stepwise the amount of sugar within the water phase it is found that already small amounts of sugar shift the phase boundaries to low temperatures (Figure 4.2 and Figure 4.4). This behavior is due to the hydration of the sugar molecules as they dissolve in water leaving less hydrate water for the surfactant headgroups. To compensate for this shift of the phase boundaries to lower temperatures the  $C_iE_j$ -surfactants are stepwise replaced with the hydrophilic sugar surfactant  $C_8G_1$  or the technical-grade analog Agnique PG 8105-G.

Figure 4.5 and Figure 4.7 show that the phase boundaries and with it the phase inversion temperature  $\tilde{T}$  shifts to higher temperatures. Continuing this systematic investigation highly viscous microemulsions containing a 75% sugar in water solution, *n*-octane as oil and either a mixture of pure or technical-grade alkylpolyglycoether/sugar surfactants are formulated (Figure 4.7).

As the focus of this work is the polymerization of highly viscous microemulsions the next step was to replace *n*-octane by a monomer. Choosing the monomer C<sub>6</sub>MA the phase boundaries shift to lower temperatures and surfactant mass fractions (Figure 4.9 to Figure 4.11). A possible explanation for this trend could be that C<sub>6</sub>MA does not only act as polymerizable oil but also partially as a hydrophobic co-surfactant. Again it was possible to compensate for this shift of the phase boundaries to lower temperatures by increasing the fraction of hydrophilic sugar surfactant in the surfactant mixture. Thus, a polymerizable highly viscous microemulsion is obtained containing 75% sugar in water, C<sub>6</sub>MA and the sugar surfactant Agnique PG 264-G or a mixture of Agnique PG 8105-G and a technical-grade alkylpolyethyleneglycoether (Figure 4.14). In order to accelerate the gelation of the microemulsion during the polymerization process the cross-linker ethylene glycol dimethacrylate (EGDMA) is added to this microemulsion and its influence on the phase behavior studied (Figure 4.12). Tuning the phase boundaries of these microemulsions to lower temperatures by increasing the amount of hydrophobic co-surfactant, their viscosity could be further increased (Figure 4.13 and Figure 4.14).

Having a polymerizable highly viscous microemulsion on hand one interesting goal is the synthesis of monodisperse nanoparticles of a defined size. In order to realize this goal, the phase behavior of a diluted monomer droplet microemulsion of the type H<sub>2</sub>O/(sucrose/trehalose) – C<sub>6</sub>MA/EGDMA – Lutensol XL 70/Agnique PG 8105-G with  $\Psi = 0.75$ ,  $\zeta = 0.38$ ,  $\delta = 0.80$  and  $\gamma_a = 0.074$  has been studied as a function of temperature and the mass fraction of monomer ( $T(w_B)$ -sections). Increasing the amount of EGDMA in the system from  $\beta = 0.00$  to  $\beta = 0.30$  shifts the phase boundary continuously to lower temperatures due to the higher hydrophilicity of EGDMA compared to C<sub>6</sub>MA (Figure 4.18).

In the next step these diluted droplet microemulsions are polymerized by adding the initiator Irgacure 819 and initiating the process with a microscopy lamp emitting mainly visible light. The polymer droplets are characterized via dynamic light scattering (DLS) providing a hydrodynamic radius of ~50 nm which is about 7 – 8 larger than the unpolymerized microemulsion droplets. However, knowing that the initiator Irgacure 819 adsorbs

wave lengths between  $\lambda = 300$  nm and  $\lambda = 400$  nm, UV-light of high intensity is used to initiate the polymerization. As a result, the mean particle radii obtained decrease by a factor of two (Figure 5.14). Furthermore, for the first time it is found that the polymer radius follows the trend of the unpolymerized microemulsion droplet radius. Thus, increasing the amount of C<sub>6</sub>MA in the microemulsion from  $w_B = 0.03$  to  $w_B = 0.043$  and polymerizing at a constant temperature of  $T = 10^\circ\text{C}$  the hydrodynamic radius of the polymer particles increases from  $R_{\text{hydr}} = 15 \pm 1$  nm to  $R_{\text{hydr}} = 20 \pm 1$  nm (Figure 5.11). Polymerizing the sample containing 3 wt.% C<sub>6</sub>MA at  $T = 20^\circ\text{C}$  a polymer radius of  $R_{\text{hydr}} = 20 \pm 1$  nm is found which again reflects the underlying microemulsion structure (Figure 5.12). However, if samples with increasing amount of C<sub>6</sub>MA are polymerized at temperatures just above the *efb* a much stronger increase of the polymer radius than expected from the radius of the unpolymerized microemulsion droplets is found. The existence of elongated and network-like monomer structures could explain this result (Figure 5.13).

Exemplarily, the polymer particles are visualized via scanning electron microscopy (SEM, Figure 5.21 and Figure 5.22) and their sizes are determined using small angle neutron scattering (SANS). The analysis of the scattering curve of the unpolymerized microemulsion containing 3 wt.% C<sub>6</sub>MA at  $T = 10^\circ\text{C}$  provides a radius of  $r = 3.3$  nm (Figure 5.19). However, the deviations between the scattering curve and the structure factor of diffuse polydisperse spheres indicate the existence of elongated network structures. The analysis of the scattering curve of the polymerized sample proves the coexistence of polymer droplets and empty micelles. Thereby, the radius of the polymer particles amounts to  $r = 9.1$  nm (Figure 5.20) which is in good agreement with the hydrodynamic radius of  $R_{\text{hydr}} = 15 \pm 1$  nm obtained by DLS. Similar results are obtained changing to the C<sub>12</sub>MA instead of C<sub>6</sub>MA (Figure 5.15 to Figure 5.17).

The main goal of this thesis was the fixation of the nanostructure of the bicontinuous microemulsion. Having formulated a highly viscous, polymerizable bicontinuous microemulsion of the type H<sub>2</sub>O/(sucrose/trehalose) – C<sub>6</sub>MA – Agnique PG 264-G/Lutensol AO8 with  $\alpha = 0.4125$ ,  $\delta = 0.93$ ,  $\Psi = 0.75$ ,  $\zeta = 0.38$  and  $\gamma = 0.12$  their length scale is determined via SANS measurements. Analyzing the scattering curve using the *Teubner-Strey* formula yields a diameter  $d_{\text{TS}}/2 \approx 23$  nm of the sugar-rich and monomer domains (Figure 6.3). However, visualizing this sample via transmission electron microscopy (TEM) a coexistence of a bicontinuous and a lamellar phase is found (Figure 6.4). To prove the assumption that the sample intrudes in this 2-phase region during the cryo-fixation a scattering curve is recorded at the respective temperature (Figure 6.2). Analyzing the obtained data

points by subtracting the fit of the bicontinuous scattering curve a lamellar peak is found from which a lamellar spacing of  $d/2 = 9.04$  nm is obtained (Figure 6.6).

Polymerizing the bicontinuous structured highly viscous microemulsion using the initiator Irgacure 819 and UV-light the SEM pictures show both polymerized lamellar and bicontinuous structures. Thus, the polymerization induces the same phase transition as the cryo-fixation. The length scales obtained for the lamellar spacing  $d/2 = 9.4$  nm for each layer (Figure 6.7, Figure 6.9, Figure 6.10) and the diameter of the bicontinuous domains  $d/2 = 23$  nm (Figure 6.11, Figure 6.13, Figure 6.14) are in good agreement with the SANS and TEM results obtained for the unpolymerized system. Thus, in this study, bicontinuous microemulsions and for the first time also lamellar liquid crystal structures have been polymerized on a one-to-one scale. That the one-to-one copy of the unpolymerized microemulsion structure is indeed possible was successfully verified polymerizing a microemulsion with a higher mass fraction  $\gamma$  of surfactant. As expected the SEM picture of the polymerized microemulsion shows a smaller domain size (Figure 6.15).

# A Appendix

## A.1 Chemicals

The substances used in this work are compiled in the following table containing the chemical structure, source of supply, molar mass and purity (if mentioned).

Table 7.1: List of substances used in this work.

substance	chemical formula	source of supply	molar mass [g/mol]	purity [wt. %]
water	H <sub>2</sub> O	---	18.00	doubly distilled
deuterated water	D <sub>2</sub> O	euriso-top	20.03	99.9
sucrose	C <sub>12</sub> H <sub>22</sub> O <sub>11</sub>	Merck	342.30	---
trehalose	C <sub>12</sub> H <sub>22</sub> O <sub>11</sub>	Merck	342.30	---
fructose	C <sub>6</sub> H <sub>12</sub> O <sub>6</sub>	Real	180.16	---
<i>n</i> -octane	C <sub>8</sub> H <sub>18</sub>	Fluka	114.23	>99.5
<i>n</i> -hexyl methacrylate	C <sub>10</sub> H <sub>18</sub> O <sub>2</sub>	Aldrich	170.25	98
<i>n</i> -dodecyl methacrylate	C <sub>16</sub> H <sub>30</sub> O <sub>2</sub>	Aldrich	254.42	96
ethylene glycol dimethacrylate	C <sub>10</sub> H <sub>14</sub> O <sub>4</sub>	Aldrich	198.22	98
C <sub>10</sub> E <sub>6</sub>	C <sub>22</sub> H <sub>46</sub> O <sub>7</sub>	Fluka	422.61	>99
C <sub>12</sub> E <sub>6</sub>	C <sub>24</sub> H <sub>50</sub> O <sub>7</sub>	Fluka	450.66	>98
C <sub>14</sub> E <sub>6</sub>	C <sub>26</sub> H <sub>54</sub> O <sub>7</sub>	Fluka	478.72	>99
C <sub>18</sub> E <sub>8</sub>	C <sub>34</sub> H <sub>70</sub> O <sub>9</sub>	Fluka	622.93	>98

substance	chemical formula	source of supply	molar mass [g/mol]	purity [wt. %]
$C_8G_1$	$C_{14}H_{28}O_6$	Calbiochem	292.37	>97
Lutensol XL 70	---	BASF	---	---
Lutensol AO 8	---	BASF	---	---
Agnique PG 264-G	$C_{12-14}G_{1.4}$	Cognis	---	47% – 50% water
Agnique PG 8105-G	$C_{8-10}G_{1.5}$	Cognis	---	35% – 38% water
Tween 20	---	Aldrich	~1228	---
PBMA- <i>b</i> -PEO	---	Goldschmidt	---	---

As the technical surfactant Agnique PG 8105-G contains 35 – 38% and Agnique PG 264-G contains 47 – 50% water these two surfactants were dried up to weight constancy (approximately one week) in a desiccator under blue gel. The other substances are not dried or purified further.

## A.2 Initial Weights of Compounds for SANS, SEM and DLS Measurements

Table 7.2: Stock solution ( $m_S$ ) of a 75% sugar solution in D<sub>2</sub>O for SANS measurements.

substance	initial weight [g]
sucrose	7.461
trehalose	4.583
D <sub>2</sub> O	4.465

Table 7.3: Initial weights of the compounds for the SANS measurements of the unpolymerized sample H<sub>2</sub>O/(sucrose/trehalose) – C<sub>6</sub>MA – Agnique PG 264-G/Lutensol AO8 at  $\alpha = 0.4125$ ,  $\delta = 0.93$ ,  $\Psi = 0.75$ ,  $\zeta = 0.38$  and  $\gamma = 0.12$ .

substance	initial weight [g]
$m_S$	1.765
$m_B$	1.2338
$m_{\text{Agnique PG 264-G}}$	0.3804
$m_{\text{Lutensol AO8}}$	0.0284

Table 7.4: Initial weights of the compounds for the SANS measurements of the unpolymerized sample  $\text{H}_2\text{O}/(\text{sucrose}/\text{trehalose}) - \text{C}_6\text{MA}/\text{ethylene glycol dimethacrylate} - \text{Agnique PG 8105-G}/\text{Lutensol XL 70}$  at  $\gamma_a = 0.074$ ,  $\delta = 0.80$ ,  $\Psi = 0.75$ ,  $\zeta = 0.38$ ,  $\beta = 0.15$  and  $w_B = 0.03$ .

<b>substance</b>	<b>initial weight [g]</b>
$m_S$	2.888
$m_B$	0.0969
$m_{\text{Agnique PG 8105-G}}$	0.1795
$m_{\text{Lutensol XL 70}}$	0.0449

Table 7.5: Initial weights of the compounds for the SANS measurements of the polymerized sample  $\text{H}_2\text{O}/(\text{sucrose}/\text{trehalose}) - \text{C}_6\text{MA}/\text{ethylene glycol dimethacrylate} - \text{Agnique PG 8105-G}/\text{Lutensol XL 70}$  at  $\gamma_a = 0.074$ ,  $\delta = 0.80$ ,  $\Psi = 0.75$ ,  $\zeta = 0.38$ ,  $\beta = 0.15$  and  $w_B = 0.03$ .

<b>substance</b>	<b>initial weight [g]</b>
$m_S$	3.1613
$m_B$	0.1067
$m_{\text{Agnique PG 8105-G}}$	0.1966
$m_{\text{Lutensol XL 70}}$	0.0491



Table 7.6: Stock solution ( $m_S$ ) of a 75% sugar solution in H<sub>2</sub>O for SEM measurements.

<b>substance</b>	<b>initial weight [g]</b>
sucrose	4.974
trehalose	3.055
H <sub>2</sub> O	2.677

Table 7.7: Initial weights of the compounds for the SEM measurements of the sample H<sub>2</sub>O/(sucrose/trehalose) – C<sub>6</sub>MA – Agnique PG 264-G/Lutensol AO 8 at  $\alpha = 0.4125$ ,  $\delta = 0.93$ ,  $\Psi = 0.75$   $\zeta = 0.38$  and  $\gamma = 0.12$ . The sample was polymerized using the microscopy lamp with stirring.

<b>substance</b>	<b>initial weight [g]</b>
$m_S$	1.723
$m_B$	1.210
$m_{\text{Agnique PG 264-G}}$	0.372
$m_{\text{Lutensol AO8}}$	0.028

Table 7.8: Initial weights of the compounds for the SEM measurements of the sample H<sub>2</sub>O/(sucrose/trehalose) – C<sub>6</sub>MA/ethylene glycol dimethacrylate – Agnique PG 264-G/Lutensol AO 8 at  $\alpha = 0.4125$ ,  $\delta = 0.91$ ,  $\beta = 0.10$ ,  $\Psi = 0.75$   $\zeta = 0.38$  and  $\gamma = 0.34$ . The sample was polymerized using the microscopy lamp with stirring.

<b>substance</b>	<b>initial weight [g]</b>
$m_S$	1.297
$m_B$	0.909
$m_{\text{Agnique PG 264-G}}$	1.034
$m_{\text{Lutensol AO8}}$	0.102

Table 7.9: Initial weights of the compounds for the SEM measurements of the sample  $\text{H}_2\text{O}/(\text{sucrose}/\text{trehalose}) - \text{C}_{12}\text{MA} - \text{Agnique PG 264-G}/\text{Lutensol AO 8}$  at  $\alpha = 0.4125$ ,  $\delta = 0.70$ ,  $\Psi = 0.75$ ,  $\zeta = 0.38$  and  $\gamma = 0.14$ . The sample was polymerized using the microscopy lamp with stirring.

<b>substance</b>	<b>initial weight [g]</b>
$m_{\text{S}}$	1.415
$m_{\text{B}}$	0.990
$m_{\text{Agnique PG 264-G}}$	0.278
$m_{\text{Lutensol AO8}}$	0.118

Table 7.10: Initial weights of the compounds for the SEM measurements of the sample  $\text{H}_2\text{O}/(\text{sucrose}/\text{trehalose}) - \text{C}_6\text{MA} - \text{Agnique PG 264-G}/\text{Lutensol AO 8}$  at  $\alpha = 0.4125$ ,  $\delta = 0.93$ ,  $\Psi = 0.75$ ,  $\zeta = 0.38$  and  $\gamma = 0.12$ . The sample was polymerized using the UV-lamp with stirring.

<b>substance</b>	<b>initial weight [g]</b>
$m_{\text{S}}$	1.341
$m_{\text{B}}$	0.940
$m_{\text{Agnique PG 264-G}}$	0.291
$m_{\text{Lutensol AO8}}$	0.022

Table 7.11: Initial weights of the compounds for the SEM measurements of the sample  $\text{H}_2\text{O}/(\text{sucrose}/\text{trehalose}) - \text{C}_6\text{MA} - \text{Agnique PG 264-G}/\text{Lutensol AO 8}$  at  $\alpha = 0.4125$ ,  $\delta = 0.93$ ,  $\Psi = 0.75$ ,  $\zeta = 0.38$  and  $\gamma = 0.12$ . The sample was polymerized using the UV-lamp without stirring.

<b>substance</b>	<b>initial weight [g]</b>
$m_S$	1.956
$m_B$	1.372
$m_{\text{Agnique PG 264-G}}$	0.423
$m_{\text{Lutensol AO8}}$	0.030

Table 7.12: Initial weights of the compounds for the SEM measurements of the sample  $\text{H}_2\text{O}/(\text{sucrose}/\text{trehalose}) - \text{C}_6\text{MA} - \text{Agnique PG 264-G}/\text{Lutensol AO 8}$  at  $\alpha = 0.4125$ ,  $\delta = 0.93$ ,  $\Psi = 0.75$ ,  $\zeta = 0.38$  and  $\gamma = 0.12$ . The sample was polymerized in the ‘‘Einfrierkuvette’’ using the UV-lamp.

<b>substance</b>	<b>initial weight [g]</b>
$m_S$	1.855
$m_B$	1.299
$m_{\text{Agnique PG 264-G}}$	0.399
$m_{\text{Lutensol AO8}}$	0.030

Table 7.13: Mean hydrodynamic radius  $R_{\text{hydr}}$  of the system  $\text{H}_2\text{O}/(\text{sucrose}/\text{trehalose}) - \text{C}_6\text{MA}/\text{EGDMA} - \text{Lutensol XL 70}/\text{Agnique PG 8105-G}$  with  $\Psi = 0.75$ ,  $\zeta = 0.38$ ,  $\delta = 0.80$ ,  $\gamma_a = 0.074$ ,  $\beta = 0.15$ ,  $w_B = 0.043$  and a polymerization temperature  $T = 10^\circ\text{C}$ .

$\chi_I$	$R_{\text{hydr}} [\text{nm}]$
0.002	---
0.01	$38 \pm 3$
0.02	$37 \pm 5$
0.05	$37 \pm 1$

Table 7.14: Mean hydrodynamic radius  $R_{\text{hydr}}$  of the system  $\text{H}_2\text{O}/(\text{sucrose}/\text{trehalose}) - \text{C}_x\text{MA}/\text{EGDMA} - \text{Lutensol XL 70}/\text{Agnique PG 8105-G}$  with  $\Psi = 0.75$ ,  $\zeta = 0.38$ ,  $\delta = 0.80$ ,  $\chi_I = 0.02$  and  $\gamma_a = 0.074$ . The corresponding oil,  $w_B$ , polymerization temperature  $T$  and  $\beta$  are given in the table.

oil	$w_B$	$T [^\circ\text{C}]$	$\beta$	$R_{\text{hydr}} [\text{nm}]$
$\text{C}_6\text{MA}$	0.043	10	0.00	$36 \pm 1$
$\text{C}_6\text{MA}$	0.043	10	0.15	$39 \pm 1$
$\text{C}_6\text{MA}$	0.043	10	0.30	$53 \pm 4$
$\text{C}_6\text{MA}$	0.043	15	0.00	$42 \pm 3$
$\text{C}_6\text{MA}$	0.043	15	0.15	$37 \pm 4$
$\text{C}_6\text{MA}$	0.043	15	0.30	$53 \pm 3$
$\text{C}_6\text{MA}$	0.043	20	0.00	$43 \pm 3$
$\text{C}_6\text{MA}$	0.043	20	0.15	$41 \pm 4$
$\text{C}_6\text{MA}$	0.043	20	0.30	$75 \pm 6$
$\text{C}_6\text{MA}$	0.03	10	0.15	$35 \pm 4$
$\text{C}_{12}\text{MA}$	0.03	10	0.15	$51 \pm 5$
$\text{C}_{12}\text{MA}$	0.03	30	0.15	$44 \pm 5$

Table 7.15: Mean hydrodynamic radius  $R_{\text{hydr}}$  of the system  $\text{H}_2\text{O}/(\text{sucrose}/\text{trehalose}) - \text{C}_6\text{MA} - \text{Lutensol XL 70}/\text{Agnique PG 8105-G}$  with  $\Psi = 0.75$ ,  $\zeta = 0.38$ ,  $\delta = 0.80$ ,  $\beta = 0.00$ ,  $\gamma_a = 0.074$  and a polymerization temperature  $T = 10^\circ\text{C}$ . The oil mass fraction  $w_B$  corresponds to the chosen  $\gamma_a$ .

$\gamma_a$	$w_B$	$R_{\text{hydr}} [\text{nm}]$
0.0247	0.0143	$36 \pm 1$
0.074	0.043	$39 \pm 7$

Table 7.16: Mean hydrodynamic radius  $R_{\text{hydr}}$  of the system  $\text{H}_2\text{O}/(\text{sucrose}/\text{trehalose}) - \text{C}_{12}\text{MA}/\text{EGDMA} - \text{Lutensol XL 70}/\text{Agnique PG 8105-G}$  with  $\Psi = 0.75$ ,  $\zeta = 0.38$ ,  $\delta = 0.80$ ,  $\beta = 0.15$ ,  $w_B = 0.03$  and  $\gamma_a = 0.074$  and a polymerization temperature of  $T = 30^\circ\text{C}$ . The polymerization has been initiated via different lamps.

initiating lamp	$R_{\text{hydr}} [\text{nm}]$
microscopy lamp	$44 \pm 5$
LED Spot Luxeon Royal Blue lamp	$35 \pm 2$
SpecBright UV-LED	$21 \pm 1$

Table 7.17: Initial weights, polymerization temperature and hydrodynamic radii obtained by DLS measurements for the UV-polymerized system H<sub>2</sub>O/(sucrose/trehalose) – C<sub>6</sub>MA/EGDMA – Lutensol XL 70/Agnique PG 8105-G with  $\Psi = 0.75$ ,  $\zeta = 0.38$ ,  $\delta = 0.80$ ,  $\chi_t = 0.02$  and  $\gamma_a = 0.074$ .

$m_{\text{stock solution}}$	$m_{\text{oil}}$	$w_B$	$T$	$\beta$	$R_{\text{hydr}}$	$R_{\text{hydr}}$	$p$
[g]	[g]		[°C]		(graph.)	(calc.)	
3.199	0.1438	0.043	10	0.15	22	22	0.046
3.055	0.1393	0.0436	10	0.15	21	21	0.049
3.02	0.1378	0.0436	10	0.15	20	20	0.051
3.027	0.1369	0.0433	10	0.15	20	21	0.039
3.092	0.1401	0.0433	10	0.15	20	20	0.064
3.196	0.1447	0.0433	10	0.30	30	31	0.056
3.037	0.1365	0.043	10	0.30	27	28	0.059
3.030	0.1375	0.0434	10	0.30	29	33	0.075
3.207	0.1438	0.0429	10	0.30	30	33	0.097
3.148	0.1405	0.0427	10	0.30	31	36	0.108
3.089	0.1390	0.0431	10	0.00	20	22	0.196
3.237	0.1461	0.0432	10	0.00	24	22	0.067
3.172	0.1437	0.0433	10	0.00	20	19	0.084
3.171	0.1414	0.0427	10	0.00	20	19	0.066
3.059	0.0957	0.0303	3	0.15	16	15	0.062
3.039	0.0928	0.0296	3	0.15	14	14	0.051
3.197	0.0989	0.0300	3	0.15	16	16	0.074
3.244	0.1011	0.0302	3	0.15	15	15	0.071
3.024	0.0950	0.0305	10	0.15	15	16	0.052
3.300	0.1022	0.0300	10	0.15	15	15	0.037
3.025	0.0936	0.0300	10	0.15	15	15	0.051

$m_{\text{stock solution}}$	$m_{\text{oil}}$	$w_B$	$T$	$\beta$	$R_{\text{hydr}}$	$R_{\text{hydr}}$	$p$
[g]	[g]		[°C]		(graph.)	(calc.)	
3.019	0.0936	0.0301	17	0.15	20	20	0.064
3.133	0.0990	0.0306	17	0.15	19	18	0.048
3.065	0.0979	0.0310	17	0.15	20	20	0.054
3.223	0.1254	0.0375	10	0.15	19	18	0.052
3.089	0.1207	0.0376	10	0.15	19	17	0.079
3.155	0.1218	0.0372	10	0.15	19	18	0.048
3.253	0.1483	0.0436	15	0.15	25	25	0.046
3.225	0.1446	0.0429	15	0.15	26	26	0.052
3.062	0.1369	0.0428	15	0.15	24	25	0.060
3.030	0.1373	0.0433	15	0.15	26	26	0.036
3.078	0.1388	0.0431	20	0.15	43	47	0.060
3.027	0.1380	0.0436	20	0.15	41	47	0.073
3.095	0.1388	0.0429	20	0.15	43	46	0.054
3.069	0.1538	0.0477	20	0.15	49	57	0.100
3.257	0.1652	0.0483	20	0.15	46	52	0.107
3.102	0.1576	0.0484	20	0.15	45	50	0.076
3.135	0.1709	0.0517	27	0.15	73	83	0.101
3.161	0.1727	0.0518	27	0.15	78	86	0.073
3.110	0.1711	0.0522	27	0.15	81	90	0.071
3.113	0.1808	0.0549	35	0.15	103	129	0.136
3.060	0.1813	0.0559	35	0.15	112	139	0.156
3.065	0.1813	0.0559	35	0.15	102	124	0.125

Table 7.18: Initial weights, polymerization temperature and hydrodynamic radii obtained by DLS measurements for the UV-polymerized system H<sub>2</sub>O/(sucrose/trehalose) – C<sub>12</sub>MA/EGDMA – Lutensol XL 70/Agnique PG 8105-G with  $\Psi = 0.75$ ,  $\zeta = 0.38$ ,  $\delta = 0.80$ ,  $\chi_1 = 0.02$  and  $\gamma_a = 0.074$ .

$m_{\text{stock solution}}$	$m_{\text{oil}}$	$w_B$	$T$	$\beta$	$R_{\text{hydr}}$	$R_{\text{hydr}}$	$p$
[g]	[g]		[°C]		(graph.)	(calc.)	
3.019	0.0949	0.0305	10	0.15	18	17	0.088
3.001	0.0930	0.0301	10	0.15	18	17	0.072
3.084	0.0951	0.0299	10	0.15	18	16	0.069
3.222	0.1009	0.0304	10	0.3	21	21	0.045
3.131	0.0963	0.0298	10	0.30	21	20	0.093
3.098	0.0965	0.0302	10	0.30	21	20	0.069
3.193	0.1001	0.0304	10	0.60	46	49	0.104
3.195	0.0974	0.0296	10	0.60	44	52	0.126
3.187	0.0976	0.0297	10	0.60	40	44	0.091
3.112	0.0637	0.0201	10	0.15	15	16	0.054
3.294	0.0666	0.0198	10	0.15	15	14	0.096
3.161	0.0316	0.0099	10	0.15	12	12	0.072
3.078	0.0307	0.0099	10	0.15	14	14	0.095
3.181	0.0321	0.0099	10	0.15	13	12	0.068



### A.3 Mechanical Drawing of “Einfrierküvette”

The “Einfrierküvette” consists of a body and an exchangeable inset of 1 mm thickness, both built of brass and sealed with a sealing ring. The microemulsion sample is prepared in a testtube and afterwards filled with a pipette in this exchangeable inset. A microscope slide covers the sample on the top which is chosen as heat transfer occurs quickly due to its small thickness (0.2 mm) but also polymerization is still possible. Then a cover again built of brass is screwed on the top for fixation. The inset is exchangeable as it may not be usable anymore after the sample has been polymerized. A thickness of 1 mm for the inset has been chosen to keep the volume of the microemulsion sample small so that the freezing process takes place quickly.

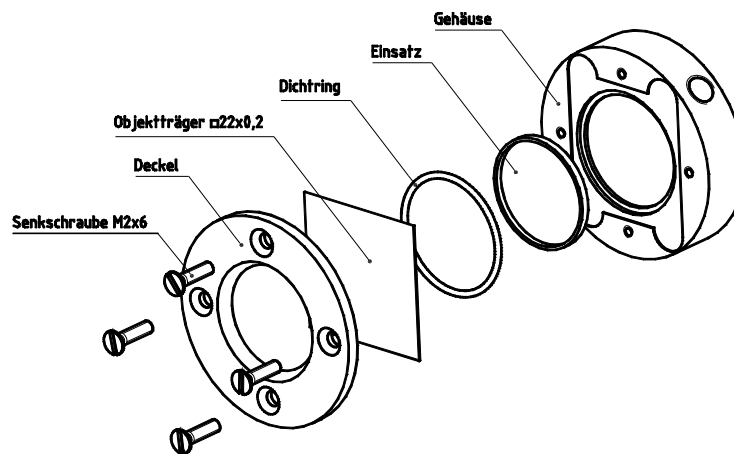


Figure 7.1: Mechanical drawing of the “Einfrierküvette”.



## References

- [1] *Microemulsions*, I.D. Plenum, New York ed. (1982).
- [2] L. M. Prince, *Microemulsions: Theory and Practice*, Academic, New York ed. (1977).
- [3] F. Lichterfeld, T. Schmeling, and R. Strey, *J. Phys. Chem.* **90** (22), 5762 (1986).
- [4] U. Olsson, U. Würz, and R. Strey, *J. Phys. Chem.* **97** (17), 4535 (1993).
- [5] S. A. Safran, *Statistical Thermodynamics of Surfaces, Interfaces, and Membranes*. (Westview Press, 1994).
- [6] W. Z. Helfrich, *Naturforsch.* **28c**, 693 (1973).
- [7] T. Sottmann and R. Strey, *J. Phys.: Condens. Matter* **8**, A39 (1996).
- [8] T. Sottmann, R. Strey, and S. H. Chen, *J. Chem. Phys.* **106** (15), 6483 (1997).
- [9] R. Strey, *Colloid Polym. Sci.* **272** (8), 1005 (1994).
- [10] W. M. Gelbart and A. Ben-Shaul, *J. Phys. Chem.* **100** (31), 13169 (1996).
- [11] O. Glatter, R. Strey, K.-V. Schubert, and E. W. Kaler, *Ber. Bunsenges. Phys. Chem.* **100** (3), 323 (1996).
- [12] M. Kahlweit, R. Strey, P. Firman, D. Haase, J. Jen, and R. Schomäcker, *Langmuir* **4** (3), 499 (1988).
- [13] H. Kunieda and K. Shinoda, *J. Colloid Interf. Sci.* **42**, 381 (1973).
- [14] J.-L. Salager, R. E. Antón, D. A. Sabatini, J. H. Harwell, E. J. Acosta, and L. I. Tolosa, *Journal of Surfactants and Detergents* **8** (1), 3 (2005).
- [15] P. A. Winsor, *Solvent Properties of Amphiphilic Compounds*, Butterworth & Co., London ed. (1954).
- [16] M. Kahlweit and R. Strey, *Angew. Chem., Int. Ed. Engl.* **24** (8), 654 (1985).
- [17] K. Shinoda, *Solvent Properties of Surfactant Solutions*. (Marcel Dekker, New York, 1967).
- [18] M. Kahlweit and R. Strey, *Angew. Chem., Int. Ed. Engl.* **24**, 654 (1985).
- [19] M. Kahlweit, R. Strey, and G. Busse, *J. Phys. Chem.* **94** (10), 3881 (1990).
- [20] M. Kahlweit, R. Strey, and G. Busse, *Phys. Rev. E* **47**, 4197 (1993).
- [21] R. Aveyard, B. P. Binks, and P. D. I. Fletcher, *Langmuir* **5**, 1210 (1989).

- [22] D. I. Fletcher and D. I. Horsup, *J. Chem. Soc. Faraday Trans.* **88**, 855 (1992).
- [23] F. M. Pavel, *Journal of Dispersion Science and Technology* **25** (1), 1 (2004).
- [24] J. O. Stoffer and T. Bone, *J. Dispersion Sci. Technol.* **1** (1), 37 (1980).
- [25] J. O. Stoffer and T. Bone, *J. Polym. Sci., Polym. Chem. Ed.* **18** (8), 2641 (1980).
- [26] J. O. Stoffer and T. Bone, *J. Dispersion Sci. Technol.* **1** (4), 393 (1980).
- [27] C. H. Chew and L. M. Gan, *J. Polym. Sci. Polym. Chem. Ed.* **23** (8), 2225 (1985).
- [28] S. D. Desai, R. D. Gordon, A. M. Gronda, and E. L. Cussler, *Current Opinion in Colloid & Interface Science* **1**, 519 (1996).
- [29] L. M. Gan and C. H. Chew, *J. Dispersion Sci. Technol.* **4** (3), 291 (1983).
- [30] L. M. Gan and C. H. Chew, *J. Dispersion Sci. Technol.* **5** (2), 179 (1984).
- [31] W. R. P. Raj, M. Sasthav, and H. M. Cheung, *Langmuir* **7** (11), 2586 (1991).
- [32] W. R. P. Raj, M. Sasthav, and H. M. Cheung, *Langmuir* **8** (8), 1931 (1992).
- [33] W. R. P. Raj, M. Sasthav, and H. M. Cheung, *J. Appl. Polym. Sci.* **47** (3), 499 (1993).
- [34] M. Sasthav and H. M. Cheung, *Langmuir* **7** (7), 1378 (1991).
- [35] M. Sasthav, W. R. P. Raj, and H. M. Cheung, *J. Colloid Interf. Sci.* **152** (2), 376 (1992).
- [36] O. Lade, *Dissertation, University of Cologne, Cuvillier Verlag Göttingen* (2001).
- [37] C. Holzscherer, J. C. Wittmann, D. Guillon, and F. Candau, *Polymer* **31**, 1978 (1990).
- [38] C. C. Co, *Soft Matter* **4**, 658 (2008).
- [39] H. Dave, F. Gao, J.-H. Lee, M. Liberatore, C.-C. Ho, and C. C. Co, *Nature materials* **6** (4), 287 (2007).
- [40] H. Dave, F. Gao, M. Schultz, and C. C. Co, *Colloids and Surfaces A* **296**, 45 (2007).
- [41] F. Gao, C.-C. Ho, and C. C. Co, *J. Am. Chem. Soc.* **126**, 12746 (2004).
- [42] F. Gao, C.-C. Ho, and C. C. Co, *Macromolecules* **39**, 9467 (2006).
- [43] A. Simperler, A. Kornherr, R. Chopra, P. A. Bonnet, W. Jones, W. D. S. Motherwell, and G. Zifferer, *J. Phys. Chem. B* **110** (39), 19678 (2006).
- [44] H. Kunieda and K. J. Shinoda, *Dispersion Sci. Technol.* **3**, 233 (1982).

- [45] K. Shinoda and S. Friberg, *Adv. Colloid Interface Sci.* **4**, 281 (1975).
- [46] G. M. Schneider, *Pure Appl. Chem.* **55**, 479 (1983).
- [47] T. Sottmann, *Dissertation, Georg-August-Universität zu Göttingen, Cuvillier Verlag Göttingen* (1997).
- [48] C. Stubenrauch, B. Paepflow, and G. H. Findenegg, *Langmuir* **13** (14), 3652 (1997).
- [49] S. Burauer, T. Sachert, T. Sottmann, and R. Strey, *Phys. Chem. Chem. Phys.* **1**, 4229 (1999).
- [50] T. Sottmann and R. Strey, in *Fundamentals of Interface and Colloid Science*, edited by J. Lyklema (Academic Press, 2005), Vol. V.
- [51] A. Evilevitch, B. T. Jönsson, U. Olsson, and H. Wennerström, *Langmuir* **17** (22), 6893 (2001).
- [52] B. Lindmann, K. Shinoda, U. Olsson, D. Anderson, G. Karlstrom, and H. Wennerström, *Colloids Surf.* **38** (1-3), 205 (1989).
- [53] R. Messenger, A. Ott, D. Chatenay, W. Urbach, and D. Langevin, *Phys. Rev. Lett.* **60** (14), 1410 (1988).
- [54] M. Gradzielski, D. Langevin, L. Magid, and R. Strey, *J. Phys. Chem.* **99** (35), 13232 (1995).
- [55] M. Gradzielski, D. Langevin, T. Sottmann, and R. Strey, *J. Chem. Phys.* **104** (10), 3782 (1996).
- [56] L. Belkoura, C. Stubenrauch, and R. Strey, *Langmuir* **20**, 4391 (2004).
- [57] A. Bernheim-Groswasser, T. Tlustý, S. A. Safran, and Y. Talmon, *Langmuir* **15** (17), 5448 (1999).
- [58] A. Bernheim-Groswasser, E. Wachtel, and Y. Talmon, *Langmuir* **16** (9), 4131 (2000).
- [59] A. Bernheim-Groswasser, R. Zana, and Y. Talmon, *J. Phys. Chem. B* **104** (17), 4005 (2000).
- [60] S. Burauer, *Dissertation, University of Cologne, Cuvillier Verlag Göttingen* (2001).
- [61] S. Burauer, L. Belkoura, C. Stubenrauch, and R. Strey, *Colloid Surface A* **228** (1-3), 159 (2003).
- [62] W. Jahn and R. Strey, *J. Phys. Chem.* **92** (8), 2294 (1988).
- [63] R. Strey, W. Jahn, G. Porte, and P. Basserau, *Langmuir* **6** (11), 1635 (1990).
- [64] T. Hellweg, A. Brulet, and T. Sottmann, *Phys. Chem. Chem. Phys.* **2** (22), 5168 (2000).

- [65] M. Kahlweit, R. Strey, T. Sottmann, G. Busse, B. Faulhaber, and J. Jen, *Langmuir* **13** (10), 2670 (1997).
- [66] D. Langevin, *Ber. Bunsenges. Phys. Chem.* **100** (3), 336 (1996).
- [67] M. Kahlweit, R. Strey, and R. Schomäcker, in *Reactions in Compartmentalized Liquids*, edited by W. K. a. R. Schomäcker (Springer-Verlag, Berlin Heidelberg, 1989).
- [68] T. Tlusty, S. A. Safran, and R. Strey, *Phys. Rev. Lett.* **86** (6), 1244 (2000).
- [69] A. G. Zilman and S. A. Safran, *Phys. Rev. E* **66**, 051107 (2002).
- [70] O. Lade, K. Beizai, T. Sottmann, and R. Strey, *Langmuir* **16**, 4122 (2000).
- [71] G. Odian, *Principles of Polymerization*. (McGraw-Hill Book Company, New York, 1970).
- [72] H. N. Friedlander, H. E. Harris, and J. G. Pritchard, *J. Polymer. Sci. A-1* (4), 649 (1966).
- [73] C. S. Marvel and C. L. Levesque, *J. Am. Chem. Soc.* **60** (2), 280 (1938).
- [74] M. Antonietti, R. Basten, and S. Lohmann, *Macromol. Chem. Phys.* **196**, 441 (1995).
- [75] M. Antonietti and C. Göltner, *Angew. Chem.* **109**, 944 (1997).
- [76] J. Barton, *Prog. Polym. Sci.* **21**, 399 (1996).
- [77] F. Candau, in *Polymerization in Organized Media*, edited by C. M. Paleos (Gordon and Breach Science Publishers, Philadelphia, 1992).
- [78] F. Candau, *Macromol. Symp.* **92**, 169 (1995).
- [79] K. M. Lusvardi, K.-V. Schubert, and E. W. Kaler, *Ber. Bunsenges. Phys. Chem.* **100**, 373 (1996).
- [80] J. Sjöblom, R. Lindberg, and S. E. Friberg, *Adv. Colloid Interface Sci.* **95**, 125 (1996).
- [81] S. S. Atik and K. J. Thomas, *J. Am. Chem. Soc.* **103**, 4279 (1981).
- [82] F. Candau, Y. S. Leong, and R. M. Fitch, *J. Polym. Sci., Polym. Chem. Ed.* **23**, 193 (1985).
- [83] M. T. Carver, F. Candau, and R. M. Fitch, *J. Polym. Sci., Part A: Polym. Chem.* **27**, 7179 (1989).
- [84] M. T. Carver, U. Dreyer, R. Knoesel, F. Candau, and R. M. Fitch, *J. Polym. Sci., Part A: Polym. Chem.* **27**, 2161 (1989).
- [85] M. T. Carver, E. Hirsch, C. Wittmann, R. M. Fitch, and F. Candau, *J. Phys. Chem.* **93**, 4867 (1989).

- [86] L. M. Gan, C. H. Chew, I. Lye, and T. Imae, *Polym. Bull.* **25**, 193 (1991).
- [87] L. M. Gan, C. H. Chew, S. C. Ng, and S. E. Loh, *Langmuir* **9**, 2799 (1993).
- [88] J. S. Guo, E. D. Sudol, M. S. El-Aasser, and J. W. Vanderhoff, *J. Polym. Sci., Part A: Polym. Chem.* **30**, 691 (1992).
- [89] P. Y. Chow and L. M. Gan, *Adv. Polym. Sci.* **175**, 257 (2005).
- [90] H.-P. Hentze and E. W. Kaler, *Current Opinion in Colloid & Interface Science* **8**, 164 (2003).
- [91] M. A. López-Quintela, *Current Opinion in Colloid & Interface Science* **8**, 137 (2003).
- [92] S. A. Miller, J. H. Ding, and D. L. Gin, *Current Opinion in Colloid & Interface Science* **4**, 338 (1999).
- [93] C. E. Martimer, *Das Basiswissen der Chemie*, 6. ed. (Thieme Georg Verlag, Stuttgart, 1996).
- [94] B. Tieke, *Makromolekulare Chemie*, 1. ed. (Wiley-VCH, Weinheim, 1997).
- [95] K. P. C. Vollhardt and N. Schore, *Organische Chemie*, 2. ed. (Wiley-VCH, Weinheim, 1995).
- [96] C. Walling, *Polym. Prepr. Am. Chem. Soc. Div. Polym. Chem.* **11**, 721 (1970).
- [97] O. Nuyken and G. Lattermann, *Handbook of Polymer Synthesis*. (Marcel Dekker, Inc., New York, 1992).
- [98] H. G. O. Becker, *Einführung in die Photochemie*, 3rd ed. (Wiley-VCH, Weinheim, 1991).
- [99] <http://www.ciba.com>.
- [100] [http://www.chemiedidaktik.uni-wuppertal.de/alte\\_seite\\_du/material/examensarbeit/pmma/pmma3.pdf](http://www.chemiedidaktik.uni-wuppertal.de/alte_seite_du/material/examensarbeit/pmma/pmma3.pdf).
- [101] O. Kratky, H. Leopold, and H. Stabinger, *Angew. Phys.* **27**, 273 (1969).
- [102] H. Stabinger, H. Leopold, and O. Kratky, *Monatsh. Chem* **98**, 436 (1967).
- [103] B. J. Berne and R. Pecora, *Dynamic Light Scattering: With Applications to Chemistry, Biology, and Physics*. (John Wiley & Sons, New York, 1978).
- [104] B. Chu, *Laser Light Scattering: Basic Principles and Practice*. (Academic Press, New York, 1985).
- [105] K. S. Schmitz, *An Introduction to Dynamic Light Scattering by Macromolecules*. (Academic Press, San Diego, 1990).
- [106] P. Stepanek, in *Dynamic Light Scattering - The method and some applications*

edited by W. Brown (Clarendon Press, Oxford, 1993).

- [107] R. S. Stock and W. H. Ray, *J. o. Polym. Sci.: Polym. Phys.* **23**, 1393 (1985).
- [108] R. Winter and F. Noll, *Methoden der Biophysikalischen Chemie*. (Teubner Studienbücher, Stuttgart, 1998).
- [109] A. J. F. Siegert, *MIT Rad. Lab. Report* **465** (1943).
- [110] B. J. Berne and R. Pecora, *Dynamic Light Scattering*. (Wiley, New York, 1976).
- [111] W. B. Russel and A. B. Glendinning, *J. Chem. Phys.* **74**, 948 (1981).
- [112] S. W. Provencher, *Comput. Phys. Commun.* **27** (3), 229 (1982).
- [113] S. W. Provencher, *Comput. Phys. Commun.* **27** (3), 213 (1982).
- [114] S. W. Provencher and P. Stepanek, *Particle & Particle Systems Characterization* **13** (5), 291 (1996).
- [115] S. H. Chen, *Annu. Rev. Phys. Chem.* **37**, 351 (1986).
- [116] O. Glatter, R. Strey, K. V. Schubert, and E. W. Kaler, *Phys. Chem. Chem. Phys.* **100** (3), 323 (1996).
- [117] P. Lindner, in *Neutrons, X-rays and Light: Scattering Methods Applied to Soft Condensed Matter*, edited by P. Lindner and T. Zemb (Elsevier, Amsterdam, 2002).
- [118] Y. B. Melnichenko and G. D. Wignall, *J. Appl. Phys.* **102** (2) (2007).
- [119] P. N. Pusey, in *Neutrons, X-rays and Light: Scattering Methods Applied to Soft Condensed matter*, edited by P. Lindner and T. Zemb (Elsevier, Amsterdam, 2002).
- [120] L. Bachmann and E. Mayer, *Physics of water and ice: Implications for cryofixation*. (Springer-Verlag, Berlin, 1987).
- [121] T. Gulik-Krzywicki, *Current Opinion in Colloid & Interface Science* **2**, 132 (1997).
- [122] H. W. Meyer and W. Richter, *Micron* **32**, 615 (2001).
- [123] H. Kunieda and N. Ishikawa, *J. Colloid Interf. Sci.* **107** (1), 122 (1985).
- [124] H. Kunieda and K. Shinoda, *J. Colloid Interf. Sci.* **107** (1), 107 (1985).
- [125] T. Sottmann, M. Lade, M. Stolz, and R. Schomäcker, *Tenside, Surfact., Deterg.* **39**, 20 (2002).
- [126] M. Kahlweit, G. Busse, and B. Faulhaber, *Langmuir* **11**, 3382 (1995).
- [127] K. Kluge, *Dissertation, University of Cologne, Logos Verlag Berlin* (2000).
- [128] K. Kluge, C. Stubenrauch, T. Sottmann, and R. Strey, *Tenside Surf. Det.* **38**, 30 (2001).



- [129] J. Schulte, S. Enders, and K. Quitzsch, *Colloid Polym. Sci.* **277**, 827 (1999).
- [130] W. v.Rybinski and K. Hill, *Angew. Chem.* **110**, 1394 (1998).
- [131] L. D. Ryan, K.-V. Schubert, and E. W. Kaler, *Langmuir* **13** (6), 1510 (1997).
- [132] H. Egger, *Diploma Thesis, University of Cologne* (1998).
- [133] L. D. Ryan and E. W. Kaler, *Langmuir* **13**, 5222 (1997).
- [134] M. H. G. Penders and R. Strey, *J. Phys. Chem.* **99**, 10313 (1995).
- [135] J. Reimer, O. Södermann, T. Sottmann, K. Kluge, and R. Strey, *Langmuir* **19**, 10692 (2003).
- [136] K. V. Schubert and E. W. Kaler, *Ber. Bunsenges. Phys. Chem.* **100**, 190 (1996).
- [137] T. Sottmann, K. Kluge, R. Strey, J. Reimer, and O. Södermann, *Langmuir* **18**, 3058 (2002).
- [138] C. C. Co, *PhD Thesis, University of Delaware* (2000).
- [139] H. Egger, T. Sottmann, R. Strey, C. Valero, and A. Berkessel, *Tenside Surf. Det.* **39** (2), 17 (2002).
- [140] C. H. Chew, T. D. Li, L. H. Gan, C. H. Quek, and L. M. Gan, *Langmuir* **14** (21), 6068 (1998).
- [141] T. H. Chieng, L. M. Gan, C. H. Chew, L. Lee, and S. C. Ng, *Langmuir* **11** (9), 3321 (1995).
- [142] H. Endo, J. Allgaier, G. Gompper, B. Jakobs, M. Monkenbusch, D. Richter, T. Sottmann, and R. Strey, *Phys. Rev. Lett.* **85** (1), 102 (2000).
- [143] H. Endo, M. Mihailescu, M. Monkenbusch, J. Allgaier, G. Gompper, D. Richter, B. Jakobs, T. Sottmann, R. Strey, and I. Grillo, *J. Chem. Phys.* **115** (1), 580 (2001).
- [144] H. Frielinghaus, D. Byelov, J. Allgaier, D. Richter, B. Jakobs, T. Sottmann, and R. Strey, *Appl. Phys. A* **74**, 408 (2002).
- [145] G. Gompper, D. Richter, and R. Strey, *J. Phys.: Condens. Matter* **13**, 9055 (2001).
- [146] B. Jakobs, T. Sottmann, and R. Strey, *Tenside Surf. Det.* **37** (6), 357 (2000).
- [147] B. Jakobs, T. Sottmann, R. Strey, J. Allgaier, L. Willner, and D. Richter, *Langmuir* **15** (20), 6707 (1999).
- [148] R. Strey, M. Brandt, B. Jakobs, and T. Sottmann, *Surface Science and Catalysis* **132**, 39 (2001).
- [149] A. Kabalnov, U. Olsson, K. Thuresson, and H. Wennerström, *Langmuir* **10** (12), 4509 (1994).

- [150] K. Thuresson, G. Karlström, and B. Lindmann, *J. Phys. Chem.* **99** (11), 3823 (1995).
- [151] K. Thuresson, S. Nilsson, and B. Lindmann, *Langmuir* **12** (10), 2412 (1996).
- [152] C. Frank, T. Sottmann, C. Stubenrauch, J. Allgaier, and R. Strey, *Langmuir* **21** (20), 9058 (2005).
- [153] M. Nilsson, O. Sodermann, and I. Johansson, *Colloid Polym. Sci.* **284** (11), 1229 (2006).
- [154] S. S. Atik and K. J. Thomas, *J. Am. Chem. Soc.* **104**, 5868 (1982).
- [155] S. S. Atik and K. J. Thomas, *J. Am. Chem. Soc.* **105**, 4515 (1983).
- [156] L. M. Gan, C. H. Chew, I. Lye, L. Ma, and G. Li, *Polymer* **34**, 3860 (1993).
- [157] C. Schaubert and G. Riess, *Makromol. Chem.* **190**, 725 (1989).
- [158] A. Jayakrishnan and D. O. Shah, *J. Polym. Sci. Polym. Chem. Ed.* **22**, 3967 (1984).
- [159] M. R. Ferrick, J. Murtagh, and J. K. Thomas, *Macromolecules* **22**, 1515 (1989).
- [160] V. H. Perez-Luna, J. E. Puig, V. M. Castano, B. E. Rodriguez, A. K. Murthy, and E. W. Kaler, *Langmuir* **6**, 1040 (1990).
- [161] L. M. Gan, C. H. Chew, K. C. Lee, and S. C. Ng, *Polymer* **35**, 2659 (1994).
- [162] L. M. Gan, C. H. Chew, J. H. Lim, K. C. Lee, and L. H. Gan, *Colloid Polym. Sci.* **272**, 1082 (1994).
- [163] J. E. Puig, V. H. Perez-Luna, M. Perez-Gonzales, E. R. Macias, B. E. Rodriguez, and E. W. Kaler, *Colloid Polym. Sci.* **271**, 114 (1993).
- [164] J. D. Morgan, K. M. Lusvardi, and E. W. Kaler, *Macromolecules* **30** (7), 1897 (1997).
- [165] J. D. Morgan and E. W. Kaler, *Macromolecules* **31**, 3197 (1998).
- [166] C. C. Co and E. W. Kaler, *Macromolecules* **31**, 3203 (1998).
- [167] S. Jiang, E. D. Sudol, V. L. Dimonie, and M. S. El-Aasser, *Macromolecules* **40** (14), 4910 (2007).
- [168] C. C. Co, P. Cotts, S. Burauer, R. d. Vries, and E. W. Kaler, *Macromolecules* **34**, 3245 (2001).
- [169] C. C. Co, R. d. Vries, and E. W. Kaler, *Macromolecules* **34**, 3224 (2001).
- [170] R. d. Vries, C. C. Co, and E. W. Kaler, *Macromolecules* **34**, 3233 (2001).
- [171] M. J. Gerber and L. M. Walker, *Langmuir* **3**, 941 (2006).

- [172] K. A. Topp, *PhD Thesis University of Sydney, Sydney, 2006*.
- [173] T. Tlusty, S. A. Safran, R. Menes, and R. Strey, *Phys. Rev. Lett.* **78**, 2616 (1997).
- [174] P. Uhrmeister, *Dissertation, University of Cologne, Cuvillier Verlag Göttingen (2002)*.
- [175] R. Strey, *Habilitationsschrift, Georg-August-Universität zu Göttingen (1992)*.
- [176] X. Gong, *pers. communication*.
- [177] W. R. P. Raj, M. Sasthav, and H. M. Cheung, *Polymer* **36** (13), 2637 (1995).
- [178] W. R. P. Raj, M. Sasthav, and H. M. Cheung, *Polymer* **34** (15), 3305 (1993).
- [179] M. Antonietti and H.-P. Hentze, *Colloid Polym. Sci.* **274**, 696 (1996).
- [180] F. Yan and J. Texter, *Soft Matter* **2**, 109 (2006).
- [181] F. Candau, Z. Zekhnini, and J. P. Durand, *J. Colloid Interf. Sci.* **114**, 398 (1986).
- [182] C. Holtzscherer and F. Candau, *Colloids Surf.* **29**, 411 (1988).
- [183] C. Holtzscherer and F. Candau, *J. Colloid Interf. Sci.* **125**, 97 (1988).
- [184] M. Antonietti, R. A. Caruso, C. G. Göltner, and M. C. Weissenberger, *Macromolecules* **32** (5), 1383 (1999).
- [185] M. Antonietti and H.-P. Hentze, *Chemie Ingenieur Technik* **69** (3), 369 (1997).
- [186] W. Meier, *Langmuir* **12** (26), 6341 (1996).
- [187] D. Pawlowski and B. Tieke, in *Progress in Colloid and Polymer Science*, edited by G. Lagaly and W. Richtering (2004), Vol. 129, pp. 24
- [188] F. Yan and J. Texter, *Adv. Colloid Interface Sci.* **128 - 130**, 27 (2006).
- [189] R. Strey, J. Winkler, and L. Magid, *J. Phys. Chem.* **95** (19), 7502 (1991).
- [190] M. Teubner and R. Strey, *J. Chem. Phys.* **87** (5), 3195 (1987).
- [191] S.-H. Chen, S.-L. Chang, and R. Strey, *J. Phys. Chem.* **93**, 1907 (1990).
- [192] S.-H. Chen, S.-L. Chang, and R. Strey, *Prog. Colloid Polym. Sci.* **81**, 30 (1990).
- [193] C. G. Vonk, J. F. Billmann, and E. W. Kaler, *J. Chem. Phys.* **88** (6), 3970 (1988).
- [194] F. Schmid and M. Schick, *Phys. Rev. E* **49** (1), 494 (1994).
- [195] F. Nallet, R. Laversanne, and D. Roux, *J. Phys. II France* **3**, 487 (1993).
- [196] A. Caillé, *Hebdo. Acad. Sci. Paris* **B 274**, 891 (1972).

- 
- [197] C. J. Glinka, J. M. Rowe, and J. G. LaRock, *J. Appl. Cryst.* **19**, 427 (1986).
- [198] Y. Suganuma, M. Imai, and K. Nakaya, *J. Appl. Cryst.* **40**, 303 (2007).
- [199] H. Frielinghaus, *pers. communication*.
- [200] R. N. Haward and R. J. Young, *The Physics of Glassy Polymers*. (Chapman Hall Press, Cambridge, 1997).
- [201] H. Ge, C.-L. Zhao, S. Porzo, L. Zhuo, H. T. Davis, and L. E. Scriven, *Macromolecules* **39** (16), 5531 (2006).

## Acknowledgement

I would like to thank Prof. Dr. Reinhard Strey for the interesting topic and the possibility to work on it independently. You helped me to solve problems by discussing various ideas whenever it was necessary. Furthermore, I am very grateful for the possibility of numerous oversea stays. Thanks for letting me go to Australia for the first 9 months of my PhD and thanks also for the opportunity to do SEM experiments in the US. I have learned a lot, not only scientifically. I treasure your trust sending me to numerous conferences. Thanks for this great time – I think my PhD was the best one could ever have.

I would also like to thank Prof. Dr. Klaus Meerholz for reviewing my thesis as a second referee and Prof. Dr. Axel Klein for taking over the chairman position during my defence.

A very big thanks goes to Dr. Thomas Sottmann. Without your help this thesis would have never become what it is now. I am very grateful for the time you spent with me discussing my research problems; without you there would not be any SEM picture of polymerized structures, probably no droplet polymerization etc. etc. Thank you also for your support while I was staying overseas – in Sydney, at conferences or at Ted`s. You did not only have time for research – you always had an open ear for me as well! Also many thanks for the in-depth correction of this work.

I would like to thank Prof. Greg Warr and his entire working group for the friendly welcoming when I arrived in Sydney. Dear Greg, thank you for all your support during the first 9 months of my PhD. You know I had a great time. If I had the choice I would have cut myself in half and one half of mine would have stayed in Australia. But I will come back – at least for a visit. At this point I would also like to thank Dr. Annabelle Blom who spent a lot of time and energy explaining me how to use the AFM. I always could rely on you and you never gave up. Thanks for this.

The SEM experiments are carried out at the University of Minnesota in collaboration with Prof. H. Ted Davis. I would like to thank you not only for the possibility to investigate the structures of my polymerized samples but also for your and Kathy`s kind hospitality. Thank you very much for letting me stay twice at your place for two weeks. You made

me feel welcome and made my stay a very positive experience. Thanks also to Dr. Xiaobo Gong who performed all the SEM experiments. Dear Xiaobo, thank you not only for all the time you spent on the samples but also for showing me around everywhere in Minneapolis. It was great to meet you and I hope I will see you and Dion again!

I would like to thank Dr. Lhouissane Belkoura for taking the electron microscopy images of my samples. Thank you for your effort and your ideas on how to solve all the problems occurred during the imaging process! I also would like to thank you for keeping the DLS experiment running and repairing the computer even on Christmas.

Dr. Mark A. Sanders and Prof. Dr. Jayesh Bellare helped me with the polarizing microscopy image.

During my PhD I had two Spezialpraktikanten. Michael Klostermann helped me investigating the influence of sugar on the phase behavior for systems containing technical-grade surfactants and Oleg Klems gave me a hand during polymerizing the oil-in-water droplets and analyzing their size with DLS. Thank you to both of you for your great help! Thanks also to Michael for reading parts of this thesis. Last but not least I would like to thank Verena Posselt for explaining me how to fit a lamellar SANS curve – thanks for your time.

The lab 253 was the best lab one could have wished. Thank you to Dr. Thomas Wielpütz, Dr. Tobias Foster and Dr. David Ghosh for having such great labmates and for the pleasant atmosphere. Without you, the time could have been much more boring. David, I am also very happy about you reading my thesis. Thanks. Michael Meyer gave his best keeping the good atmosphere in lab 253 after the others left – and I think he did a great job. Thanks for joining me and for reading my thesis. Good luck with your PhD.

Mein kleiner Indianer, thank you for all your support during the last years. Kleine Indianer grow up, der Häuptling slowly disappears (hopefully!) and I am looking forward to the future!

Last but not least I would like to thank my parents for their outstanding support during my studies. Thank you not only for financing my studies but also for taking over so much

other work whenever there was no time for me to deal with it. You were always there when I needed you.

This research project was partly financed by the Arbeitsgemeinschaft industrieller Forschungsvereinigungen "Otto von Guericke" e.V. I am grateful to the DFG for sponsoring two conferences, both in the US, and one following research stay at the University of Minnesota.





Ich versichere, dass ich die von mir vorgelegte Dissertation selbstständig angefertigt, die benutzten Quellen und Hilfsmittel vollständig angegeben und die Stellen der Arbeit – einschließlich Tabellen, Karten und Abbildungen –, die anderen Werken im Wortlaut oder dem Sinn nach entnommen sind, in jedem Einzelfall als Entlehnung kenntlich gemacht habe; dass die Dissertation noch keiner anderen Fakultät oder Universität zur Prüfung vorgelegen hat; dass sie – abgesehen von unten angegebenen Teilpublikationen – noch nicht veröffentlicht worden ist sowie, dass ich eine solche Veröffentlichung vor Abschluss des Promotionsverfahrens nicht vornehmen werde. Die Bestimmungen der Promotionsordnung sind mir bekannt. Die von mir vorgelegte Dissertation ist von Prof. Dr. Reinhard Strey betreut worden.

Köln, den 19. August 2008



# Curriculum Vitae

Regina Schwering name

21.03.1978 born

## academic carrier

PhD under Prof. Strey, Institut für Physikalische Chemie, Universität zu Köln, in collaboration with Prof. Warr, School of Chemistry, University of Sydney, Australia, and Prof. Davis, Department of Chemical Engineering & Materials Science, University of Minnesota, U.S. since 07/2005

diploma thesis under Prof. Strey, Universität zu Köln  
“Sugar-based microemulsions as candidates for templates of nanostructured materials” 11/2004 – 06/2005

Dipl. Chemikerin, Universität zu Köln 10/2000 – 06/2005

Dipl. Finanzwirtin (FH), Fachhochschule für Finanzen, Nordkirchen 08/1997 – 08/2000

## research experience

Prof. Wandrey, Institut für Biotechnologie der Forschungszentrum Jülich GmbH 08/2002

Prof. Deacon, School of Chemistry, Monash University, Australia 11/2003 – 05/2004

Prof. Warr, School of Chemistry, University of Sydney, Australia 07/2005 – 03/2006

Prof. Davis, Department of Chemical Engineering & Materials Science, University of Minnesota, U.S. 07/2007 and 04/2008

## school

high school, Marienschule Euskirchen, Abitur 1988 - 1997

primary school, Schule Amelsbüren, Münster, and Franziskusschule, Euskirchen 1984 - 1988